Hydrocarbon Phase Behaviors and Water-driven Flow in Kerogen Nanoporous Media

by

Yinuo Zhao

A thesis submitted in partial fulfillment of the requirements for the degree of

Doctor of Philosophy

in

Petroleum Engineering

Department of Civil and Environmental Engineering

University of Alberta

ABSTRACT

Hydrocarbon recovery from shale media has greatly contributed to the global energy supply and has been constantly reshaping the energy sector. Unlike conventional reservoirs, shale has an extensive network of tiny pores in the range of a few nanometers. Besides, an extensive amount of nanopores can be connected to macropores/natural fractures where the confinement effect can be negligible, resulting in the total volume of nanopores comparable to that of connected macropores/natural fractures. The multi-scale structure of shale can significantly affect the phase behaviors of multi-component hydrocarbon mixtures during the production process, which plays a crucial role in the estimation of ultimate oil recovery, well productivity, and reserve estimation as well as ultimately the policy making.

To understand the multi-phase transitions of the multi-component fluid mixtures in multi-scale volumes, Density functional theory (DFT) is used by explicitly considering fluid-surface interaction, inhomogeneous density distribution in nanopores and interplay between nanopores and connected bulk. We find that as system pressure decreases, while lighter components are continuously released from nanopores, heavier components accumulate within. The bubble point pressure of nanoconfined hydrocarbon mixtures is thus significantly suppressed from the bulk bubble point, to below the bulk dew point, in line with our previous experiments. The interplay effect between nanoscale pore and connected fracture/macropore is studied by varying the volume partition of these two regions. We find that due to the competitive adsorption in nanopores, the bulk bubble point pressure increases in line with previous experimental work. vapor-like and liquid-like phases can coexist in nanopores when pressure is between the bubble and dew point pressures of nanoconfined fluids, both of which are much lower than those of the originally

injected hydrocarbon mixtures. Furthermore, the heterogeneous PSD effect is studied by including different sizes of nanopores in the multi-scale system. We find phase transitions first occur in the bulk region, then the larger pores followed by the smaller pores. When fluids in one specific pore begin to vaporize, in other pores, the heavier component would be adsorbed, while the lighter component would be released, which suppresses the phase transitions in the smaller pores because of the heavier component accumulation. Thereafter, by comparing the phase behaviors of nanoconfined C_1-C_3 mixture in a canonical ensemble from Engineering DFT and EOS-based models, we find that adding adsorption layer effect is imperative for vapor phase properties and critical density calculation in the canonical ensemble. These works should provide important insights into the effect of PSD and interplay between nanopores and macropores/fractures in actual shale oil production processes as well as the applicability of PR-EOS in nanoconfinement.

On the other hand, there are numerous ultra-narrow pore throats (sub-2-nm) exist in shale media. The ultra-narrow pore throats can result in excessively high capillary pressure for water-oil two-phase displacement, which is closely related to oil migration and ultimate productivity. we study water-oil two-phase displacement through 2-nm kerogen pore throats from a molecular perspective. MD simulation is used as a benchmark to access the applicability of the Young-Laplace equation. We find that although the Type II-C kerogen is generally oil-wet, water has an excellent displacement efficiency without oil film on the substrate thanks to the hydrogen bonding. Unlike previous works about inorganic pore throats, we find that the capillary pressure from the Y-L equation has an excellent agreement with the breakthrough pressure from the MD simulations for ~2 nm kerogen pore throats. This work should provide important guidance to numerical modeling of the oil recovery process in shale formations as well as optimization of shale/tight oil recovery.

PREFACE

A version of Chapter 2 has been published as Zhao, Y., Wang, Y., Zhong, J., Xu, Y., Sinton, D., & Jin, Z. (2018). Bubble Point Pressures of Hydrocarbon Mixtures in Multiscale Volumes from Density Functional Theory. Langmuir, 2018, 34, 14058-14068. Zhao, Y. is responsible for performing DFT calculation, analysis data, and manuscript composition. Wang, Y. is responsible for performing DFT calculations. Zhong, J. is responsible for revising the manuscript. Xu, Y. is responsible for drawing the schematic figure for shale reservoir. Sinton, D. is responsible for revising the manuscript. Jin Z. is the supervisory author and is involved in conceiving the problem, designing the project and manuscript composition.

A version of Chapter 3 has been published as Zhao, Y., & Jin, Z. (2019). Hydrocarbon-Phase Behaviors in Shale Nanopore/Fracture Model: Multiscale, Multicomponent, and Multiphase. SPE J, 24 (06), 2526-2540. Zhao, Y. is responsible for performing DFT calculation, analysis data, and manuscript composition. Jin Z. is the supervisory author and is involved in theoretical development, conceiving the problem, designing the project and manuscript composition.

A version of Chapter 4 has been published as Zhao, Y., & Jin, Z. (2021). Hydrocarbon mixture phase behavior in multi-scale systems in relation to shale oil recovery: The effect of pore size distributions. Fuel, 291 (2021), 120141. Zhao, Y. is responsible for the theoretical development, performing DFT calculation, analysis data, and manuscript composition. Jin Z. is the supervisory author and is involved in theoretical development, conceiving the problem, designing the project and manuscript composition.

A version of Chapter 6 has been submitted to SPE J. for publication as Zhao, Y., Li, W., Zhan, S., & Jin, Z. (2021). Oil Displacement by Water Through an Ultra-Narrow Kerogen Pore Throat: a

Molecular Dynamic Study. Zhao, Y. is responsible for the model construction, performing molecular simulation, analysis, and manuscript composition. Li, W. is responsible for the IFT simulation guidance, H-bond analysis guidance and partial revision of the manuscript. Zhan. S. is responsible for kerogen pore simulation guidance and VMD software guidance. Jin Z. is the supervisory author and is involved in conceiving the problem, designing the project and manuscript composition.

Chapter 5 is from a work done by Zhao, Y. Lu, C. & Jin, Z. (2020). This work has never been published elsewhere. Zhao, Y. is responsible for performing DFT calculation, analysis data, and writeup composition. Lu, C. is responsible for performing PR-EOS calculations. Jin Z. is involved in conceiving the problem, designing the project and writeup composition.

Chapter 1 (Introduction Chapter) outlines the research background, problem statement, research objectives, and structure of the thesis. Chapter 7 (Conclusion Chapter) summarizes the conclusions reached in this thesis as well as the recommendations for future research.

DEDICATION

This thesis work is dedicated to my dearest parents: my mother Mrs. Lili Zhang and my father Mr. Qinglin Zhao, who have always loved me unconditionally and have been a constant source of support and encouragement during the challenges of doctoral studies.

This thesis work is also dedicated to my supervisor: Mr. Zhehui Jin, who has guided me step by step on the way of research so that I could make enormous progress from zero research experience.

ACKNOWLEDGMENTS

This thesis paper would not have been possible without the support of many people. I would like to express my sincere gratitude to my supervisor, Dr. Zhehui Jin, who provided continued guidance, fascinating idea, valuable comments and financial support. His rigorous attitude towards research and science is something I hope to carry forward throughout my career. My sincere thanks also go to the four members of my candidacy examination committee members (Dr. Huazhou Andy Li, Dr. Nobuo Maeda, Dr. Hongbo Zeng, Dr. Hao Zhang) and the four final examination committee members (Dr. Huazhou Andy Li, Dr. Nobuo Maeda, Dr. Hongbo Zeng, Dr. Hadi Nasrabadi) for their instructive suggestions, insightful comments, time and help they devoted in my study journey. A special thanks to Junjie Zhong, Chang Lu, Wenhui Li and Shiyuan Zhan, from the collaboration works with whom, I gained a lot of things not only the published paper can cover. I gratefully recognize the support from all my friends in Canada and China, their friendships are valuable treasures in my life. I would like to thank the colleagues in our research group (Yingnan Wang, Wenhui Li, WanYing Pang, Yiling Nan, Mingshan Zhang, Shiyuan Zhan, Chang Lu, Dengke Liu, Yanqing He, Xianfeng Peng, Xiaofei Hu, Wei Zhang, Shasha Zhang, Yuanyuan Tian, Yandong Yang, Juan Zhou and Zeya Huang). Thanks for their friendship, insightful comments and questions which help me a lot to improve.

A special thanks to my boyfriend Yingnan Wang, who has been supporting me throughout the entire research process and every day.

Further, yet importantly, a deep sense of gratitude goes to my father Mr. Qinglin Zhao, mother Mrs. Lili Zhang for their strong support economically as well as regular encouragement in every step to make me in the present stage.

Table of Contents

List of Tables

List of Figures

CHAPTER 1 INTRODUCTION

1.1 Research Background

Driven by population and economic growth, global energy demand will continue to rise 47% by 2050, with oil remaining the largest energy source just ahead of surging renewables [1]. While renewable technologies require technological breakthroughs, shale oil is seen as a constituting fix due to its massive reserves and depletion of conventional oil resources [2]. Unlike the conventional reservoirs, pores in shale formations are predominantly in nanoscale [3], the ratio of surface area to pore volume is significant and the strong fluid-surface interaction can greatly alter fluid properties in nanopores [4, 5]. As a result, phase behaviors of nanoconfinement fluids deviate from those in bulk. On the other hand, hydraulic fracturing techniques have been widely implemented to create fractures in shale reservoirs, which form the flow route for the hydrocarbons stored in shale nanoporous matrix [6]. The total volume of macropores and fractures which are connected to the vast nano-scale pores can be comparable to that of the latter [7]. Besides, pore size distribution in shale matrix is heterogeneous, since fluids can freely exchange between heterogeneous nanopores and macropores/fractures, such heterogeneous multi-scale system in shale reservoir further complicates the *in-situ* fluid properties. As a result, oil production from shale sub formation is a pressure drawdown process, in which multi-component hydrocarbon mixtures confined in heterogeneous nano-sized pores are released into macro-sized fractures [8] resulting in multiple phases. As hydrocarbon mixture phase behaviors in shale media play a crucial role in the predictions of well productivity, ultimate oil recovery and the applications of enhanced oil recovery (EOR) technologies [6], it is imperative to understand the hydrocarbon mixture phase

behaviors in multi-scale systems and the interplay between heterogeneous nanopores and macropores/fractures.

Efforts have been devoted from experimental aspects to explore fluids phase behaviors in nano-porous media. Indirect methods such as differential scanning calorimetry method [9] or observing slope change in pressure-volume plot [10, 11] indicate the phase transition of nanoconfined fluids without direct observation. However, it's always hard to distinguish nanopore region and connected bulk region from indirect methods. With technology development, the nanofluidic experiments have largely enabled accurate characterization of the nanoconfined hydrocarbon phase behavior through direct visualization [12-15]. Usually in these experiments, the volume of the connected microchannels is much larger than that of the nanochannels and heterogenous PSD effect is not included. Although the experimental works provide important insights into phase behaviors of nanoconfinement fluids, the studied temperature and pressure conditions are lower than those *in-situ* conditions due to technical difficulties and equipment limitations. Besides, the underlying mechanism of the nanoconfinement effects on phase behaviors of hydrocarbon mixtures in both nanoconfined and connected bulk region which occur at molecular level are not accessible from experiments.

Major efforts to study phase behaviors of nanoconfinement fluids are from theoretical works. One popular theoretical model to describe multi-phase fluid properties under nanoconfinement is by using Equation-of-State (EOS) based modeling in which the confinement effect is taken into account by capillary pressure (P_{cap}) [16-18] or shifted critical points (CPs) [16, 18, 19]. This model generally predicts suppressed bubble point and lower dew point pressures as well as elevated upper dew point pressures compared to those in bulk. However, it has been shown that the critical properties of nanoconfined fluids are shifted [20-23]. By taking into account the shifted CPs with

EOS-based modeling, the pressure-temperature (P-T) diagram of nanoconfined hydrocarbon mixture shrinks [16, 18, 19]. Although EOS-based models are easy to implement with a minimal computational cost, they do not explicitly consider fluid-surface interactions and inhomogeneous density distributions under nanoconfinement [5]. As a result, the applicability of EOS-based models for the phase behaviors of nanoconfined fluids has been under debate [9, 24]. [9, 25, 26]. Compared with EOS-based models, statistical thermodynamic methods can explicitly consider fluid-surface interactions and inhomogeneous density distributions in nanopores. As a result, using statistical thermodynamic methods to assess the validity of various EOS-based models and further providing foundations and guidance to improve the performance of the EOS-based models is of significant meaning. Besides, EOS-based models study the equilibrium state of a closed system by finding the minimum of Helmholtz free energy (V-T flash) or the Gibbs free energy (P-T flash), while the statistical thermodynamic methods calculate the minimum of grand potential for an open system at equilibrium. As a result, the statistical thermodynamic methods have wide applications in shale multi-scale structure and the interplay effect and heterogeneous PSD effect can be considered. Thereafter, using the statistical thermodynamic methods, which can simultaneously consider the effects of fluid-surface interaction, the interplay between nanopores and macropores/fractures, heterogeneous PSD inherent in shale matrix to investigate phase behaviors and fluids recovery in the actual shale oil production process has a significant meaning.

On the other hand, an extensive number of nano-scale pores and ultra-narrow pore throats (sub-2 nm) exist in shale, the ultra-narrow pore throats can result in excessively high capillary pressure for water-oil two-phase displacement, which is closely related to oil migration and ultimate productivity. The breakthrough pressure of oil displacement by water through pore throats has been widely described by the capillary pressure based on the Young-Laplace (Y-L) equation which

is built from a macroscopic perspective [27]. However, drastically different fluid flow behaviors may emerge in nanoscale pore throats in contrast to micro-meter scale ones due to strong fluid-surface interactions [28, 29]. Thus, the validity of Y-L equation in nanoscale pore throats to predict the capillary pressure remains questionable [30]. Understanding the underlying mechanism of two-phase displacement process and the applicability of Y-L in ultra-narrow pore throat can provide important guidance to numerical modeling of the oil recovery process in shale formations as well as optimization of shale/tight oil recovery.

There have been some theoretical works reported on oil-water two-phase displacement through nanoscale pore throats. Wang *et al.* [31] found that for hydrophobic capillaries, an oil layer always forms on the pore surface, while in hydrophilic ones, oil molecules can be fully displaced. In their work, the surface hydrophobicity/hydrophilicity is tuned by adjusting energy parameters for fluid-surface interaction instead of using a full atomistic description of the pore surface. In addition, several molecular dynamics (MD) simulation works built full atomistic models to describe specific mineral types, such as mica, quartz, calcite, hydrophilic kaolinite, and moderately-lipophilic kaolinite. They generally reported that water thin films form on inorganic pore surfaces, which can alter the effective pore throat sizes. Using the effective pore throat diameter in the conventional Young-Laplace (Y-L) equation, Fang *et al.* (2018) [27] reported that while the breakthrough pressure agrees well with the capillary pressure from the Y-L equation for 4 nm and 6 nm pore throat, there is a noticeable deviation for 2 nm pore throat. While all these works provided important insights into two-phase displacement process through various inorganic pore throats in shale, the displacement process through kerogen pore throats has not been studied yet.

MD simulations can explicitly consider intermolecular interactions as well as atomistic and molecular level characteristics, using MD simulation to study water-oil two phase displacement

through 2-nm kerogen pore throats from a molecular perspective and access the applicability of the Young-Laplace equation is of significant meaning.

1.2 Problem Statement

While a number of theoretical works have been devoted to investigating phase behaviors of nanoconfinement fluids and two-phase displacement process through nano-scale pores, there are still some unsolved problems that are essential for shale oil exploration. The main issues are addressed as follows:

- While the lab-on-a-chip experiments show that the bubble point of nanoconfined hydrocarbon mixtures is largely depressed, theoretical works show different results in terms of the bubble point of nanoconfined fluids. The mechanisms behind phenomena observed in experiment are unclear.
- Only limited works considered the volume ratio of nanopores and connected bulk. These works only study the bubble point of fluids in outside bulk, the fluids phase behaviors in nanopores are unclear. Besides, the volume ratio effect on fluids phase behaviors in both nanopores and outside bulk is unclear as well.
- Although many previous works studied pore size effect, a single-nanopore model is generally used and fluid behaviors in various nanopores are independent of each other. Some works studied heterogeneous PSD effect without considering the interplay between nanopores and macropores/fractures. Only limited works use EOS-based models to study PSD effect. However, these works only lower the pressure to a value higher than the bulk dew point so that the information about bulk dew point and phase transitions, as well as fluid depletions in nanopores, are missing.

- Although some previous works provided important insights into the phase behaviors of nanoconfined hydrocarbon mixtures from DFT and EOS-based models, these comparisons are not conducted in the same ensemble. A direct comparison in the same ensemble has not been conducted yet.
- For two-phase displacement process in shale matrix, some works provide important insights about the underlying mechanisms and breakthrough pressure for inorganic nanopores. An explicit investigation of oil displacement by water through kerogen ultra-narrow pore throats has not been reported.

1.3 Objective

The objectives of this research are to explore: 1) the effect of nanoconfinement effect, volume partition of bulk and nanopores and heterogeneous PSD on fluids phase behaviors and fluids properties during real production process; 2) underlying mechanisms of water-driven oil flow through kerogen pore throats as well as access the validity of conventional Young-Laplace equation in ultra-narrow kerogen pore throat. The detailed objectives are listed below:

- Study the effects of nanoconfinement on bubble point of hydrocarbon mixtures and explore the underlying mechanism;
- Study the effects of volume partition of nanopores and connected bulk on phase behaviors of hydrocarbon mixtures in shale multi-scale structure and explore the underlying mechanism;
- Study the effects of heterogeneous pore size distribution on phase behaviors of hydrocarbon mixtures in shale multi-scale structure and explore the underlying mechanism;
- Comparison phase behavior of hydrocarbon mixtures under nanoconfinement in canonical ensemble obtained from density functional theory and equation-of-state based models;

- Study the underlying mechanisms of water-oil two-phase displacement process through ultra-narrow kerogen pore throats and access the applicability of conventional Yong-Laplace equation.

1.4 Thesis Structure

There are seven chapters in this dissertation. Chapter 1 introduces the research background, addresses the problem statement, and presents the major research objectives. Chapter 2 explores the nanoconfinement and pore size effect on phase behaviors of hydrocarbon mixtures based on DFT calculation. Chapter 3 probes volume partition effect on phase behaviors of hydrocarbon mixtures in shale multi-scale structure by considering material balance when conducting DFT calculation. Chapter 4 includes different sizes of nanopores in the multi-scale structure to study heterogeneous PSD effect during CCE and CVD process. Chapter 5 presents phase diagrams and fluids properties of hydrocarbon mixtures in nanoconfinement from DFT and several EOS-based models, the applicability of EOS-based models in nano-scale pores is discussed. Chapter 6 reveals the underlying mechanism of water-oil two-phase displacement process through ultra-narrow kerogen pore throat, the applicability of the conventional Young-Laplace equation has been accessed according to the comparison of breakthrough pressure obtained from MD simulation. Chapter 7 summarizes the conclusions of the research and raises some potential directions for future work.

CHAPTER 2 BUBBLE POINT PRESSURES OF HYDROCARBON MIXTURES IN MULTISCALE VOLUMES FROM DENSITY FUNCTIONAL THEORY

A version of this chapter has been published in Langmuir.

2.1 Introduction

Hydrocarbon mixture bubble point pressure plays an important role in the accurate prediction of ultimate oil recovery (UOR) and well productivity, and is thus a key parameter for reservoir simulations [32, 33]. Unlike conventional reservoirs, where pores are generally in the range of micrometers [34], shale reservoirs which have greatly changed the figure of global energy supply in the past decade [35], are largely nanoporous [3, 36-38]. Large quantities of hydrocarbons can be stored in the organic matters (i.e. mainly kerogen) in shale. In nanopores, due to strong fluid-surface interactions, molecular distributions are inhomogeneous and properties can be very different from those in bulk [39]. As a result, the hydrocarbon mixture bubble point pressures in nanopores cannot be readily described by the conventional equation of state (EOS) modeling [9, 40]. At nanoscale, explicit consideration of fluid-fluid and fluid-surface interactions from molecular perspective is necessary. In addition, the understanding of properties of fluid mixtures under nanoconfinement has broad applications in gas storage [41], catalysis [42], fuel cell [43], and gas mixture separation [44].

A number of experimental measurements using unconsolidated nanoporous media have been reported on the bubble point of nanoconfined fluids [9-11, 45]. Because the fluid behavior in nanoporous media is not directly viewable, some experimental methods including differential scanning calorimetry (DSC) [9] and slope change in pressure-volume plot [10, 11, 45] have been widely used. These indirect measurements have shown mixing results. For example, while Pathak *et al*. [10] and Cho *et al*. [11, 45] found that the bubble point pressures of nanoconfined methane/n-decane and methane/n-octane mixtures are slightly reduced, Liu *et al.* [46] observed that the bubble point pressure of N_2/n-butane mixture in a crushed shale sample containing PVT cell is higher than that of the originally injected fluids. They further claimed that the measured bubble point is that

of bulk free fluids and the increase is due to the competitive adsorption between N_2 and n-butane in nanoporous media. On the other hand, development of nanofluidic devices [13-15, 47] has largely enabled accurate characterization of nanoconfined hydrocarbon phase behavior through direct visualization. Recently, we used dual nano-micro channel systems in which nanochannels of 8-, 80-, and 800-nm deep are connected with microchannels to study bubble point pressure of nanoconfined methane/propane mixtures [48]. Throughout slow pressure decline process, hydrocarbon fluids in nanochannels and microchannels are in chemical potential equilibrium. In addition, since the nanochannel volumes are much smaller than those of microchannels, competitive adsorption and phase transition in nanochannels have negligible effects on the fluids in microchannels. We found that at isothermal conditions, evaporation in nanochannels only occurs after the fluids in microchannels are completely vaporized, indicating that the bubble point pressure of nanoconfined hydrocarbon mixtures is substantially lowered, and can be below the bulk dew point. Such drastically reduced bubble point pressure of confined hydrocarbon mixtures has not been observed previously. While these measurements are valuable, the underlying mechanisms of the confinement effects on the bubble point pressures of hydrocarbon mixtures in both nanoconfined and free spaces which occur at molecular level are not accessible from experiments.

Major efforts have been from theoretical works which can study mechanisms of phase behavior of confined hydrocarbons at nanoscale. A common approach is to couple the capillary pressure model with the EOS modeling [15, 40, 49-52], assuming homogeneous density distributions and ignoring fluid-surface interactions. This approach has been coupled into reservoir simulators to model shale well productivity [53]. It generally predicts that the bubble point pressure decreases under nanoconfinement, and the shift decreases as pore size increases. None of these works has predicted

the substantially lowered bubble point pressure of confined hydrocarbon mixtures as observed in our experiments [48]. It is because the system settings and nanopore-bulk partitioning are not in line with our measurements. Pitakbunkate *et al*. [54, 55] used grand canonical Monte Carlo (GCMC) simulations to study the effect of nanoconfinement on hydrocarbon properties and found that bubble point pressures in nanopore may be either lower or higher than that of the bulk mixture. The fluid composition specified in their pressure-temperature diagram is that in nanopores, which can be very different from bulk and is difficult to obtain in experiments. In addition, molecular simulations usually come with expensive computational costs, especially for high pressure conditions.

Engineering density functional theory (DFT) [34, 56] is a powerful tool to study the underlying mechanisms of bubble point pressure of nanoconfined hydrocarbon mixtures. Within the framework of DFT, fluid-fluid and fluid-surface interactions as well as the inhomogeneous density distributions due to nanoconfinement can be explicitly considered [56]. Comparing to molecular simulations, DFT can significantly reduce calculation time. While our work [48] and Liu *et al*. [46] provided important insights into hydrocarbon mixture phase behavior in both nanopores and free spaces, this work elaborates the effects of pore size and nanopore-bulk partitioning from molecular perspectives.

In this work, we use DFT to study two different cases: (a) nanopores are connected to infinite bulk reservoirs similar to shale reservoir conditions, where nanopores are connected to relatively very large hydraulic fractures (volume ratio $>10^3$); (b) nanopores are connected to finite bulk volume reservoirs characteristic of relatively small macropores/natural fractures (volume ratio $<10^3$) [3, 57]. In both cases, nanoconfined hydrocarbons are in chemical equilibrium with bulk fluids. While in the former case, phase change and competitive adsorption in nanopores do not alter the fluid

properties in bulk, that is not the case for the latter one as in Liu *et al*. [46]. In the former case, besides the results from our work [48] that bubble point in nanopore P_p^{bub} is lower than bulk dew point pressure P_b^{dew}, we find that as pore size increases, P_p^{bub} approaches P_b^{dew} and hysteresis between bubble and dew points of confined hydrocarbon mixtures decreases. While bulk region is in two-phase, hydrocarbon average density in nanopore increases as pressure decreases and approaches that of bulk liquid phase as pore size increases. In the latter case, the finite connected volume affects partitioning between the nanopores and bulk region and constant composition expansion (CCE) method is applied to simulate real shale/tight oil production. As system pressure decreases, the total fluid in the whole (nanopore-bulk) system remains constant, and the fluid properties in nanopores and bulk are determined by material balance and chemical equilibrium. Similar to the first case with infinitely connected volume, we find that capillary evaporation under nanoconfinement does not occur when system pressure is above or equal to the dew point pressure of bulk region. The bubble point pressure of bulk region is higher than that of originally injected fluids in line with Liu *et al*. [46].

Collectively, these simulation cases demonstrate the underlying mechanisms leading to the deeply decreased bubble points of nanoconfined hydrocarbon mixtures, as well as the influence of the surrounding system on the mixture composition and thus phase behavior in shale nanopores. Our findings indicate that large quantities of heavier hydrocarbons are still trapped in nanopore as pressure declines, asking for advanced enhanced oil recovery (EOR) technologies.

2.2 Methods

Here a nanopore of pore size W and volume V_p is connected to a bulk region of volume V_b as depicted in **Figure 2-1**. For simplicity, we use structureless carbon slit pore to simulate nanopore.

Such smooth carbon nanopore structures have been used to simulate gas adsorption [34, 56], hydrocarbon phase behavior [58] in kerogen nanopores and shown excellent agreement with experimental data. We do not consider confinement effect in the bulk region. In this work, we use C_1-C_3 mixtures to represent hydrocarbon fluids. While the actual shale oil fluids are usually much heavier than C_1-C_3 mixtures, the fundamental properties are the same.

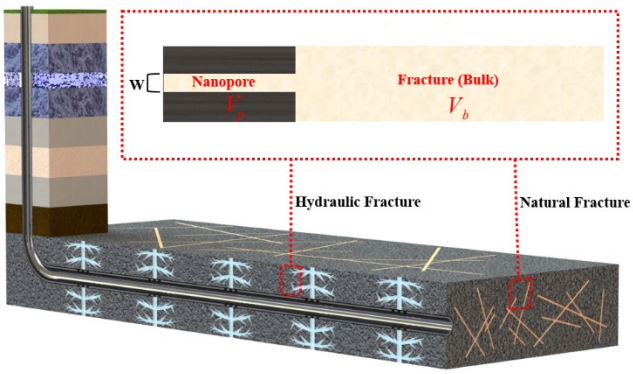

Figure 2-1. Schematic representation of shale oil extraction operation, where nanopores are connected to fractures (bulk). In our work, nanopore of pore size W and volume V_p is connected to a bulk region of volume V_b.

We consider two different scenarios: 1) infinite connected bulk volume (IBV), i.e., $V_b / V_p = \infty$; 2) finite connected bulk volume (FBV), i.e., with initial bulk volume $V_b^i / V_p = 10^1, 10^2, 10^3$. The system pressure P is dictated by the bulk region pressure. In both cases, we assume that as P declines, V_p remains the same, while in FBV case, V_b increases. For IBV case, fluid compositions in the bulk region stay constant and chemical potentials of species in nanopores are the same as those in bulk. For FBV case, we apply CCE method to the whole nanopore-bulk system; the fluid properties in nanopore and bulk region are determined by the chemical equilibrium and material balance (MB). Details about our DFT calculations can be referred to **Appendix A.**

For IBV case, adsorption in nanopores does not alter the fluid properties in bulk. At isothermal conditions, we gradually reduce P to simulate the shale oil production process. We use a successive-substitution iteration to update the density distributions obtained from **Eq.(A-10)** (**Appendix A**). At the first pressure, bulk density is used for initialization. We use results from the preceding pressure as initial guess for the next pressure condition and proceed iterations till the last pressure condition. In the bulk two-phase zone, fluid chemical potentials in vapor and liquid phases are the same. Thus, we use the chemical potentials of liquid phase obtained from the Peng-Robinson EOS (PR-EOS) as input for DFT calculations. Ravikovitch *et al*. claimed that while capillary condensation (vapor to liquid transition, dew point) occurs close to the metastable condensation point, capillary evaporation (liquid to vapor transition, bubble point) in nanopores occurs close to the equilibrium transition point [59]. The equilibrium transition associated with condensation/evaporation metastability occurs at a point where adsorption/desorption branches have the same grand potential (GP) values as given in **Eq. (A-1)** (**Appendix A**) [59]. In this work, we use the equilibrium transition point as P_p^{bub}.

For FBV case, due to competitive adsorption in nanopores, the bulk overall composition $\{y_{i,b}\}$ is different from the overall nanopore-bulk system composition $\{Z_i\}$, while fluid properties in nanopores are dependent on the bulk chemical potentials as depicted in **Eq. (A-10)** (**Appendix A**). In this work, we decrease P until the lower dew point of bulk region since the abandonment pressure of in-situ shale reservoir is always much higher than the oil lower dew point pressure. The MB calculations are illustrated in two different pressure conditions: a) at P above the bubble point pressure in the bulk region P_b^{bub} ($P > P_b^{bub}$); b) at P between P_b^{bub} and P_b^{dew} ($P_b^{bub} > P > P_b^{dew}$).

a) $P > P_b^{bub}$

In this condition, the bulk region is in a single liquid phase. For given $\{y_{i,b}\}$ at P, the average densities of hydrocarbons in bulk $\rho_{i,b}$ and nanopores $\rho_{i,p}$ are obtained from the PR-EOS and DFT, respectively. The total mole numbers of hydrocarbons N_i of each component is given as

$$N_i = \rho_{i,b} V_b + \rho_{i,p} V_p, \quad i = C_1, C_3 \tag{2.1}$$

Then, $\{Z_i\}$ is given as

$$Z_i = N_i / \sum_j N_j, \quad i = C_1, C_3 \tag{2.2}$$

$\{N_i\}$ are determined by the given $\{Z_i\}$ and initial pressure P^i through iterative calculations. At subsequent $P < P^i$, V_b expands, while $\{N_i\}$ remain the same. By rewriting **Eq. (2.1)**,

$$V_b = \left(N_i - \rho_{i,p} V_p\right) / \rho_{i,b}, \quad i = C_1, C_3 \tag{2.3}$$

As shown in **Eq. (2.3)**, the equilibrium V_b for given P can be obtained from C_1 and C_3 MB equations. For given P and T, by varying trial C_3 composition in the bulk region $x_{C_3,b}$ (increasing/decreasing), we find the intercept between two $V_b - x_{C_3,b}$ curves from C_1 and C_3 to determine the equilibrium $\{y_{i,b}\}$.

b) $P_b^{bub} > P > P_b^{dew}$

In this condition, the bulk region is in a two-phase. Unlike Eq. (2.1), $\{N_i\}$ are given as,

$$N_i = \rho_{i,b(L)} V_{b(L)} + \rho_{i,b(V)} V_{b(V)} + \rho_{i,p} V_p, \quad i = C_1, C_3 \tag{2.4}$$

where $\rho_{i,b(L)}$ and $\rho_{i,b(V)}$ represent densities of component i in the bulk liquid and vapor phases, respectively; $V_{b(L)}$ and $V_{b(V)}$ are volumes of the bulk liquid and vapor phases, respectively. We run the PR-EOS to get the bulk liquid phase and vapor phase properties for given bulk overall mole fractions $\{y_{i,b}\}$. Bulk liquid phase chemical potentials from the PR-EOS are used as an input for DFT calculations. By rewriting **Eq. (2.4)**, we have,

$$V_{b(L)} = \left(N_i - \rho_{i,p} V_p\right) / \left[\rho_{i,b(L)} + \left(V_{b(V)} / V_{b(L)}\right)\rho_{i,b(V)}\right], \quad i = C_1, C_3 . \tag{2.5}$$

According to $V_{b(V)} / V_{b(L)}$ from PR-EOS, $V_{b(V)}$ is given as,

$$V_{b(V)} = \left(V_{b(V)} / V_{b(L)}\right) V_{b(L)} \tag{2.6}$$

Then, we have

$$V_{b(V)} = \left(V_{b(V)} / V_{b(L)}\right) V_{b(L)} \tag{2.7}$$

As in $P > P_b^{bub}$ case, for given P and T, by varying trial overall bulk phase C_3 composition $x_{C_3,b}$ (increasing/decreasing), we find the intercept between two $V_b - x_{C_3,b}$ curves from C_1 and C_3 to determine the equilibrium $\{y_{i,b}\}$.

2.3 Results and discussion

In this section, we first present the average densities in nanopores and the bubble point pressure from DFT for IBV case. We set $P^i = 45$ bar and $T = 288.15$ K. The bulk composition is given as $y_{C_1,b} / y_{C_3,b} = 0.2 / 0.8$ and we consider four different sets of pore sizes of 5, 10, 20, and 50 nm. Then, we investigate FBV case by varying V_b^i with the same P^i and T with overall nanopore-bulk composition given as $Z_{C_1} / Z_{C_3} = 0.2 / 0.8$.

a) IBV

The $P-T$ diagram of bulk C_1-C_3 mixtures of $y_{C_1,b} / y_{C_3,b} = 0.2/0.8$ from the PR-EOS are given in **Figure A1** (**Appendix A**). At 288.15 K, bulk bubble point pressure P_b^{bub} and dew point pressure P_b^{dew} are 37.679 bar and 9.422 bar, respectively. At $P^i = 45$ bar, bulk C_1-C_3 mixture is in a pure liquid phase.

In **Figure 2-2**, we present the C_1 and C_3 average densities in 5 nm pores. While bulk hydrocarbon mixtures are in a single liquid phase or liquid-vapor two phases, the fluids in nanopores are always in a liquid-like phase. Thus, the complete fluid evaporation in nanopore is greatly suppressed as observed in our experiment [48]. When $P_b^{bub} > P > P_b^{dew}$, due to the competitive adsorption, while C_1 average density in nanopore $\rho_{C_1,p}$ decreases as P decreases, the opposite is true for C_3 average density in nanopore $\rho_{C_3,p}$. When $P < P_b^{dew}$, hydrocarbon mixtures in nanopores show hysteresis. As shown by Ravikovitch *et al*. [59], evaporation in nanopore occurs close to the equilibrium transition, which is determined by the GP equality from pressure increasing/decreasing branches as depicted in **Figure A2** (**Appendix A**). Unlike fluids in bulk, such evaporation occurs spontaneously. The pressure points when sudden drop/jump in GP occur during pressure decrease/increase processes are metastable evaporation/condensation. When $P > P_b^{dew}$, there is no hysteresis observed in nanopore, i.e., the pressure increasing/decreasing processes are reversible.

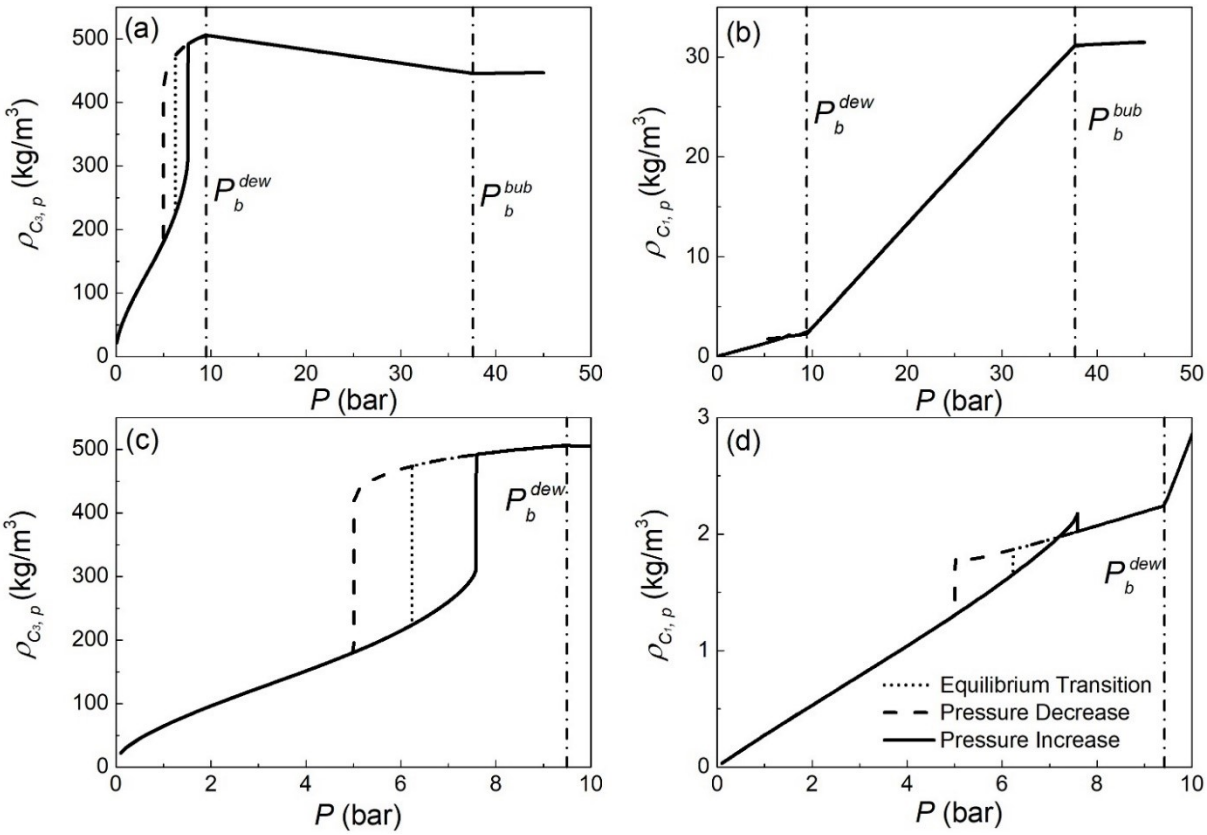

Figure 2-2. Average densities of (a) C_3; (b) C_1 in nanopores of $W = 5$ nm at 288.15K from pressure increasing/decreasing processes. For clarity, we present the average densities of (c) C_3; (d) C_1 up to P_b^{dew}.

In **Figure 2-3**, we present the metastable condensation/evaporation and equilibrium transition points in various nanopores at 288.15 K. We observe that as pore size increases, metastable condensation (i.e., dew point in nanopores P_p^{dew}) and equilibrium transition points (i.e., P_p^{bub}) get closer, in line with our experiment [48]. As pore size increases, P_p^{dew} approaches P_b^{dew}, similar phenomenon was observed in experimental work done by Zhong *et al* [60]. In our previous work [58], hysteresis is defined as the difference between the metastable condensation and evaporation, which increases with pore size and then reaches a constant.

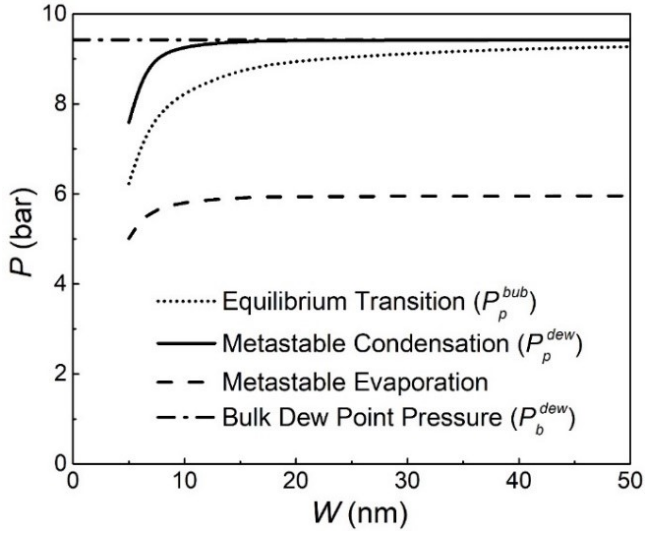

Figure 2-3. The metastable condensation/evaporation and equilibrium transition of C_1-C_3 mixtures in nanopores of various pore sizes from engineering DFT. For comparison, we also present the corresponding P_b^{dew} at $T = 288.15$ K from the PR-EOS.

In **Figure 2-4**, we present the $\rho_{C_1,p}$ and $\rho_{C_3,p}$ in different nanopores at 288.15 K for pressure decreasing process. We use the equilibrium transition which indicates the global GP minimum to represent the hysteresis zone. For comparison, we also depict the C_1 and C_3 densities in bulk C_1-C_3 mixtures, $\rho_{C_1,b}$ and $\rho_{C_3,b}$, respectively. While bulk C_1-C_3 mixtures are in two-phase, we use the liquid phase densities. When $P > P_b^{dew}$, as pore size increases, both $\rho_{C_1,p}$ and $\rho_{C_3,p}$ approach the bulk values. It is because as pore size increases, fluid-surface interactions become less significant. While $\rho_{C_1,p}$ decreases as P decreases, $\rho_{C_3,p}$ increases as P decreases for $P_b^{dew} < P < P_b^{bub}$. At $P = P_p^{bub} < P_b^{dew}$, both $\rho_{C_1,p}$ and $\rho_{C_3,p}$ show sudden drops. In in-situ conditions, because P_b^{dew} is generally very low for oil, the complete evaporation in nanopores might be extremely difficult. Due to competitive adsorption, $\rho_{C_3,p}$ can be one to two orders of magnitude larger than $\rho_{C_1,p}$. As a result, C_3 dominates within nanopores. **Figure 2-4** also indicates

that to produce the heavier component from nanopores, one needs to lower the pressure below P_p^{bub}. In addition, the lighter component can be released from nanopores throughout the pressure decline process.

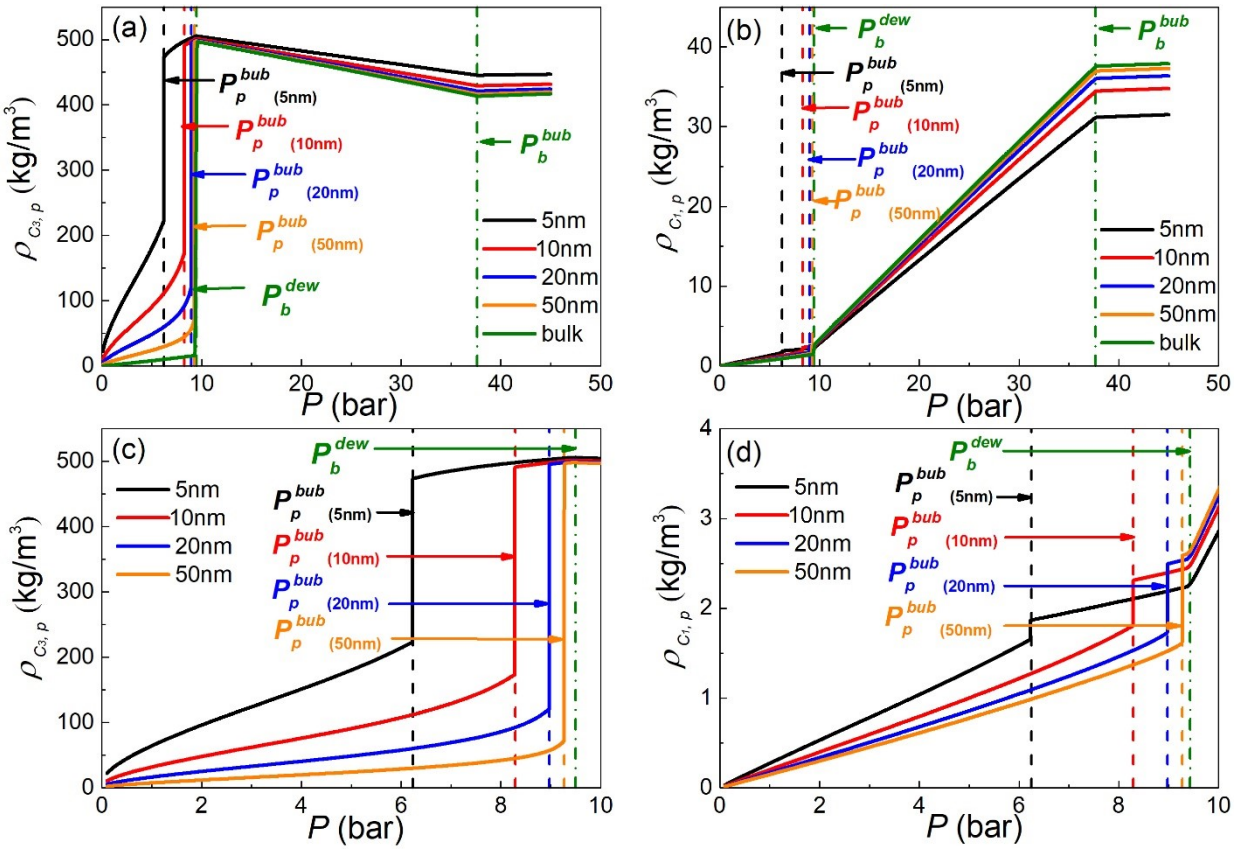

Figure 2-4. Average density of (a) C_3; (b) C_1 in various nanopores at 288.15K for the C_1-C_3 mixtures ($y_{C_1,b} / y_{C_3,b} = 0.2 / 0.8$) during pressure decreasing process. For clarity, we present the average densities of (c) C_3; (d) C_1 up to P_b^{dew}.

Our results indicate that while lighter hydrocarbons could be produced during pressure decline process, heavier hydrocarbons would be trapped in nanopores causing loss of enormous amount of these components during shale oil production. It may be one of the reasons that shale oil recovery factor is usually low, i.e. less than 10 % [61]. Feasible EOR techniques such as miscible gases, surfactant, and low-salinity water flooding should be used to enhance UOR.

b) FBV

For FBV case, we need to obtain the bulk properties at the initial points which satisfies the overall mole fractions (i.e., $Z_{C_1} / Z_{C_3} = 0.2 / 0.8$) by iteratively solving **Eq. (2.2)**. The range of trial calculation is from the bulk bubble point $y_{C_3,b}^{bub} = 0.754$ to $y_{C_3,b} = 0.999$ at $P^i = 45$ bar and $T = 288.15$ K as given in **Figure A3 (a)** (**Appendix A**). Within this range, C_1-C_3 mixture in bulk is in a pure liquid-phase. In **Table 2-1**, we present the equilibrium C_3 mole fraction $y_{C_3,b}$ in bulk C_1-C_3 mixtures for various nanopores and V_b^i / V_p at P^i. When V_b^i / V_p is large (i.e., $V_b^i / V_p = 10^3$), the equilibrium $y_{C_3,b}$ is close to Z_{C_3}. As V_b^i / V_p decreases, $y_{C_3,b}$ decreases, because C_3 adsorption in nanopores are greatly enhanced due to stronger C_3-surface interaction than that of C_1-surface. As W increases, due to weaker fluid-surface interactions, $y_{C_3,b}$ increases. In the following section, we use $V_b^i / V_p = 10$ as an example to illustrate the CCE process.

Table 2-1. The equilibrium $y_{C_3,b}$ of C_1-C_3 mixtures in the bulk region for various nanopores and V_b^i / V_p at $P^i = 45$ bar and $T = 288.15$ K.

	Equilibrium $y_{C_3,b}$			
W (nm)	$V_b / V_p = \infty$	$V_b^i / V_p = 10^3$	$V_b^i / V_p = 10^2$	$V_b^i / V_p = 10^1$
5	0.8	0.79996	0.79962	0.79642
20	0.8	0.79999	0.79991	0.79915

As shown in **Figure A3 (b)** (**Appendix A)**, at $P < P^i$, we run the trial bulk C_3 mole fraction $x_{C_3,b}$ ranging from $y_{C_3,b} = 0.001$ to $y_{C_3,b} = 0.999$ to obtain the equilibrium $y_{C_3,b}$, which satisfies $Z_{C_1} / Z_{C_3} = 0.2 / 0.8$. In **Figure 2-5 (a)**, we present the $V_b - x_{C_3,b}$ plots from C_1 and C_3 branches as given in **Eqs. (2.5) -(2.7)** at $P = 42$ bar. The cross between two branches dictates the equilibrium

$y_{C_3,b}$. We also depict the results from $x_{C_3,b}$ increasing/decreasing processes to observe hysteresis. At $P = 42$ bar, the dew point and bubble point C_3 compositions in bulk region are 0.26025 and 0.77238, respectively. Only when fluids in the bulk region are in a single-vapor phase, hysteresis in V_b with respect to $x_{C_3,b}$ is observed (highlighted hysteresis zones can be referred to **Figure A-4** (**Appendix A)**. The cross between two branches occurs at 0.79639, where fluids in the bulk region are in a single-liquid phase. As further decreasing P, such cross-point shifts toward lower equilibrium $y_{C_3,b}$. As shown in Figure 5(b), we find that at $P = 38.249$ bar, the cross occurs at the bubble point in the bulk region, with equilibrium $y_{C_3,b} = 0.79635$. P_b^{bub} is higher than that of C_1-C_3 mixtures with $Z_{C_1} / Z_{C_3} = 0.2 / 0.8$ (i.e., 37.679 bar) in line with Liu *et al*. [46]. Due to competitive adsorption in nanopore, the heavier component composition in bulk region is lower than that of overall hydrocarbon mixtures. At a lower pressure $P = 25$ bar, the cross occurs at equilibrium $y_{C_3,b} = 0.78966$, which is in a liquid-vapor coexisting phase, as depicted in **Figure 2-5 (c)**. At $P = 9.677$ bar, the cross occurs at the dew point in the bulk region with equilibrium $y_{C_3,b} = 0.78173$ as shown in **Figure 2-5 (d)**. P_b^{dew} is higher than that of C_1-C_3 mixtures with $Z_{C_1} / Z_{C_3} = 0.2 / 0.8$ (i.e., 9.422 bar). Throughout the pressure decline process, as shown in **Figure A-4** (**Appendix A**), hysteresis zone gets larger and shifts toward higher equilibrium $y_{C_3,b}$. However, until P_b^{dew}, hysteresis is not observed in nanopore.

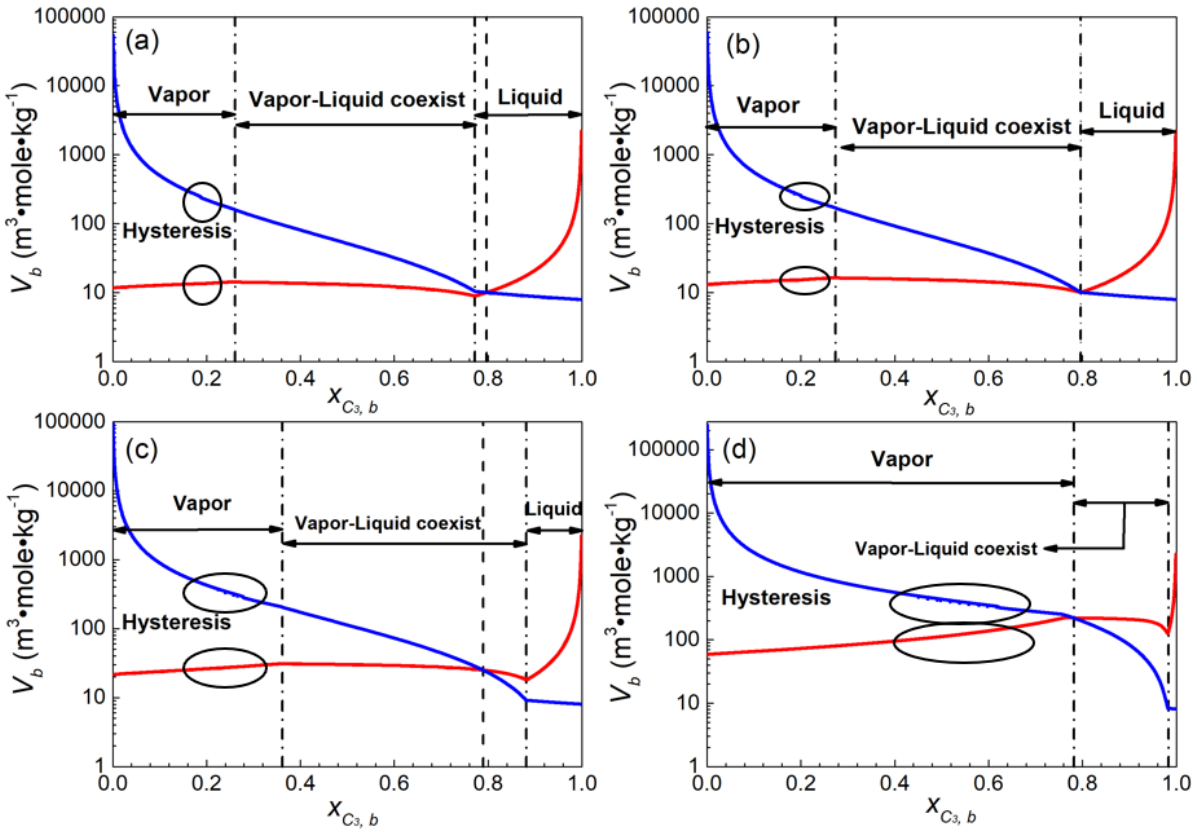

Figure 2-5. The $V_b - x_{C_3,b}$ plots from C_1 and C_3 branches at (a) $P = 42$ bar; (b) $P = 38.249$ bar; (c) $P = 25$ bar; (d) $P = 9.677$ bar at $T = 288.15$ K for $V_b^i / V_p = 10$ and $W = 5$ nm. The solid and dotted lines represent $x_{C_3,b}$ increasing and decreasing processes, respectively; the red and blue lines depict C_1 and C_3 branches, respectively. The dashed line depicts the crossing point. The dash-dotted lines represent the saturation points.

We present the corresponding instantaneous $P-T$ diagram of equilibrium C_1-C_3 mixtures in the bulk region at various pressures in **Figure A-5** (**Appendix A**). As pressure decreases, both P_b^{bub} and P_b^{dew} increase. The increases in P_b^{bub} and P_b^{dew} are more significant for smaller pores and V_b^i / V_p as shown in **Table 2-2** and **2-3**, respectively. As pressure declines, the equilibrium $y_{C_3,b}$ decreases as shown in **Figure 2-6 (a)**. It is observed that as pore size increases, the equilibrium

$y_{C_3,b}$ increases. In **Figure 2-6 (b)**, we present the average density of C_3 in various nanopores during CCE process. For comparison, we also depict the C_3 density in the bulk region. When the bulk fluids are in a liquid-vapor coexisting phase, we use the C_3 density in bulk liquid phase. When $P > P_b^{bub}$, C_3 average density in nanopores decreases as pressure decreases. However, the opposite is true for $P_b^{dew} \le P \le P_b^{bub}$. This behavior is in line with IBV case as shown in **Figure 2-4**. As W increases, the C_3 average density in nanopores approaches that of bulk liquid phase.

Table 2-2. P_b^{bub} at $T = 288.15$ K during CCE process.

	P_b^{bub} (bar)			
W (nm)	$V_b / V_p = \infty$	$V_b^i / V_p = 10^3$	$V_b^i / V_p = 10^2$	$V_b^i / V_p = 10^1$
5	37.679	37.685	37.739	38.249
20	37.679	37.680	37.693	37.814

Table 2-3. P_b^{dew} at $T = 288.15$ K during CCE process.

	P_b^{dew} (bar)			
W (nm)	$V_b / V_p = \infty$	$V_b^i / V_p = 10^3$	$V_b^i / V_p = 10^2$	$V_b^i / V_p = 10^1$
5	9.422	9.425	9.447	9.677
20	9.422	9.425	9.447	9.671

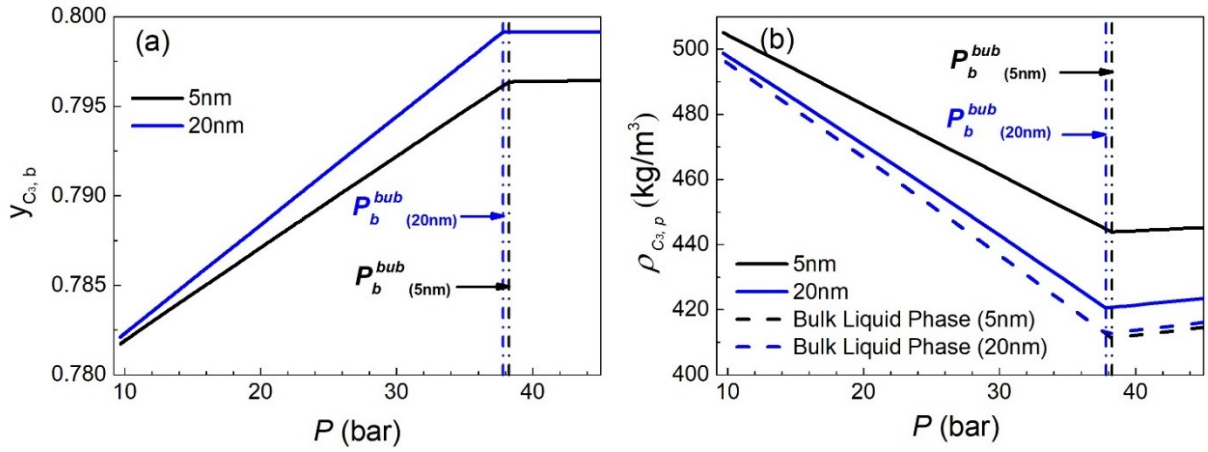

Figure 2-6. (a) The equilibrium $y_{C_3,b}$ during CCE process at $T = 288.15$ K for $V_b^i / V_p = 10$ and various nanopores. (b) Average density of C_3 in various nanopores at $T = 288.15$ K for $V_b^i / V_p = 10$ during CCE process. For comparison, we also present the bulk C_3 density. When the bulk fluids are in liquid-vapor coexisting phase, we use the C_3 density in bulk liquid phase. The black and blue solid lines represent $W = 5$ nm and $W = 20$ nm, respectively; the dash-dotted lines depict the bubble point pressure in the bulk region.

In **Figure 2-7**, we depict the average density of C_1 and C_3 in various nanopores for different V_b^i / V_p. The evaporation of hydrocarbon mixtures in nanopore is not observed throughout the process. It is observed that when the bulk fluids are in a liquid-vapor coexisting phase, the average densities of C_1 and C_3 remain the same for various FBV and IBV cases. It is because even though the equilibrium $\{y_{i,b}\}$ are different, the properties of bulk vapor and liquid phases remain the same at given pressure based on the tie-line in pressure-composition diagram.

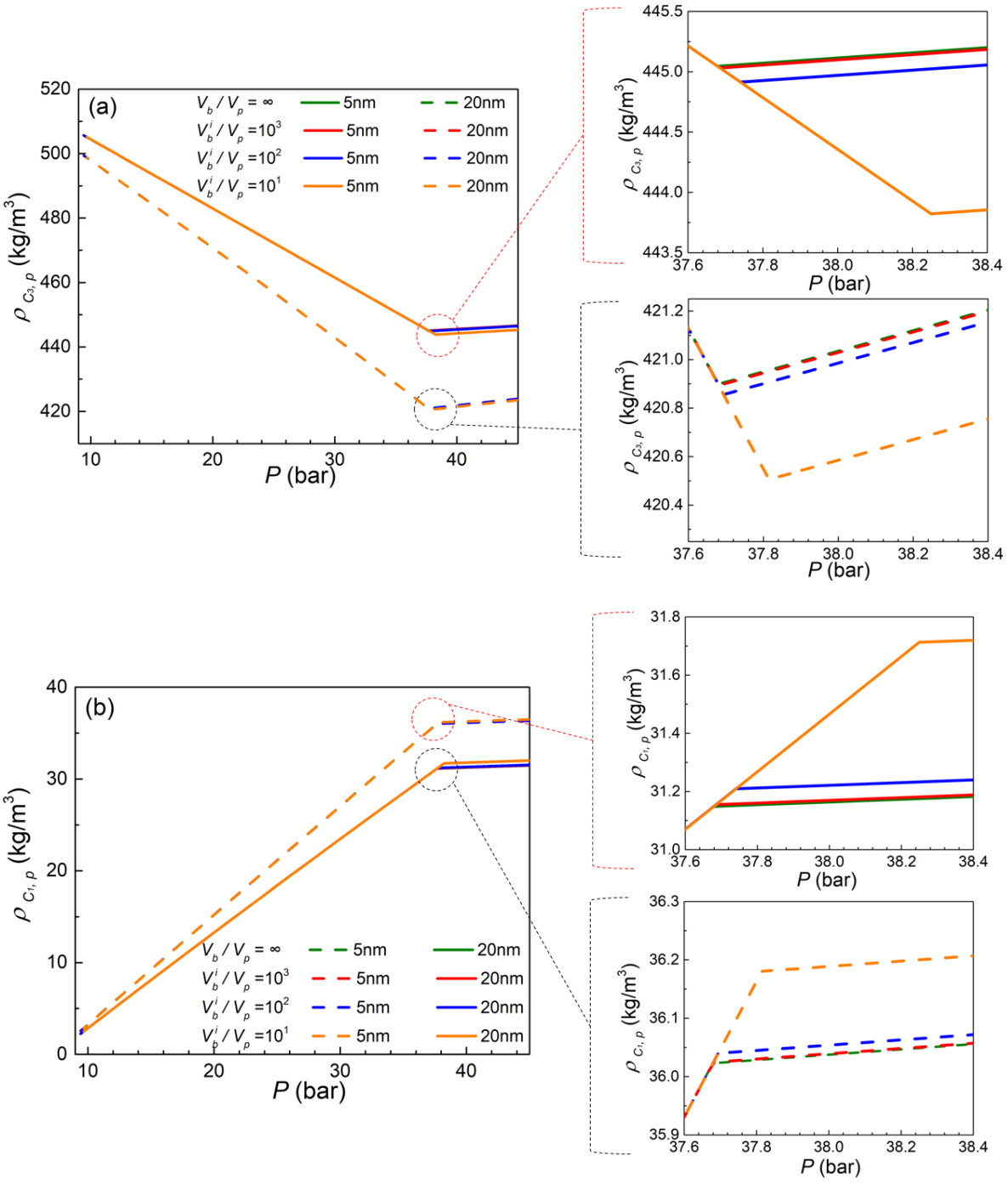

Figure 2-7. Average density of (a) C_3; (b) C_1 in various nanopores for different V_b^i / V_p at $T = 288.15\,\mathrm{K}$ during CCE process. $V_b / V_p = \infty$ represents the IBV case.

Our results indicate that both pore size and nanopore-bulk partitioning could influence bubble point of shale matrix surrounding nanoconfinement. However, when bulk fluids are in two-phase,

fluid properties in nanopores are dependent on pore size and pressure, but not on the nanopore-bulk partitioning. Drastically different properties of hydrocarbon mixtures in nanopores and bulk region and the effect of nanopore-bulk partitioning indicate that pore size distribution could provide important information on the accurate prediction of fluid phase behavior in shale media.

2.4 Summary and Conclusion

In this work, we use DFT to study the bubble point of nanoconfined C_1-C_3 mixtures. Unlike the commonly used EOS coupled with capillarity model, DFT can explicitly consider the fluid-surface interactions and the inhomogeneous density distributions. We considered both IBV and FBV cases.

For IBV case, we found that the bubble point pressure (when capillary evaporation occurs) is below the lower dew point of bulk fluids. Unlike fluids in bulk, such evaporation occurs spontaneously. As pore size increases, both bubble and dew points in nanopores approach the bulk lower dew point pressure and hysteresis between them decreases. These observations are in line with our recent experiments [48]. As pressure declines, due to competitive adsorption, the average density of the heavier component in nanopore increases, while that of the lighter component decreases. While bulk fluids are in a liquid-vapor coexisting phase, average density in nanopore approaches liquid phase density in bulk as pore size increases.

For FBV case, bubble point pressure in the bulk region increases due to the presence of nanopore, which is in line with Liu *et al*. [46]. It is because the lighter component composition in the bulk region is higher than that of the originally injected fluid mixtures due to competitive adsorption. As pore size decreases, the bubble and dew points in the bulk region increases. However, the bubble and dew point pressures in the bulk region are very different from that in nanopore. Thus, the slope change in pressure-volume curve of nanoporous media containing PVT cell [10, 11, 45,

46] cannot reveal the true phase behavior of nanoconfined fluids. When bulk fluids are in a liquid-vapor coexisting phase, fluid properties in nanopore only depend on pressure and pore size. The bubble point pressure in nanopore is not observed until the liquid phase in the bulk region is completely evaporated, i.e., P_b^{dew}.

Collectively, both cases predict that the bubble point of nanoconfined hydrocarbon mixtures are greatly suppressed. Due to such suppressed bubble point pressure, vapor phase does not evolve in nanopores during shale oil production process, which is beneficial to oil flow in porous media [40]. However, on the other hand, the heavier components trapping in nanopores could severely dampen the production of these more valuable oil fractions, which asks for advanced EOR strategies. Our work should provide important insights and implications into shale reservoir assessment and production optimization.

Acknowledgements

This research was enabled in part by support provided by Westgrid (www.westgrid.ca) and Compute Canada (www.computecanada.ca). The authors also greatly acknowledge a Discovery Grant from Natural Sciences and Engineering Research Council of Canada (NSERC RGPIN-2017-05080). As a part of the University of Alberta's Future Energy Systems research initiative, this research was made possible in part thanks to funding from the Canada First Research Excellence Fund.

CHAPTER 3 HYDROCARBON PHASE BEHAVIORS IN SHALE NANOPORE-FRACTURE MODEL: MULTI-SCALE, MULTICOMPONENT AND MULTIPHASE

A version of this chapter has been published in SPE J.

3.1 Introduction

Phase behavior and properties of fluid mixtures under nano-confinement are critical to shale/tight oil and gas production [62-64]. Shale oil production has attracted significant attention due to the continuous depletion of conventional oil reservoirs around the world [65]. Unlike conventional reservoirs, where pores are in the range of several micrometers, shale contains abundant pores ranging from a few to hundreds of nanometers [3, 38]. In nanopores, due to strong fluid-surface interactions, fluid distribution is inhomogeneous [66]. As a result, hydrocarbon mixtures behave very differently from the bulk [5, 25] and cannot be described by the conventional equation of state (EOS) modeling [9]. Oil production from shale subformation is a pressure drawdown process, in which multi-component hydrocarbon mixtures confined in nano-sized pores are released into macro-sized fractures [8] resulting in multiple phases. Therefore, the understanding of multi-phase and multi-component hydrocarbon behavior in multi-scale volumes plays a key role in the prediction of well productivity and ultimate oil recovery [67].

Numerous theoretical studies have been reported on the phase behavior of fluid mixtures under nano-confinement. One popular choice is to use the EOS plus capillary pressure (EOS-P_{cap}) model [15, 26, 50, 52]. EOS-P_{cap} generally predicts that the bubble point and lower dew point pressures of nano-confined hydrocarbon mixtures are reduced, while the upper dew point pressures increase. On the other hand, EOS with shifted critical points (CP) model predicts [16, 68] that the upper dew point and bubble point pressure decrease, while the lower dew point pressure increases. By using grand canonical Monte Carlo (GCMC) simulation, Pitakbunkate *et al*. [54, 55] studied the phase diagram of binary mixtures with given compositions in various nanopores. They found that dew point pressures in nanopores are higher than that of bulk, while bubble point pressure of confined fluids can be higher or lower than that of bulk. While these works provide important

insights into the phase behavior of confined hydrocarbon mixtures, they did not consider multi-scale volumes in which nanopores are connected to macropores, which is at the heart of shale oil production.

On the other hand, nanofluidic experiments have enabled direct observation of phase transitions of multi-component fluids in multi-scale volumes [69, 70]. Wang *et al*. [47] observed that for pure n-pentane, evaporation first takes place in the microchannel followed by the occurrence in nanochannel. For ternary alkane mixtures, no evaporation is observed in nanochannel, while fluids in microchannel evaporate completely. Very recently, by using the state-of-the-art nanofluidic devices, in which nanochannels are connected to microchannels, Zhong *et al*. [12] and Jatukaran *et al*. [67] found that the capillary evaporation (bubble point) pressure in nanopores is significantly reduced and can be even below the lower dew point pressure of originally injected fluids. Because the pore volume of nanochannels is negligible comparing to that of microchannels, the liquid-to-vapor transition in nanochannels occurs instantly and no two-phase coexistence in nanochannels is observed. These observations are in line with the engineering density functional theory (DFT) calculations by considering the interplay between the nanochannels and microchannels [8, 12].

In fact, in shale reservoirs, extensive amount of nanopores can be connected to macropores/natural fractures [3, 57], where the confinement effect can be negligible, resulting in the total volume of nanopores comparable to that of connected macropores/natural fractures [7, 71]. Thus, the interplay between nanopores and fractures can significantly affect multi-component hydrocarbon phase behavior in multi-scale volumes. Liu *et al*. [46] observed higher bubble point pressure of N_2/n-butane mixture in a crushed shale sample containing pressure-volume-temperature (PVT) cell than that of the originally injected fluids. Luo *et al*. [72] used PR EOS/capillary pressure model in their multi-scale systems and observed a lightly suppressed bulk bubble point. Bi *et al.* [73]

used modified isothermal-isobaric Gibbs ensemble Monte Carlo to study phase behavior of fluid mixtures in multi-scale volume considering volume partition and found a slightly increased bulk bubble point pressure. Very recently, we used engineering DFT to explicitly consider the fluid-surface interactions in the nanopores as well as the nano-micro pore interplay and found that the hydrocarbon mixtures in nanopores stay as liquid phase, even though those in bulk volume completely evaporate [8]. While this work can well explain the nanofluidic observations [12, 67], the complete phase transitions of multi-component fluids in multi-scale volumes, especially in nanopores, have not been revealed yet.

Thus, in this work, we use engineering DFT to study the phase transitions of hydrocarbon mixtures in multi-scale volumes, in which the nanopores are connected to finite bulk volume reservoirs (FBV). Our engineering DFT and nanopore-bulk model yield an excellent agreement with nanofluidic experimental findings, where the volume of nanochannels is negligible comparing to that of the microchannels [8, 12, 67]. Such excellent agreement with nanofluidic experiments in extreme conditions ensures that they can provide important insights into the actual shale oil production and ultimate recovery. As in our previous work [8], we apply constant composition expansion (CCE) method to the entire nanopore-bulk system at isothermal condition to simulate real shale oil production. The total amount and composition of hydrocarbon mixtures in the system are fixed, while matters can freely exchange between nanopore and connected bulk volume as pressure decreases. The fluid properties in nanopores and bulk are determined by materials balance and chemical equilibrium. We found that in nanopores, the vaporization takes place when the pressure is lower than the bulk dew point and vapor-like as well as liquid-like phases can coexist. As the volume ratio of bulk at the initial condition to pore decreases, both bubble and dew points in nanopores increase and pore two-phase region expands. Within the pore two-phase region, both

C_1 and C_3 are released from the nanopores to the bulk volume. Meanwhile, both liquid and vapor phases become denser as pressure drops, while the amount of liquid phase decreases as pressure drops. Throughout the process, the bulk phase composition varies, which is in line with the field observation [74].

Collectively, this work indicates that the competitive adsorption and volume partitioning play a key role in such multi-component and multi-scale volume problems. Besides, it demonstrates that the phase behavior of hydrocarbon mixtures in multi-scale volumes, which are critical in shale oil production and reservoir simulation, are very different from the previous modeling predictions.

3.2 Methods

Similar to our previous work [8], we assume that a nanopore of pore size W and pore volume V_p is connected to a bulk region of volume V_b as depicted in **Figure 3-1**. In this multi-scale volume, which commonly exists in shale structures, the nanopore is simulated as oil-wet structureless carbon slit pore, while we do not consider the confinement effect in the bulk region [12]. In this work, we study three different multi-scale volume cases ($V_b^i / V_p = 1$, 5, 10, in which V_b^i is the initial bulk volume) and infinite connected bulk volume (IBV) case to demonstrate the effect of volume partitioning on phase behavior. C_1-C_3 mixtures are used to represent hydrocarbon mixtures and the system temperature is set as 288.15 K, as in the previous works [8, 12]. The actual shale/tight oil formation temperatures are typically higher than 288.15 K. In addition, C_1-C_3 mixtures are lighter than the actual shale oil. However, C_1 and C_3 are in the same homologous series of typical shale oil components such as hexane, heptane, octane, as so on [75]. In fact, two-component systems which are in the same homologous series as the multi-component systems have been widely used to study the general phase behaviors [76]. Thus, as long as the system

temperature is lower than the critical temperature of C_1-C_3 mixtures, they can mimic the phase behaviors of the actual shale oil formations in such multi-scale and multi-component systems.

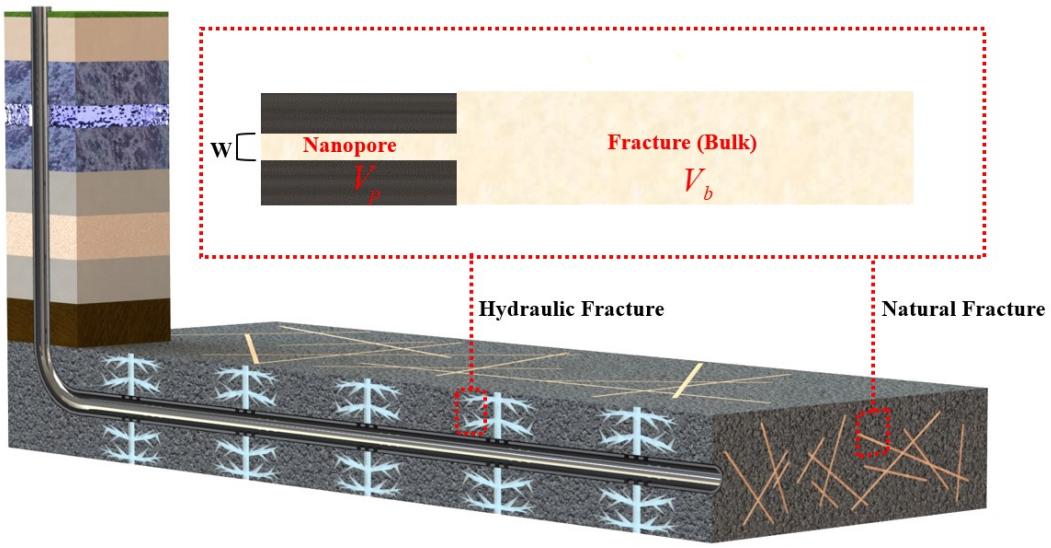

Figure 3-1. Schematic representation of shale oil extraction operation, where nanopores are connected to fractures (bulk)[8]. In our work, nanopore of pore size W and volume V_p is connected to a bulk region of volume V_b.

We apply CCE method to the multi-scale volume system to simulate the shale oil production process. We specify composition in the entire multi-scale volume $\{Z_i\}$ at initial condition, which is different from the bulk region composition $\{y_{i,b}\}$, due to competitive adsorption in nanopores [46]. At isothermal conditions, we gradually reduce system pressure P (dictated by the bulk region pressure) by expanding V_b, while V_p is fixed throughout the process. Total amount of hydrocarbon mixtures in the entire multi-scale volume is fixed. The fluid properties in nanopore and bulk region are determined by materials balance (MB) and chemical equilibrium [8]. In the bulk two-phase zone, we use liquid phase chemical potentials from the Peng-Robinson EOS (PR-EOS) to calculate fluid properties in nanopore, due to the same chemical potentials of bulk fluids

in vapor and liquid phases. Since the nanopore is liquid-wet, based on our previous work [8], we assume that only if P is less than the bulk region dew point pressure P_b^{dew}, phase transition can occur in nanopore. Details about our DFT calculations can be referred to **Appendix A**. Our engineering DFT has shown excellent agreements with experimental data and molecular simulations for bubble/dew point of nanoconfined hydrocarbon fluids [12, 58] and sorption in organic nanopores and shale nanoporous media [5, 77], in which fluid distributions are inhomogeneous and surface adsorption plays an important role. Parameters needed to apply this theory and model in shale oil studies can be divided into two categories: (1) Reservoir properties: reservoir temperature T; reservoir pressure P; pore size distributions; rock properties. (2) Fluids properties: initial fluid composition in bulk region $\{y_{i,b}\}$; critical temperature T_c, critical pressure P_c, acentric factor ω, molar weight M_w, volume shift parameter VSP, and attraction energy parameter ε_g in the QDE for each component.

The MB calculations are illustrated in three different pressure conditions: **a)** P above the bubble point pressure in the bulk region P_b^{bub} ($P > P_b^{bub}$); **b)** P between P_b^{bub} and P_b^{dew} ($P_b^{bub} > P > P_b^{dew}$); **c)** P below P_b^{dew} ($P < P_b^{dew}$).

a) $P > P_b^{bub}$

In this condition, the bulk region is in a single liquid phase. For given $\{y_{i,b}\}$ at P, the average densities of component i in bulk, $\rho_{i,b}$ and nanopores, $\rho_{i,p}$ are obtained from the PR-EOS and DFT, respectively. The total mole numbers of component i, N_i is given as

$$N_i = \rho_{i,b} V_b + \rho_{i,p} V_p, \quad i = C_1, C_3 \tag{3.1}$$

Then, $\{Z_i\}$ is given as

$$Z_i = N_i / \sum_j N_j, \quad i = C_1, C_3 \tag{3.2}$$

$\{N_i\}$ are determined by the given $\{Z_i\}$ and initial pressure P^i through iterative calculations. At subsequent $P < P^i$, V_b expands, while $\{N_i\}$ remain the same. By rewriting **Eq. (3.1)**,

$$V_b = \left(N_i - \rho_{i,p} V_p\right) / \rho_{i,b}, \quad i = C_1, C_3 \tag{3.3}$$

As shown in **Eq. (3.3)**, the equilibrium V_b for given P can be obtained from C_1 and C_3 MB equations. For given P and T, as $x_{C_3,b}$ increases/decreases, adsorption/desorption hysteresis can occur in nanopores [8]. In this work, we use the grand potential (GP) minimum branch to represent the hydrocarbon mixture behavior within the hysteresis zone [59], as shown in **Figures 3-2** and **3-3**. Thus, at equilibrium transition point, there is a discontinuity in average density in nanopores of component i, $\rho_{i,p}$, as shown in **Figure 3-3**. By varying trial C_3 composition in the bulk region $x_{C_3,b}$, we find the intersection between two $V_b - x_{C_3,b}$ curves from C_1 and C_3 to determine the equilibrium $\{y_{i,b}\}$ as shown in **Figure 3-4 (a)** and **3-4 (a')**.

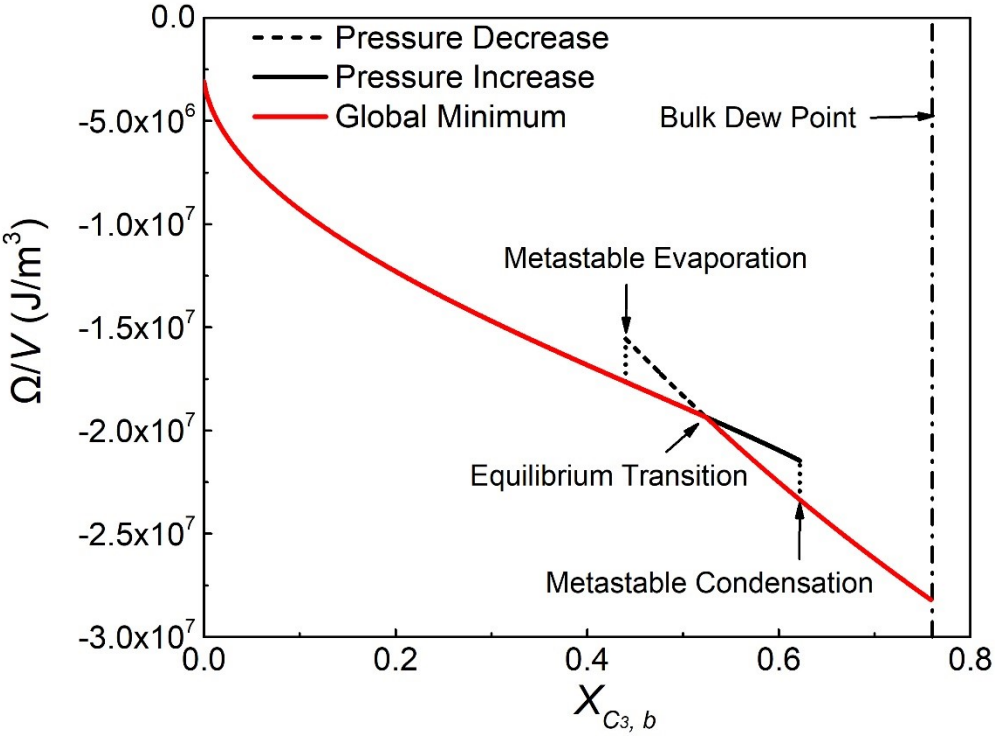

Figure 3-2. GP from pressure increasing/decreasing branches and global minimum branch in nanopores of $W = 5$ nm at 10 bar and 288.15K.

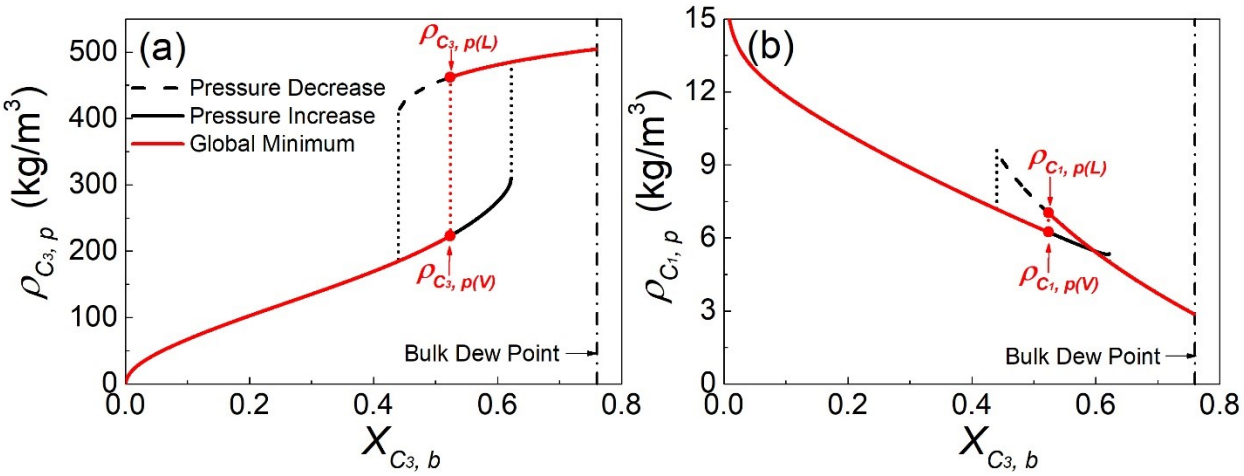

Figure 3-3. Average density of (a) C_3; (b) C_1 in nanopores from pressure increasing/decreasing and global minimum branches at $T = 288.15$ K and $P = 10$ bar for $W = 5$ nm.

b) $P_b^{bub} > P > P_b^{dew}$

In this condition, the bulk region is in two-phase. Unlike **Eq. (3.1)**, $\{N_i\}$ are given as,

$$N_i = \rho_{i,b(L)} V_{b(L)} + \rho_{i,b(V)} V_{b(V)} + \rho_{i,p} V_p, \quad i = C_1, C_3 \tag{3.4}$$

where $\rho_{i,b(L)}$ and $\rho_{i,b(V)}$ represent densities of component i in the bulk liquid and vapor phases obtained from PR-EOS, respectively; $V_{b(L)}$ and $V_{b(V)}$ are volumes of the bulk liquid and vapor phases, respectively. Bulk liquid phase chemical potentials from the PR-EOS are used as an input for DFT calculations. By rewriting **Eq. (3.4)**, we have,

$$V_{b(L)} = \left(N_i - \rho_{i,p} V_p\right) / \left[\rho_{i,b(L)} + \left(V_{b(V)} / V_{b(L)}\right) \rho_{i,b(V)}\right], \quad i = C_1, C_3 \tag{3.5}$$

According to $V_{b(V)} / V_{b(L)}$ from PR-EOS, $V_{b(V)}$ is given as,

$$V_{b(V)} = \left(V_{b(V)} / V_{b(L)}\right) V_{b(L)} \tag{3.6}$$

Then, we have

$$V_b = V_{b(V)} + V_{b(L)} \tag{3.7}$$

As in $P > P_b^{bub}$ case, for given P and T, by varying $x_{C_3,b}$, we find the intersection between two $V_b - x_{C_3,b}$ curves from C_1 and C_3 to determine the equilibrium $\{y_{i,b}\}$ as shown in **Figure 3-4 (b)** and **3-4 (b')**.

c) $P < P_b^{dew}$

In this condition, the bulk region is in a single vapor phase. When nanopores region is also in single phase (liquid or vapor), $\{N_i\}$ and the equilibrium V_b for given P are the same as in **Eqs. (3.1)** and **(3.4)**, respectively. The equilibrium $\{y_{i,b}\}$ is determined by the intersection between two

$V_b - x_{C_3,b}$ curves from C_1 and C_3 as shown in **Figure 3-4 (c)** and **3-4 (c')** for nanopore liquid phase and **Figure 3-4 (e)** and **3-4 (e')** for nanopore vapor phase.

When nanopores region is in vapor-liquid coexistence, no intersection between $V_b - x_{C_3,b}$ curves (V_b obtained from **Eq. (3.3)**) exist, which is due to the discontinuity in $\rho_{i,p}$. Within the nanopore two-phase region, $\{N_i\}$ is given as

$$N_i = \rho_{i,b} V_b + \rho_{i,p(L)} V_{p(L)} + \rho_{i,p(V)} V_{p(V)}, \quad i = C_1, C_3 \tag{3.8}$$

where $\rho_{i,p(L)}$ and $\rho_{i,p(V)}$ represent densities of component i in the nanopore liquid and vapor phases, respectively; $V_{p(L)}$ and $V_{p(V)}$ are volumes of the nanopore liquid and vapor phases, respectively. The equilibrium $\{y_{i,b}\}$ is determined as $x_{C_3,b}$, when there is discontinuity in $V_b - x_{C_3,b}$ curves as shown in **Figure 3-4 (d)** and **3-4 (d')**. We note that for a given pressure, V_b discontinuities in C_1 and C_3 branches occur at the same $X_{C_3,b}$ and they only exist within the bulk vapor phase region as shown in **Figure 3-4**. $V_{p(L)}$ and $V_{p(V)}$ have the relationship as follows,

$$V_{p(L)} + V_{p(V)} = V_p \tag{3.9}$$

By combining **Eqs. (3.8)** and **(3.9)**, $V_{p(L)}$, $V_{p(V)}$, and V_b are given as

$$V_{p(V)} = \frac{N_{C_1}\rho_{C_3,b} - N_{C_3}\rho_{C_1,b} - \rho_{C_1,p(L)}\rho_{C_3,b} + \rho_{C_3,p(L)}\rho_{C_1,b}}{\left(\rho_{C_1,p(V)} - \rho_{C_1,p(L)}\right)\rho_{C_3,b} - \left(\rho_{C_3,p(V)} - \rho_{C_3,p(L)}\right)\rho_{C_1,b}} \tag{3.10}$$

$$V_{p(L)} = V_p - V_{p(V)} \tag{3.11}$$

$$V_b = \left(N_i - \rho_{i,p(L)} V_{p(L)} - \rho_{i,p(V)} V_{p(V)}\right) / \rho_{i,b}, \quad i = C_1, C_3 \tag{3.12}$$

3.3 Results and Discussion

In this section, we first investigate the effect of volume partition on hydrocarbon mixtures phase transition and fluid properties in both nanopore and connected bulk region by varying V_b^i / V_p with initial bulk pressure $P^i = 45$ bar and $T = 288.15$ K. Then, we study the effect of nano-confinement by varying W. The overall C_1-C_3 mole fraction in the nanopore-bulk system is fixed as $Z_{C_1} / Z_{C_3} = 0.2 / 0.8$.

In **Figure 3-4**, we present different scenarios in the equilibrium conditions of nanopore-bulk system for $V_b^i / V_p = 1$ and $W = 5$ nm. At $P^i = 45$ bar, the cross between two branches occurs at $x_{C_3,b} = 0.77819$ as shown in **Figure 3-4 (a)**, where fluids in both nanopore and bulk region are in single-liquid phase. As P declines, the intersection which represents equilibrium $y_{C_3,b}$ shift to a lower value of $x_{C_3,b}$. At $P = 35$ bar, the intersection occurs in the bulk two-phase coexistence region, while nanopores is in a single-liquid phase as shown in **Figure 3-4 (b)**. At $P = 10$ bar, the intersection occurs in bulk single-vapor phase region, as depicted in **Figure 3-4 (c)**. However, fluids in nanopore still remain as a single-liquid phase. At $P = 7$ bar, there is no intersection due to discontinuity in V_b versus $x_{C_3,b}$ as shown in **Figure 3-4 (d)**, indicating the liquid-vapor two phase coexistence in nanopore, while the bulk is in a single-vapor phase. At $P = 6$ bar, the intersection occurs in a single-vapor phase in both bulk and nanopores.

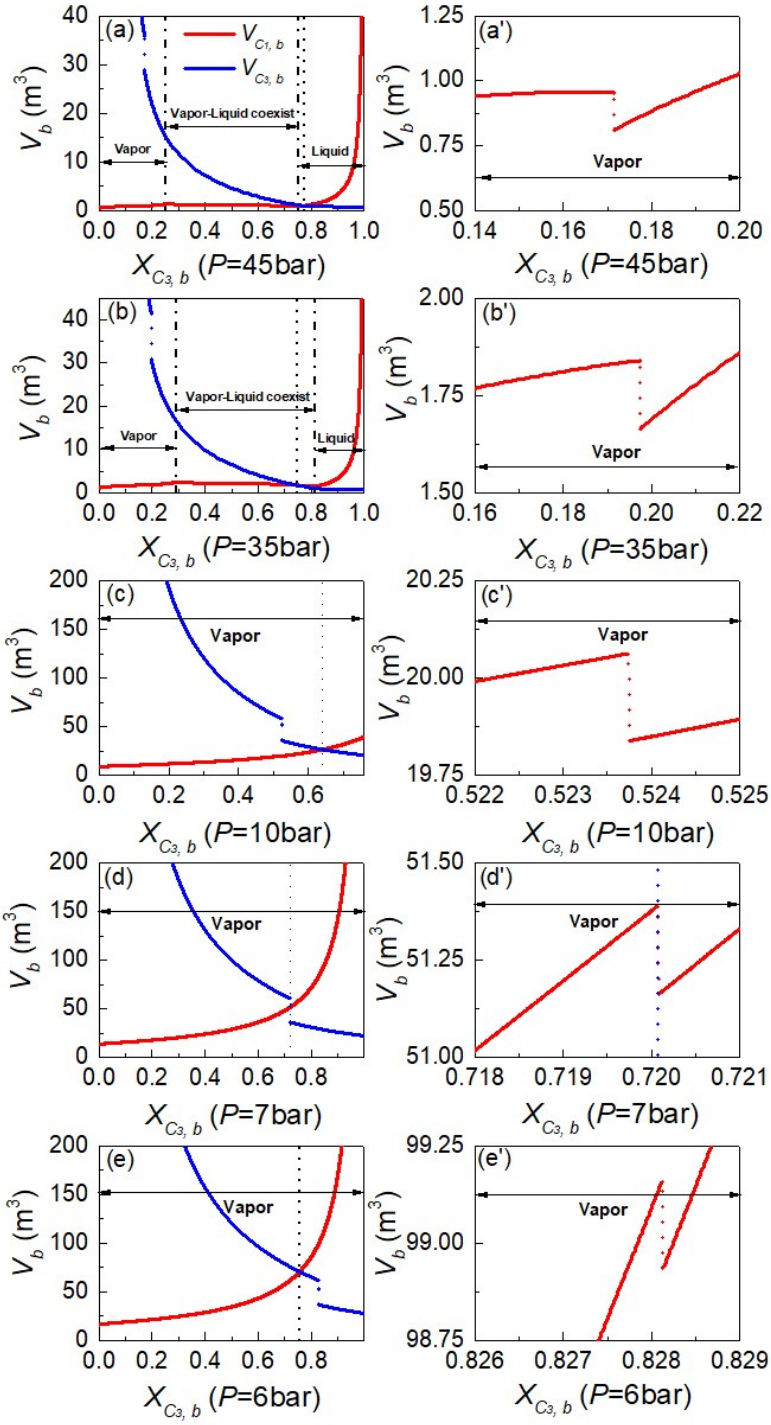

Figure 3-4. $V_b - X_{C_3,b}$ plots from C_1 (red lines) and C_3 branches (blue lines) at $T = 288.15$ K for $V_b^i / V_p = 1$ and $W = 5$ nm. (a) $P > P_b^{bub}$ ($P = 45$ bar); (b) $P_b^{bub} > P > P_b^{dew}$ ($P = 35$ bar); (c) $P_b^{dew} > P > P_p^{bub}$ ($P = 10$ bar); (d) $P_p^{bub} > P > P_p^{dew}$ ($P = 7$ bar); (e) $P < P_p^{dew}$ ($P = 6$ bar). The

corresponding magnified discontinuities in C_1 branches in (a); (b); (c); (d) and (e) are shown in (a'); (b'); (c'); (d') and (e').

In **Figure 3-5**, we present the corresponding $V_b - x_{C_3,b}$ curves at P_b^{bub}, P_b^{dew}, P_p^{bub}, and P_p^{dew} during CCE process. For P_b^{bub} and P_b^{dew}, we decrease $x_{C_3,b}$ from 1 to 0 as shown in **Figure 3-5 (a)** and **(b)** to study the phase transitions in the bulk region. For P_p^{bub} (**Figure 3-5 (c)**) and P_p^{dew} (**Figure 3-5 (d)**), we decrease $x_{C_3,b}$ from the bulk dew point composition to 0, since the phase transitions in the nanopores can only occur when the bulk fluids are in a single vapor phase [8]. At $P = P_b^{bub} = 41.136$ bar, the intersection occurs exactly at the bubble point in the bulk region, with equilibrium $y_{C_3,b} = 0.77789$. At $P = P_b^{dew} = 12.300$ bar, the intersection occurs at the dew point in the bulk region, with $y_{C_3,b} = 0.63631$. Both P_b^{bub} and P_b^{dew} are higher than that of C_1-C_3 mixtures with $Z_{C_1} / Z_{C_3} = 0.2 / 0.8$, due to the competitive adsorption in nanopore leading to the larger fraction of the lighter component in bulk region. $P = P_p^{bub} = 7.81536$ bar is the highest pressure when there is no intersection between two $V_b - x_{C_3,b}$ curves from C_1 and C_3, while $P = P_p^{dew} = 6.67608$ bar is the lowest one.

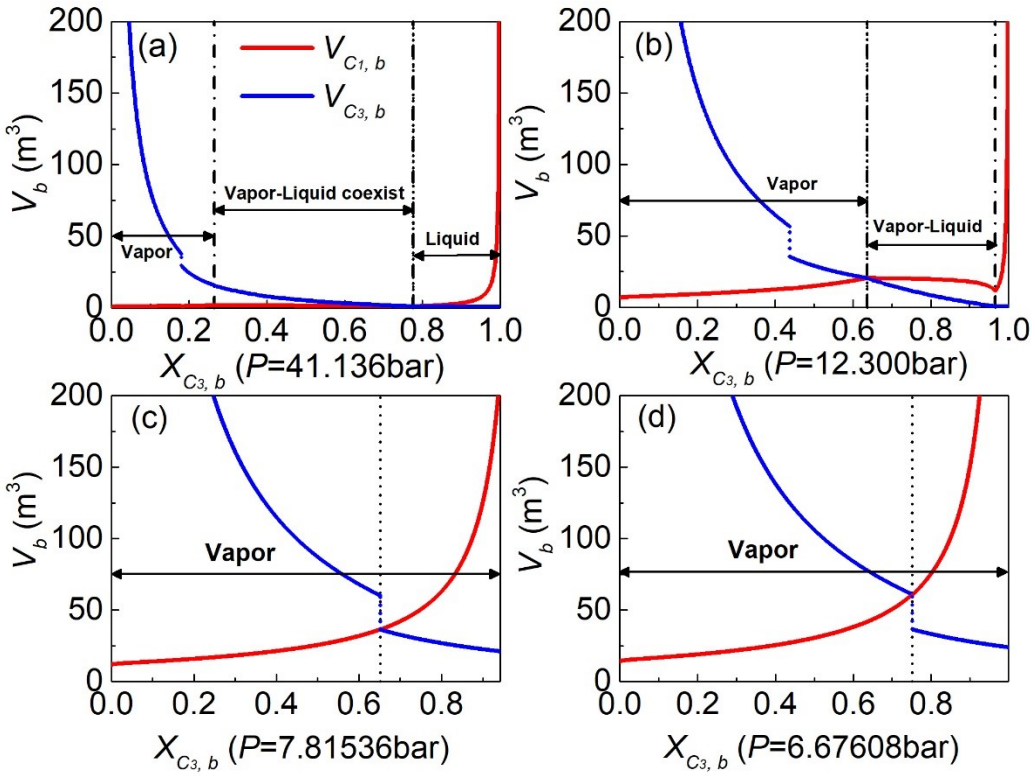

Figure 3-5. $V_b - X_{C_3,b}$ from C_1 (red lines) and C_3 branches (blue lines) at $T = 288.15$ K for $V_b^i / V_p = 1$ and $W = 5$ nm. (a) $P = P_b^{bub} = 41.136$ bar; (b) $P = P_b^{dew} = 12.300$ bar; (c) $P = P_p^{bub} = 7.81536$ bar; (d) $P = P_p^{dew} = 6.67608$ bar.

We depict $\rho_{C_3,p}$ and $\rho_{C_1,p}$ in 5 nm nanopore in multi-scale volume system for various V_b^i / V_p cases during CCE process in **Figure 3-6**. As P decreases, the lighter component can be released from nanopores, while heavier component cannot be released until $P < P_b^{dew}$. When the bulk fluids are in a liquid-vapor coexistence phase, as P declines, $\rho_{C_3,p}$ increases while $\rho_{C_1,p}$ decreases. Furthermore, for given P and T, even though the overall composition of bulk C_1-C_3 mixtures are different for various V_b^i / V_p cases, according to the Gibbs phase rule, the bulk liquid and vapor

phase properties are set. Therefore, $\rho_{C_3,p}$ and $\rho_{C_1,p}$ are the same for various V_b^i / V_p cases based on the chemical equilibrium.

When the pore fluids are in a liquid-vapor coexistence phase, both C_1 and C_3 are released from the nanopores to the bulk. It is also observed that as V_b^i / V_p increases, the pore two-phase region shrinks. For $V_b^i / V_p = \infty$, P_p^{bub} and P_p^{dew} become the same and the liquid-to-vapor phase transition occurs instantly as in the nanofluidic measurement [12]. In their experiments, they found that the vaporization of C_1-C_3 mixtures in three different nanochannels (depth of 8, 80, 800 nm), which are connected to the microchannels during equilibrium pressure drawdown process takes place effectively instantly and in full at the bubble point pressures of nanoconfined fluids. The phase diagram for mixtures in the connected nanochannels does not present a two-phase envelope, which is rather similar to that of pure component [12].

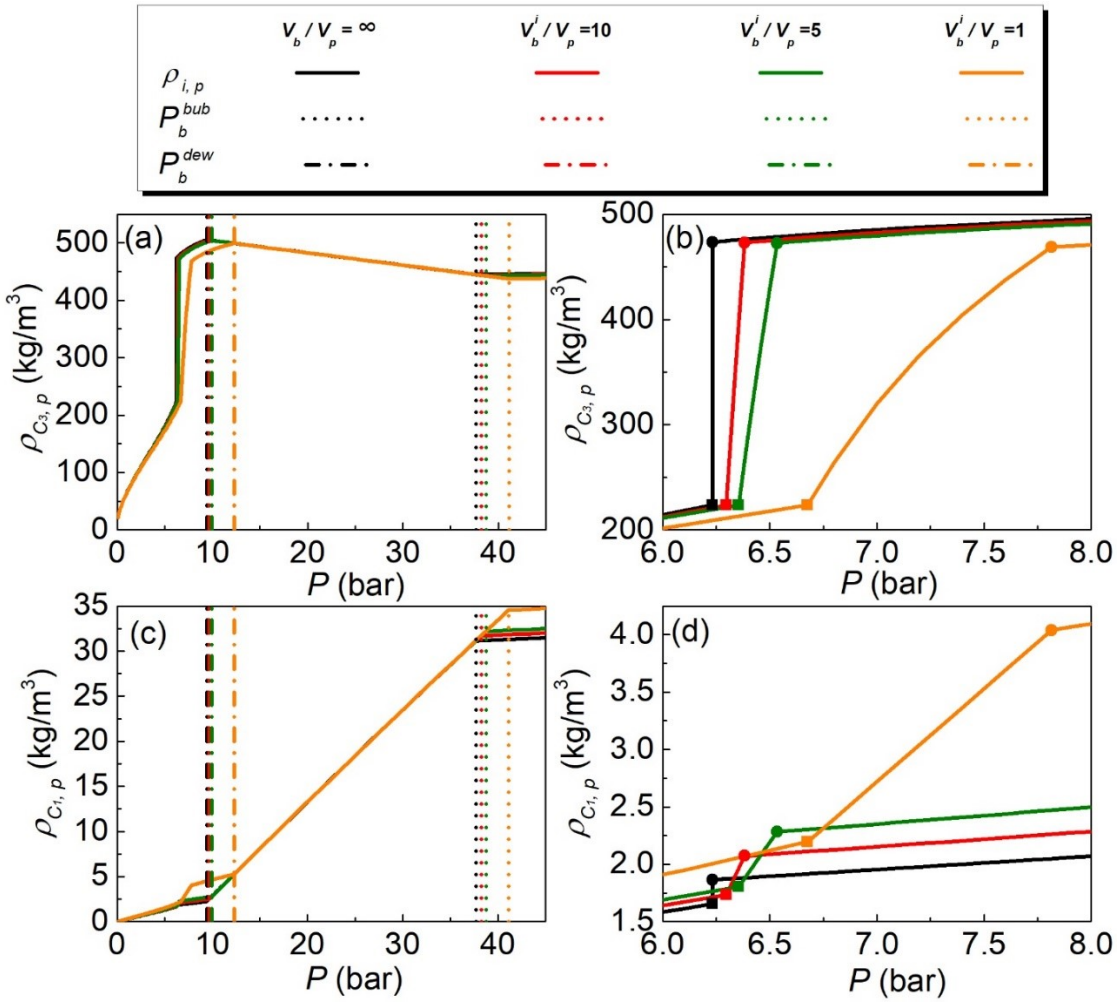

Figure 3-6. Average density of (a) C_3; (c) C_1 for various V_b^i / V_p at 288.15 K in 5 nm pore during the CCE process. For clarity, we highlight the average density of (b) C_3; (d) C_1 in nanopore two-phase region. Circles present P_p^{bub} while squares stand for P_p^{dew}.

In **Figure 3-7**, we present the average density of C_1 and C_3 in nanopore liquid and vapor phases for $V_b^i / V_p = 1$ and $W = 5$ nm as well as the mole fraction of C_3 in nanopore liquid and vapor phases, when $P_p^{bub} \geq P \geq P_p^{dew}$. The volume for liquid and vapor phases in nanopore is shown in **Figure 3-8.** When nanopore fluids are in a liquid-vapor coexistence phase, the average densities of C_3 in both liquid and vapor phases increase, while the average densities of C_1 decrease as P

drops, resulting in the increase of C_3 fractions in both liquid and vapor phases. In nanopores, liquid phase volume shrinks, while vapor phase volume increases as P declines. As a result, both C_1 and C_3 can be released from the nanopore. Fluids in nanopore completely vaporize when $P < P_p^{dew}$. The fluid properties in the nanopore multiphases for various V_b^i / V_p cases are shown in **Figure 3-9**.

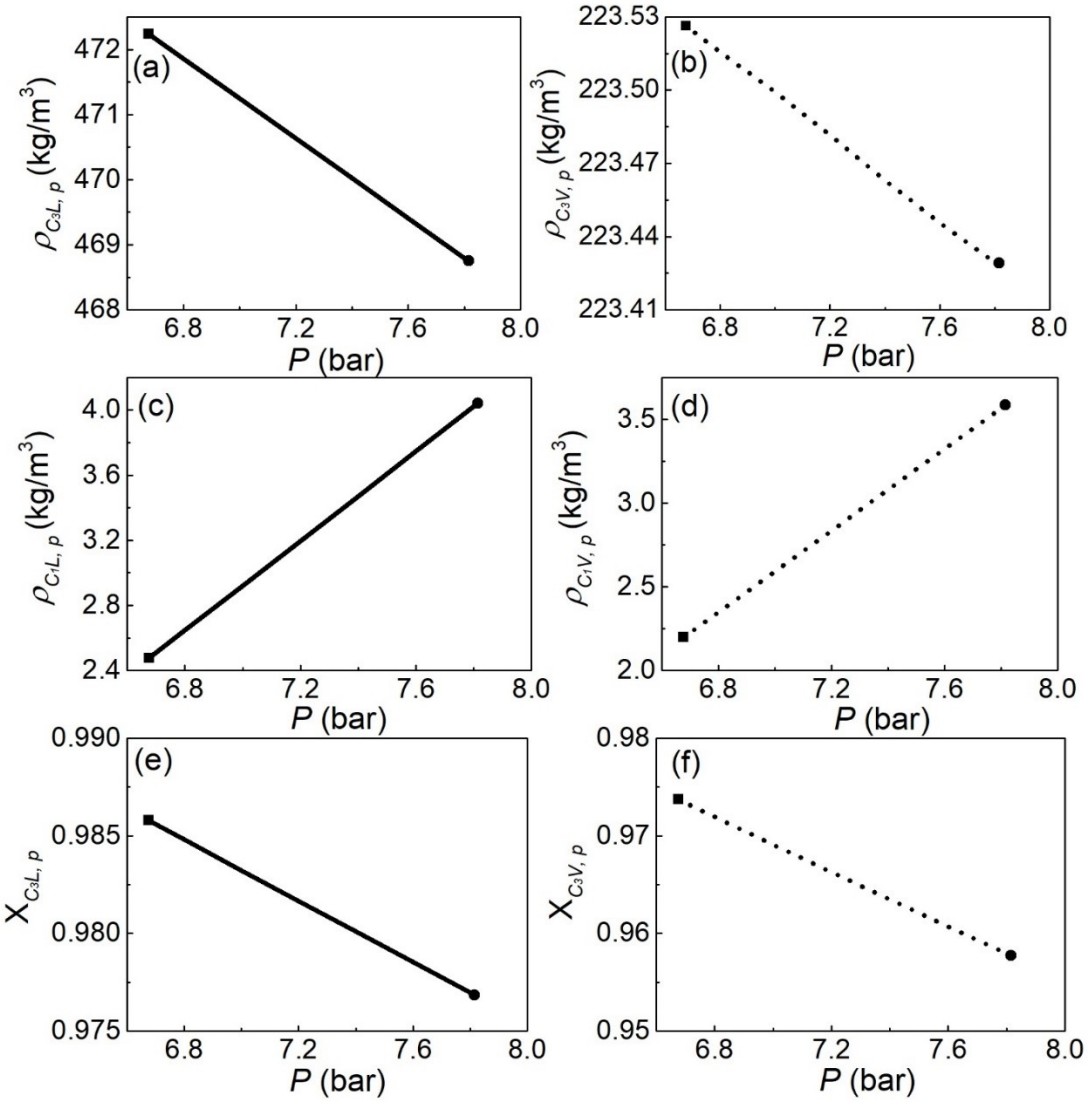

Figure 3-7. Average density of (a) C_3 in liquid phase; (b) C_3 in vapor phase; (c) C_1 in liquid phase; (d) C_1 in vapor phase; mole fraction of (e) C_3 in liquid phase; (f) C_3 in vapor phase in nanopore

liquid-vapor coexistence of $W = 5$ nm at $T = 288.15$ K and $V_b^i / V_p = 1$. Circles and squares represent P_p^{bub} and P_p^{dew}, respectively.

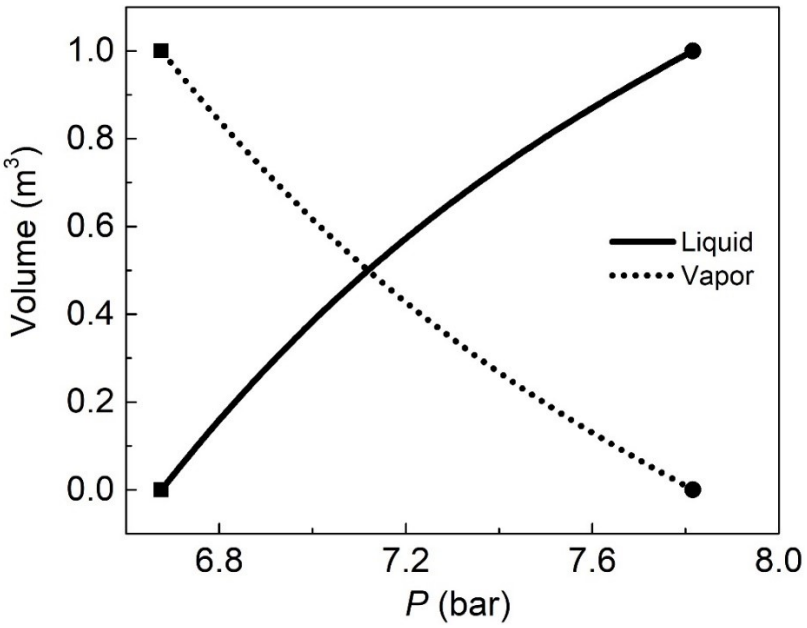

Figure 3-8. Pore liquid and vapor phase volumes for $P_p^{bub} \geq P \geq P_p^{dew}$ at $T = 288.15$ K for $V_b^i / V_p = 1$ and $W = 5$ nm. Circles and squares represent P_p^{bub} and P_p^{dew}, respectively.

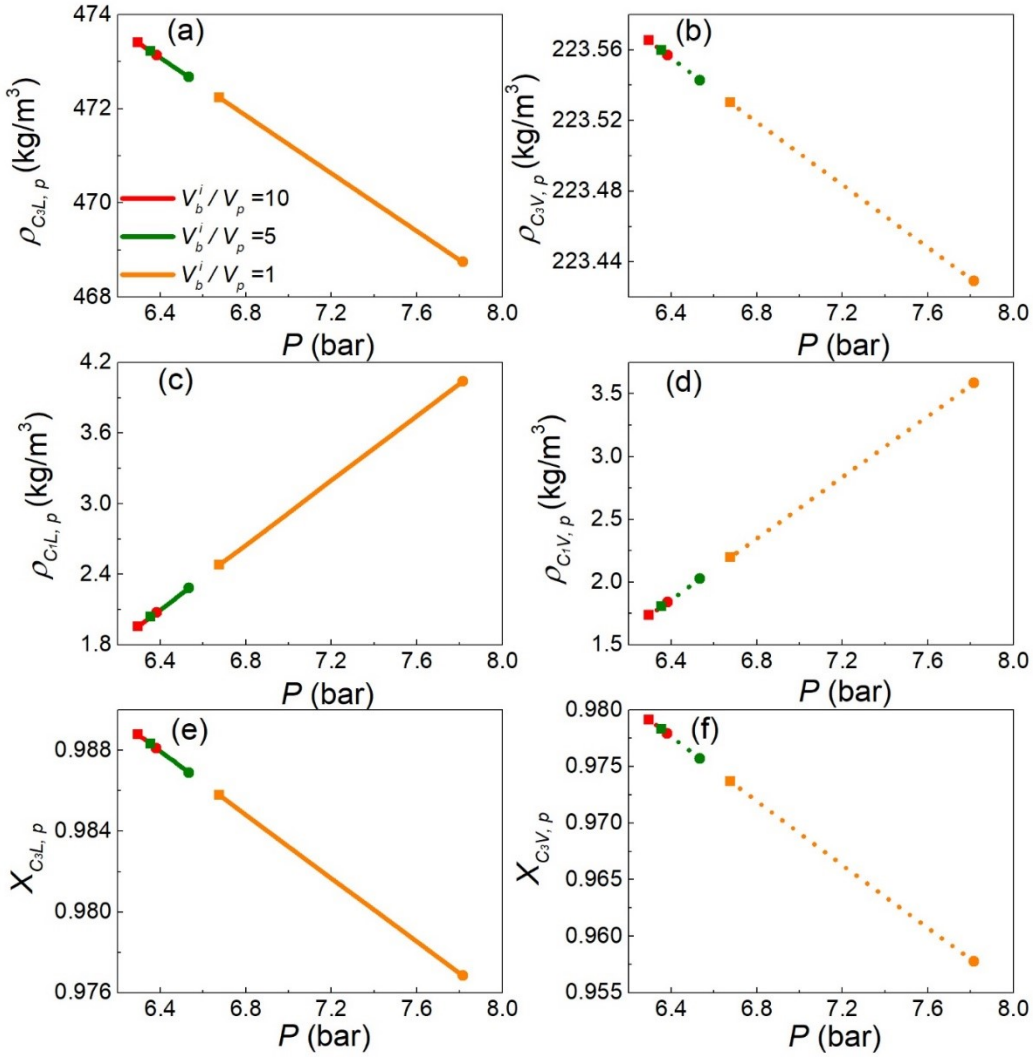

Figure 3-9. Average density of (a) C_3 in liquid phase; (b) C_3 in vapor phase; (c) C_1 in liquid phase; (d) C_1 in vapor phase; mole fraction of (e) C_3 in liquid phase; (f) C_3 in vapor phase in nanopore liquid-vapor coexistence at $T = 288.15$ K of $W = 5$ nm and various V_b^i / V_p cases. Circles and squares represent P_p^{bub} and P_p^{dew}, respectively.

In **Figure 3-10**, we depict the equilibrium C_3 compositions in nanopore and bulk for various V_b^i / V_p cases and $W = 5$ nm at 288.15 K. The equilibrium C_3 composition in nanopore $y_{C_3,p}$ is given as

$$y_{C_3,p} = \frac{N_{C_3,p}}{N_{C_1,p} + N_{C_3,p}} \ , \tag{3.13}$$

in which $N_{C_1,p}$ and $N_{C_3,p}$ represent the mole number of C_1 and C_3 in nanopore, respectively. While $y_{C_3,b}$ decreases as P declines for $P_b^{dew} \le P \le P_b^{bub}$, it increases as P decreases at $P \le P_b^{dew}$. On the other hand, for $V_b^i / V_p \ge 5$, only for $P_p^{dew} \le P \le P_p^{bub}$, $y_{C_3,p}$ decreases as P decreases, while for other P ranges, the opposite is true. It is because when pore fluid is in a single vapor-phase or liquid-phase, as P decreases, C_3 molecules can occupy the space released by C_1 due to stronger fluid-surface interactions. When the pore fluid is in a vapor-liquid coexistence phase, as P decreases, $V_{p(L)}$ shrinks, thus resulting in the decrease in $y_{C_3,p}$. However, as P drops, C_3 compositions in both pore liquid and vapor phases increase as shown in **Figure 3-7 (e)** and **(f)**. Due to the competition between liquid volume shrinkage and composition variation in multi-phases, for $V_b^i / V_p = 1$, within the pore two-phase zone, as P decreases, $y_{C_3,p}$ first increase then decrease as highlighted in **Figure 3-10 (b)**.

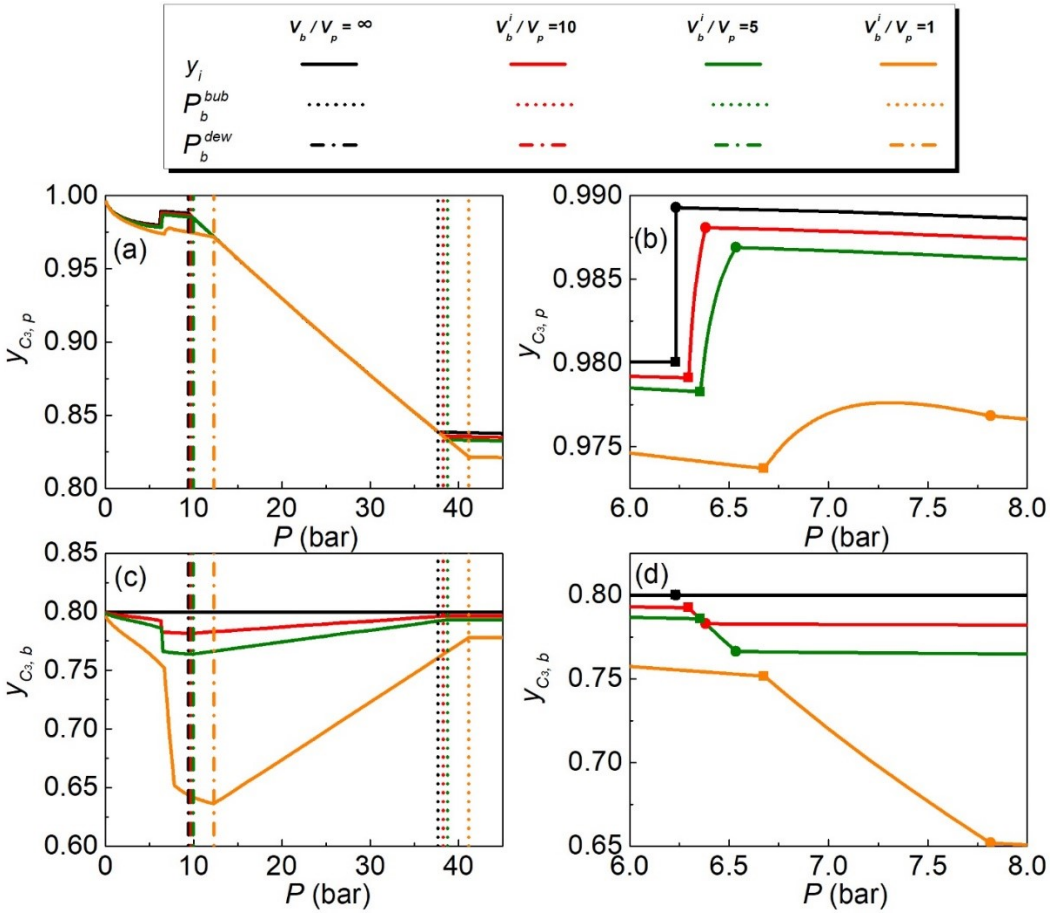

Figure 3-10. Equilibrium $y_{C_3,p}$ and $y_{C_3,b}$ during the CCE process at 288.15 K for $W = 5$ nm and various V_b^i / V_p cases. (a) C_3 composition in nanopore; (c) C_3 composition in bulk; For clarity, we present the equilibrium $y_{C_3,p}$ and $y_{C_3,b}$ around pore two-phase region: (b) C_3 composition in nanopore and (d) C_3 composition in bulk. Circles and squares represent P_p^{bub} and P_p^{dew}, respectively.

To better illustrate the multi-phase behavior in multi-scale volumes, in **Figure 3-11**, we present the pressure-composition diagram of C_1-C_3 mixtures in bulk and 5-nm pore at $T = 288.15$ K. For IBV case, $y_{C_3,b}$ remains as 0.8 [8]. Meanwhile, $y_{C_3,p}$ keeps increasing as P decreases, except for $P_p^{dew} \le P \le P_p^{bub}$ as discussed above. For FBV case (i.e. $V_b^i / V_p = 1$), due to competitive adsorption

in nanopore, $y_{C_3,b}$ shifts to a lower value. Meanwhile, $y_{C_3,p}$ increases as P declines, except for $P_p^{dew} \le P \le P_p^{bub}$. Note that $y_{C_3,p}$ remains the same when bulk fluids are in a two-phase coexistence. Interestingly, $y_{C_3,b}$ and $y_{C_3,p}$ present slope changes at P_b^{bub}, P_b^{dew}, P_p^{bub} and P_p^{dew}, as shown in **Figure 3-11 (b).**

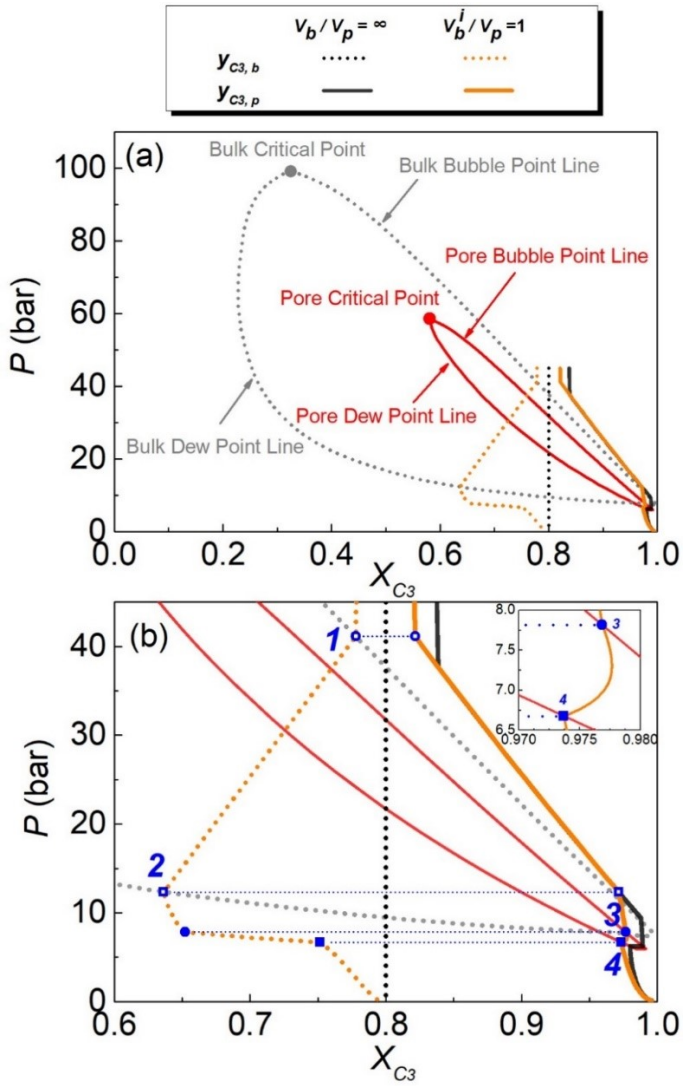

Figure 3-11. (a) Pressure-composition diagram of C_1-C_3 mixtures in bulk (gray dotted lines) and nanopore of $W = 5$ nm (red solid lines) at $T = 288.15$ K and the corresponding equilibrium $y_{C_3,b}$ (black dotted lines for $V_b / V_p = \infty$, yellow dotted lines for $V_b^i / V_p = 1$) and $y_{C_3,p}$ (black solid lines

for $V_b / V_p = \infty$, yellow solid lines for $V_b^i / V_p = 1$). (b) Highlighted part of (a), which includes equilibrium $y_{C_3,p}$ and $y_{C_3,b}$ at (1) P_b^{bub}, (2) P_b^{dew}, (3) P_p^{bub} and (4) P_p^{dew}.

We present C_1 and C_3 average densities in various nanopores during the CCE process in **Figure 3-12**. As pore size increases, two-phase region in nanopore expands and more C_3 is released from the nanopore to the bulk region. In **Figure 3-13**, we depict $y_{C_3,b}$ and $y_{C_3,p}$ for $V_b^i / V_p = 1$ and various nanopores. We find that as pore size increases, $y_{C_3,p}$ shifts to a lower value, while $y_{C_3,b}$ shifts to a larger value. It is because compared to smaller nanopore, larger pores have weaker fluid-surface interaction, thus adsorb fewer heavier components. The fluid properties in various sizes of nanopores' multi-phases are shown in **Figure 3-14.**

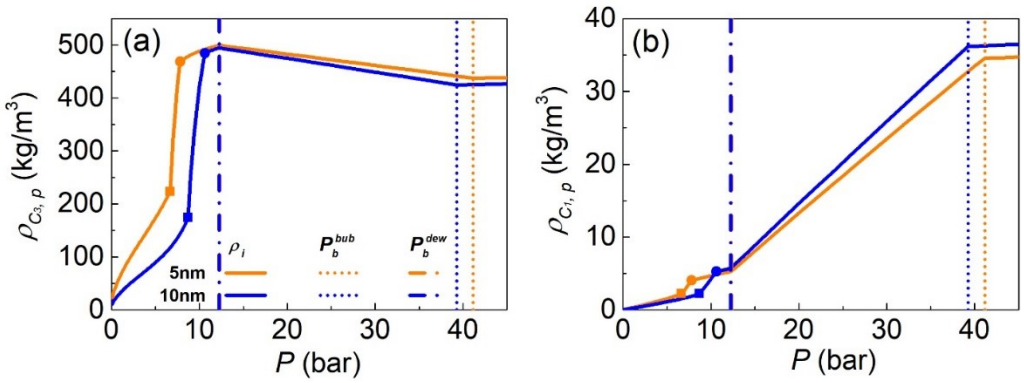

Figure 3-12. (a) C_1; (b) C_3 average densities in various nanopores at 288.15 K and $V_b^i / V_p = 1$ during the CCE process. Circles and squares represent P_p^{bub} and P_p^{dew}, respectively.

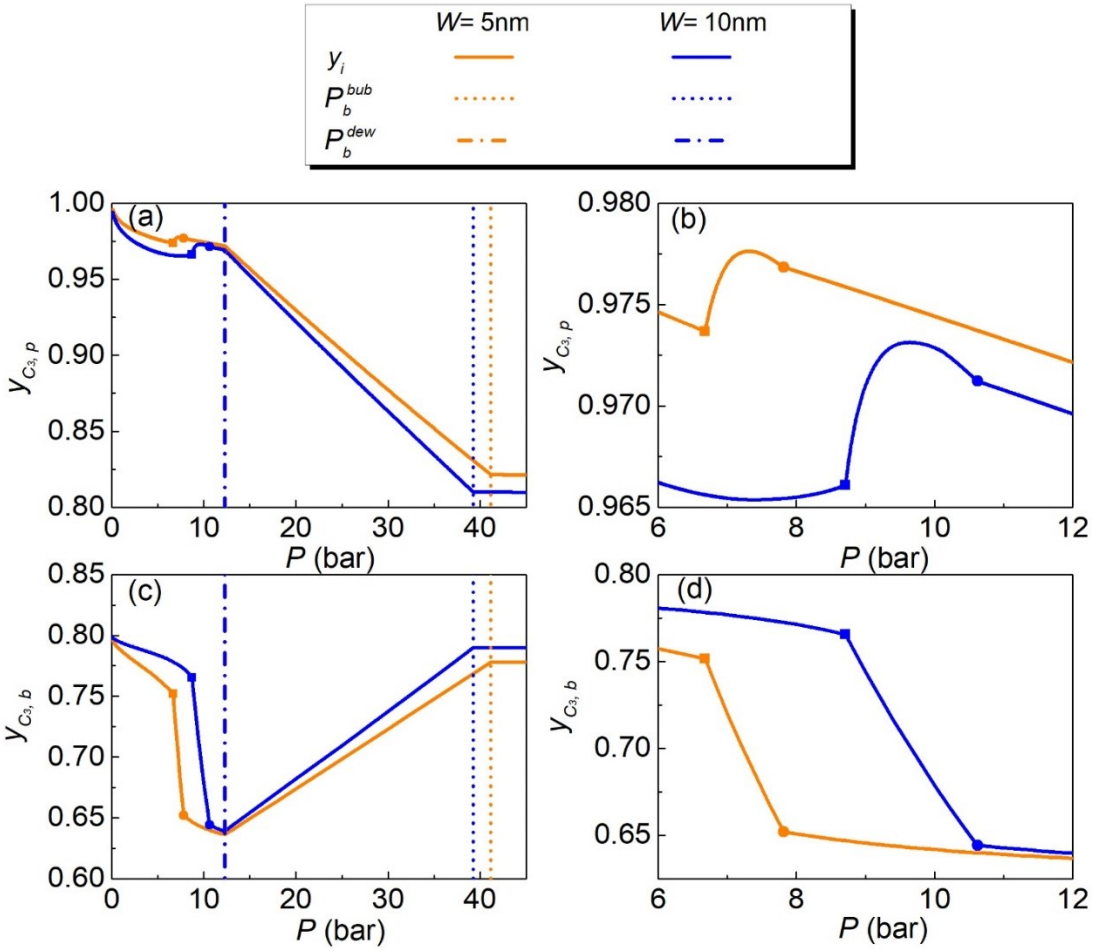

Figure 3-13. Equilibrium (a) $y_{C_3,p}$; (c) $y_{C_3,b}$ during the CCE process at 288.15 K for $V_b^i / V_p = 1$ and various nanopores. For clarity, we present the equilibrium (b) $y_{C_3,p}$; (d) $y_{C_3,b}$ in pore two-phase region. Circles and squares represent P_p^{bub} and P_p^{dew}, respectively.

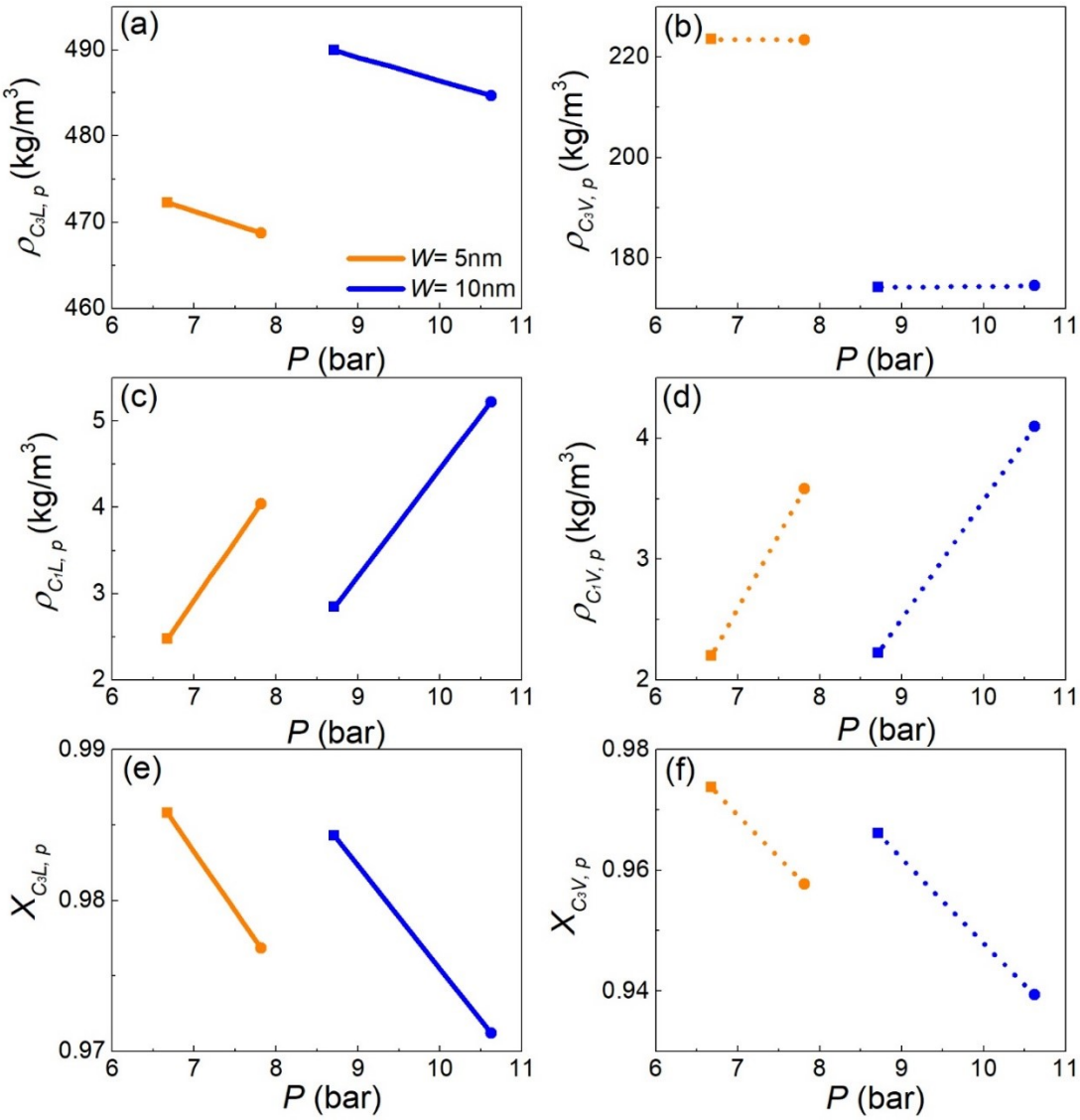

Figure 3-14. Average density of (a) C_3 in liquid phase; (b) C_3 in vapor phase; (c) C_1 in liquid phase; (d) C_1 in vapor phase; mole fraction of (e) C_3 in liquid phase; (f) C_3 in vapor phase in nanopore liquid-vapor coexistence at $T = 288.15$ K of $V_b^i / V_p = 1$ and various sizes of nanopores cases. Circles and squares represent P_p^{bub} and P_p^{dew}, respectively.

In **Table 3-1**, we summarize P_b^{bub}, P_b^{dew}, P_p^{bub}, P_p^{dew}, and the sizes of bulk two-phase region ($\Delta P_b = P_b^{bub} - P_b^{dew}$) and nanopore two-phase region ($\Delta P_p = P_p^{bub} - P_p^{dew}$) at $T = 288.15$ K during

CCE process for various volume partitions and nanopores. As V_b^i / V_p decreases, both bubble and dew points in nanopores increase and pore two-phase region expands as shown in **Figure 3-15**. Smaller fraction of the heavier components in nanopores results in the increase in both P_p^{bub} and P_p^{dew}. Furthermore, as W increases, ΔP_b decreases while ΔP_p increases. In larger nanopores, there are fewer heavier components, while bulk region contains more heavier components, comparing to smaller nanopores.

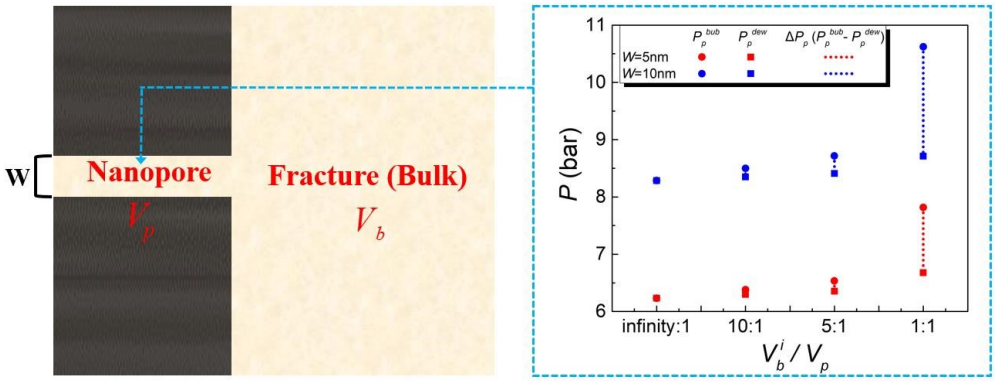

Figure 3-15. P_p^{bub} , P_p^{dew}, and the size of nanopore two-phase region ($P_p^{bub} - P_p^{dew}$) at $T = 288.15$ K during the CCE process for various volume partitions and various sizes of nanopores.

Table 3-1. P_b^{bub} , P_b^{dew} , P_p^{bub} , P_p^{dew} , the sizes of bulk two-phase region ($\Delta P_b = P_b^{bub} - P_b^{dew}$) and nanopore two-phase region ($\Delta P_p = P_p^{bub} - P_p^{dew}$) at $T = 288.15$ K during CCE process for various volume partitions and pore sizes.

W (nm)	V_b^i / V_p	P_b^{bub} (bar)	P_b^{dew} (bar)	P_p^{bub} (bar)	P_p^{dew} (bar)	ΔP_b (bar)	ΔP_p (bar)
5	∞ : 1	37.679	9.422	6.232	6.232	28.257	0
	10 : 1	38.249	9.677	6.38270	6.29665	28.572	0.08605

	5 : 1	38.742	9.939	6.53500	6.35481	28.803	0.18019
	1 : 1	41.136	12.300	7.81536	6.67608	28.836	1.13928
	∞ : 1	37.679	9.422	8.285	8.285	28.257	0
	10 : 1	37.955	9.673	8.4984	8.3511	28.282	0.1473
10	5 : 1	38.190	9.931	8.7163	8.4092	28.259	0.3071
	1 : 1	39.271	12.235	10.6224	8.7123	27.036	1.9101

3.4 Conclusions

In this work, we use DFT which can explicitly consider the fluid-surface interactions and the inhomogeneous density distributions to study the multi-phase transitions of C_1-C_3 mixtures in multi-scale volumes. This work intends to unlock the thermodynamic phenomena arising from the multicomponent and multiphase fluids in multiscale geometries which is at the heart of shale/tight reservoirs.

We found that vapor-like and liquid-like phases can coexist in nanopores, when P is between P_p^{bub} and P_p^{dew}. The emergence of two-phase in nanoscale pore can cause serious pore blocking problems due to extremely high capillary pressures. Within pore two-phase region, both C_1 and C_3 are released from the nanopores to the bulk region and both liquid and vapor phases become denser as pressure drops. Only further decreasing P below P_p^{dew}, C_3 in nanopores can be recovered. As W increases, two-phase region in nanopore expands and more C_3 are released from nanopore to bulk. As V_b^i / V_p decreases, both bubble and dew points in nanopores increase and pore two-phase region expands. On the other hands, as W increases, the bulk two-phase region shrinks.

Collectively, this work indicates that due to competitive adsorption and volume partitioning, multi-component fluids can render complex multi-phase behaviors in multi-scale volumes which are in the heart of shale oil production. Such complex phenomena have strong influences and far-reaching impacts on hydrocarbon recovery optimization, reserve estimation as well as energy security [12].

Our work emphasizes the importance of volume partition in such multi-scale, multi-component and multi-phase systems, which has not been taken into account in the current state-of-the-art nanofluidic devices where nanochannels are connected to microchannels. While such non-negligible volume partition effects have been verified by using molecular simulations [73], it also asks for nanofluidic experiment verifications in future.

Acknowledgement

This research was enabled in part by support provided by Westgrid (www.westgrid.ca) and Compute Canada (www.computecanada.ca). The authors also greatly acknowledge a Discovery Grant from Natural Sciences and Engineering Research Council of Canada (NSERC RGPIN-2017-05080). As a part of the University of Alberta's Future Energy Systems research initiative, this research was made possible in part thanks to funding from the Canada First Research Excellence Fund.

CHAPTER 4 HYDROCARBON MIXTURE PHASE BEHAVIORS IN MULTI-SCALE SYSTEMS IN RELATION TO SHALE OIL RECOVERY: THE EFFECT OF PORE SIZE DISTRIBUTIONS

A version of this chapter has been published in Fuel.

4.1 Introduction

In recent decades, the exploitation and production of unconventional oil and gas have drastically increased as the global energy consumption continuously increases and conventional reservoirs gradually deplete [65, 78, 79]. Unlike the conventional reservoirs, pores in shale formations are predominantly in nanoscale [3]. As a result, the conventional equations of state (EOS) modeling becomes inapplicable for the prediction of shale fluid properties [9, 25, 26]. On the other hand, hydraulic and natural fractures connected to the vast nano-scale pores form the recovery flow routes for the hydrocarbons stored in shale nanoporous matrix [6]. Since fluids can freely exchange between nanopores and macropores/fractures (the so-called interplay between nanopores and macropores/fractures), such nanopore-fracture multi-scale system in shale formations further complicates the in-situ fluid properties, which are multi-component and multi-phase [8, 12]. As hydrocarbon mixture phase behaviors in shale media play a crucial role in the predictions of well productivity, ultimate oil recovery and the applications of enhanced oil recovery (EOR) technologies [6], it is imperative to understand the hydrocarbon mixture phase behaviors in the multi-scale systems and the interplay between nanopores and macropores/fractures.

In this regard, there have been a number of experimental measurements using indirect and direct observations to study hydrocarbon mixture phase behavior in nanoporous media. The indirect (observation) methods include using differential scanning calorimetry (DSC) [9, 80] and slope change in pressure-volume plot [10, 11, 45]. While Deo and his coworkers observed that the bubble point pressures of nanoconfined methane/n-decane and methane/n-octane mixtures are slightly reduced [10, 11], Liu et al. [46] observed that the bubble point pressure of nitrogen/n-butane mixture in a crushed shale sample containing PVT cell is higher than the bulk due to the competitive adsorption of nitrogen and n-butane in nanopores. They also indicate that the interplay

between nanopores and macropores/fractures can influence the properties of hydrocarbon mixtures in multi-scale systems [46]. Besides the indirect method, the lab-on-a-chip technology can achieve direct observations of phase transitions of nanoconfined fluids in a near-equilibrium process. Wang et al. [47] found that a ternary mixture of n-butane/iso-butane/n-octane in nanochannels do not vaporize, even when the hydrocarbon mixtures in connected microchannels completely vaporize. Alfi et al. [81] used the lab-on-a-chip technology to directly visualize the phase transitions of binary hydrocarbon mixtures (pentane/hexane and pentane/heptane) and a ternary hydrocarbon mixture (pentane/hexane/heptane) in 10-nm, 50-nm and 100-nm nanochannels. They found that while the bubble point temperature of hydrocarbon mixtures in the 10-nm nanochannels increases significantly, those in the 50-nm and 100-nm nanochannels are close to the bulk. Zhong et al. [12] directly visualized the instantaneous phase transitions of hydrocarbon mixtures (methane/propane) in nanochannels, which are connected to microchannels. The bubble point pressure of hydrocarbon mixtures in 8-nm nanochannels is severely suppressed to be below their bulk dew point pressure and the confinement effect magnifies as pore size decreases. Although these advanced nanofluidic technologies have shed lights on hydrocarbon phase behaviors in nanopores, the interplay between nanopores and macropores/fractures inherent in shale matrix is difficult to realize due to the drastic volume difference between microchannels and nanochannels [12]. As a result, the effect of interplay between nanochannels and connected microchannels on fluid properties in the multi-scale system is negligible, while the fluids in the microchannels behave as bulk.

Underlying mechanisms of fluids phase behaviors in nanopores-facture multi-scale system have been studied from theoretical and simulation perspectives. By using a pore-size-dependent equation of state modeling (PR-C EOS), Luo et al. [72] found that when the pore volume of 15-nm nanopores and the connected bulk region are comparable at the initial condition, the bubble

point pressure of oil in the bulk region is reduced. By using a modified isothermal-isobaric Gibbs ensemble Monte Carlo simulation, Bi and Nasrabadi [73] observed an increased bulk bubble point pressure P_b^{bub} of a binary hydrocarbon mixture (methane/ethane), which are connected to 4-nm pores. Recently, we used an engineering density functional theory (DFT) to study phase behaviors of methane-propane mixtures in nanopores which are connected to bulk regions [24]. We found that two-phases could coexist in nanopores, and nanopore two-phases region expands as pore size increases. However, we used a uniform pore size model, which does not consider pore size distribution (PSD) inherent in shale studies [3]. Since PSD is crucial for characterization of shale reservoirs, accurate estimation of reservoir storage, understanding fluid flow mechanisms and production behavior [82-86], using a uniform pore size model may become inapplicable. Although many previous works studied pore size effect [25, 87, 88], a single-nanopore model is generally used and fluid behaviors in various nanopores are independent of each other. Some work [89, 90] studied PSD effect without considering the interplay between nanopores and macropores/fractures. However, in shale media, various nanopores are connected with macropores/fractures, forming a complex multi-scale system, in which fluid properties are affected by their interplay [91, 92].

In this regard, Wang et al. [93, 94] used the Peng-Robinson equations of state (PR-EOS) plus capillary pressure model to study continuous phase transitions in shale nanoporous media consisting of four representative nanopores and fractures. They assumed that the phase transitions in nanopores occur at varying pressures for nanopores of different pore sizes. They further assumed that the smaller pores are saturated with liquids, while the larger pores have liquid-to-vapor phase transitions. Even though these works provided important insights into hydrocarbon phase behaviors in various nanopores connected with fractures, such EOS-based models do not consider the fluid-surface interactions and inhomogeneous density distributions under nano-confined

environment. Luo et al. [72, 95] considered fluid-surface interactions in their triple-scale PR-C EOS model, in which 5-nm and 15-nm nanopores are connected to fractures. They found a suppressed bulk bubble point P_b^{bub} during constant composition expansion (CCE) process. However, these works only lower the pressure to a value higher than the bulk dew point P_b^{dew} so that the information about P_b^{dew} and phase transitions as well as fluid depletions in nanopores are missing. As a result, the phase behaviors of hydrocarbon mixtures in nanopores with PSD connected with macropores/fractures are still not clear yet.

In this work, we simultaneously consider the effect of fluid-surface interaction, interplay between nanopores and macropores/fractures, PSD inherent in shale media to investigate phase behaviors of C1/C3 mixture. We use a simplified carbon slit-pore to represent the nanoconfinement effect in kerogen, which plays a dominant role in fluid-in-place in shale reservoirs [39, 54, 58, 96]. Slit-shaped pores are widely distributed in kerogen [7, 97]. Both kerogen and carbon surfaces are strongly oil wet [98-101] and carbon slit pores have been widely used to model kerogen pores in molecular simulations [102, 103]. Both CCE and constant volume depletion (CVD) processes are discussed by comparing three different nanopore-fracture multi-scale systems, which consist of various nanopores of different sizes and a fracture (bulk region). While we explicitly consider the fluid-surface interactions in nanopores, the fluids in fractures are treated as bulk. Based on the multi-scale model, we study continuous phase transitions and hydrocarbon mixture recovery in various nanopores and the bulk region. This work should provide important insights into the effect of PSD and interplay between nanopores and macropores/fractures in actual shale oil production processes.

4.2 Methods

4.2.1 The Nanopores-Bulk Model

In this work, we construct a multi-scale system with PSD effect in which two different nanopores of pore sizes as 5 nm and 10 nm are considered. As in our previous work [8, 24], the fluids in nanopores and bulk region are in chemical equilibrium. In our previous nanofluidic measurements [12], we found that in a near-equilibrium pressure drawdown process, in which the pressure drawdown rate is set as ~0.035 MPa/min, equivalently ~50.4 MPa/day, C_1-C_3 vaporization dynamics and initiations can be captured by the engineering DFT which is conducted at the equilibrium state. In contrast, the pressure drawdown rate during an actual shale production is generally less than 1 MPa/day [104, 105]. Therefore, we use the equilibrium pressure drawdown to convey the knowledge about the actual shale oil production process.

We use C_1/C_3 mixture to illustrate the effect of PSD on hydrocarbon mixture phase behavior in a multi-scale system. As shown in **Figure 4-1**, three different systems are studied, in which the pore volumes of nanopores and bulk region volume ratio are given as: 1) **Case A**: $V_{5\text{nm}}:V_{10\text{nm}}:V_b^{int}=1:0:1$; 2) **Case B**: $V_{5\text{nm}}:V_{10\text{nm}}:V_b^{int}=0.5:0.5:1$; 3) **Case C**: $V_{5\text{nm}}:V_{10\text{nm}}:V_b^{int}=0:1:1$, where $V_{5\text{nm}}$ and $V_{10\text{nm}}$ represent the pore volumes in 5-nm and 10-nm pores, respectively, and V_{b}^{int} is initial bulk volume which is comparable to the total volume of nanopores according to inherent characteristics of shale [38, 71]. The nanopores are simulated as structureless carbon slit pores which is completely oil wet, while the bulk region represents macropores/fracture without confinement effect [8]. The fluid properties in the nanopores and bulk region are determined by materials balance (MB) and chemical equilibrium [24]. We use the Peng-Robinson EOS (PR-EOS) [106] to calculate bulk chemical potentials. When the bulk fluids are in

a vapor-liquid coexistence phase, due to the equal chemical potentials in vapor and liquid phases, liquid phase chemical potentials are used to calculate fluid compositions in nanopores [24]. The details of DFT calculation are shown in **Appendix A**.

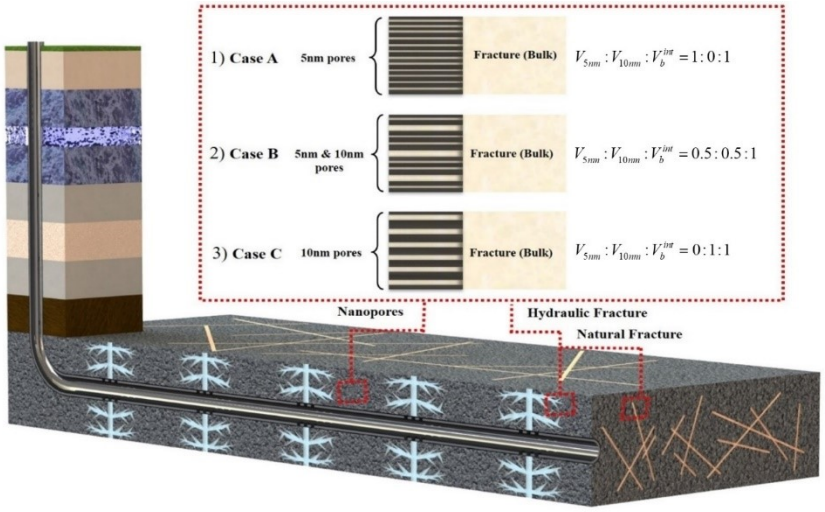

Figure 4-1. Schematic representation of shale oil extraction operation, where nanopores are connected to fractures/macropores (bulk) [8]. In our work, nanopores of pore volumes V_p are connected to a bulk region of volume V_b. 1) Case A: $V_{5\text{nm}}:V_{10\text{nm}}:V_b^{int}=1:0:1$; 2) Case B: $V_{5\text{nm}}:V_{10\text{nm}}:V_b^{int}=0.5:0.5:1$; 3) Case C: $V_{5\text{nm}}:V_{10\text{nm}}:V_b^{int}=0:1:1$.

4.2.2 Material Balance

CCE and CVD processes are simulated under an isothermal condition of $T=288.15$ K. We specify the initial bulk region C_3 composition $y_{C_3,b}$ as 0.8 and the initial pressure P^{int} as 45 bar in all cases. We illustrate the MB calculations of the CCE and CVD processes in two separate subsections. The flowcharts of the calculation procedures for the CCE and CVD processes are shown in **Figures C-1** and **C-2** (**Appendix C**), respectively.

4.2.2.1 CCE

In CCE process, as system pressure P (dictated by the bulk region pressure) decreases, the bulk region volume V_b increases, while the nanopore volumes of various sizes V_p remain constant. The total amount of hydrocarbons in the nanopores-bulk system is constant. MB calculations are illustrated in three different pressure conditions: **a)** P above the bubble point pressure in the bulk region P_b^{bub} ($P > P_b^{bub}$); **b)** P between P_b^{bub} and P_b^{dew} ($P_b^{bub} > P > P_b^{dew}$); **c)** P below P_b^{dew} ($P < P_b^{dew}$).

a) $P > P_b^{bub}$

In this case, the bulk region is in a single liquid-phase. For given $\{y_{i,b}\}$ at P, the average densities of component i in bulk, $\rho_{i,b}$ and nanopores, $\rho_{i,p}$ are obtained from the PR-EOS and DFT, respectively. The total molar number of component i at the initial condition (for a given initial pressure P^{int}), N_i^{int}, is given as,

$$N_i^{int} = \rho_{i,b}^{int} V_b^{int} + \sum \rho_{i,p}^{int} V_p, \quad i = C_1, C_3, \quad p = 5\text{nm}, 10\text{nm}, \tag{4.1}$$

in which $\rho_{i,b}^{int}$ and $\rho_{i,p}^{int}$ represent the average molar densities of component i in bulk and nanopores of p at P^{int}**.** Note that $\{N_i^i\}$ remain constant during the CCE process. As P decreases, V_b increases, which is given as,

$$V_b = \left(N_i^{int} - \sum \rho_{i,p} V_p \right) / \rho_{i,b}, \quad i = C_1, C_3, \quad p = 5\text{nm}, 10\text{nm}. \tag{4.2}$$

As shown in **Eq. (4.2)**, the equilibrium V_b for given P can be obtained from C_1 and C_3 MB equations. As in our previous work [24], for given P and T, by varying trial C_3 composition in

the bulk region $x_{C_3,b}$, we find the intercept between two $V_b - x_{C_3,b}$ curves from C_1 and C_3 to determine the equilibrium $\{y_{i,b}\}$ as shown in **Figure C-3** (**Appendix C**). The equilibrium phase transition point determined from the grand potential (GP) minimum branch [59] is used to represent the hydrocarbon mixture behaviors. At equilibrium, GP is minimum for an open system in which the fluids in nanopores are in chemical equilibrium with those in bulk [107].

b) $P_b^{bub} > P > P_b^{dew}$

In this case, the bulk region is in a vapor-liquid coexistence phase. Unlike **Eq. (4.1)**, $\{N_i^{int}\}$ are given as,

$$N_i^{int} = \rho_{i,b(L)} V_{b(L)} + \rho_{i,b(V)} V_{b(V)} + \sum \rho_{i,p} V_p, \quad i = C_1, C_3, \quad p = 5\text{nm}, 10\text{nm}, \tag{4.3}$$

where $\rho_{i,b(L)}$ and $\rho_{i,b(V)}$ represent molar densities of component i in the bulk liquid and vapor phases obtained from PR-EOS, respectively; $V_{b(L)}$ and $V_{b(V)}$ are volumes of the bulk liquid and vapor phases, respectively. The bulk liquid phase chemical potentials from the PR-EOS are used as an input for DFT calculations. By rewriting **Eq. (4.3)**, we have the liquid volume as,

$$V_{b(L)} = \left(N_i^{int} - \sum \rho_{i,p} V_p \right) / \left[\rho_{i,b(L)} + \left(V_{b(V)} / V_{b(L)} \right) \rho_{i,b(V)} \right], \quad i = C_1, C_3, \quad p = 5\text{nm}, 10\text{nm}. \tag{4.4}$$

According to $V_{b(V)} / V_{b(L)}$ from PR-EOS, the vapor volume after expansion, $V_{b(V)}$, is given

$$V_{b(V)} = \left(V_{b(V)} / V_{b(L)} \right) V_{b(L)}. \tag{4.5}$$

Then, the total volume after expansion is given as

$$V_b = V_{b(V)} + V_{b(L)}. \tag{4.6}$$

As in $P > P_b^{bub}$ case, for given P and T, by varying $x_{C_3,b}$, we find the intercept between two $V_b - x_{C_3,b}$ curves from C_1 and C_3 to determine the equilibrium $\{y_{i,b}\}$ as shown in **Figure C-3 (a)**. The highest and lowest pressures when there is an intercept between the two $V_b - x_{C_3,b}$ curves from C_1 and C_3 within bulk vapor-liquid coexist region are P_b^{bub} (see **Figure C-3 (b)**) and P_b^{dew} (see **Figure C-3 (d)**), respectively.

c) $P < P_b^{dew}$

In this case, the bulk region is in a single vapor-phase. When nanopores region is also in a single-phase (liquid or vapor), $\{N_i^{int}\}$ and the equilibrium V_b for given P are the same as in **Eqs. (4.1)** and **(4.2)**, respectively. The equilibrium $\{y_{i,b}\}$ is determined by the intercept between two $V_b - x_{C_3,b}$ curves from C_1 and C_3 as shown in **Figures C-4 (a)** and **C-4 (e)**.

When a specific nanopore is in a vapor-liquid coexistence phase, no intercept between $V_b - x_{C_3,b}$ curves (V_b obtained from **Eq. (4.2)**) exists as shown in **Figures C-4 (c)** and **C-4 (g)**, which is due to the discontinuity in $\rho_{i,p}$. We find that for a given P, the discontinuities in $\rho_{i,p}$ in different nanopores occur at different $x_{C_3,b}$. We use 10-nm pore as an example to illustrate. Within the 10-nm pore two-phase region, $\{N_i^{int}\}$ is given as

$$N_i^{int} = \rho_{i,b} V_b + \rho_{i,10\text{nm}(L)} V_{10\text{nm}(L)} + \rho_{i,10\text{nm}(V)} V_{10\text{nm}(V)} + \rho_{i,5\text{nm}} V_{5\text{nm}}, \quad i = C_1, C_3 \tag{4.7}$$

where $\rho_{i,10\text{nm}(L)}$ and $\rho_{i,10\text{nm}(V)}$ represent average molar densities of component i in the 10-nm pore liquid and vapor phases, respectively; $V_{10\text{nm}(L)}$ and $V_{10\text{nm}(V)}$ are volumes of the 10-nm pore liquid

and vapor phases, respectively. The equilibrium $\{y_{i,b}\}$ is determined as $x_{C_3,b}$, when there is discontinuity in $V_b - x_{C_3,b}$ curves. $V_{10\text{nm}(L)}$ and $V_{10\text{nm}(V)}$ have the relationship as following,

$$V_{10nm(L)} + V_{10nm(V)} = V_{10\text{nm}}. \tag{4.8}$$

By combining **Eqs. (4.7)** and **(4.8)**, $V_{p(L)}$, $V_{p(V)}$, and V_b are given as

$$V_{10\text{nm}(V)} = \frac{N_{C_1}^{int}\rho_{C_3,b} - N_{C_3}^{int}\rho_{C_1,b} - \rho_{C_1,10\text{nm}(L)}\rho_{C_3,b}V_{10\text{nm}} + \rho_{C_3,10nm(L)}\rho_{C_1,b}V_{10\text{nm}} - \rho_{C_1,5\text{nm}}\rho_{C_3,b}V_{5\text{nm}} + \rho_{C_3,5\text{nm}}\rho_{C_1,b}V_{5\text{nm}}}{\left(\rho_{C_1,10\text{nm}(V)} - \rho_{C_1,10\text{nm}(L)}\right)\rho_{C_3,b} - \left(\rho_{C_3,10nm(V)} - \rho_{C_3,10\text{nm}(L)}\right)\rho_{C_1,b}}$$

(4.9)

$$V_{10\text{nm}(L)} = V_{10nm} - V_{10\text{nm}(V)}, \tag{4.10}$$

$$V_b = \left(N_i^{int} - \rho_{i,10nm(L)}V_{10nm(L)} - \rho_{i,10\text{nm}(V)}V_{10\text{nm}(V)} - \rho_{i,5\text{nm}}V_{5\text{nm}}\right)/\rho_{i,b} \quad i = C_1, C_3. \tag{4.11}$$

The highest pressure when there is an intercept between the two $V_b - x_{C_3,b}$ curves from C_1 and C_3 within 10-nm pore phase transition region is the bubble point in 10-nm pores $P_{10\text{nm}}^{bub}$ as shown in **Figure C-4 (b)**, while the lowest pressure is the dew point $P_{10\text{nm}}^{dew}$ as shown in **Figure C-4 (d)**. When phase transitions occur in 5-nm nanopores, the fluids in 10-nm pores are in single vapor phase, and the bubble point and dew point in 5-nm nanopores, $P_{5\text{nm}}^{bub}$ and $P_{5\text{nm}}^{dew}$, can be obtained by applying the same method as shown in **Figures C-4 (f)** and **C-4 (h)**.

4.2.2.2 CVD

During a CVD process, after V_b increases as P decreases, the fluids in the expanded bulk volume are depleted from the nanopores-bulk multi-scale system and V_b recovers to V_b^{int} [94]. Note that 1 bar is used as the pressure gradient in our CVD calculation. The MB calculations under different pressure conditions are as same as those in CCE process. The only difference is the extra volume

depletion process followed by the bulk volume expansion for each pressure drop process. The corresponding volume depletion is illustrated below.

a) $P > P_b^{bub}$

In this case, for each pressure drawdown, the expanded bulk volume at equilibrium condition could be obtained by **Eq. (4.2)**, then the depleted volume V_b^d is given as,

$$V_b^d = V_b - V_b^{int} . \tag{4.12}$$

The produced fluids from the system N_i^d and remaining fluids in the system N_i^r are given as,

$$N_i^d = \rho_{i,b} V_b^d , \tag{4.13}$$

$$N_i^r = N_i^{int} - N_i^d . \tag{4.14}$$

For the next pressure condition, the N_i^r would be the new N_i^{int}.

b) $P_b^{bub} > P > P_b^{dew}$

When the bulk fluids split into vapor-liquid two phases, the expanded bulk volume can be obtained from **Eqs. (4.4)** – **(4.6)**. We assume that only the bulk vapor phase is depleted, considering that vapor phase viscosity is much lower than that of the liquid phase [108]. Then, the depleted vapor phase volume is given as

$$V_{b(V)}^d = V_b - V_b^{int} , \tag{4.15}$$

The produced fluids from the system N_i^d and remaining fluids in the system N_i^r are given as,

$$N_i^d = \rho_{i,b(V)} V_{b(V)}^d , \tag{4.16}$$

$$N_i^r = N_i^{int} - N_i^d , \tag{4.17}$$

where $\rho_{i,b(V)}$ represents densities of component i in the bulk vapor phase obtained from the PR-EOS. For the next pressure condition, the N_i^r would be the new N_i^{int}.

c) $P < P_b^{dew}$

In this case, hydrocarbons in the bulk region is in a single vapor-phase. After obtaining equilibrium expanded bulk volume according to **Eqs. (4.9)** – **(4.11)**, the depleted volume V_b^d, produced fluids from system N_i^d and remaining fluids in the system N_i^r can be calculated from **Eqs. (4.12)** – **(4.14)**.

4.3 Results and Discussions

Both CCE and CVD methods have been widely used to study hydrocarbon mixture phase behaviors [109]. In CCE process, the system pressure is lowered stepwise by incrementally expanding the volume of outside bulk. The phase behaviors and properties of fluids in nanopores vary as the connected bulk volume expansion. The CVD process mimic the real production process by depleting the fluids in the excess bulk volume at each pressure step. In this section, we first investigate phase behaviors and fluid properties in the nanopore-bulk multi-scale system for the CCE process, then we conduct the CVD process. Finally, the PSD effect on bubble point and dew point in nanopores-bulk multi-scale system is discussed.

4.3.1 CCE

In **Figure 4-2**, we present the schematic diagram for phase transitions in **Case B** during the CCE process at 288.15 K. At initial condition of $P^{int} = 45$ bar, C_1/C_3 mixture in the whole multi-scale system is in pure liquid phase as shown in **Figure 4-2 (a)**. After pressure decreases to be below bulk bubble point pressure P_b^{bub}, C_1/C_3 mixture in the bulk region split into vapor and liquid two

phases while those in nanopores remain as liquid phase as shown in **Figure 4-2 (c)**. It is because the competitive adsorption enhances the composition of heavier component in nanopores as we will discuss later. Note that the competitive adsorption in this work refers to the competition between the light and heavy components in nanopores. After fluids in bulk region completely vaporize, phase transitions happen in 10-nm pores firstly as shown in **Figure 4-2 (f)**. Only after fluids in the 10-nm pores completely vaporize, phase transition could occur in the 5-nm pores as shown in **Figure 4-2 (i)**. This is not only because of the stronger confinement effect in the smaller pores, but also the heavier component accumulation induced by interplay between nanopores and bulk. Overall, the phase transitions in the multi-scale system with PSD effect following the sequence of bulk, larger pores and small pores as pressure decreases. This phenomenon is in line with the experimental work by Wang *et al.* [47, 94] and the gauge-GCMC molecular simulation results [89].

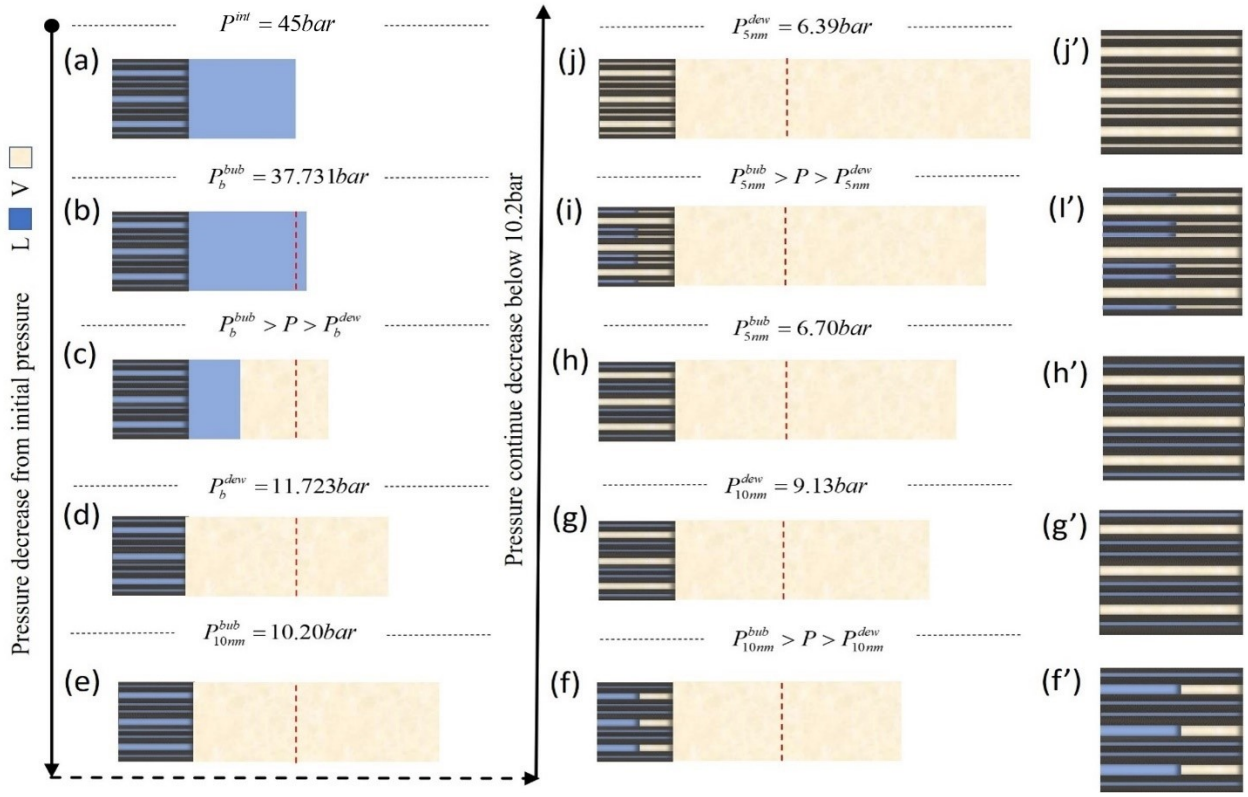

Figure 4-2. The schematic diagram for phase transitions in Case B during the CCE process at 288.15 K. (a) $P^{int} = 45$ bar; (b) $P_b^{bub} = 37.731$ bar; (c) $P_b^{dew} > P > P_{10\text{nm}}^{bub}$; (d) $P_b^{dew} = 11.723$ bar; (e) $P_{10\text{nm}}^{bub} = 10.20$ bar; (f) $P_{10\text{nm}}^{bub} > P > P_{10\text{nm}}^{dew}$; (g) $P_{10\text{nm}}^{dew} = 9.13$ bar; (h) $P_{5\text{nm}}^{bub} = 6.7$ bar; (i) $P_{5\text{nm}}^{bub} > P > P_{5\text{nm}}^{dew}$; (j) $P_{5\text{nm}}^{dew} = 6.39$ bar. (f'); (g'); (h'); (i') and (j') are enlarged parts for nanopores in (f); (g); (h); (i) and (j), respectively. The blue color represents C_1/C_3 mixture in liquid phase while the yellow color represents vapor phase in nanopores or bulk region. The red dashed line provides a reference for the volume of bulk at initial condition.

The equilibrium $y_{C_3,b}$ for different cases are presented in **Figure 4-3**. The equilibrium $y_{C_3,b}$ varies as P decreases, which is in line with the field observation [74]. At initial condition of $P^{int} = 45$ bar, the equilibrium $y_{C_3,b}$ in different cases are same. As P decreases, comparing to **Case B** and **C**, the molar fraction of C_3 in fluids released from the nanopores to the bulk region in **Case A** is smaller, resulting in a lower $y_{C_3,b}$ and a higher P_b^{bub}. At P below P_b^{bub}, fluids in bulk region split into vapor and liquid two phases. Fluid properties in bulk vapor-liquid two phases are the same, while the molar ratio of vapor and liquid phases in bulk varies among different cases. The nanoconfinement effect in **Case A** is stronger compared with **Case B** and **C**. The stronger competitive adsorption in nanopores induces a smaller increase in the bulk vapor phase molar fraction. Since the bulk vapor-phase contains less C_3 compared to the bulk liquid-phase, a higher $y_{C_3,b}$ and a lower P_b^{dew} is observed in **Case A**. The equilibrium $y_{C_3,b}$ increases until $P < P_b^{dew}$. When phase transition occurs in nanopores, $y_{C_3,b}$ decreases in different cases. When a given nanopore is in vapor-liquid two-phase in different cases, vapor and liquid phases coexist with equal chemical potentials as proposed by Evans *et al.* [110], the equilibrium $y_{C_3,b}$ is the same. For multi-

scale system with PSD effect, $y_{C_3,b}$ decreases continuously as P declines due to the continuous phase transitions from the larger pores to the smaller pores.

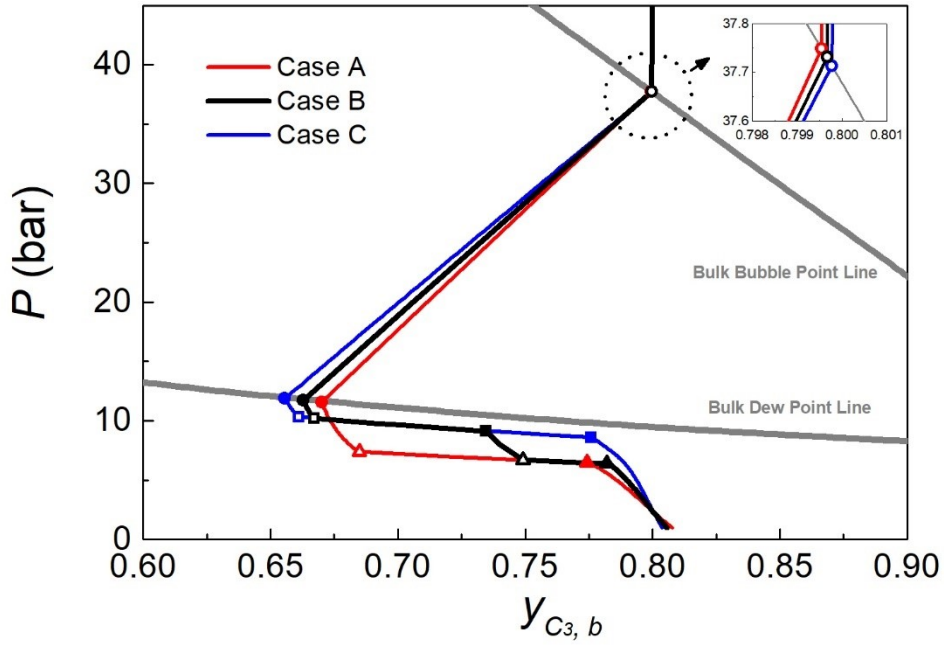

Figure 4-3. The equilibrium $y_{C_3,b}$ for Case A, B, and C during the CCE process. The open circles represent P_b^{bub}, the solid circles represent P_b^{dew}, the open squares represent $P_{10\text{nm}}^{bub}$, the solid squares represent $P_{10\text{nm}}^{dew}$, the open triangles represent $P_{5\text{nm}}^{bub}$, and the solid triangles represent $P_{5\text{nm}}^{dew}$.

In **Figure 4-4**, we present the equilibrium composition of C_3 in 10-nm pores, $y_{C_3,10\text{nm}}$, for **Case B** and **C**. When $P > P_b^{bub}$, the equilibrium $y_{C_3,10\text{nm}}$ increases more in **Case C** than **Case B** as P decreases. The molar fraction of C_3 in fluids released from the nanopores to the bulk region in **Case C** is larger, which increases C_3 concentration in the bulk region in **Case C**. Based on chemical potential equilibrium between nanopore and bulk, the equilibrium $y_{C_3,10\text{nm}}$ in **Case C** is higher than that in **Case B**. For $P_b^{bub} > P > P_b^{dew}$, $y_{C_3,10\text{nm}}$ are the same in **Case B** and **C** due to the same liquid phase properties in bulk. As P further decreases below P_b^{dew}, phase transition first occurs in the

10-nm pores, and the equilibrium $y_{C_3,10\text{nm}}$ decreases more in **Case B** than **Case C** as P decreases. As fluids in 10-nm pores split into liquid-vapor two phases, the properties of vapor and liquid two phases are the same in **Case B** and **Case C**. However, the volume fractions of those two phases are different due to different volume ratios of pores and bulk. Within the two-phase region of 10-nm pores, liquid phase density increases, while its volume decreases as P decreases [24]. The competition between density and volume causes the different trend of equilibrium $y_{C_3,10\text{nm}}$ in **Case B** and **C**. After the fluids in 10-nm pores completely vaporize, phase transitions can occur in 5-nm pores for **Case B**, and as fluids vaporize in 5-nm pores, $y_{C_3,10\text{nm}}$ increases in 10-nm pores. It is because the chemical potential of C_3 in bulk, which is equal to the liquid-phase chemical potential of C_3 in 5-nm pores, increases as P decreases within the 5-nm pores two-phase region. Such phenomena also affects the fluid properties in 10-nm pores as molar fraction of C_3 in them increases. On the other hand, the equilibrium compositions of C_3 in 5-nm pores, $y_{C_3,5\text{nm}}$, for **Case A** and **B**, are shown in **Figure 4-5**. For **Case B**, the equilibrium $y_{C_3,5\text{nm}}$ increases as P decreases when phase transition occurs in the 10-nm pores due to the interplay between nanopores and bulk, which suppresses the phase transitions (both $P_{5\text{nm}}^{bub}$ and $P_{5\text{nm}}^{dew}$) in 5-nm pores. In contrast to **Case A**, both $P_{5\text{nm}}^{bub}$ and $P_{5\text{nm}}^{dew}$ are lower in **Case B**.

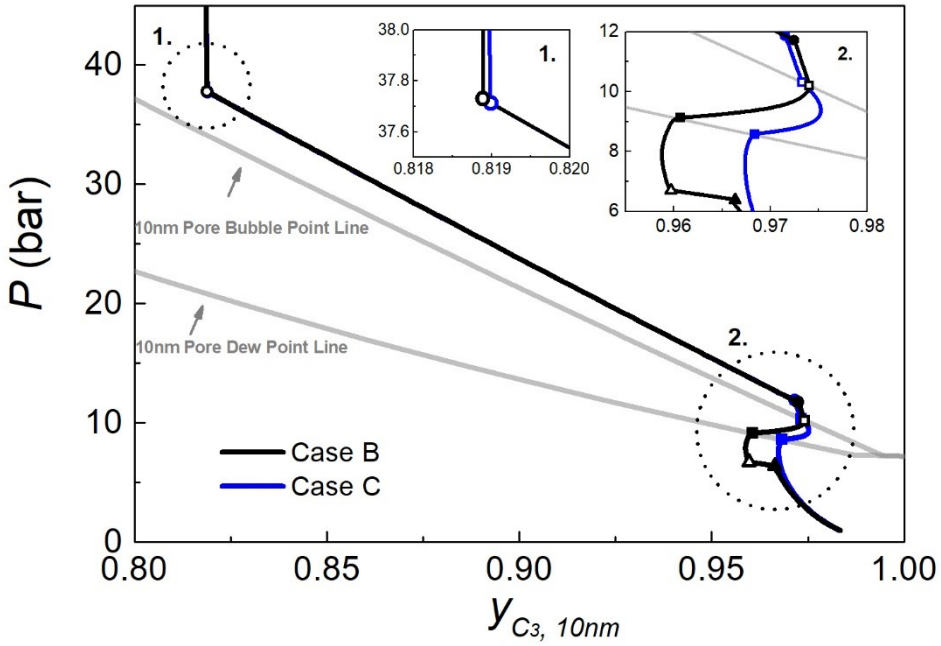

Figure 4-4. The equilibrium $y_{C_3,10\text{nm}}$ for Case B and C during the CCE process. The open circles represent P_b^{bub}, the solid circles represent P_b^{dew}, the open squares represent $P_{10\text{nm}}^{bub}$, the solid squares represent $P_{10\text{nm}}^{dew}$, the open triangles represent $P_{5\text{nm}}^{bub}$, and the solid triangles represent $P_{5\text{nm}}^{dew}$.

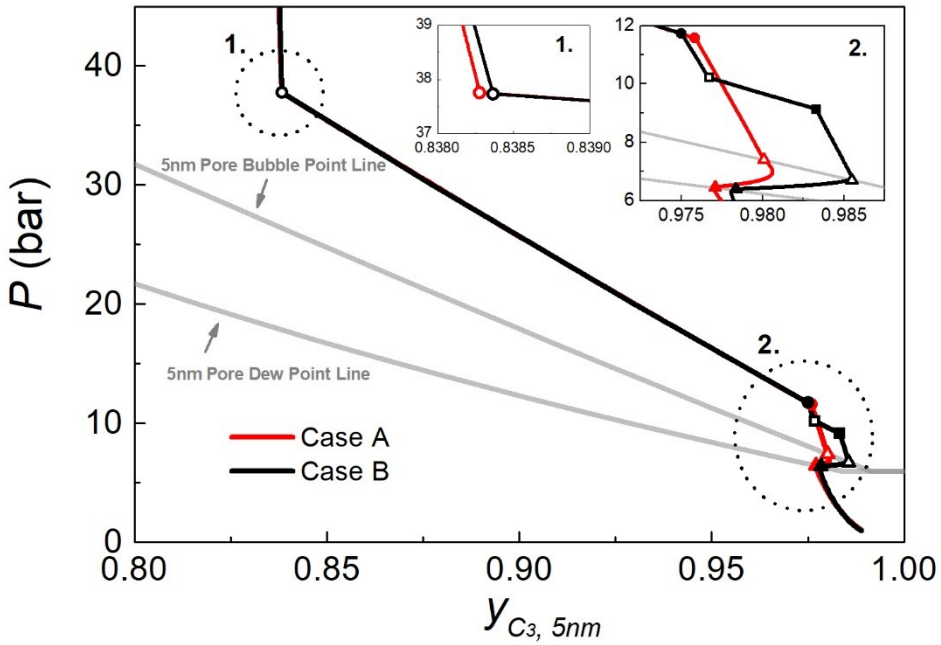

Figure 4-5. The equilibrium $y_{C_3,5\text{nm}}$ for Case A and B during the CCE process. The open circles represent P_b^{bub}, the solid circles represent P_b^{dew}, the open squares represent $P_{10\text{nm}}^{bub}$, the solid squares represent $P_{10\text{nm}}^{dew}$, the open triangles represent $P_{5\text{nm}}^{bub}$, and the solid triangles represent $P_{5\text{nm}}^{dew}$.

In **Figure 4-6**, we summarize the equilibrium C_3 composition in bulk, 10-nm and 5-nm pores when phase transitions occur in **Case B**. Within the bulk vapor-liquid two phases region, C_3 composition in bulk region decreases while those in 10-nm and 5-nm pores increase as P declines. It is because the competitive adsorption enhances the composition of the heavier component in nanopores as shown in **Figures 4-4** and **4-5**. When $P_{10\text{nm}}^{dew} \le P \le P_{10\text{nm}}^{bub}$, C_3 composition in 10-nm pores decreases, while those in bulk and 5-nm pore increases. When $P_{5\text{nm}}^{dew} \le P \le P_{5\text{nm}}^{bub}$, C_3 compositions in bulk and 10-nm pores increases, while that in 5-nm pores decreases. Thanks to the stronger confinement effect in the smaller pores as well as the heavier component accumulation induced by interplay between nanopores and bulk, phase transition in the smaller pores occurs at lower pressures in shale multi-scale system. Overall, in the multi-scale system with PSD effect, when phase transition occurs in one specific region (bulk, 10-nm or 5-nm pores), the heavier component composition in this region decreases, while those in other regions increase. This interplay effect is in line with nanofluidic experiments by Wang *et al.* [47] and Jatukaran *et al.* [67].

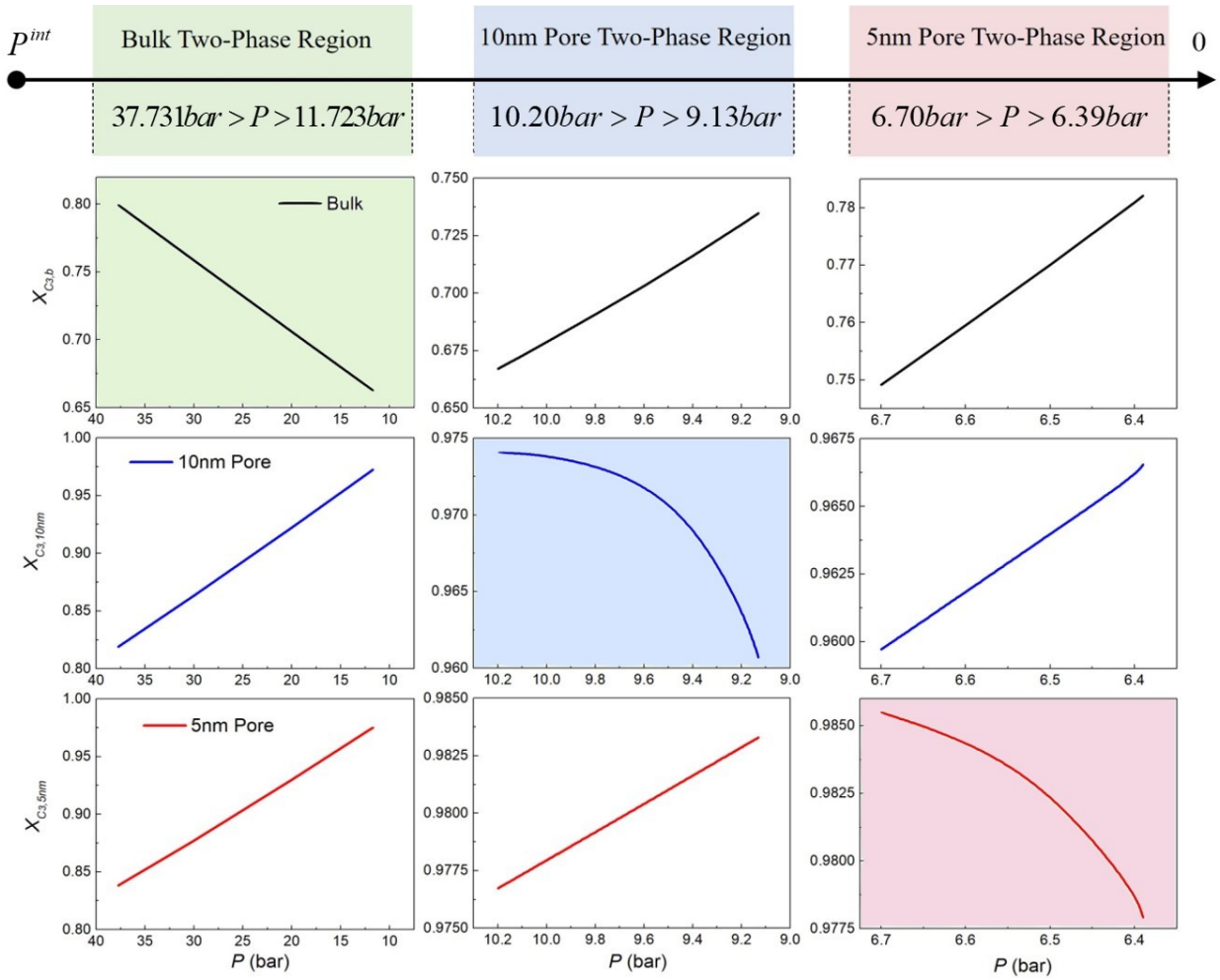

Figure 4-6. The equilibrium y_{C_3} in bulk, 10nm and 5nm pores when phase transitions happen in Case B.

In **Figure 4-7**, we present the ratio of molar percentage of C_3 in bulk to that in the total system for **Case A**, **B** and **C**. The effect from different PSD becomes significant when pressure is below P_b^{dew}, which is also the main pressure range when C_3 can be released from nanopores. The higher volume ratio of the smaller pores in the system suppresses C_3 release process to a lower pressure condition and results in the smaller percentage of C_3 in the bulk region. It is because not only the effect of fluid-surface interaction becomes stronger as pore size decreases, but also the heavier component accumulates in the smaller pores when phase transition occurs in the larger pores.

Overall, C_3 adsorbed into nanopores within bulk vapor-liquid coexist region due to competitive adsorption while it released from nanopore to outside bulk when bulk fluids in single phase, especially when phase transition happens in nanopores. Compared to C_3, C_1 can be continually released from nanopores to the bulk region for the entire pressure range as shown in **Figure C-5 (Appendix C)**.

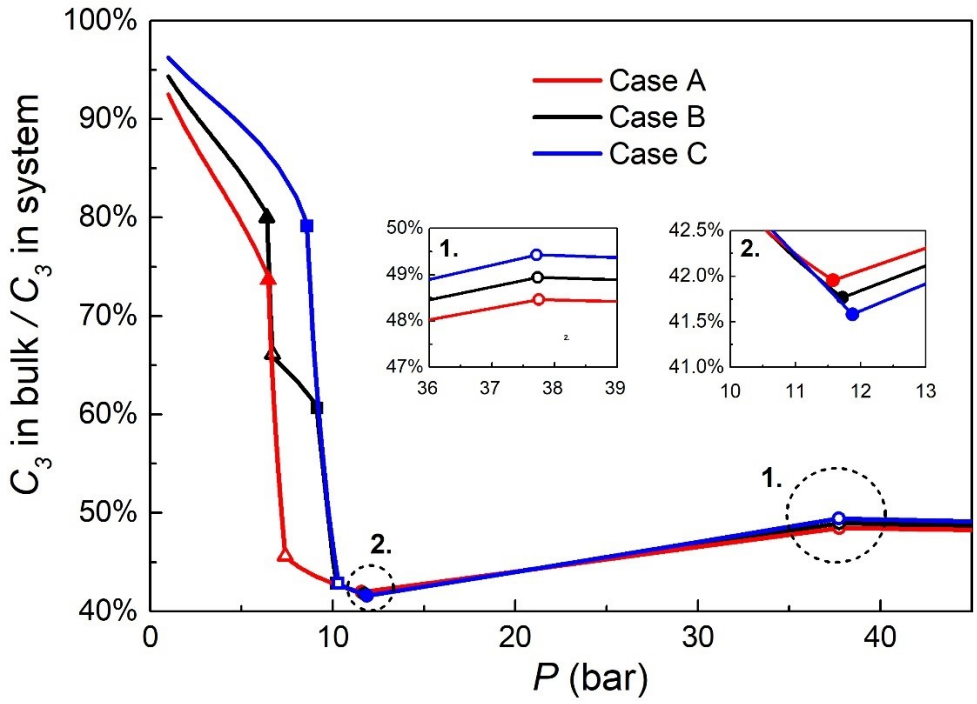

Figure 4-7. Ratio of molar percentage of C_3 in bulk to that in total system for Case A, B, and C during the CCE process. The open circles represent P_b^{bub}, the solid circles represent P_b^{dew}, the open squares represent $P_{10\text{nm}}^{bub}$, the solid squares represent $P_{10\text{nm}}^{dew}$, the open triangles represent $P_{5\text{nm}}^{bub}$, and the solid triangles represent $P_{5\text{nm}}^{dew}$.

4.3.2 CVD

Figure 4-8 presents the schematic diagram for phase transitions happened in **Case B** during the CVD process at 288.15 K. Similar to the CCE process, phase transitions occur in the multi-scale

system following the sequence of bulk, larger pores, smaller pores as P declines. Different from CCE, C_1-C_3 mixtures in excess volume is depleted to keep the volume of bulk recover back to V_b^i as P decreases. Due to competitive adsorption in nanopores, the depleted fluids in bulk region has a lower C_3 composition compared to the overall C_3 composition in the system. As a result, the remaining fluids in the total system become heavier as pressure drops. The heavier fluids in the system lead to instantaneous phase transitions in nanopores as shown in **Figure 4-8 (f) and 4-8 (h).**

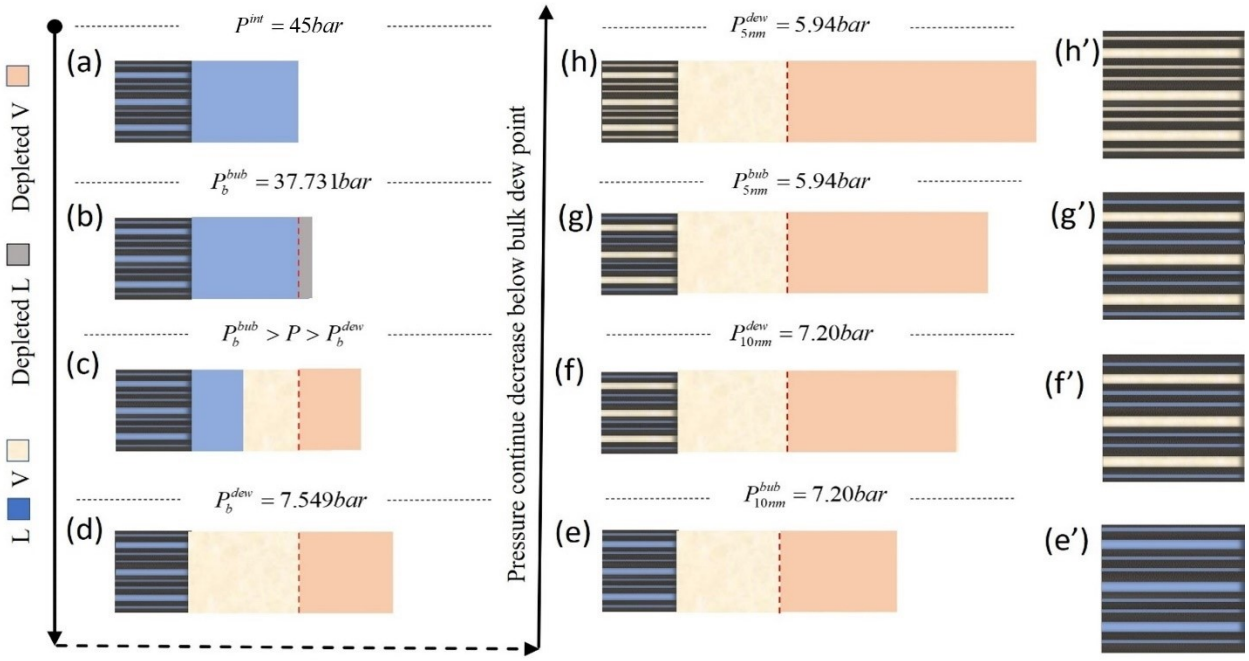

Figure 4-8. The schematic diagram for phase transitions in Case B during the CVD process at 288.15 K. (a) $P^{int} = 45$ bar; (b) $P_b^{bub} = 37.731$ bar; (c) $P_b^{dew} > P > P_{10\text{nm}}^{bub}$; (d) $P_b^{dew} = 7.549$ bar; (e) $P_{10\text{nm}}^{bub} = 7.20$ bar; (f) $P_{10\text{nm}}^{dew} = 7.20$ bar; (g) $P_{5\text{nm}}^{bub} = 5.94$ bar; (h) $P_{5\text{nm}}^{dew} = 5.94$ bar. (e'); (f'); (g'); (h') are enlarged parts for nanopores in (e); (f); (g); (h) respectively. The blue color represents C_1/C_3 mixture in liquid phase while the yellow color represents vapor phase remained in nanopores or

bulk region after depleting process. The gray color represents depleted C_1/C_3 mixture in liquid phase while the orange color represents depleted vapor phase in bulk region after excess volume depletion. The red dashed line provides a reference for the volume of bulk at initial condition.

In **Figure 4-9**, we present the equilibrium $y_{C_3,b}$ for different cases in CVD process. When $P > P_b^{bub}$, the expanded bulk volumes in the CVD process recover back to V_b^i by depleting excess volume of pure liquid fluids in the bulk region. The nanoconfinement effect on the bulk fluid properties is stronger in CVD process compared to CCE, which leads to a lower bulk C_3 composition and a slightly higher P_b^{bub}. However, the difference between P_b^{bub} from CCE and CVD processes is negligible due to the small liquid phase volume expansion in bulk. For $P_b^{bub} > P > P_b^{dew}$, the bulk region begins to vaporize and a bulk vapor-phase emerges. The vapor phase in the bulk liquid-vapor two phases is depleted from the system, which alters the composition of remaining bulk fluids. As pressure decreases, because C_3 is adsorbed into the nanopores, the equilibrium C_3 composition in the bulk region decreases. Then, the C_3 composition in bulk increases due to the excess bulk vapor-phase depletion. Overall, the effect of depletion is stronger than that of adsorption. Bulk C_3 composition keeps increasing during the CVD process, which decreases P_b^{dew} compared to the CCE process. Further decreasing P below P_b^{dew}, phase transition occurs instantaneously in nanopores following the sequence of pore size from large to small. The change of equilibrium composition of C_3 in 10-nm pores and 5-nm pores, $y_{C_3,10\text{nm}}$ and $y_{C_3,5\text{nm}}$, are similar to the CCE process.

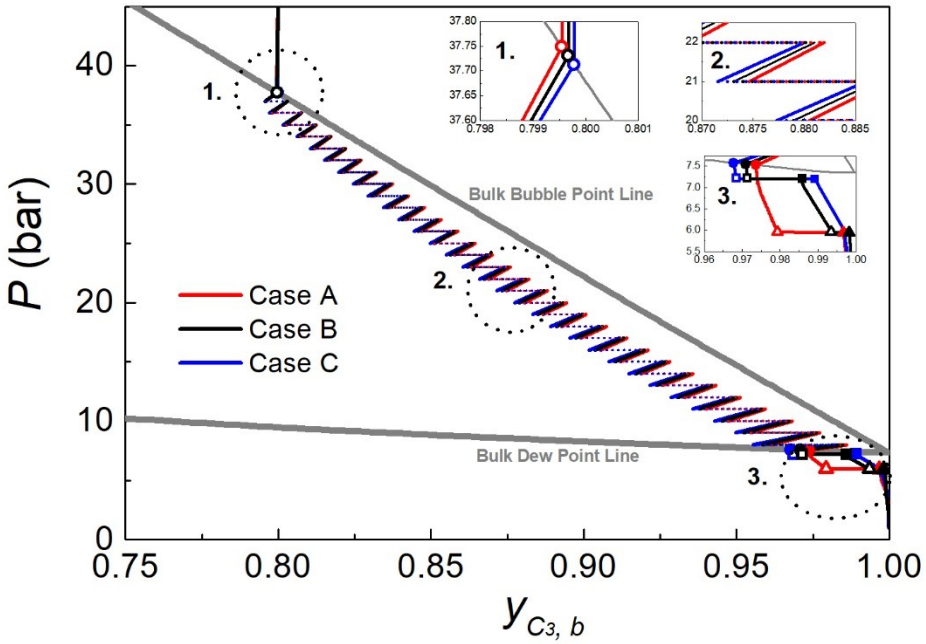

Figure 4-9. The equilibrium $y_{C_3,b}$ for Case A, B, and C during the CVD process. The open circles represent P_b^{bub}, the solid circles represent P_b^{dew}, the open squares represent $P_{10\text{nm}}^{bub}$, the solid squares represent $P_{10\text{nm}}^{dew}$, the open triangles represent $P_{5\text{nm}}^{bub}$, and the solid triangles represent $P_{5\text{nm}}^{dew}$. In subfigure 2, the solid lines represent one stage of pressure decrease, the dotted lines represent one stage of excess volume depletion process.

The ratio of molar percentage of produced C_3 to that in the initial system during the CVD process in different systems are shown in **Figure 4-10.** The release of the C_1/C_3 mixture shifts from the larger pores to the smaller pores. Recently, Li *et al.* [111] and Ma *et al.* [112] observed a similar phenomenon during CO_2 huff-n-puff and they claimed that the oil from the smaller pores is hard to be produced. Only around 30% of C_3 in the initial system could be produced until P decreases to P_b^{dew}. More than 60% of C_3 are produced when $P < P_b^{dew}$, which is the pressure range when the effect of PSD becomes significant. The higher volume ratio of the smaller pores in the system suppresses C_3 production process.

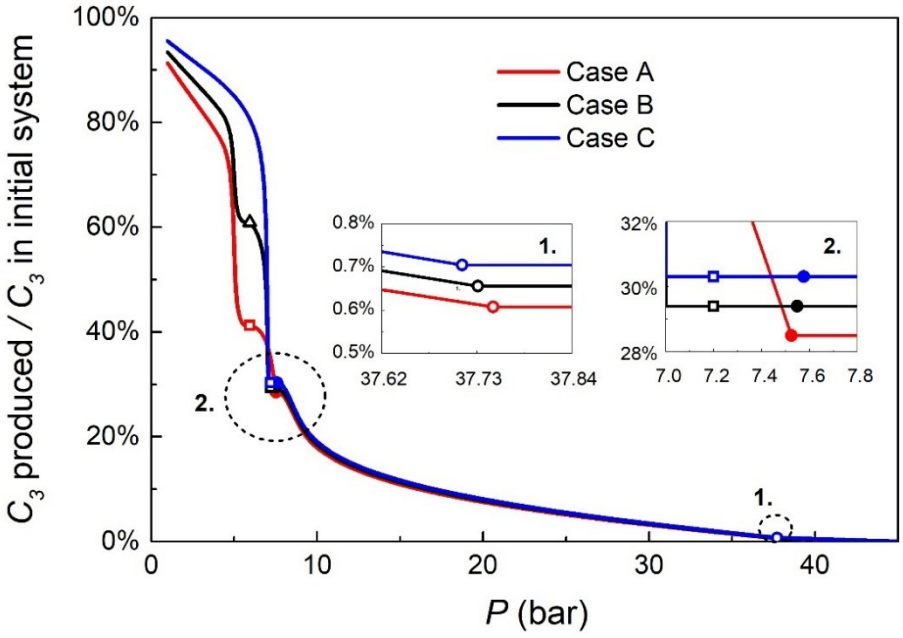

Figure 4-10. Ratio of molar percentage of produced C_3 to that in total system for Case A, B, and C during the CVD process. The open circles represent P_b^{bub}, the solid circles represent P_b^{dew}, the open squares represent $P_{10\text{nm}}^{bub}$, the solid squares represent $P_{10\text{nm}}^{dew}$, the open triangles represent $P_{5\text{nm}}^{bub}$, and the solid triangles represent $P_{5\text{nm}}^{dew}$.

4.3.3 Bubble Point and Dew Point Pressures

In **Figure 4-11**, we summarize P_b^{bub}, P_b^{dew}, P_p^{bub}, P_p^{dew} in different nanopore-bulk multi-scale systems during the CCE and CVD process. The higher volume ratio of the smaller pores in the system results in a higher P_b^{bub} and a lower P_b^{dew}. As a result, the bulk two-phase region expands from **Case C** to **Case A**. The bulk two-phase regions in CVD process are larger than those in CCE process due to the lower P_b^{dew}, which is caused by keep depleting lighter component in excess volume depleting process. For nanopores, the breadths of vapor-liquid two phases regions are relatively narrow and mainly influenced by the volume ratio of bulk and nanopores [24]. In CCE

process, the phase transition in 10-nm pores occurs at a higher pressure in the PSD model compared to the uniform pore size model. Under PSD effect, the phase transition in the smaller pores occurs at a lower condition compared to the uniform pore size case due to the heavier component accumulation. For CVD process, depleting lighter component from the total system further narrows the breadth of two-phase region in nanopores. In fact, the C_1-C_3 mixtures in nanopores become almost pure C_3, which leads to instantaneous phase transitions. Due to the PSD in shale media, phase transitions in the shale multi-scale system is a continuous process which cannot be described by a specific phase diagram by EOS based methods.

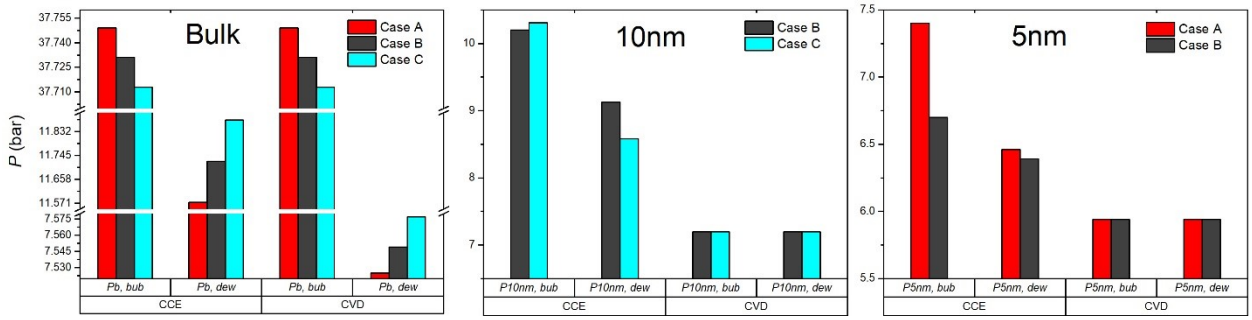

Figure 4-11. The bubble point and dew point in bulk, 10-nm pores, and 5-nm pores during CCE and CVD processes for Case A, B and C.

4.4 Conclusion

In this work, we simultaneously consider the effect of fluid-surface interaction, interplay between nanopores and macropores/fractures, PSD inherent in shale media to investigate phase behaviors of C_1/C_3 mixture during CCE and CVD processes.

For both CCE and CVD processes, under the PSD effect, fluid phase transitions occur in the sequence of bulk, the larger pores, and the smaller pores, as pressure declines. When phase transition occurs in one specific region (bulk, 10-nm or 5-nm pores), the heavier component composition in this region decreases, while those in other regions increase. The effects of PSD

become obvious when $P < P_b^{dew}$, which is also the main pressure range when C_3 can be released from the nanopores. In the CVD process, more than 60% of C_3 are produced when $P < P_b^{dew}$. Overall, the higher volume ratio of the smaller pores in the system suppresses the heavier component production process. This is not only because of the stronger confinement effect in the smaller pores, but also the heavier component accumulation induced by interplay between nanopores and bulk.

For bubble point and dew point in bulk, P_b^{bub} and P_b^{dew}, when the volume fraction of the smaller pores in the system is higher, P_b^{bub} is higher, while P_b^{dew} is lower, leading to an expanded bulk two-phase region. Compared with CCE process, the bulk two-phase regions in CVD process are larger due to a lower P_b^{dew}. For two-phase regions in nanopores, in CCE process, for a given nanopore, two-phase region expands as the volume ratio of pores to the initial bulk region increases [24]. In CVD process, phase transitions happen instantaneously in nanopores at a lower pressure condition compared to CCE process. It is because with lighter component depleted from the entire system, the heavier component composition in pores is higher and the C_1/C_3 mixture in nanopores becomes predominantly as pure C_3.

Our findings are also in line with the nanofluidic measurements for ternary hydrocarbon mixtures [67]. Model two-component systems (synthetic fluids) which are in the same homologous series as the multi-component systems (actual shale oil) have been widely used to study the underlying mechanisms of phase behaviors [76]. Thus, we believe that our work can provide important insights into hydrocarbon mixture phase behavior in shale formations. Based on thorough understandings about the phase behaviors in multi-scale shale matrix, this work evaluates the PSD effect on hydrocarbon thermodynamic properties and productions in shale matrix, which is

imperative for the accurate prediction of well productivity, ultimate oil recovery and future EOR consideration.

Acknowledgement

This research was enabled in part by support provided by Westgrid (www.westgrid.ca) and Compute Canada (www.computecanada.ca). The authors also greatly acknowledge a Discovery Grant from Natural Sciences and Engineering Research Council of Canada (NSERC RGPIN-2017-05080).

CHAPTER 5 REVISITING THE COMPARISON BETWEEN DENSITY FUNCTIONAL THEORY AND EQUATION-OF-STATE BASED MODELS ON PHASE BEHAVIOR OF HYDROCARBON MIXTURES UNDER NANOCONFINEMENT: CANONICAL ENSEMBLE

5.1 Introduction

Phase behaviors and properties of fluid mixtures under nano-confinement are crucial to a number of engineering applications, including gas separation [44], energy storage [113], catalytic reaction [114], water purification [115], climate engineering [116, 117], surface treatment [118, 119], drying process [120, 121], fuel cell [43] and nanomaterials [122-124]. Recently, shale/tight oil exploitation has become an important energy resource to meet the global energy demand [125], in which hydrocarbon mixtures are confined in nanoscale pores [3]. Laboratory measurements, including adsorption-desorption isotherms [126-128], differential scanning calorimetry [9], and nanofluidics [12, 60, 129] have shown that the phase behaviors of hydrocarbon mixtures confined in nanopores are different from those in bulk. However, it is challenging to provide a full description of fluid phase behaviors under nanoconfinement by experimental measurements [130, 131]. As a result, the understanding about fluid properties under nanoconfinement by theoretical methods becomes largely important [132].

One popular theoretical model to describe multi-phase fluid properties under nanoconfinement is by using Equation-of-State (EOS) based modeling in which the confinement effect is taken into account by capillary pressure (P_{cap}), while assuming homogeneous fluid distributions and unshifted critical points (CPs) [16-18]. This model generally predicts suppressed bubble point and lower dew point pressures as well as elevated upper dew point pressures compared to those in bulk. However, it has been shown that the critical properties of nanoconfined fluids are shifted [20-23]. By taking into account the shifted CPs with EOS based modeling, the pressure-temperature (P-T) diagram of nanoconfined hydrocarbon mixture shrinks [16, 18, 19]. Besides the P-T flash (given pressure and temperature conditions), the volume-temperature (V-T) flash has shown good applicability in dynamic optimization[133], compositional reservoir simulations[134-

136] and fluids phase behaviors calculation[137-139]. Recently, V-T flash has been developed to study phase behaviors of nanoconfined fluids in the canonical ensemble [140, 141]. By taking P_{cap} into account, V-T flash presents decreased bubble point and lower dew point densities, while increased upper dew point densities of nanoconfined hydrocarbon mixtures [140]. It should be noted that these works use P_{cap} to consider the confinement effect, while the shifted CPs are not fully taken into consideration. Although EOS based models are easy to implement with a minimal computational cost, they do not explicitly consider fluid-surface interactions and inhomogeneous density distributions under nanoconfinement [5]. As a result, the applicability of EOS based models for the phase behaviors of nanoconfined fluids has been under debates [9, 24]. A few theoretical models other than EOS based models have been developed. Rangarajan *et al*. [142] developed simplified local density model (SLD) by superimposing the fluid-solid interaction on the wan der Waals equation of state with a local density approximation. While SLD model can capture the adsorption behavior, it may predict an unphysical phase transition as it leads to an abrupt vapor-liquid interface. Shapiro *et al*. [143] developed multicomponent potential theory of adsorption (MPTA) based on the potential concept originally suggested by Polanyi [144, 145]. By applying the same equations of state for the adsorbate under confinement as in the bulk phase, a direct thermodynamic connection between the adsorbate and bulk fluid is established. Both pressure compressibility and compositional segregation of adsorbed mixture are taken into consideration. The predicted binary mixture composition in activated carbon has a good agreement with experimental data. Besides, this model can accurately predict molar densities of adsorbate close to dew points. Travalloni *et al*. [146, 147] extended the van der Walls equation to describe confined fluid phase behaviors. Their model provides a consistent description of adsorption system in a wide range of pore sizes, while it can describe adsorption isotherm with vapor-liquid phase

transitions. Sandoval *et al*. [148] developed a new flash algorithm by taking into account the capillarity and surface adsorption to predict phase behavior of nano-confined fluid mixtures. They found that the phase envelope of hydrocarbon mixtures shrinks significantly due to surface adsorption and capillarity and the critical temperature decreases.

Compared with EOS based models, statistical thermodynamic methods can explicitly consider fluid-surface interactions and inhomogeneous density distributions in nanopores. Jin and Firoozabadi [5] compared the phase diagrams of pure nC_4 in 2-nm pores from EOS plus shifted CPs with engineering density functional theory (DFT). They found that EOS plus shifted CPs underestimates the saturation densities of nC_4 in both liquid and vapor phases under nanoconfinement. Wang *et al*. [149] compared the saturation pressures of C_3 under nanoconfinement from the Peng-Robinson EOS (PR-EOS) plus P_{cap} and engineering DFT. They concluded that the EOS based model shows a large deviation from the engineering DFT for pores smaller than 8 nm. They also found that adding an adsorption layer thickness into the EOS based model could improve its performance in pores as small as 5 nm. For hydrocarbon mixtures, by using PR-EOS plus P_{cap} and engineering DFT, Liu *et al.* [150] observed that, the lower dew point pressures of confined C_1-nC_6 mixtures from engineering DFT approach bulk, when pore size is 20 nm. However, for this pore size, the upper dew point shows a large deviation from that in bulk. Zhong *et al.* [12] reported that the bubble point pressures of C_1-C_3 mixtures in 8-nm pores predicted from engineering DFT is drastically reduced to be lower than the bulk dew point pressure of injected fluids in an excellent agreement with nanofluidic measurements. On the other hand, the PR-EOS plus P_{cap} model predicts only slightly reduced bubble point pressures compared to those in bulk. Although these works provided important insights into the phase behaviors of nanoconfined hydrocarbon mixtures from DFT and EOS based models, these comparisons are not

conducted in the same ensemble. In the engineering DFT, fluid properties in nanopores are calculated in the grand canonical ensemble, in which the given pressure and fluid composition (ultimately chemical potentials) refer to those in bulk, while the fluid composition within nanopores is largely different from that in bulk due to fluid-surface interactions. On the other hand, EOS based models are conducted under the P-T flash, while the specified fluid composition represents the overall mixture composition within nanopores. In general, in these models, the given pressure presents the vapor phase pressure, while P_{cap} and/or shifted CPs are used to represent the confinement effect. As a result, the drastically different definitions of fluid composition and pressure lead to an indirect comparison between the engineering DFT and EOS based models. In contrast, in the canonical ensemble with specified fluid composition, volume, and temperature under nanoconfinement, it would be straightforward to calibrate the EOS based models by comparing to the statistical thermodynamic methods.

Pitakbunkate *et al.* [55] used the grand-canonical Monte Carlo (GCMC) simulations to study P-T diagrams of C_1-C_2 mixtures with a fixed composition within 5-nm slit graphite pores, in which the pressure corresponds to that in bulk. While this work provides important information for hydrocarbon mixture phase behaviors in the canonical ensemble, the fluid densities within nanopores are not revealed. Pathak *et al.* [10] presented temperature-density (T-c) diagrams of decane/methane (90:10 molar ratio) mixtures in 3.5-nm graphite slit pores by the Gibbs Ensemble Monte Carlo (GEMC) simulations. They found that the bubble point densities decrease, while the dew point densities increase compared to the bulk values. Then, they extrapolated the liquid and vapor phase equilibrium branches to obtain the critical point. Both critical density and critical temperature of confined mixtures are suppressed. However, Liu and Zhang [130] argued that the fitted critical density values in their work may be unreliable as these results are obtained without

a theoretical foundation. To the best of our knowledge, an explicit comparison between EOS based models and statistical thermodynamic method on the phase behaviors of hydrocarbon mixtures in the canonical ensemble has not been reported yet.

This work aims to assess the validity of various EOS based models, including the PR-EOS plus P_{cap}, the PR-EOS plus shifted CPs, and the PR-EOS plus shifted CPs and P_{cap}, on the phase behaviors of hydrocarbon mixtures under nanoconfinement by comparing to the engineering DFT in the canonical ensemble. These EOS based models have been widely implemented into the reservoir simulators thanks to their minimal computation cost [151]. Therefore, the calibration of these models would help improve the accuracy of reservoir simulation predictions. The whole T-c phase diagrams and critical properties in various nanopores are discussed. We find that EOS based models render a relatively poor performance in terms of dew point branches, vapor phase properties and critical densities of nano-confined mixtures even with the consideration of P_{cap} and the shifted CPs. This work provides foundations and guidance to improve the performance of the EOS based models in the canonical ensemble.

5.2 Methods

The engineering DFT [152] extends the PR-EOS [106] into the heterogeneous conditions by using the weighted-density approximation (WDA) [153] and quadratic-density expansion (QDE) [154], which can explicitly take into account fluid-surface interactions and inhomogeneous density distributions. At equilibrium, the grand potential is minimum for an open system in which the fluids in the system (nanopores in this work) are in chemical equilibrium with bulk [107]. This approach has shown an excellent agreement with experimental data and molecular simulations for bubble/dew points of confined hydrocarbon fluids [12, 155], adsorption in nano-porous media [5] and interfacial tensions [156]. In contrast to the engineering DFT, EOS based models take into

account the confinement effect in an implicit manner by using P_{cap} and/or shifted CPs, ignoring the fluid-surface interactions and inhomogeneous density distributions. The detailed descriptions for the engineering DFT and EOS based models are illustrated below, while their key differences are highlighted in **Table 5-1**. We note that in this work, we use the PR-EOS to represent the EOS based models as it is one of the most accurate and widely used EOS models for petroleum fluids [106]. The canonical ensemble describes a system with fixed number of moles, volume and temperature [157]. For the phase behaviors in the canonical ensemble, it is convenient to use molar densities, phase volume fractions and mole fractions to express the equilibrium conditions [139]. As a result, the overall mole density, overall molar volume and temperature are used as thermodynamic variables in this work. C_1-C_3 mixtures are used to represent hydrocarbon mixtures, which can explain the general phase behaviors of hydrocarbon mixtures since the phase behavior of a binary system is very similar to that of multi-component fluids [76]. In this work, we study C_1-C_3 mixture phase behaviors in structureless carbon slit pores with a liquid-wetting feature with an overall composition as $x_{C_1,p}^{eq} : x_{C_3,p}^{eq} = 0.2 : 0.8$.

5.2.1 Engineering DFT

Within the framework of engineering DFT, the chemical potentials μ_i of component i in nanopores and bulk are the same at equilibrium. The equilibrium properties in nanopores can be obtained by the minimization of grand potential functional $\Omega\left[\left\{\rho_i(\mathbf{r})\right\}\right]$, which is the functional of density distributions $\left\{\rho_i(\mathbf{r})\right\}$ and related to the Helmholtz free energy functional $F\left[\left\{\rho_i(\mathbf{r})\right\}\right]$ [158],

$$\Omega\left[\left\{\rho_i(\mathbf{r})\right\}\right] = F\left[\left\{\rho_i(\mathbf{r})\right\}\right] + \sum_i \int \rho_i(\mathbf{r})\left[\Psi_i(\mathbf{r}) - \mu_i\right] d\mathbf{r}, \tag{5.1}$$

where $d\mathbf{r}$ is differential volume, and $\rho_i(\mathbf{r})$ is the density distribution of component i at position $\mathbf{r}$; $\Psi_i(\mathbf{r})$ is the external potential of the component i at position $\mathbf{r}$; μ_i is chemical potential of component i in pores which is equal to that in bulk obtained from the PR-EOS (parameters of PR-EOS are shown in **Table 5-2**). Note that the binary interaction coefficient between C_1 and C_3 is fixed as 0.006, which is obtained by fitting with experimental data [12]. The attraction energy parameter ε_g in the QDE [156] for C_1 and C_3 are used as ε_g / k_B=1178 K for C_1 and 1866 K for C_3, respectively. The detailed calculation process for the Helmholtz free energy $F\left[\{\rho_i(\mathbf{r})\}\right]$ and the external potential Ψ_i in a slit pore is shown in **Appendix A**.

At equilibrium, the grand potential functional is minimum,

$$\frac{\delta\Omega\left[\{\rho_i(\mathbf{r})\}\right]}{\delta\rho_i(\mathbf{r})}=0. \tag{5.2}$$

In **Eq. (5.2)**, the symbol δ represents the functional derivative.

In a carbon slit pore, the density distributions only vary in the direction perpendicular to the solid surfaces. Symbol z presents position along the direction perpendicular to the solid surfaces and $\rho_i(z)$ presents density of component i at position z. The density distribution in nanopore $\rho_i(z)$, could be solved numerically using the Picard-type iterative method at given bulk status. The average density of component i in nanopore $\rho_{i,p}$ is given as,

$$\rho_{i,p}=\frac{\int_0^W \rho_i(z)dz}{W_{eff}}, \tag{5.3}$$

where W represents pore size, W_{eff} is the effective pore size which is calculated as the pore size minus the diameter of wall molecule, i.e., $W_{eff}=W-\sigma_w$.

As the engineering DFT is constructed in the grand canonical ensemble, to study the confined C_1-C_3 mixture phase behaviors in the canonical ensemble, we apply special procedures (taking 5-nm pores and 288.15 K as an example) as following: 1) We assume that the confined fluids are in a chemical equilibrium with a pseudo-outside bulk reservoir (POBR), while the equilibrium C_1-C_3 composition in nanopores $\left\{x_{i,p}^{eq}\right\}$ can be different from that in bulk $\left\{y_{i,b}^{eq}\right\}$; 2) For a given temperature condition, both pressure-bulk C_3 composition ($P-y_{C_3,b}$) and pressure-pore C_3 composition ($P-x_{C_3,p}$) diagrams [24] could be obtained as shown in **Figure D-1** (**Appendix D**). The equilibrium conditions can be illustrated in five different ranges in terms of the pressure P in POBR: a) P higher than the pore upper critical point ($P \geq P_{c,p}^{upper}$); b) P higher than the pore bubble point but lower than pore upper critical point ($P_{c,p}^{upper} > P > P_p^{bub}$); c) P higher than the pore dew point but lower than the pore bubble point ($P_p^{bub} \geq P \geq P_p^{dew}$); d) P lower than the pore dew point but higher than the pore lower critical point ($P_p^{dew} > P > P_{c,p}^{lower}$); e) P lower than the pore lower critical point ($P \leq P_{c,p}^{lower}$). These pressure ranges correspond to single-phase liquid region for a) and b), two-phase liquid-vapor coexistence region for c), and single-phase vapor region for d) and e) of nanoconfined C_1-C_3 mixtures which can satisfy $x_{C_1,p}^{eq} : x_{C_3,p}^{eq} = 0.2 : 0.8$. 3) For given pressure P in POBR and temperature T, we adjust $\left\{y_{i,b}\right\}$ to obtain the equilibrium bulk composition $\left\{y_{i,b}^{eq}\right\}$ which can satisfy $x_{C_1,p}^{eq} : x_{C_3,p}^{eq} = 0.2 : 0.8$. Various types of $x_{C_3,p} - y_{C_3,b}$ diagrams at different POBR pressure conditions are shown in **Figure D-3** (**Appendix D**).

a) $P \geq P_{c,p}^{upper}$

In this case, for a given P, nanoconfined C_1-C_3 mixtures are in a single-phase liquid region as shown in **Figure D-1** (**Appendix D**). When P is higher than the bulk upper critical pressure ($P \geq P_{c,b}^{upper}$), bulk fluids are also in a single-phase liquid region. By varying the trial $y_{C_3,b}$ from 0 to 1, the average density of component i in nanopores, $\rho_{i,p}$, is readily available (as shown in **Figure D-2 (a-1)(a-2)** (**Appendix D**), and there is no phase transition in nanopores. On the other hand, when $P_{c,b}^{upper} > P \geq P_{c,p}^{upper}$, by varying $y_{C_3,b}$ from 0 to 1, bulk fluids may split into vapor and liquid phases depending on $y_{C_3,b}$ (as shown in **Figure D-1** (**Appendix D**)), while the bulk bubble and dew point compositions, y_b^{bub} and y_b^{dew}, respectively, for given T and P can be obtained from the PR-EOS. Within the bulk two-phase region, the liquid phase chemical potentials are used to calculate $\rho_{i,p}$ [24]. According to the Gibbs phase rule [24], the bulk liquid/vapor phase fluid properties are fixed within the two-phases region, which leads to unchanged $\rho_{i,p}$ as shown in **Figure D-2 (a-3)(a-4)** (**Appendix D**). Based on $\rho_{i,p}$, the overall average density of the C_1-C_3 binary mixtures in nanopores $\rho_{t,p}$ is given as

$$\rho_{t,p} = \sum_i \rho_{i,p}, \quad i = C_1, C_3 . \tag{5.4}$$

The corresponding C_3 composition in nanopore, $x_{C_3,p}$ is given as,

$$x_{C_3,p} = \frac{\rho_{C_3,p}}{\rho_{t,p}} \tag{5.5}$$

For given T and P, in the range of trial $y_{C_3,b}$ from 0 to 1, the equilibrium $y_{C_3,b}^{eq}$ which can satisfy $x_{C_1,p}^{eq} : x_{C_3,p}^{eq} = 0.2 : 0.8$ could be identified as shown in **Figure D-3 (a-1)(a-2)(a-3)(a-4)** (**Appendix**

D). The equilibrium densities of component i in nanopore, $\rho_{i,p}^{eq}$, are used to calculate overall nanoconfined molar density of C_1-C_3 mixtures in canonical ensemble as,

$$c_{p,overall} = \sum_i \rho_{i,p}^{eq}, \quad i = C_1, C_3 \tag{5.6}$$

b) $P_{c,p}^{upper} > P > P_p^{bub}$

In this case, by varying the trial $y_{C_3,b}$ from 0 to 1, a sudden change in $\rho_{i,p}$ indicates that phase transition takes place in nanopores, when bulk fluids is in single vapor phase, as shown in **Figure D-2 (b)** (**Appendix D**), which is in line with the experimental finding [12]. In this work, the equilibrium transition route corresponding to the minimum grand potential (GP) value is used to represent the equilibrium hydrocarbon mixture behaviors in hysteresis region [59]. By generating the $x_{C_3,p} - y_{C_3,b}$ diagram, the equilibrium C_3 composition in nanopore, $x_{C_3,p}$, is identified in pure liquid phase region of nanoconfined fluids as shown in **Figure D-3 (b)** (**Appendix D**). The equilibrium C_3 composition in outside bulk, $y_{C_3,b}^{eq}$, shifts from bulk liquid phase to bulk vapor phase as pressure drops, as shown in **Figure D-1** (**Appendix D**). Again, according to the Gibbs phase rule [24], the bulk liquid phase properties within bulk two-phase region are same. As a result, within the bulk two-phase region, $y_{C_3,b}^{eq}$ is a horizontal line. The overall average density of the C_1-C_3 binary mixtures ($\rho_{t,p}$), the corresponding C_3 composition ($x_{C_3,p}$) and the overall average molar densities ($c_{p,overall}$) of nanoconfined C_1-C_3 mixtures ($x_{C_1,p}^{eq} : x_{C_3,p}^{eq} = 0.2 : 0.8$) can be obtained from **Eqs. (5.4)** – **(5.6)**, respectively.

c) $P_p^{bub} \geq P \geq P_p^{dew}$

In the two-phase liquid-vapor coexistence region of nanoconfined C_1-C_3 mixture ($x^{eq}_{C_1,p} : x^{eq}_{C_3,p} = 0.2 : 0.8$), the equilibrium C_3 composition in pore, $x^{eq}_{C_3,p}$, is within the phase transition region of nanoconfined fluids (as shown in **Figure D-3 (c-2)** (**Appendix D**)). The phase transition region could be identified by a sudden increase in $\rho_{C_3,p}$ when varying trial $y_{C_3,b}$ from 0 to 1 as shown in **Figure D-2 (c-2)** (**Appendix D**). The $\rho_{i,p}$ after the sudden jump corresponds to the liquid phase density of component i at bubble point in nanopore for given T , P and W , $\rho^{bub}_{i,p}$; while the $\rho_{i,p}$ before the sudden jump corresponds to the vapor phase density of component i at dew point in nanopore for given T , P and W , $\rho^{dew}_{i,p}$. The overall average density of the C_1-C_3 mixtures and C_3 composition at bubble point and dew point for given T , P and W are given as,

$$\rho^{bub}_{t,p} = \sum_i \rho^{bub}_{i,p} \quad i = C_1, C_3, \tag{5.7}$$

$$\rho^{dew}_{t,p} = \sum_i \rho^{dew}_{i,p} \quad i = C_1, C_3, \tag{5.8}$$

$$x^{bub}_{C_3,p} = \frac{\rho^{bub}_{C_3,p}}{\rho^{bub}_{t,p}}, \tag{5.9}$$

$$x^{dew}_{C_3,p} = \frac{\rho^{dew}_{C_3,p}}{\rho^{dew}_{t,p}}. \tag{5.10}$$

Bubble point pressure in nanopore, P^{bub}_p , is defined as the P in POBR which satisfy $x^{eq}_{C_3,p} = x^{bub}_{C_3,p} = 0.8$ as shown in **Figure D-3 (c-1)** (**Appendix D**). The dew point pressure P^{dew}_p could satisfy $x^{eq}_{C_3,p} = x^{dew}_{C_3,p} = 0.8$ as shown in Figure S3(c-3). For $P^{bub}_p > P > P^{dew}_p$, fluids in nanopore split

into liquid and vapor two phases when $x_{C_3,p}^{eq} = 0.8$. The liquid and vapor phases overall equilibrium densities and C_3 compositions are obtained as

$$c_{p,l} = \rho_{t,p}^{bub}, \tag{5.11}$$

$$c_{p,v} = \rho_{t,p}^{dew}, \tag{5.12}$$

$$x_{C_3,p,l} = \frac{\rho_{C_3,p}^{bub}}{\rho_{t,p}^{bub}}, \tag{5.13}$$

$$x_{C_3,p,v} = \frac{\rho_{C_3,p}^{dew}}{\rho_{t,p}^{dew}}, \tag{5.14}$$

where $c_{p,l}$ and $c_{p,v}$ present overall equilibrium densities of nanoconfined fluids in liquid- and vapor phase, respectively; $\rho_{C_3,p}^{bub}$ and $\rho_{C_3,p}^{dew}$ present C_3 average densities in pores at bubble point and dew point for given T, P and W; $\rho_{t,p}^{bub}$ and $\rho_{t,p}^{dew}$ present the overall average densities of the C_1-C_3 binary mixtures in pores at bubble point and dew point for given T, P and W, respectively; $x_{C_3,p,l}$ and $x_{C_3,p,v}$ present equilibrium C_3 compositions of nanoconfined fluids in the liquid- and vapor phase, respectively.

The liquid phase saturation (liquid phase volume fraction) is calculated as

$$S_{p,l} = (0.8 - x_{C_3,p,v}) / \left(x_{C_3,p,l} - x_{C_3,p,v}\right), \tag{5.15}$$

where $S_{p,l}$ is the liquid phase saturation of nanoconfined C_1-C_3 mixture ($x_{C_1,p}^{eq} : x_{C_3,p}^{eq} = 0.2 : 0.8$), $x_{C_3,p,l}$ and $x_{C_3,p,v}$ present C_3 compositions in the liquid- and vapor-phase as calculated in **Eqs. (5.13)** and **(5.14)**, respectively.

The overall average molar densities of nanoconfined C_1-C_3 mixtures ($x_{C_1,p}^{eq} : x_{C_3,p}^{eq} = 0.2 : 0.8$) $c_{p,overall}$ are calculated as

$$c_{p,overall} = c_{p,l} \times S_{p,l} + c_{p,v} \cdot (1 - S_{p,l}), \tag{5.16}$$

where $c_{p,l}$ and $c_{p,v}$ are the liquid- and vapor phase overall equilibrium densities calculated as **Eqs. (5.11)** and **(5.12)**, and $S_{p,l}$ is the liquid phase saturation calculated by **Eq. (5.15)**.

d) $P_p^{dew} > P > P_{c,p}^{lower}$

When P is still higher than both the bulk and pore lower critical point, both bulk and nanopore two-phase regions can be observed by varying trial $y_{C_3,b}$ from 0 to 1 (as shown in **Figure D-2 (d)** (**Appendix D**)). However, the equilibrium C_3 composition in nanopore, $x_{C_3,p}^{eq}$, is identified in pure vapor phase region of nanoconfined fluids as shown in **Figure D-3 (d)** (**Appendix D**). By varying trial $y_{C_3,b}$ from 0 to 1, the overall average densities of the C_1-C_3 binary mixtures ($\rho_{t,p}$) and the corresponding C_3 composition ($x_{C_3,p}$) can be obtained from **Eqs. (5.4)** and **(5.5)**, respectively. The overall average molar densities ($c_{p,overall}$) of nanoconfined C_1-C_3 mixtures ($x_{C_1,p}^{eq} : x_{C_3,p}^{eq} = 0.2 : 0.8$) is calculated as shown in **Eq. (5.6)**.

e) $P \le P_{c,p}^{lower}$

As the pressure further below the pore lower critical point, for a given P, nanoconfined C_1-C_3 mixtures are in a single-phase vapor region as shown in **Figure D-1** (**Appendix D**). Since P is also lower than the bulk lower critical pressure, bulk fluids are also in a single-phase vapor region. By varying the trial $y_{C_3,b}$ from 0 to 1, there is no phase transition in both the nanopore and bulk as shown in **Figure D-2 (e)** (**Appendix D**). The overall average density of the C_1-C_3 binary

mixtures ($\rho_{t,p}$), the corresponding C_3 composition ($x_{C_3,p}$) and the overall average molar densities ($c_{p,overall}$) of nanoconfined C_1-C_3 mixtures ($x^{eq}_{C_1,p} : x^{eq}_{C_3,p} = 0.2 : 0.8$) can be obtained from **Eqs. (5.4) – (5.6)**, respectively.

In this regard, the overall molar density ($c_{p,overall}$), overall molar volume (v) and temperature (T) are fixed in nanopore and corresponding fluids properties are studied in canonical ensemble.

5.2.2 EOS plus Pcap in the Canonical Ensemble

Considering P_{cap} and assuming that the liquid phase completely wets the pore surfaces, the phase equilibrium in the EOS plus P_{cap} model is obtained by satisfying [141]:

$$P^V\left(V^V, T, n^V_{C_1}, n^V_{C_3}\right) - P^L\left(V^L, T, n^L_{C_1}, n^L_{C_3}\right) = P_{cap} \tag{5.17}$$

and

$$\mu_i^V\left(V^V, T, n^V_{C_1}, n^V_{C_3}\right) = \mu_i^L\left(V^L, T, n^L_{C_1}, n^L_{C_3}\right) \quad i = C_1, C_3 \tag{5.18}$$

in which, T is the system temperature; V^V and V^L represent the vapor and liquid phase volumes, respectively; P^V and P^L depict the vapor and liquid phase pressures, respectively; μ_i^V and μ_i^L represent the chemical potentials of C_1 and C_3 in the vapor phase and liquid phase, respectively; $n^L_{C_1}$ and $n^L_{C_3}$ depict the mole numbers of C_1 and C_3 in the liquid phase, respectively; $n^V_{C_1}$ and $n^V_{C_3}$ represent the mole numbers of C_1 and C_3 in the vapor phase, respectively.

We assume that hydrocarbon mixtures are confined by two infinitely large homogeneous planar slits separated by W . Thus, based the Young-Laplace equation [17] with zero contact angle, P_{cap} can be calculated as:

$$P_{cap} = \frac{\sigma}{W} \tag{5.19}$$

where σ is the vapor-liquid interfacial tension (IFT), which can be obtained by the equation provided by Weinaug and Katz [159]:

$$\sigma = \left[\sum_{i=C_1,C_3} \chi_i \left(x_i \rho_m^L - y_i \rho_m^V \right) \right]^4, \tag{5.20}$$

in which χ is the Parachor number, ρ_m^L and ρ_m^V are the molar densities of the liquid phase and vapor phase, respectively; x_i and y_i are the mole fractions of component i in the liquid phase and vapor phase, respectively.

To solve the chemical potential equilibrium in **Eq. (5.18)**, Mikyška and Firoozabadi [139] proposed a modeling framework based on the volume function rather than fugacity. The volume function is defined as an effective partial volume of a real fluid. Similarly, a dimensionless parameter volume function coefficient Φ is proposed to relate the ideal fluid volume to the volume function, which plays an analogous role to the fugacity coefficient in the P-T Flash. In terms of volume function coefficient Φ_i^V and Φ_i^L, **Eq. (5.18)** can be expressed as [139]:

$$\frac{n_i^V}{V^V \Phi_i^{\,V} \left(V^V, T, n_{C_1}^V, n_{C_3}^V \right)} = \frac{n_i^L}{V^L \Phi_i^{\,L} \left(V^L, T, n_{C_1}^L, n_{C_3}^L \right)}, \quad i = C_1, C_3 \tag{5.21}$$

In this work, the volume function coefficient is obtained from the PR-EOS, which is given as [106]:

$$P\left(V, T, n_{C_1}, n_{C_3}\right) = \frac{nRT}{V - B} - \frac{A}{V^2 + 2BV - B^2} \tag{5.22}$$

where R is the universal gas constant, n is the total mole number. The coefficients A and B are given as

$$A = \sum_{i=C_1,C_3} \sum_{j=C_1,C_3} n_i n_j a_{ij} \tag{5.23}$$

$$a_{ij} = (1-k_{ij})\sqrt{a_i a_j} \tag{5.24}$$

$$B = \sum_{i=C_1,C_3} n_i b_i \tag{5.25}$$

in which, a_i is the attraction parameter and b_i is the repulsion parameter for component i, respectively; k_{ij} is the binary interaction parameter (BIP) between the component i and j. BIP is selected to match the lower dew point and bubble point of C_1-C_3 mixtures from PR-EOS with experiments [12]. a_i and b_i are given by

$$a_i = 0.45724 \frac{R^2 T_{i,c}^2}{P_{i,c}} \left[1 + m_i (1 - \sqrt{T_{r,i}})\right]^2 \tag{5.26}$$

$$b_i = 0.0778 \frac{R T_{i,c}}{P_{i,c}} \tag{5.27}$$

and

$$T_{r,i} = \frac{T}{T_{i,c}} \tag{5.28}$$

$$m_i = \begin{cases} 0.37464 + 1.54226\omega_i - 0.26992\omega_i^2 & \omega_i < 0.5, \\ 0.3796 + 1.485\omega_i - 0.1644\omega_i^2 + 0.01667\omega_i^3 & \omega_i \geq 0.5, \end{cases} \tag{5.29}$$

where $T_{i,c}, P_{i,c}$, and ω_i are critical temperature, critical pressure and acentric factor of component i, respectively. The volume function coefficient for the PR-EOS is given as [106]:

$$\ln \Phi_i = \ln \frac{V-B}{V} - \frac{b_i n}{V-B} + \frac{A b_i}{BRT} \frac{V}{V^2 - 2BV - B^2} - \frac{1}{\sqrt{2}BRT} \left[\frac{A b_i}{2B} - \sum_{j=1}^{m} n_j a_{ij} \right] \ln \left| \frac{V + (1+\sqrt{2})B}{V + (1-\sqrt{2})B} \right| \tag{5.30}$$

An iterative method is used to track the saturation points by the V-T flash with a capillary pressure algorithm. In the inner loop, the interior point method is used to solve the vapor-phase fraction. In the outer loop, the volume fraction of the vapor phase is updated by solving **Eq. (5.17)**, and then the equilibrium ratio K is updated by solving the chemical potential equilibrium equation. We continue the iterations until the variation is less than a tolerance parameter. The tangent plan distance (TPD) function includes the capillarity effect into the Helmholtz free energy, while the sign of TPD function is used as the criterion to determine the phase stability [160]. Only the binodal points (bubble/dew points) which stand for phase stability limit for stable and unstable states are included. The vapor-liquid phase equilibrium is identified by minimizing the Helmholtz free energy and fluid properties are obtained from the global free energy minimum. At bubble point and upper dew point, for vapor-liquid two phase coexistence, the vapor phase fraction is close to 0, while the liquid phase fraction is close to 1. At lower dew point, the vapor phase fraction is close to 1, while the liquid phase fraction is negligible. The related parameters are presented in **Table 5-2**.

5.2.3 EOS plus Shifted CPs in the Canonical Ensemble

Under nanoconfinement, the critical temperature and pressure of pure components are shifted. EOS plus shifted CPs model takes into account such shifted CPs to predict fluid phase behaviors under nanoconfinement [130]. In this work, the shifted CPs of C_1 and C_3 in various nanopores are obtained from separate engineering DFT calculations as shown in **Table 5-3**. EOS plus shifted CPs and P_{cap} model could further couple the P_{cap} effect upon the EOS plus shifted CPs model by following the same procedure mentioned in **Section 5.2.2**.

5.3 Results and Discussions

In this section, we first present the T-$c_{p,overall}$ (c is the overall molar density) phase diagrams and critical properties of nano-confined C_1-C_3 mixtures ($x_{C_1,p}^{eq} : x_{C_3,p}^{eq} = 0.2 : 0.8$) in the canonical ensemble by the EOS based models and the engineering DFT. Three different sets of pore sizes (5, 8 and 10 nm) are considered. Then, we compare the fluid properties in vapor and liquid phases within the vapor-liquid coexist regions at $T = 288.15$ K. Finally, we illustrate the necessity of considering fluid-surface interactions and surface adsorption in the EOS based models.

The T-$c_{p,overall}$ phase diagrams of C_1-C_3 mixtures of $x_{C_1,p}^{eq} : x_{C_3,p}^{eq} = 0.2 : 0.8$ in various nanopores from the engineering DFT and the EOS based models are presented in **Figure 5-1**. Based on the engineering DFT calculations, the T-$c_{p,overall}$ diagrams of C_1-C_3 mixtures shrinks due to the nanoconfinement effect. In general, for a given temperature T, the dew point density is higher than the bulk dew point density due to strong surface adsorption, and such phenomena is in line with previous DFT [5, 39, 161] and molecular simulation [131, 162-165] studies for pure substances. For bubble point density of nanoconfined C_1-C_3 mixtures, when $W = 5$ nm, it is always lower than that in bulk. However, for $W \geq 8$ nm, it could be rather higher or lower than that in bulk, depending on temperature. As W decreases, the differences between bubble point and dew point densities decrease. The critical temperature of nanoconfined C_1-C_3 mixtures does not correspond to the highest temperature point, rendering the presence of the cricondentherm temperature. On the other hand, the EOS based models generally predict that dew point lines are close to the bulk thanks to the negligence of fluid-surface interaction and surface adsorption. The PR-EOS plus P_{cap} model predicts smaller bubble point densities and lower dew point densities, while higher upper dew point densities compared to those in bulk. The PR-EOS plus shifted CPs model predicts shrunk T-$c_{p,overall}$ diagrams of confined C_1-C_3 mixtures as it uses the shifted CPs

from the engineering DFT. Similar to the EOS plus P_{cap} model, this method underestimates the molar densities $c_{p,overall}$ in the entire phase diagram (including bubble point line, dew point line, critical point) due to the negligence of fluid-surface interactions. Further considering P_{cap} shows a negligible effect. Compared to the engineering DFT, in 5-nm pores, PR-EOS with effect of capillarity and shifted critical properties underestimate the dew point and bubble point densities by ~90% and ~50%, respectively. As pore size increases, the deviation from the engineering DFT decreases.

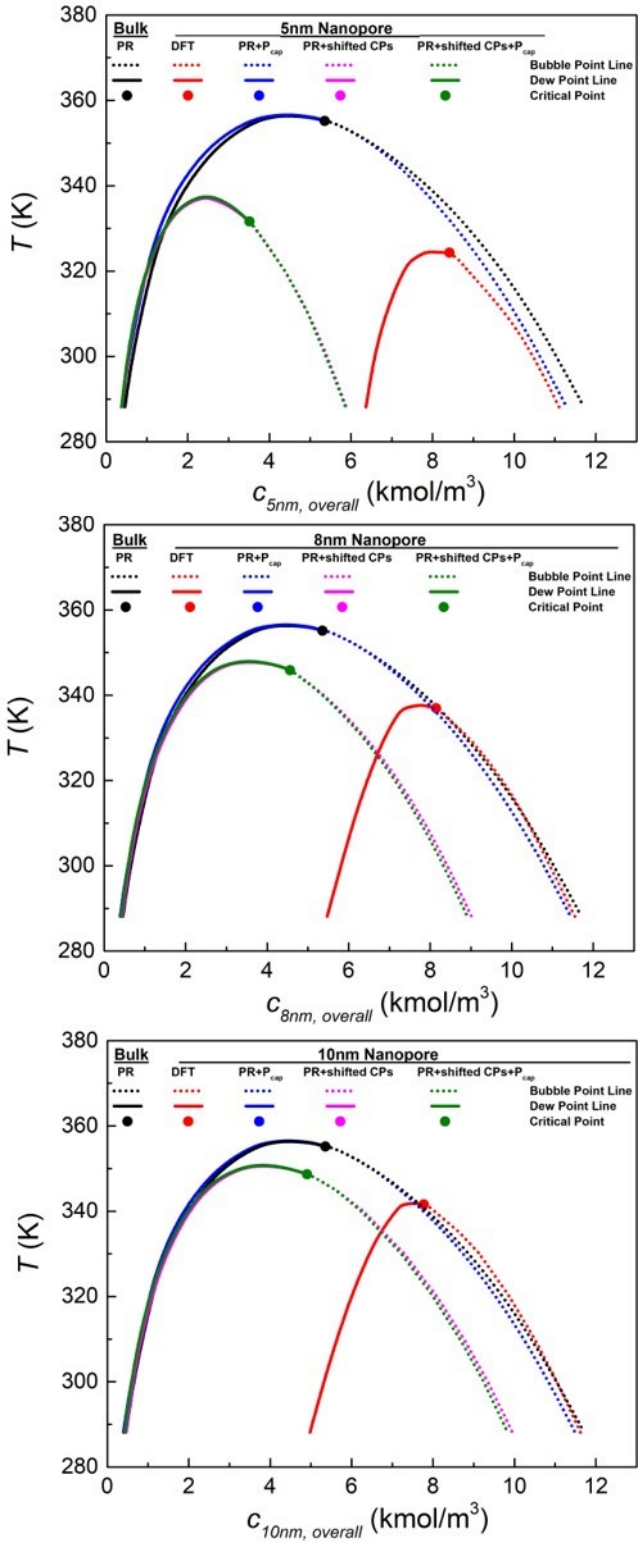

Figure 5-1. T-$c_{p,overall}$ diagrams of C_1-C_3 mixtures ($x_{C_1,p}^{eq} : x_{C_3,p}^{eq} = 0.2 : 0.8$) in 5, 8 and 10 nm pores from the EOS based models and the engineering DFT.

The density profiles of C_1 and C_3 of C_1-C_3 mixtures ($x^{eq}_{C_1,p} : x^{eq}_{C_3,p} = 0.2 : 0.8$) at bubble point and dew point densities at 288.15 K in various pores are shown in **Figure 5-2**. As W decreases, surface adsorption plays a more significant role on the average densities of C_1 and C_3 in nanopore because of stronger fluid-surface interactions. Compared with the liquid phase, the surface adsorption influences the vapor phase average density more significantly due to the large density differences between adsorption layer and the vapor phase in the middle of pores. As the EOS based models neglect the surface adsorption, the dew point densities are severely underestimated as shown in **Figure 5-1**.

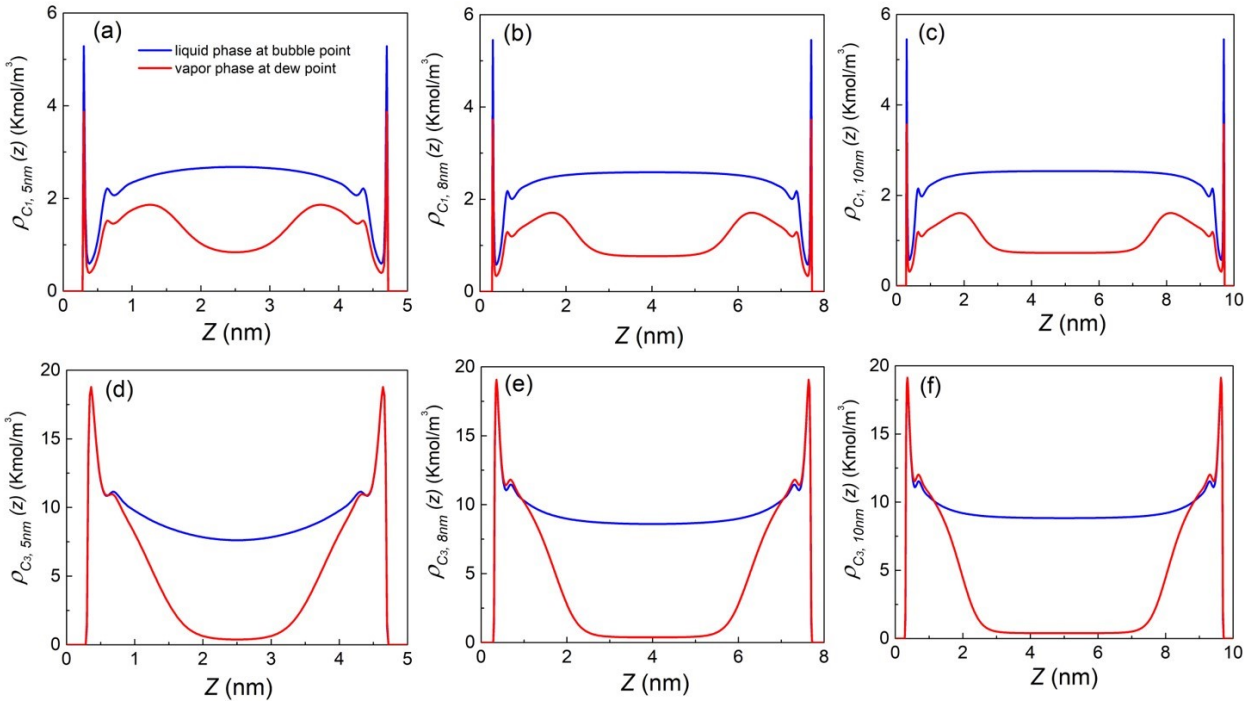

Figure 5-2. The density profiles of C_1 and C_3 of C_1-C_3 mixtures ($x^{eq}_{C_1,p} : x^{eq}_{C_3,p} = 0.2 : 0.8$) from engineering DFT at bubble point and dew point at 288.15 K in 5 nm: (a) C_1; (d) C_3, 8 nm: (b) C_1; (e) C_3, 10 nm: (c) C_1; (f) C_3, respectively.

The reduced pore critical temperatures (the ratio of critical temperature in nanopores to that in bulk, $T_{c,p} / T_{c,b}$) and the reduced pore critical densities (the ratio of critical density in nanopore to

that in bulk, $c_{c,p}/c_{c,b}$) from the engineering DFT and the EOS based models are presented in **Figure 5-3 (a)** and **(b)**, respectively. In **Figure 5-3 (a)** , both the engineering DFT and the EOS based models predict that the critical temperatures of C_1-C_3 mixtures confined in nanopores ($T_{c,p}$) increase and approach bulk ($T_{c,b}$) as W increases, which is similar to pure substances [39, 131, 161-165]. Compared with the engineering DFT, the EOS plus shifted CPs model overestimates $T_{c,p}$ for around 3%, as it does not consider the fluid-surface interactions. On the other hand, the engineering DFT shows higher critical densities of C_1-C_3 mixture in nanopores ($c_{c,p}$) compared to the bulk $c_{c,b}$, while $c_{c,p}$ decreases and approaches $c_{c,b}$ as W increases. Similar phenomena are also observed in pure substances from molecular simulations and statistical thermodynamic methods [39, 131, 161-165]. However, the EOS plus shifted CPs model shows a lowered $c_{c,p}$ due to the negligence of the fluid-surface interactions. In 5-nm pores, the critical density is underestimated by ~60% compared to the engineering DFT, the underestimation decreases with pore size increases.

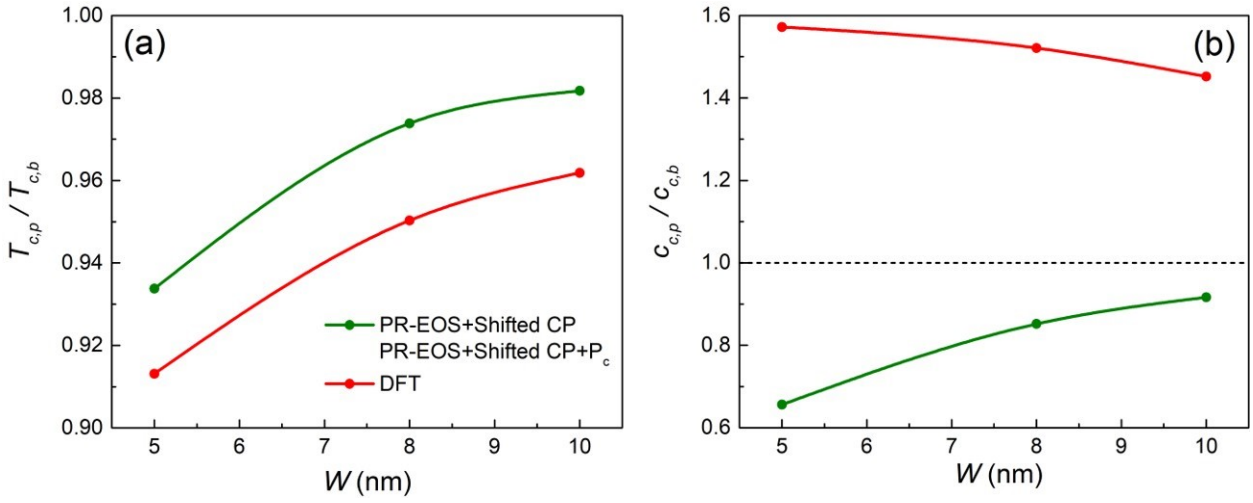

Figure 5-3. (a) The reduced pore critical temperatures (the ratio of critical temperature in pores to that in bulk); (b) the reduced pore critical density (the ratio of critical density in pores to that in

bulk) of C_1-C_3 mixtures ($x_{C_1,p}^{eq} : x_{C_3,p}^{eq} = 0.2 : 0.8$) in various nanopores from the EOS based methods and the engineering DFT.

We further study the vapor and liquid phase properties in two-phase liquid-vapor coexistence region in nanopores at $T = 288.15$ K, which is far away from the critical temperatures. The vapor phase average densities in nanopores ($c_{p,v}$) and C_3 mole fractions in the vapor phase ($x_{C_3,p,v}$) in various nanopores are shown in **Figure 5-4**. We also present the fluid properties in middle of pores obtained from the density profiles from the engineering DFT for comparison. The engineering DFT predicts that as W increases, the two-phase region expands, while $c_{p,v}$ decreases in line with **Figure 5-1**. From the dew point (solid square) to the bubble point (solid circle), $c_{p,v}$ increases as the overall molar density ($c_{p,overall}$) increases, while $x_{C_3,p,v}$ decreases. In contrast, the EOS based models significantly underestimates $c_{p,v}$ and $x_{C_3,p,v}$. In 5-nm pores, the underestimation of $c_{p,v}$ and $x_{C_3,p,v}$ can be up to ~% 80and ~60%, respectively. On the other hand, $c_{p,v}$ and $x_{C_3,p,v}$ in the middle of the pores from the engineering DFT agrees well with those from the EOS based methods. These comparisons underscore the importance of surface adsorption for nanoconfined hydrocarbon mixtures, which are generally neglected in most EOS based models.

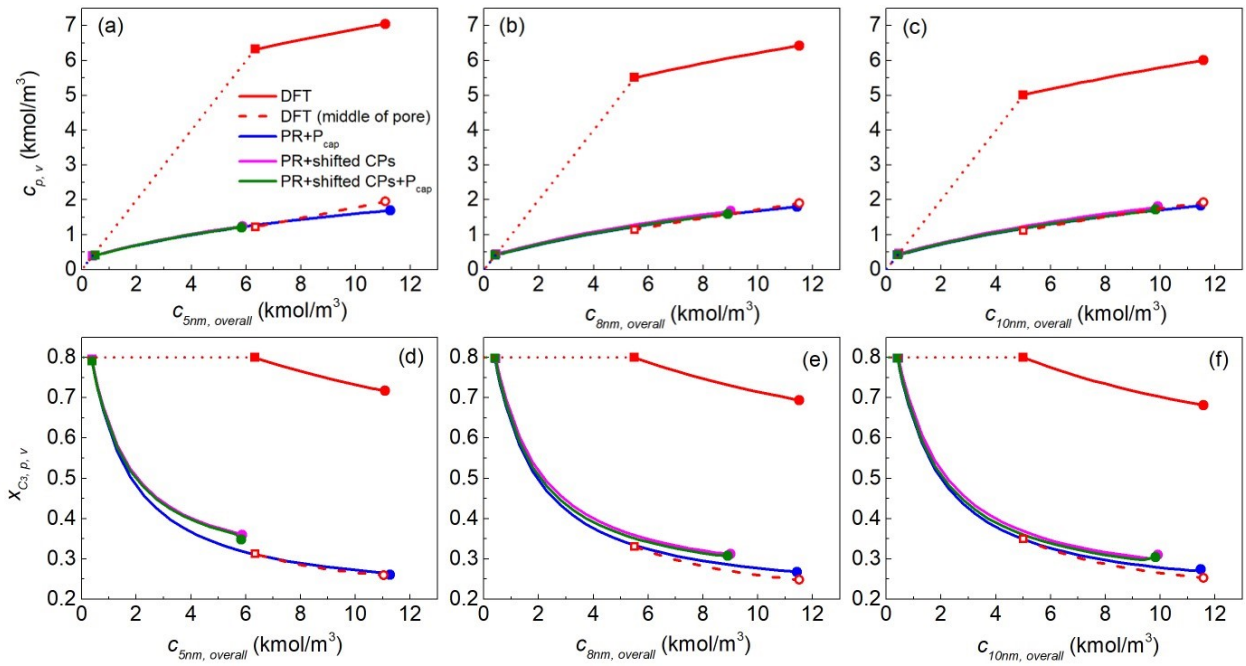

Figure 5-4. The vapor phase properties of C_1-C_3 mixtures ($x^{eq}_{C_1,p} : x^{eq}_{C_3,p} = 0.2 : 0.8$) within the liquid-vapor coexist region at T=288.15 K. (a) (b) and (c) present vapor phase molar density in 5, 8 and 10 nm pores, respectively. (d) (e) and (f) present C_3 molar fraction in vapor phase in 5, 8 and 10 nm pores, respectively. Squares are used to present dew point while circles stand for bubble point. The red dashed line presents vapor phase properties in the middle of pore from DFT. The dotted line is a reference line to show the fluid properties in pure vapor phase region.

In **Figure 5-5**, we present the liquid phase properties in two-phase liquid-vapor coexistence region in nanopores from the engineering DFT and the EOS based models. Compared to the engineering DFT, the EOS plus shifted CPs model underestimates the liquid phase molar densities ($c_{p,l}$) as well as the C_3 mole fraction in the liquid phase ($x_{C_3,p,l}$). Compared with vapor phase properties, the deviations between the EOS plus shifted CPs model and the engineering DFT in liquid phase properties become smaller as W increases. It is because the effect of surface adsorption is less significant on the liquid phase properties comparing to the vapor phase. In fact, the deviations are

much smaller than those in the vapor phase when $W \geq 8$ nm. Further adding capillary effect on the EOS plus shifted CPs model shows little effect on liquid phase properties. Interestingly, $c_{p,l}$ and $x_{C_3,p,l}$ predicted by the EOS plus P_{cap} model agrees well with the predictions from the engineering DFT. Even though the surface adsorption is not considered, the unshifted CPs are used which leads to a quite good prediction in terms of liquid phase properties. We also note that $x_{C_3,p,l}$ in the middle of the pores from engineering DFT can be less than 0.8 due to surface adsorption.

The liquid phase saturations (liquid phase volume fractions) $S_{p,l}$ from the engineering DFT and the EOS based models are presented in **Figure 5-6**. At 288.15 K, from the bubble point to the dew point, $S_{p,l}$ decreases from 1 to 0 in a narrower $c_{p,overall}$ range, but corresponding to higher $c_{p,overall}$ from the engineering DFT compared to EOS plus shifted CPs model. It is because DFT predicts higher $c_{p,l}$ and $c_{p,v}$ within two-phase liquid-vapor coexistence region in nanopores with surface adsorption. On the other hand, as the effect of surface adsorption on the $c_{p,v}$ is much stronger than that on the $c_{p,l}$, the difference between $c_{p,l}$ and $c_{p,v}$ predicted from DFT is narrower compared to that obtained from EOS plus shifted CPs model . For a given $c_{p,overall}$, according to **Eq. (5.16)**, EOS plus shifted CPs model overestimates the liquid phase saturation $S_{p,l}$ as surface adsorption is not considered. Unlike the EOS plus shifted CPs model, the EOS plus P_{cap} model uses bulk critical properties, which are higher than those in nanopores. Based on the EOS plus P_{cap} model without the shift of CPs, the liquid phase densities are higher while the vapor phase densities are lower compared to those from the engineering DFT. In contrast to the engineering DFT, the difference between $c_{p,l}$ and $c_{p,v}$ is more significant from EOS plus P_{cap} model, which leads to

$S_{p,l}$ decreases from 1 to 0 in a wider range of $c_{p,overall}$. For a given $c_{p,overall}$, the EOS based models always overestimates $S_{p,l}$, especially at low $c_{p,overall}$ conditions.

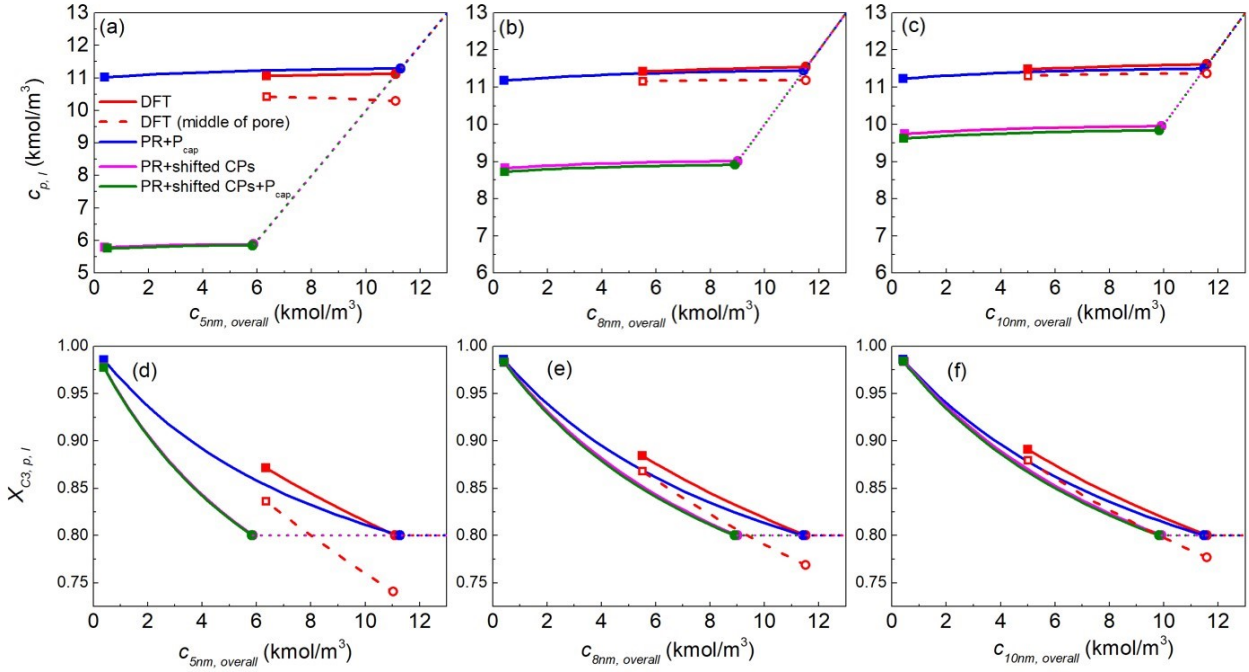

Figure 5-5. The liquid phase properties of C_1-C_3 mixtures ($x^{eq}_{C_1,p} : x^{eq}_{C_3,p} = 0.2 : 0.8$) within the liquid-vapor coexist region at T=288.15K. (a) (b) and (c) present liquid phase molar density in 5, 8 and 10nm pores, respectively. (d) (e) and (f) present C_3 molar fraction in liquid phase in 5, 8 and 10nm pores, respectively. Squares are used to present dew point while circles stand for bubble point. The red dashed line presents liquid phase properties in the middle of pore from DFT. The dotted line is a reference line to show the fluid properties in pure liquid phase region.

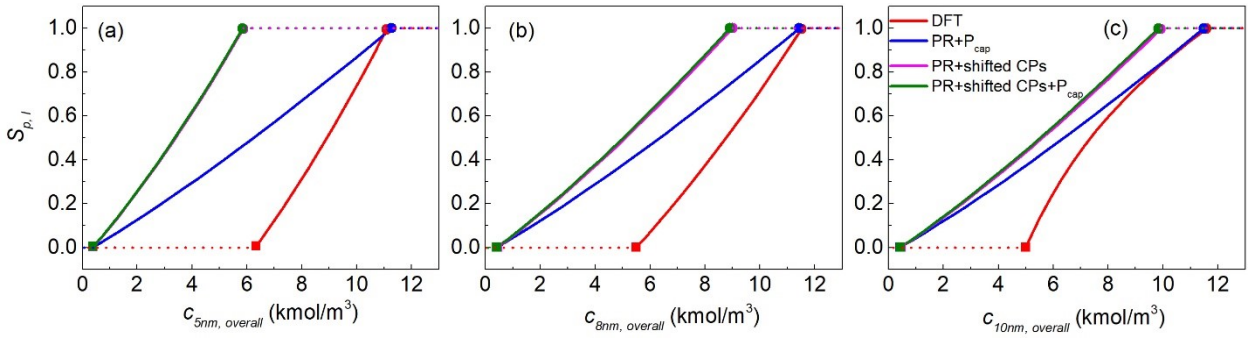

Figure 5-6. The liquid phase saturation of C_1-C_3 mixtures ($x_{C_1,p}^{eq} : x_{C_3,p}^{eq} = 0.2 : 0.8$) within the liquid-vapor coexist region at 288.15 K in (a) 5 nm; (b) 8 nm; (c) 10 nm pores, respectively. The squares represent the dew points and the circles represent the bubble points. The dotted lines are reference lines to show the liquid phase saturation in pure vapor and liquid phase regions.

In **Figure 5-7**, we present the average densities and C_3 mole fractions in both liquid and vapor phases of C_1-C_3 mixtures in nanopores from the engineering DFT. For comparison, we also depict their properties in the middle of pores. Overall, the surface adsorption effect on vapor phase fluid densities $c_{p,v}$ and compositions $x_{C_3,p,v}$ is significant even when $W = 10$ nm. For liquid phase, surface adsorption effect is less significant, especially when $W \geq 8$ nm. In pure vapor phase region, $c_{p,v}$ decreases more significantly compared to that of fluids in middle of pore as $c_{p,overall}$ decreases. It is because the fraction of adsorbed fluids to the overall fluids under confinement gradually decreases. On the other hand, the C_3 concentration in the middle of pores shows different trends in various nanopores. In 5-nm pores, the C_3 concentration in the middle of pores decreases as $c_{p,overall}$ decreases. In 8 and 10 nm pores, as $c_{p,overall}$ decreases, the C_3 concentration in the middle of pore first increases then decreases. Overall, the surface adsorption effect is significant in pure vapor phase. In pure liquid phase region, as $c_{p,overall}$ increases, the surface adsorption effect on $c_{p,l}$ becomes less significant.

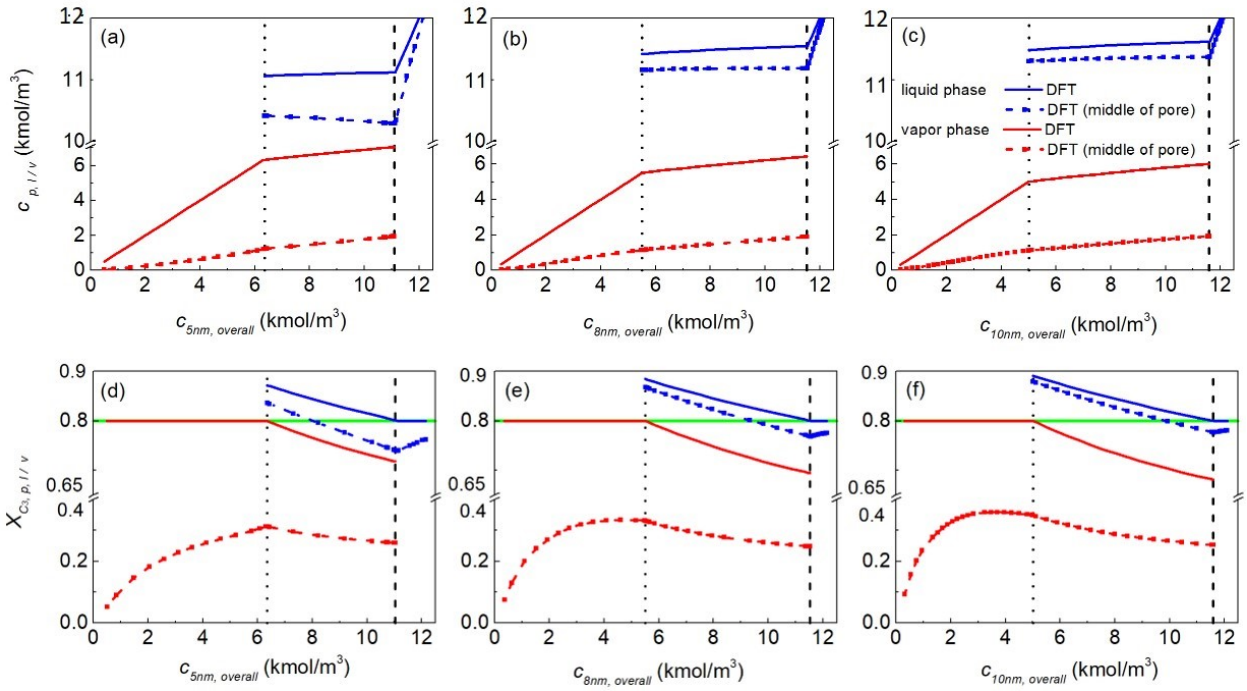

Figure 5-7. The liquid and vapor phase properties of C_1-C_3 mixtures ($x^{eq}_{C_1,p} : x^{eq}_{C_3,p} = 0.2 : 0.8$) within the liquid-vapor coexist region at T=288.15K. (a) (b) and (c) present molar density in 5, 8 and 10nm pore, respectively. (d) (e) and (f) present C_3 molar fraction in 5, 8 and 10nm pore, respectively. The black dotted line presents dew point density, which divided the pure vapor phase region and two-phase region. The black dashed line divides two-phase region and pure liquid phase region, it presents bubble point density. The green line is a reference line to show the C_3 concentration of nanoconfined mixture.

5.4 Conclusions

In this work, we studied phase behaviors of nanoconfined hydrocarbon mixtures in canonical ensemble by the engineering DFT and various EOS based models to assess the viability of the latter.

Based on the engineering DFT results, we find that in the canonical ensemble, the T-$c_{p,overall}$ phase diagram of C_1-C_3 mixture shrinks due to nano-confinement, which is in line with molecular

simulation and statistical thermodynamic methods for pure substances [39, 131, 161-165]. Unlike the pure substances, when $W \geq 8$ nm, the dew point density could be either higher or lower than that in bulk, depending on temperature. Besides, the cricondentherm temperature exists for the nano-confined hydrocarbon mixtures.

By comparing phase diagrams and fluid properties from EOS based models with the engineering DFT, we find that the negligence of fluid-surface interactions in the EOS based models can result in significant discrepancies. In fact, all the EOS based models discussed in this work fail to show confinement effect for dew point line in T-$c_{p,overall}$ phase diagram. Both the engineering DFT and EOS plus shifted CPs model predict that the pore critical temperature $T_{c,p}$ is lower than the bulk $T_{c,b}$. On the other hand, while the engineering DFT predicts that the pore critical density $c_{c,p}$ can be higher than the bulk $c_{c,b}$, the EOS plus shifted CPs model presents an opposite trend. For the vapor and liquid phase properties within two-phase liquid-vapor coexistence region in nanopores, EOS based models greatly underestimate the vapor phase densities $c_{p,v}$ and C_3 mole fractions in vapor phase $x_{C_3,p,v}$ due to the negligence of surface adsorption.

Collectively, this work presents that surface adsorption and fluid-surface interaction can play an important role in the phase behaviors of nano-confined hydrocarbon mixtures in the canonical ensemble, as the overall density is used as an input. Implementing surface adsorption in the EOS based models is imperative for accurate phase behavior predictions in the canonical ensemble [148], especially for vapor phase properties, dew point branch, and critical density predictions. Our work should provide theoretical foundations and important insights into the improvement of the EOS based models in the prediction of nano-confined hydrocarbon mixtures in the canonical ensemble.

Acknowledgement

This research was enabled in part by support provided by Westgrid (www.westgrid.ca) and Compute Canada (www.computecanada.ca). The authors also greatly acknowledge a Discovery Grant from Natural Sciences and Engineering Research Council of Canada (NSERC RGPIN-2017-05080).

CHAPTER 6 OIL DISPLACEMENT BY WATER THROUGH AN ULTRA-NARROW KEROGEN PORE THROAT: A MOLECULAR DYNAMIC STUDY

A version of this chapter has been submitted in SPE J.

6.1 Introduction

The shale revolution [166] has been gradually reshaping the global energy landscapes and shale media have become an important source to meet the growing energy demand [2]. Unlike conventional reservoirs, where pore size ranges from μm to mm scale and geofluids behave as bulk, there are numerous nanoscale pores and ultra-narrow pore throats (sub 2-nm) in shale media [167, 168]. Thanks to the development of horizontal and hydraulic fracturing technologies, oil production from shale formations has increased significantly [169]. Driven by external forces, oil can be displaced by water through ultra-narrow pore throats [170], which needs to overcome excessively-high capillary pressure. As a result, pore throats in shale media might govern oil migration and determine their ultimate productivity [171]. Therefore, the knowledge about the threshold capillary pressure for oil displacement by injected water through ultra-narrow pore throats is imperative to well productivity [172], which can provide theoretical guidance to shale/tight oil exploitations [173].

A number of works have been reported on the capillary pressure of multi-phase displacement process by experimental measurements, including the porous diaphragm (or restored capillary pressure) method [174-176], the centrifugal method [177], the mercury injection method [176, 178, 179] and the dynamic capillary pressure method [176, 180]. However, enormous challenges emerge during the direct observations of displacement process and measurement of capillary pressure in nanoscales [170]. Besides, it is difficult to differentiate the effect of various microscopic interactions among water, oil and minerals. On the other hand, from theoretical perspectives, the Young-Laplace (Y-L) equation has been widely applied to predict capillary pressure arising from nanoscale pore throats [181-184]. However, drastically different fluid flow behaviors may emerge in nanoscale pore throats in contrast to micro-meter scale ones due to strong

fluid-surface interactions [28, 29]. Thus, the validity of Y-L equation in nanoscale pore throats to predict the capillary pressure remains questionable [30]. In this regard, molecular dynamic (MD) simulations are a powerful tool to study the two-phase oil-water displacement process through nanoscale pore throats with given mineral types. By explicitly considering structural and dynamic properties of geofluids at atomistic and molecular levels [185], MD simulation can reveal the underlying mechanisms of two-phase oil-water displacement through ultra-narrow pore throats and serve as a benchmark to validate the Y-L equation.

Several simulation works have been reported on two-phase oil-water displacement through nanoscale pore throats. Chen *et al*. [170] used many-body dissipative particle dynamics (MDPD) simulations to study two-phase oil-water displacement through a cylindrical pore throat. They found that the external driving force should overcome a certain threshold force to displace oil through the pore throat. Sedghi *et al*. [186] used none equilibrium molecular dynamic (NEMD) to simulate displacement of oil by water through nanopores with varying surface wettability. They found that the threshold capillary pressures (i.e., breakthrough pressures) are in a good agreement with those calculated from the Mayer-Stowe-Princen (MSP) method. Wang *et al*. [31] used MD simulations to study two-phase oil-water displacement mechanisms in hydrophobic and hydrophilic capillaries. Instead of using full atomistic description of pore surface, they tuned the surface hydrophobicity/hydrophilicity by adjusting the energy well-depth parameter of water-surface interaction in the standard pairwise 12-6 Lennard-Jones (L-J) potential. They found that in hydrophobic capillaries, an oil layer always forms on the pore surface, while in hydrophilic ones, oil molecules can be fully displaced. In addition, to study the two-phase displacement process through nanoscale capillary with a specific mineral type, a number of MD simulation works build full atomistic models to take into account individual molecular configurations, atomistic details,

and specific intermolecular interactions (such as hydrogen bonding with pore surface). Sedghi *et al*. [172] conducted a series of MD simulations to study the confinement effect on the breakthrough pressure of oil invading into calcite mesopores filled with brine. They found that the breakthrough pressures from MD simulations are higher than the capillary pressures from the MSP method due to the water film on pore surfaces. Fang *et al*. [27] studied methane invasion into mica nanopores filled with water and found that a water film with thickness less than 1 nm forms on the pore surfaces. By taking into account the water film, the Y-L equation could predict methane breakthrough pressure well for 4-nm and 6-nm pore throats. However, for 2-nm pore throats, the capillary pressure from the Y-L equation with the correction of water film thickness still significantly underestimates the breakthrough pressure. Zhang *et al*. [173] investigated oil charging into quartz pore throats filled with water with their pore sizes ranging from 2 to 15 nm. They found that due to the water thin film on pore surfaces, the capillary pressure from the Y-L equation is generally lower than the breakthrough pressure, especially for narrow pore throats. Zhang and Guo [187] used the MD simulations to investigate the two-phase oil-water displacement through quartz, calcite, hydrophilic kaolinite, and moderately-lipophilic kaolinite pore throats. They also observed water thin films on pore surfaces in all systems, which can alter the effective pore throat diameters. While all these works provided important insights into two-phase displacement process through various inorganic pore throats in shale, the displacement process through kerogen pore throats which is one of the main constituents in shale [188-190] has not been reported yet.

Therfore, in this work, we use MD simulations to study the underlying mechanism of oil (represented by nC_8) displacement by water through ultra-narrow kerogen (represented by Type II-C kerogen [191]) pore throats (~2 nm) under various external pressure conditions at a typical

reservoir temperature (330 K). The breakthrough pressure P_B in the displacement process is compared against the capillary pressure P_{cap} from the Y-L equation, which is dependent on nC_8-H_2O interfacial tension (IFT) and nC_8-H_2O-kerogen contact angle (θ). Separate MD simulations are conducted to obtain nC_8-H_2O IFT and contact angle at 330 K and various pressure conditions. In addition, helium adsorption [192] and geometric insertion [193] methods are used to obtain the effective kerogen pore throat size. We find that the kerogen substrate is generally nC_8-wet and θ decreases as the diameter of H_2O droplet decreases. On the other hand, water has an excellent displacement efficiency due to the hydrogen bonding (H-bonding) between H_2O and heteroatoms on kerogen surface. Thanks to the H-bonding, there is no nC_8 adsorption layer on kerogen substrate in contrast to Wang *et al*. [31]. P_{cap} from the Y-L equation shows a good agreement with P_B obtained from MD simulations for the ~2 nm kerogen pore throat. This work affords important knowledge about the oil-water two-phase displacement process through ultra-narrow kerogen pore throat, which can provide important guidance to numerical modeling of oil recovery process in shale formations as well as optimization of shale/tight oil recovery.

6.2 Methodology

Type II-C kerogen molecule model from Ungerer *et al*. [191] is used to construct kerogen pore throats consisting of two identical kerogen matrices with a thickness of ~3.91 nm each built through annealing process as illustrated in **Appendix E**. The type II-C kerogen corresponds to the middle of oil formation zones according to the samples from the Duvernay series [191]. The density of kerogen matrix is 1.22 g/cm^3, which is in line with experimental results (1.18−1.25 g/cm^3) [191]. The details about constructing kerogen pore throat in oil-water two-phase

displacement system and the kerogen matrix in the nC_8-H_2O-kerogen contact angle calculation are illustrated in **Appendix E.**

6.2.1 Oil-Water Two-Phase Displacement Process

The entire system for the oil-water two-phase displacement process through an ultra-narrow kerogen pore throat is shown in **Figure 6-1 (a)**. Initially, the kerogen pore throat with a length of ~17 nm (in the *x*-direction) is filled with nC_8. At both ends of the pore throat, two nC_8 slabs with a length of ~5 nm each are placed. In the Upstream Reservoir, an H_2O slab with a length of ~10 nm is placed next to an nC_8 slab on the left, which represents the injected water. The number of nC_8 and H_2O molecules in the oil-water two-phase displacement system is given in **Table E-1** (**Appendix E**). The cross-sectional area in the *y*-*z* plane is 5.11 nm × 9.8 nm, resulting in a ~2 nm kerogen pore throat with a slit geometry. In addition, to simulate water flooding process, we impose an external force along the *x*-direction on a piston positioned at the left end of the H_2O slab to represent the upstream pressure (P_u), and an opposite force on the other piston positioned at the rightmost of the nC_8 slab to represent the downstream pressure (P_d). Both pistons consist of rigid graphene sheets. Beyond the two pistons, we place 10 nm thick of vacuums on each side to eliminate the interactions with images due to the periodic boundary conditions (PBCs). Finally, the dimension of the simulation box is 57 × 5.11 × 9.8 nm^3, and the origin is set at the lower left corner of the simulation box as highlighted in **Figure 6-1 (a)**. The system is first equilibrated for 2 ns with $P_u = P_d = 300$ bar, then, pressure difference ($P_e \equiv P_u - P_d$) is imposed by increasing P_u, while keeping P_d constant. We run the simulation for 100 ns to determine whether the water phase breakthrough can occur at a given P_e. When $P_e < P_B$, the length of the invaded water phase inside the kerogen pore throat is always smaller than the pore throat diameter; When $P_e > P_B$, the water

phase can pass through the kerogen pore throat thoroughly without stoppage. To investigate the external pressure effect on complete displacement process, we increase P_e from 500bar to 1500 bar and the total simulation time varies from ~110 ns to ~10 ns for the displacement process accomplished. In shale reservoirs, pore throats can be as narrow as a few nanometers [168], resulting in an extremely-high breakthrough pressure. Therefore, we use large P_e to study P_B in ultra-narrow kerogen pore throats. On the other hand, while a high P_e might result in an excessively-high pressure gradient, we note that the objective of this work is the breakthrough pressure characterization rather than the flow process.

6.2.2 Young-Laplace Equation

The Y-L equation [194, 195] has been widely used to describe P_{cap} which is a function of IFT (γ), θ and the principal radii of curvature (R_1 and R_2),

$$P_{cap} = \gamma \cos\theta \left(1/R_1 + 1/R_2\right). \tag{6.1}$$

For slit geometry, R_1 and R_2 are $W_{eff}/2$ and ∞, respectively, where W_{eff} represents the effective pore width. Therefore, to compare P_B with P_{cap}, the parameters γ, θ and W_{eff} need to be obtained by separate simulations. In the following subsections, the details about system settings to obtain each parameter are illustrated.

6.2.3 nC8-H2O-Kerogen Contact Angle

To calculate the nC_8-H_2O-kerogen contact angle, we build a system with an H_2O droplet immersed in nC_8 residing on kerogen substrate as shown in **Appendix E**. The general procedure to construct such a system is: First, a certain number of H_2O molecules are packed into a prismatic box by PACKMOL package. The box length in the *y*-direction is set as 5.11 nm (the same as the dimension

of the kerogen substrate shown in **Figure E-1 (b)** (**Appendix E**)). To test the effect of H_2O droplet size on θ, we consider various H_2O box lengths in the *x*- and *z*-directions (2 nm, 3 nm, 4 nm, 5 nm, 5.5 nm, 6 nm, and 7 nm). Then, two prismatic boxes containing nC_8 molecules are positioned on the left and right sides of the H_2O box. These two nC_8 boxes have the same dimensions in the *y*- and *z*-directions as the H_2O box, while their lengths in the *x*-directions (~7.5 nm, ~7 nm, ~6.5 nm, ~6 nm, ~5.75 nm, ~5.5 nm, ~5 nm) are adjusted to ensure that the total length of the H_2O and nC_8 boxes in the *x*-direction is the same as that of the kerogen substrate. Another nC_8 box is placed above the H_2O box with its lengths in the *x*- and *y*-direction as ~17 nm and 5.11 nm, respectively, while its length in the *z*-direction is adjusted to ensure that the entire simulation box length in the *z*-direction is equal to 12 nm. The number of H_2O and nC_8 molecules is obtained according to their bulk densities at given temperature and pressure conditions from NIST, which are given in **Table E-2**. The original dimensions of H_2O and nC_8 molecules in the *x*- and *z*-directions in nC_8-H_2O-kerogen contact angle system are summarized in **Table E-3**. A schematic representation of initial configuration (H_2O box length in the *x*- and *z*-direction equal to 5.5 nm) is shown in **Figure E-1 (a)** (**Appendix E**). A 2 ns NP_zT simulation is performed under three-dimensional (3-D) PBC at 330 K. The Parrinello-Rahman barostat [196] is used to control pressure condition, ranging from 100 to 1000 bar. The H_2O droplet evolves toward a cylindrical one as shown in **Figure E-1 (b)** (**Appendix E**). Next, we construct the contact angle system by placing kerogen substrate, H_2O droplet in nC_8, piston, and vacuum from bottom to top as shown in **Figure E-1 (c)** (**Appendix E**). The length of vacuum is ~4 times of the fluid system in the *z*-direction. The piston consists of a graphene sheet with a dimension of 17 nm × 5.1 nm in the *x*-*y* plane. Only repulsive interactions between graphene sheet and fluid molecules are considered. Different external forces are applied to the piston to represent various pressure conditions from 100 to 1000 bar. Then, we conduct at

least 50 ns of *NVT* runs to achieve the equilibrium condition as shown in **Figure E-1 (d)** (**Appendix E**). The diameter of the final H_2O droplets on the kerogen substrate in the *x*-*z* plane (D) are used to represent different droplet sizes, which is obtained by conducting a circle fit to H_2O density profiles as we discuss later. The corresponding D for various H_2O droplet cases are given in **Table E-2** (**Appendix E**). Each contact angle calculation is based on 10,000 snapshots from a production run of 5 ns.

6.2.4 nC8-H2O Interfacial Tension

To obtain H_2O-nC_8 IFT, we construct a system in which H_2O slab is placed in the middle of a rectangular simulation box (8 nm thick in the *z*-direction) with nC_8 slabs (9 nm thick in the *z*-direction) placed on each side as shown in **Figure E-1** (**Appendix E**). The dimension in the *x*-*y* plane is 6 nm × 6 nm. The number of H_2O and nC_8 molecules in the IFT calculation is given in **Table E-4** (**Appendix E**). 3-D PBCs are applied. Various pressure conditions ranging from 100 to 1000 bar at 330 K are considered. An equilibration run of 100 ns run is followed by a production run of 24 ns in the NP_zT ensemble.

6.2.5 Effective Pore Width

To obtain W_{eff} , helium adsorption method [192] is used as shown in **Figure E-1** (**Appendix E**). In the *x*-direction, the kerogen pore throat in the oil-water two-phase displacement system is filled with helium molecules. At both ends of the pore throat, two helium slabs with a length of 10 nm each are placed with a cross-sectional area in the *y*-*z* plane as 5.11 nm × 9.8 nm. The initial number of helium molecules in the system is obtained based on NIST databank as shown in **Table E-5** (**Appendix E**) and the helium force field parameters are from Talu *et al.* [197]. Two pistons with a dimension of 17 nm × 5.1 nm in the *x*-*y* plane consisting of rigid graphene sheets are set at the end of the left and right helium slabs to control system pressure. The same external forces are

exerted on both pistons to control the system pressure as 300 bar and only repulsive interactions between graphene sheet and helium molecules are considered. Beyond the two pistons, vacuums of 10 nm thick are placed on each side to eliminate the interactions with images due to PBCs. Finally, the dimension of the simulation box is $57 \times 5.11 \times 9.8$ nm^3. An equilibration run of 50 ns in the *NVT* ensemble is conducted. To avoid the pore end effect, an analysis region of ~10 nm along the *x*-direction in the middle of the pore throat is used to obtain the effective pore volume as highlighted in **Figure E-1** (**Appendix E**). W_{eff} is calculated based on 10,000 snapshots generated by a production run of 5 ns.

On the other hand, W_{eff} can also be obtained by the geometric insertion method [193]. Based on the "Connolly Surface" [198] of the kerogen pore throat, for a given random position inside the pore throat, the largest insertion sphere which can access the void space inside the pore throat can be repeatedly obtained. After collecting a large quantity of the largest accessible sub-volumes at random positions inside the pore throat, the diameter size distribution of insertion sphere inside the kerogen pore throat can be obtained by calculating the fraction of sub-volumes. Finally, W_{eff} is obtained based on the largest insertion sphere diameters and their weight fractions. More details about this method can be referred to Gelb and Gubbins [193].

6.2.6 Simulation details

The simulation systems in this work are assembled by PACKMOL package [199] and all MD simulations are performed by using GROMACS software (version 2019.5) [200, 201]. The kerogen matrices are described by the consistent valence force field (CVFF), which has been widely used to model kerogen and its interactions with water [202, 203] and hydrocarbons [202-204]. H_2O and nC_8 molecules are modeled by SPC/E [205] and Trappe-UA [206], respectively.

The kerogen matrices are fixed throughout the simulations. H_2O molecules are constrained by the SETTLE algorithm [207], while the bond length for nC_8 molecules are constrained via the LINCS algorithm [208]. For all the systems in this work, temperature is controlled by a velocity rescaling thermostat [209]. For the oil-water two-phase displacement system, P_e is determined by the difference of external forces applied to the pistons in the Upstream Reservoir and Downstream Reservoir; for the contact angle calculation, pressure conditions are represented by the external forces applied to the piston; for the IFT calculation, a semi-isotropic Parrinello-Rahman barostat [196] is used to control pressure; for the effective pore width calculation, the same external forces are applied on both sides of pistons to control system pressure.

To account for the Van der Waals interactions, LJ potential with a cut-off distance of 1.2 nm with the tail corrections [210] is applied. The LJ interaction between different molecules or in unlike pairs further than three bonds is calculated by geometric average [211]. Long-range electrostatic interactions beyond the cut-off distance is addressed by the Particle-Mesh-Ewald (PME) algorithm [212]. All systems are first relaxed by the steepest descent algorithm until the maximum force on any atom is less than 1000 kJ/(mol·nm). The time step is set as 2 fs for all the simulations in this work.

6.3 Results and Discussion

In this section, we first study the effect of P_e on the oil-water two-phase displacement process through kerogen pore throat and obtain P_B. Then, θ and γ are obtained from H_2O-nC_8-kerogen contact angle system and H_2O-nC_8 IFT system, respectively, while W_{eff} is obtained by helium adsorption method [192] or geometric insertion method [193]. Thereafter, P_{cap} is obtained by the Y-L equation, which is compared with P_B from MD simulation.

6.3.1 Oil-Water Two-Phase Displacement

Figure 6-1 (a) shows the initial condition for the oil-water two-phase displacement system, while **Figure 6-1 (b)** depicts the final configuration under various P_e conditions. When $P_e \leq 400$ bar, while the H_2O phase can push the nC_8 phase toward the Downstream Reservoir, it is stuck at the entrance of the kerogen pore throat. Taking $P_e = 300$ bar as a representative, we present the two-dimensional (2-D) density contour plots of H_2O and nC_8 in the *x*-*z* plane in **Figure 6-2 (a)** and **(b)**. The H_2O phase forms a convex meniscus stuck at the entrance of the kerogen pore throat, while several nC_8 molecules are left at the entrance of kerogen pore throat. We also present nC_8 density profile along the *z*-direction at $X = 320$ A in **Figure 6-2 (d)**. The peak positions of the first nC_8 adsorption layer on the upper and lower kerogen matrices are at $Z_0^{'} = 58.94$ A and $Z_0 = 41.00$ A, respectively. Then, the H_2O stuck angle θ_s as shown in **Figure 6-2 (a)** can be calculated based on the H_2O-nC_8 and nC_8-kerogen interfaces,

$$\theta_s = \arcsin(a_s / R_s), \tag{6.2}$$

where R_s is the radius of the fitted sphere based on H_2O-nC_8 interface and a_s is the half length of the interaction line of the fitted sphere nC_8-kerogen interface. The H_2O-nC_8 interface is determined by the H_2O density contour line with its density equal to the half of bulk H_2O density [213]; the nC_8-kerogen interface is determined by the first nC_8 adsorption layer ($Z_0 = 41.00$ A). As shown in **Figure 6-2 (b)**, when $P_e = 100$ bar, θ_s is close to 90 degrees. As P_e increases, θ_s gradually increases and approaches the static contact angle θ obtained from nC_8-H_2O-kerogen contact angle system as discussed in **nC_8-H_2O-Kerogen Contact Angle** part. We note that the difference

between θ_s and θ at higher pressures is probably because different methods are used to obtain them.

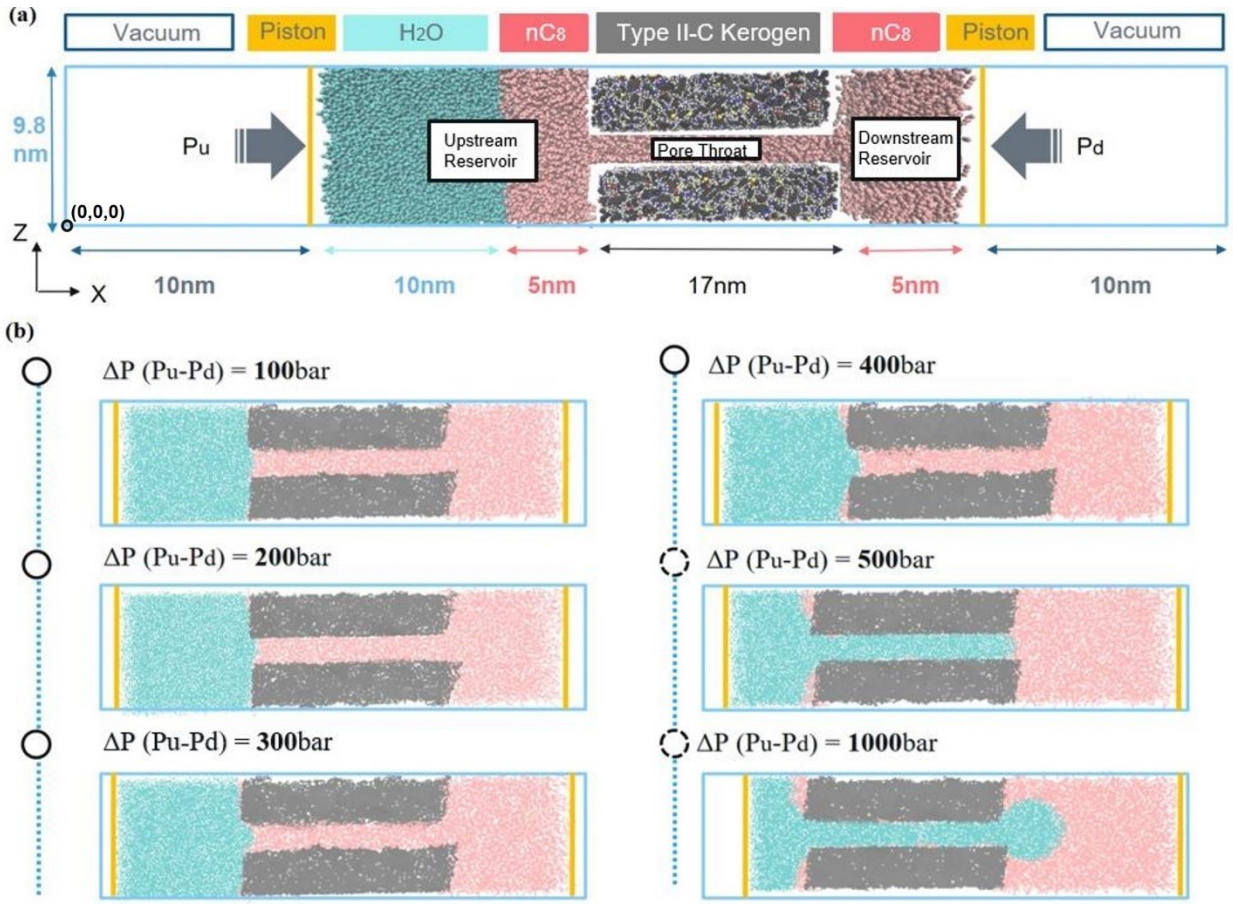

Figure 6-1. (a) Schematic representation of oil-water two-phase displacement stystem; (b) Pressure difference on displacement process.

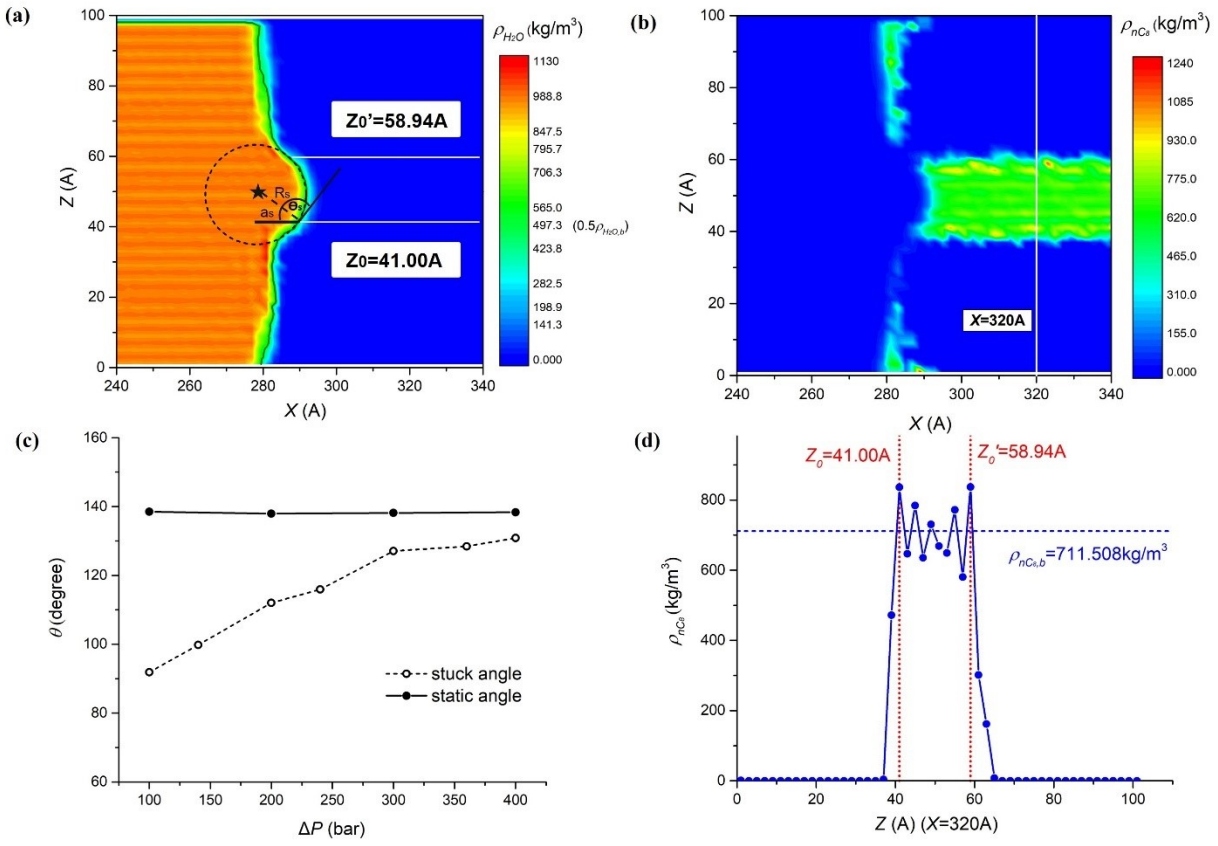

Figure 6-2. (a) 2-D density contour plot of H_2O; (b) 2-D density contour plot of nC_8; (c) H_2O stuck angle and static H_2O-nC_8-kerogen contact angle; (d) nC_8 density profile along the *z*-direction at $X = 320$ A for $P_e = 300$ bar.

On the other hand, when $P_e \geq 500$ bar, the H_2O phase can push the nC_8 phase through the kerogen pore throat. In addition, no nC_8 layer exists on the kerogen surface, despite kerogen being an nC_8-wet substrate as we show later. This phenomenon is in a stark contrast to Wang *et al*. [31], in which the full atomistic details of substrate surface are not taken into consideration. In **Figure 6-3 (a)**, we present the *x*-*y* plane view of molecular configurations of nC_8 and H_2O near Surface A ($283 \text{ A} < X < 453 \text{ A}$) at various P_e conditions. For $P_e = 500$ bar, as the H_2O phase invades into the kerogen pore throat, almost all nC_8 molecules are displaced. The excellent nC_8 displacement

efficiency is due to the formation of H-bonding between H_2O and heteroatoms (N, O, and S) on kerogen surface as shown in **Figure 6-3 (b)**. H-bonding is determined when the donor-acceptor distance is less than 0.35 nm and the angle between the vectors of donor-hydrogen and hydrogen-acceptor is less than 30 degree [214]. As P_e increases, more nC_8 molecules remain on the kerogen surface (see **Figure 6-3 (c)**), while the number of H-bonding between H_2O and kerogen heteroatoms decreases (see **Figure 6-3 (b)**).

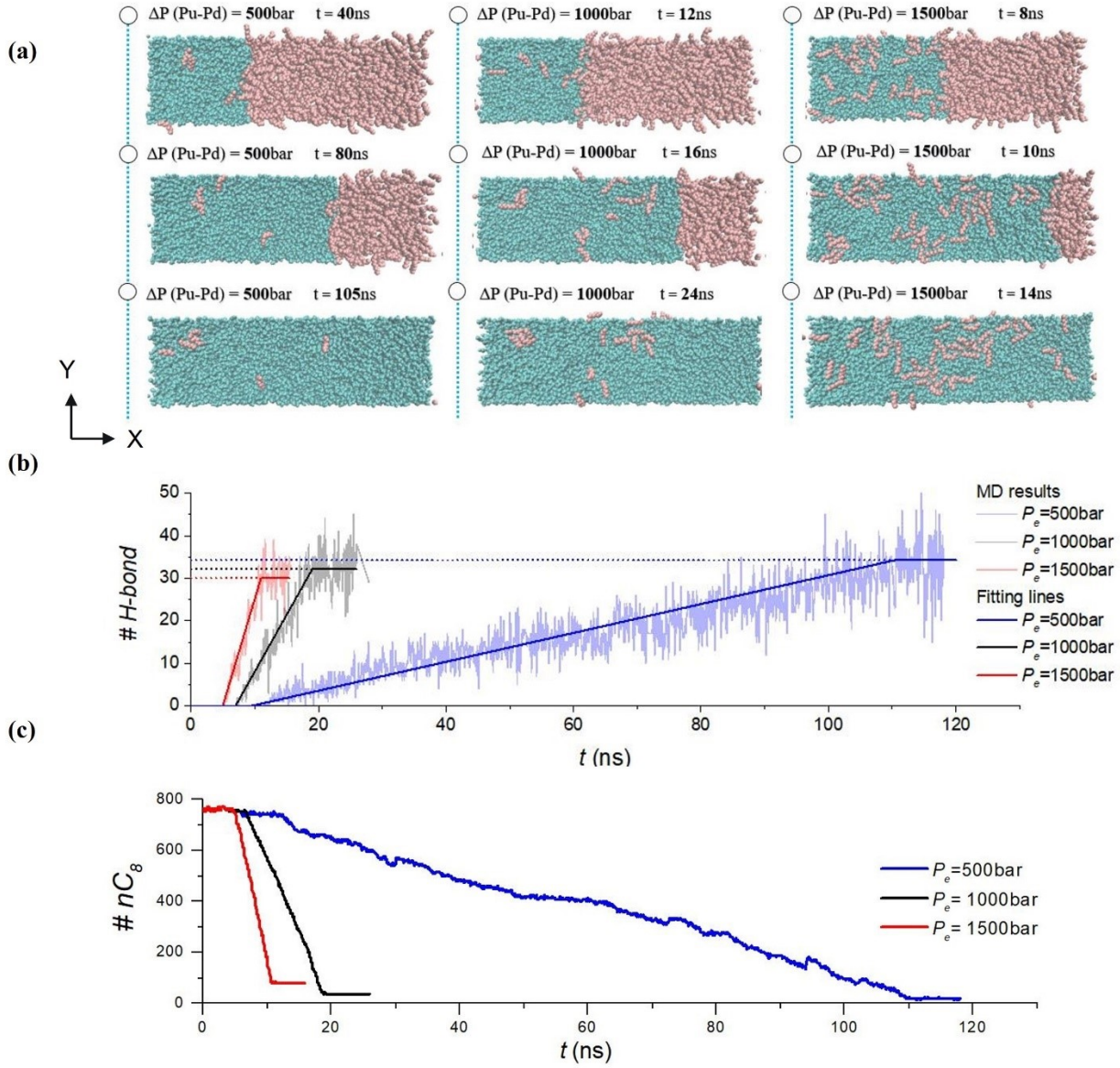

Figure 6-3. (a) *x-y* plane view of molecular configurations for nC_8 and H_2O near the kerogen Surface A ($283\ \text{A} < X < 453\ \text{A}$); (b) The evolusion of the number of hydrogen bonding between H_2O molecules and heteroatoms (N, O, and S) on kerogen surface during displacement; (c) The evolusion of the number of nC_8 molecules inside kerogen pore throat.

To determine P_B, a series of simulations with different P_e (pressure interval of 10 bar) are performed. As shown in **Figure 6-4 (a)**, starting from a configuration in which the H_2O phase is in the Upstream Reservoir, the breakthrough can only take place when $P_e \geq 430$ bar. As a result, the P_B from MD simulations is between 420 and 430 bar. However, through this process, the pore entrance could create an extra energy barrier for H_2O phase breakthrough [27], which is not considered in the Y-L equation. To test the pore entrance effect, as shown in **Figure 6-4 (b)**, we start from a different configuration in which the H_2O phase has already half-invaded into the kerogen pore throat under $P_e = 500$ bar. By decreasing P_e, the pressure condition when the H_2O phase recedes back into the Upstream Reservoir can be identified, which is determined to be in the range between 410 and 420 bar. The lower value is probably due to the Jamin effect [215, 216]. We also test the system size effect on P_B, in which we use a larger system with more fluid molecules but the same kerogen pore throat as shown in **Appendix E**. We find that the system size has a minor effect on P_B. In addition, we study the pressure effect on P_B by using different P_d. P_B slightly decreases as P_d decreases as shown in **Table 6-1**. It is probably because the nC_8-H_2O IFT increases as pressure increases as we discuss in **nC_8-H_2O Interfacial Tension** section.

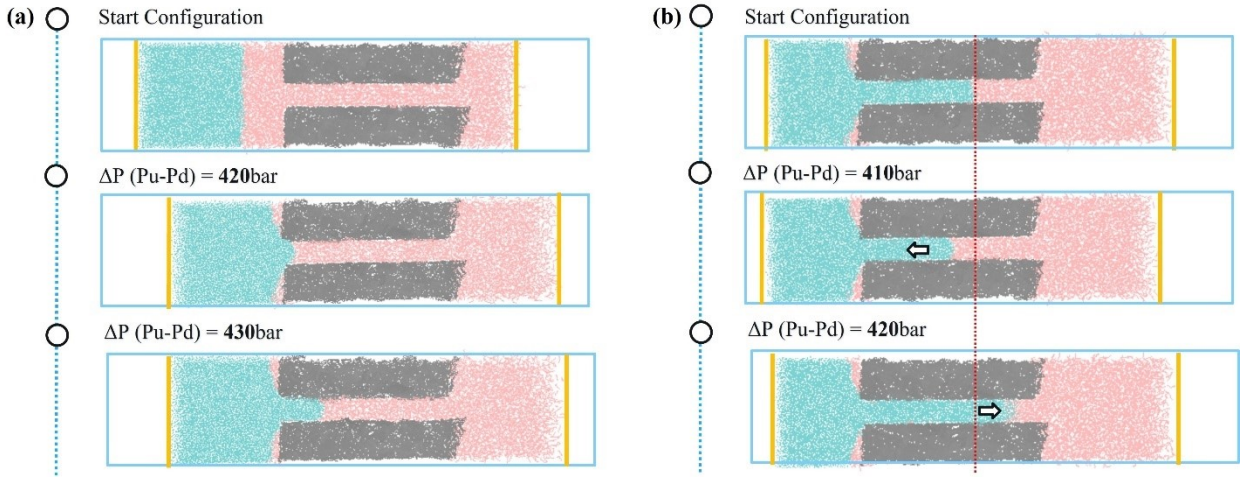

Figure 6-4. (a) P_B (420~430 bar) from simulation; (b) P_{cap} in the middle of the pore (410~420 bar) from simulation.

P_d **(bar)**	**100**	**300**	**500**	**700**	**1000**
P_B **(bar)**	**410 ~ 420**	**420 ~ 430**	**420 ~ 430**	**430 ~ 440**	**450 ~ 460**

Table 6- 1. The effect of P_d on P_B

6.3.2 nC8-H2O-Kerogen Contact Angle

The schematic diagram of nC_8-H_2O-kerogen contact angle system with an H_2O droplet with $D = 64.92$ A at 300 bar and 330 K as a representative is shown in **Figure 6-5**. The corresponding 2-D density contour plots of H_2O and nC_8 molecules are shown in **Figure 6-6**. It indicates that the type II-C kerogen is generally nC_8-wet, which is in line with the experimental finding for kerogen with a high maturity [217]. In **Figure 6-6 (c)**, we present the H_2O density profile along the *z*-direction at $X = 0$. H_2O shows a modest adsorption layer on the kerogen substrate at $Z_0 = 41.368$ A. Previous studies have shown that fluid adsorption layer becomes modest on a rough kerogen substrate [218]. In addition, H_2O density profile along the *x*-direction at $Z = 51$ A is shown in **Figure 6-6 (e)**. It shows that inside the H_2O droplet, H_2O density is the same as its bulk value at

given T and P condition, while it gradually decreases close to the H_2O-nC_8 interface. On the other hand, there is no nC_8 adsorption layer between H_2O droplet and kerogen substrate as shown in **Figure 6-6 (b)**, even though kerogen substrate is seemingly nC_8-wet. This is also verified by the nC_8 density profile along the *z*-direction at $X = 0$ as shown in **Figure 6-6 (d)**. However, away from the H_2O droplet (*e.g.* $X = 45$ A), two nC_8 adsorption layers on the kerogen substrate are observed as shown in **Figure 6-6 (f)**. The non-existent nC_8 layer between H_2O and kerogen is due to the H-bonding between H_2O and kerogen. To calculate H-bonding formed by kerogen heteroatoms, the N and O atoms in the kerogen molecule are divided into several subgroups: the N atoms in pyrrole and pyridine groups are denoted as Nprl and Nprd, respectively; the O atoms in ether, carbonyl, and hydroxyl groups are denoted as Oe, Oc, and Oh, respectively; the S represents all the S atoms in the molecules. As shown in **Figure 6-7 (a)**, the O atoms (especially Oc and Oe) have the highest H-bonding surface density followed by N atoms (especially Nprl). Thanks to H-bonding, H_2O molecules accumulate around the heteroatoms (i.e., O, N, and S) and displace the adsorbed nC_8 molecules from the kerogen substrate.

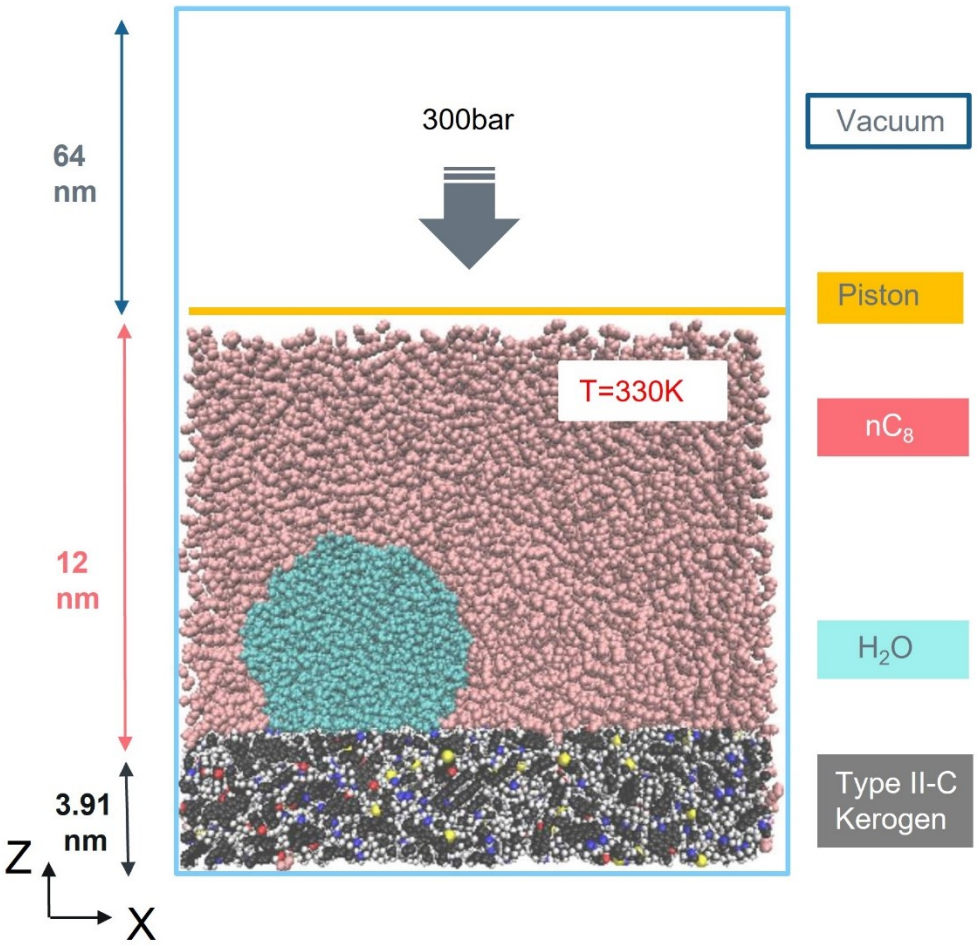

Figure 6-5. Schematic diagram of nC_8-H_2O-kerogen contact angle calculation at 300 bar and 330 K.

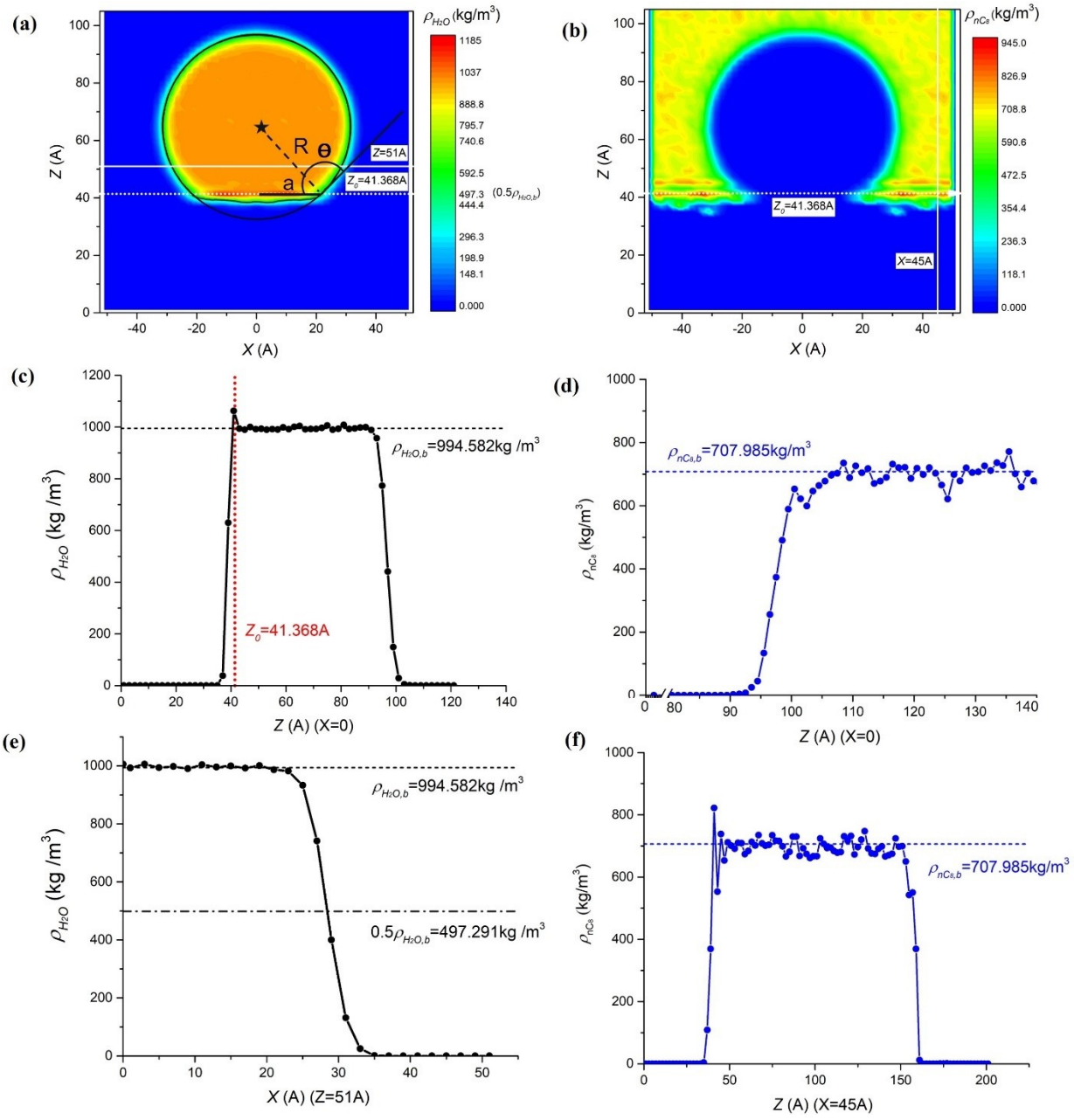

Figure 6-6. For $D = 64.92$ A: (a) 2-D density contour plot of H_2O; (b) 2-D density contour plot of nC_8; (c) H_2O density profile along the *z*-direction at $X = 0$; (d) nC_8 density profile along the *z*-direction at $X = 0$; (e) H_2O density profile along the *x*-axis at $Z = 51$ A; (f) nC_8 density profile along the *z*-direction at $X = 45$ A. The pressure and temperature are set as 300 bar and 330 K, respectively.

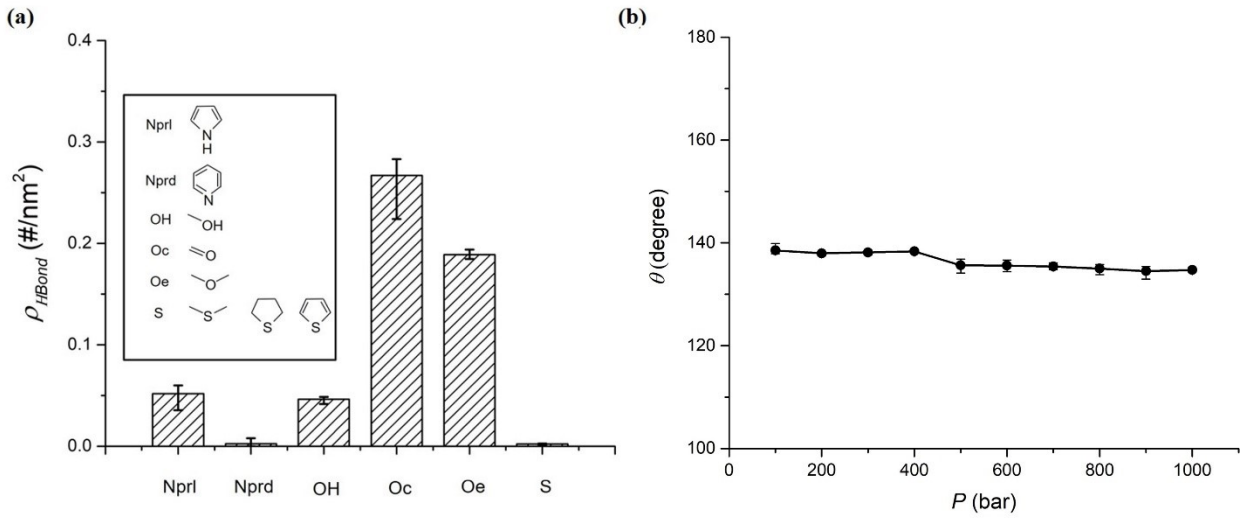

Figure 6-7. For $D = 64.92$ A: (a) Hydrogen bonding surface density of various kerogen hetratoms with H_2O; (b) nC_8-H_2O-kerogen contact angle at various pressure conditions and 330 K.

On the other hand, the 2-D H_2O density contour line equal to half of its bulk density is used to define the H_2O-nC_8 interface as shown in **Figure 6-6 (a)**. Then, the static nC_8-H_2O-kerogen contact angle θ is given as,

$$\theta = \arcsin\left(a / R\right) \tag{6.3}$$

where $R = D/2$ is the radius of the fitted sphere based on the H_2O-nC_8 interface and a is the half length of the interaction line of the fitted sphere H_2O-kerogen interface. In **Figure 6-7 (b)**, we present the nC_8-H_2O-kerogen contact angle for water droplet with $D = 64.92$ A at various pressure conditions and 330 K. It shows that θ is insensitive to pressure. Hansen *et al.* [219] reported that the effect of pressure on the contact angle of mica/water/n-decane system is negligible.

Unlike the sessile drop experiment [220-222], which has been widely used to determine the contact angle of macroscale droplet, θ of a nanoscale droplet which is commonly employed in molecular simulations is dependent on droplet size [223-226]. It has been suggested to conduct a series of simulations with different droplet sizes, while taking the contact angle value at $D = \infty$ in the θ

versus $1/D$ plot [223]. In **Figure 6-8**, we present the schematic diagrams of nC_8-H_2O-kerogen contact angle systems for various droplet sizes and the dependence of θ on D. As D decreases, θ decreases. Scocchi *et al.* [224] reported that as droplet becomes smaller, the cohesive forces for molecules near the contact line decreases, leading to a decrease in θ. Based on the $\cos\theta$ versus $1/D$ curve, by extrapolating, we obtain θ at $D=\infty$ limit [223, 225]. θ values for various D and that at $D=\infty$ limit are given in **Table 6-2**. In addition, we also test the kerogen surface morphology effect on θ by using another II-C kerogen substrate as shown in **Appendix E**. We note that this substrate is constructed by a similar annealing process but with a different geometrical size and slightly different surface morphology. Therefore, the drastic surface roughness effect [218] is not fully considered. We find that θ is not sensitive to the substrate in our study.

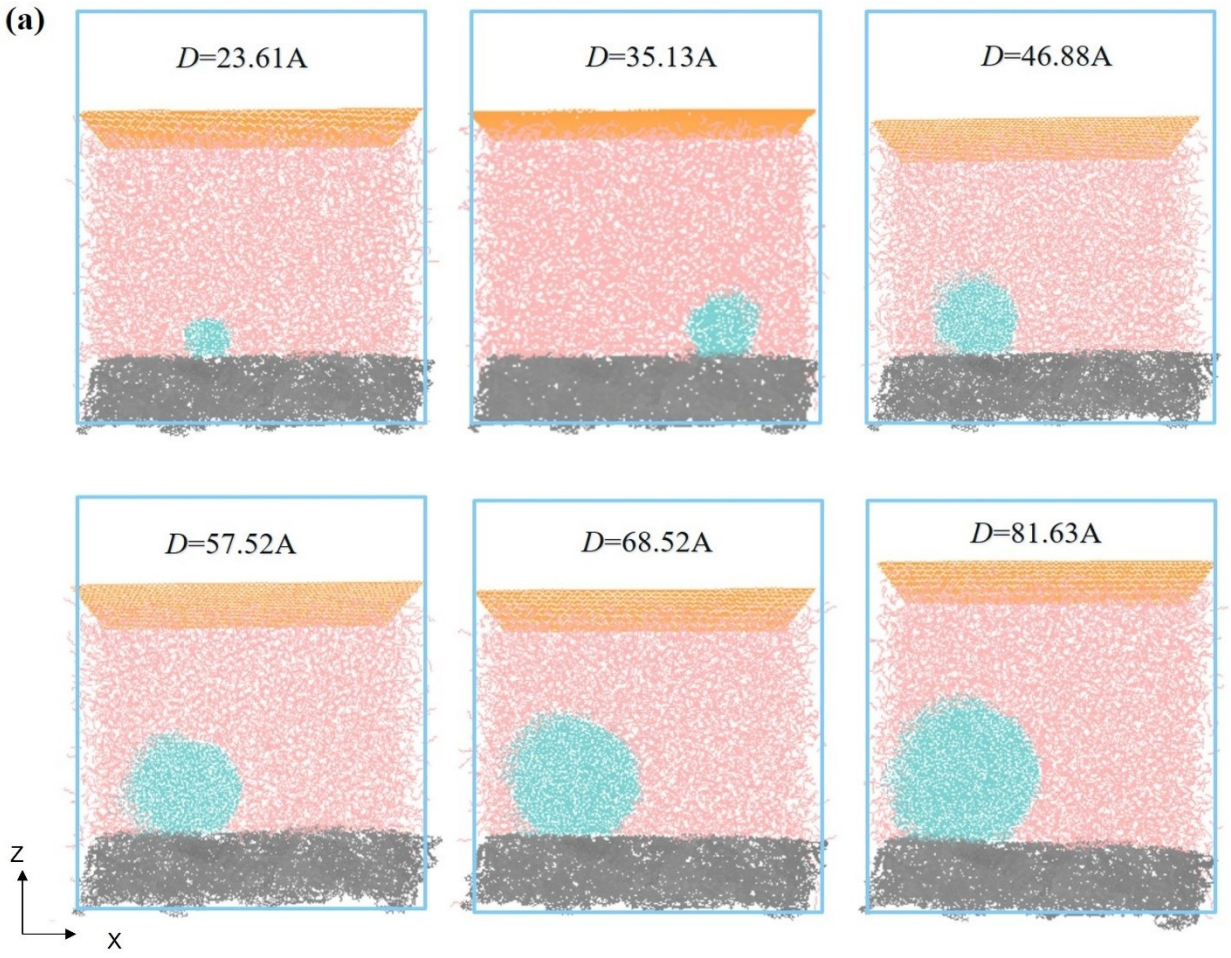
(a)
D=23.61A
D=35.13A
D=46.88A
D=57.52A
D=68.52A
D=81.63A
Z
X

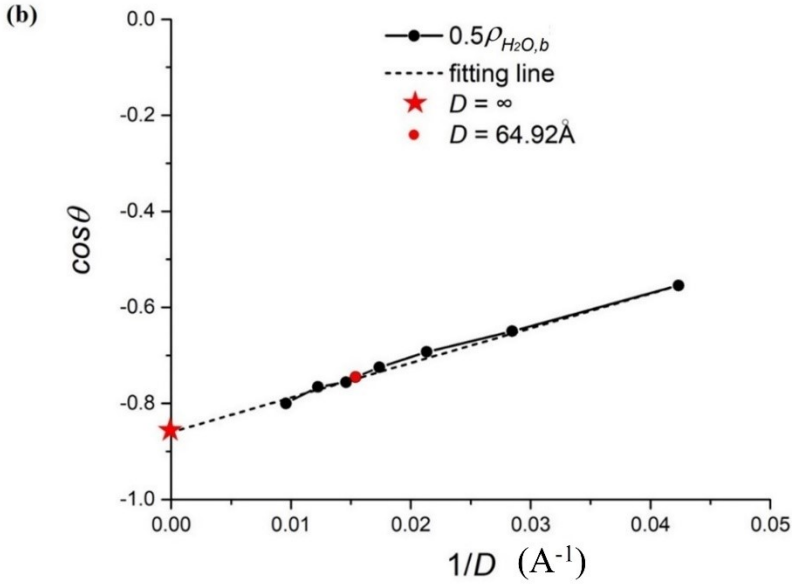
(b)
0.5ρH2O,b
fitting line
D = ∞
D = 64.92Å
cosθ
0.0
-0.2
-0.4
-0.6
-0.8
-1.0
0.00
0.01
0.02
0.03
0.04
0.05
1/D (A-1)

Figure 6-8. (a) Schematic diagrams of nC_8-H_2O-kerogen contact angle systems with various H_2O droplet sizes; (b) Dependence of θ on the H_2O droplet size at $T = 330$ K and $P = 300$ bar.

D **(A)**	**23.61**	**35.13**	**46.88**	**57.52**	**68.52**	**81.63**	**104.40**	∞
θ **(degree)**	**123.66**	**130.52**	**133.85**	**136.47**	**139.09**	**139.97**	**143.12**	**149.32**

Table 6-2. The effect of D on θ at 300 bar

6.3.3 nC8-H2O Interfacial Tension

The nC_8-H_2O IFT γ can be obtained from Kirkwood and Buff [227] as

$$\gamma = \frac{L_z}{2}\left(\langle P_{zz} \rangle - \frac{\langle P_{xx} \rangle + \langle P_{yy} \rangle}{2} \right), \tag{6.4}$$

where L_z is the simulation box size in the *z*-direction and $\langle P_{\alpha\alpha} \rangle$ is the ensemble average of normal pressure in the α-direction. In **Figure 6-9**, we depict the dependence of γ on P_z (*i.e.*, the pressure perpendicular to the nC_8-H_2O interface). We find that as P_z increases, γ increases, which is in line with experimental findings [228].

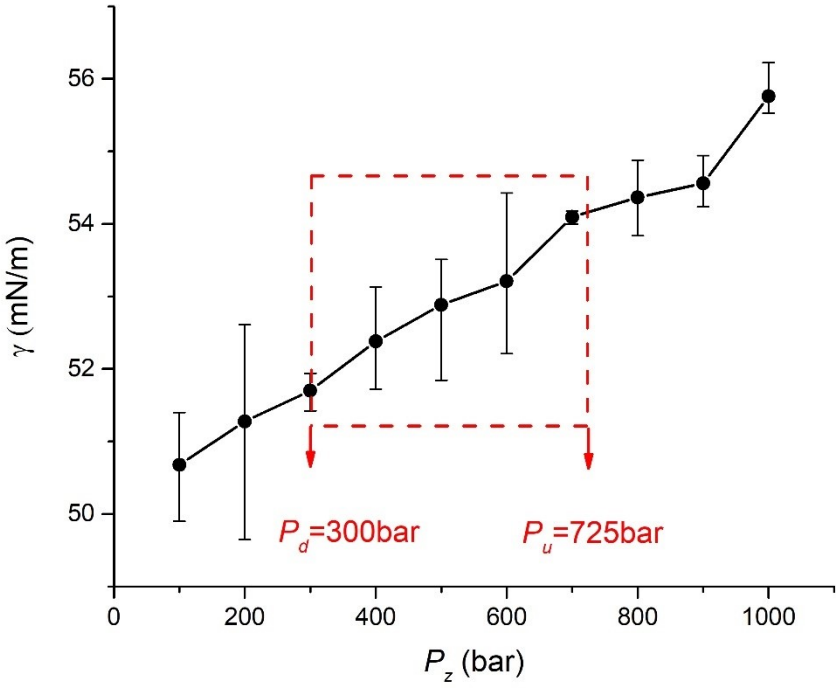

Figure 6-9. The dependence of nC8-H2O IFT on P_z.

6.3.4 Effective Pore Width

Helium adsorption method [192] has been widely used to obtain the effective pore volume of porous media from both experimental [3] and simulation aspects [192, 229]. Assuming that helium molecule is inert, which has a negligible adsorption on the pore surface, the overall helium uptake volume can be converted to obtain the effective pore volume as well as W_{eff} (assuming a certain pore geometry, such as slit geometry in this work) [192]. The corresponding effective pore width W_{eff} is given as

$$W_{eff} = N_{He} / \rho_{He,b} / d_y / \Delta x, \tag{6.5}$$

where N_{He} stands for the total helium number in the analysis region, $\rho_{He,b}$ presents the bulk number density of helium at 300 bar and 330 K, d_y stands for the kerogen dimension in the *y*-direction, and Δx stands for the length of the analysis region in the *x*-direction. Based on helium

adsorption method, $W_{eff} = 22.75$ A. However, as shown in **Figure 6-10 (a)**, there are helium adsorption layers on the kerogen surface, indicating a possible overestimation of W_{eff}.

Another method could be used to calculate W_{eff} is the geometric insertion method [230, 231]. After 10000 trials of finding the largest insertion sphere which include given random positions and tangent with the kerogen surface, the insertion sphere diameter size distribution (DSD) inside the kerogen pore throat is obtained as shown in **Figure 6-10 (b)**. According to DSD, W_{eff} can be given as,

$$W_{eff} = \int D_{LIS} \cdot f_{V,LIS} dD \tag{6.6}$$

where W_{LIS} stands for the diameter of the largest insertion sphere (LIS) and $f_{V,LIS}$ stands for the volume faction of this sphere in the cumulative DSD curve. Accordingly, $W_{eff} = 21.825$ A from the geometric insertion method, which is smaller than that obtained from the helium adsorption method.

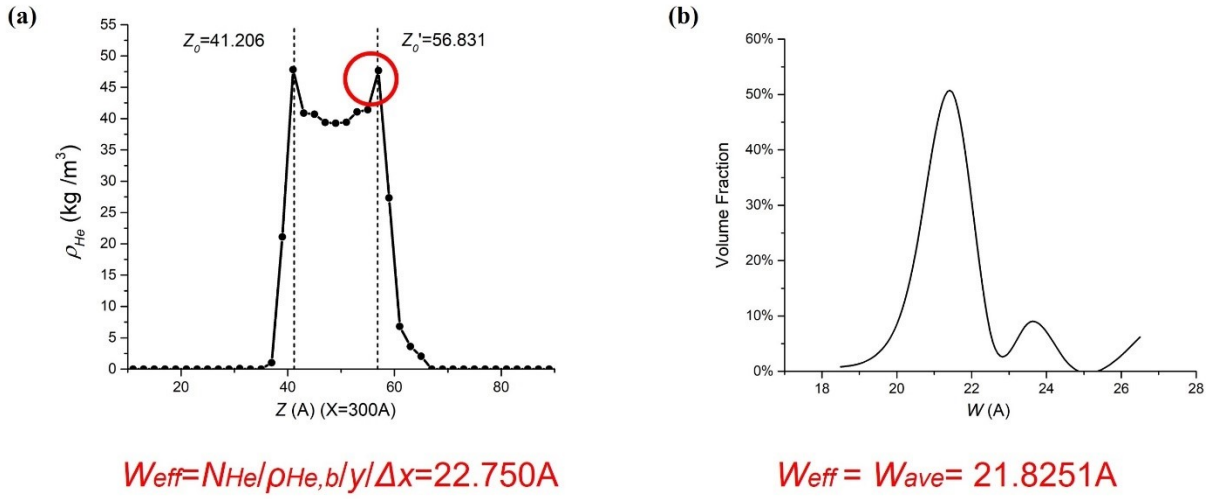

Figure 6-10. (a) Helium density profile at $X = 300$ A. (b) Insertion sphere diameter size distribution inside kerogen pore throat from geometric insertion method [193].

6.3.5 PB from MD v.s. Pcap from Y-L equation

Based on the θ, γ as well as W_{eff} obtained from previous three sections**,** respectively, P_{cap} from the Y-L equation can be readily obtained. For γ, the lowest and highest values in the pressure range of 300~725 bar are used to get the limits of P_{cap} as highlighted in **Figure 6-9**, where 300 bar and 725 bar are the values of P_d and P_u (we take the middle value for P_u which is between 720 and 730 bar) in MD simulation, respectively, when the breakthrough phenomenon takes place. The θ value at $D=\infty$ limit and 300 bar is used assuming that θ is independent of pressure. The W_{eff} values are from both helium adsorption and geometric insertion methods. Then, the P_{cap} range from the Y-L equation can be obtained as shown in **Eq. (6.1)**. The comparison between P_B from MD simulation and P_{cap} from the Y-L equation is shown in **Table 6-3**. Interestingly, P_{cap} from the Y-L equation shows an excellent agreement with P_B from MD simulations. Compared with the geometric insertion method, P_{cap} obtained by using helium adsorption method is underestimated.

Methods	**MD**	**Y-L (*D*= ∞)**	
	***P*_B**	***P*_{cap} (Helium adsorption)**	***P*_{cap} (Geometric insertion)**
P (bar)	**420 ~ 430**	**388.77~411.48**	**405.24~428.92**
Error*	**-**	**-5.85% ± 3.82%**	**-1.86% ± 3.98%**

*: The error is calculated based on the middle points of *P* ranges for P_B and P_{cap}; the error bars are calculated based on the maximum and minmum *P* values in ranges for P_B and P_{cap}.

Table 6-3. P_B from MD simulation and P_{cap} from the Y-L equation.

Comparing with a number of previous works, our study presents a few fresh views. In contrast to Wang *et al*. [31], in which the full atomistic descriptions of substrate are not considered, oil film always forms on a hydrophobic surface during breakthrough processes. By fully describing the atomistic details, we find that there is no oil film on the kerogen substrate which is oil-wet. It clearly indicates that the macroscopic properties (such as contact angle) may not fully capture microscopic phenomena (such as hydrogen bonding formation and thin film formation), which can drastically influence the prediction of capillary pressure in ultra-narrow pore throats. On the other hand, in separate works [27, 172, 173], MD simulations have shown that water film exists on hydrophilic substrates with full atomistic details. By taking into account the water thin film thickness, Fang *et al*. [27] found that the capillary pressure from the modified Y-L equation can provide an excellent agreement with the breakthrough pressure from MD simulations down to 4-nm mica pore throat, while showing a noticeable deviation in 2-nm mica pore throat. They argued that the deviation probably stems from the difference between C_1 and H_2O diffusivities. In addition, with the correction of water film thickness, the capillary pressures for 5.1-nm calcite [172] and 3-nm quartz [173] pore throats from the Y-L equation are still largely underestimated. All the substrates [27, 172, 173] they considered have a very ordered structure so that the water molecules in the film might have an ordered orientation [232]. The effect of substrate smoothness and crystallinity on two-phase displacement process is one intriguing question needs to be addressed.

While our simulation can provide important insights into the breakthrough pressure during oil-water two-phase displacement through ultra-narrow kerogen pore throats, there are a few notable limitations. First, in actual kerogen matrices, pore throats have varying degrees of surface roughness [218] and pore tortuosity [62], while in our work, we used a relatively-smooth kerogen

substrate with a simple slit geometry. One motivation for this selection is to provide a fair comparison against the prediction from the Y-L equation in which surface roughness and pore tortuosity are not considered. In addition, by using a simple geometry, we still observe that the intermolecular interactions and individual atomistic and molecular characteristics determine the local molecular configurations inside the kerogen pore throats which regulate the displacement process. Second, kerogen matrices consisting of its macromolecules have varying degree of flexibility which can deform under different pressure strains. While the kerogen flexibility has been considered in gas adsorption [233] and diffusion [234] studies, its effect on the oil-water two-phase displacement is not fully taken into account. Furthermore, we observe that a number of nC_8 molecules remain at the entrance of kerogen pore throats which might affect P_B. The quantities of these nC_8 molecules might be dependent on pressure difference (see **Figure 6-1 (b)**), kerogen substrate shape and its surface morphology. Besides, shale/tight oil is a hydrocarbon mixture containing polar components [235] while the underground water (either injected or connate) contains a large number of salt ions (so-called brine). The oil and water phase compositions and individual molecular characteristics might play an important role on θ and γ as well as the breakthrough procedure.

6.4 Conclusions

In this work, MD simulation is used to study nC_8 displacement by H_2O through ~2 nm kerogen (represented by Type II-C kerogen) pore throats. We find that when P_e is lower than P_B, H_2O phase is stuck at the entrance of kerogen pore throat, while the H_2O-nC_8-kerogen interface curvature is dependent on P_e. When $P_e > P_B$, the H_2O phase can pass through the ultra-narrow kerogen pore throat and displace the nC_8 phase. Although the Type II-C kerogen is generally nC_8-

wet based on H_2O-nC_8-kerogen contact angle calculations, H_2O has an excellent displacement efficiency thanks to the hydrogen bonding between H_2O and heteroatoms (such as O, N, and S) on kerogen surface. We also compared P_B and P_{cap} from the Y-L equation with θ and IFT obtained from separate MD simulations. Interestingly, P_{cap} from the widely used Y-L equation shows a good agreement with P_B obtained from MD simulations for the ~2 nm kerogen pore throat.

Collectively, our work indicates that intermolecular interactions as well as atomistic and molecular level characteristics play a dominant role in oil-water two-phase displacement through ultra-narrow pore throats. The fundamental understanding from this work has far-reaching impacts in numerical simulation on tight/shale oil exploitation and ultimate oil recovery estimation.

Acknowledgements

This research was enabled in part by support provided by Westgrid (www.westgrid.ca) and Compute Canada (www.computecanada.ca). The authors also greatly acknowledge a Discovery Grant from Natural Sciences and Engineering Research Council of Canada (NSERC RGPIN-2017-05080). As a part of the University of Alberta's Future Energy Systems research initiative, this research was made possible in part thanks to funding from the Canada First Research Excellence Fund.

CHAPTER 7 CONCLUSIONS, CONTRIBUTIONS AND RECOMMENDATIONS

7.1 Conclusions and Scientific Contributions to the Literature

In this dissertation, the phase behaviors of hydrocarbon mixtures in shale multi-scale structures are investigated through Density Functional Theory. The pore size effect, interplay between nanopores and connected fractures as well as the heterogeneous pore size distribution effect have been carefully studied during the real production process (CCE and CVD). The validity of conventional EOS-based methods has been accessed by comparing the phase diagrams and properties of hydrocarbon mixtures in Canonical Ensemble from Engineering Density Functional Theory and various EOS-based methods. On the other hand, the underlying mechanisms of the two-phase displacement process through ultra-narrow kerogen pore throat are investigated through Molecular Dynamic Simulation. The applicability of conventional Young-Laplace Equation for water-oil two-phase displacement process through nano-scale kerogen pore throat has been discussed. The main conclusions of this thesis are summarized as follows:

In **Chapter 2**, we use density functional theory (DFT) to study the effect of nanoconfinement on the hydrocarbon mixture bubble point pressure, by explicitly considering fluid-surface interaction and inhomogeneous density distribution in nanopores. We find that as system pressure decreases, while lighter components are continuously released from nanopores, heavier components accumulate within. The bubble point pressure of nanoconfined hydrocarbon mixtures is thus significantly suppressed from the bulk bubble point, to below the bulk dew point, in line with our previous experiments. When bulk fluids are in two-phase, the confined hydrocarbon fluids are in a single liquid-like phase. As pore size increases, the bubble point pressure of confined fluids increases and the hydrocarbon average density in nanopore approaches the liquid phase density in bulk when the bulk is in a two-phase region. For a finite volume bulk bath, we find that due to the competitive adsorption in nanopores, the bulk bubble point pressure increases in line with previous

experimental work. Our work demonstrates how mixture dynamics and nanopore-bulk partitioning influence phase behavior in nanoconfinement and enables the accurate estimation of hydrocarbon mixture bubble point pressure in shale nanopores.

In **Chapter 3**, we use density functional theory (DFT) to explicitly consider fluid-surface interactions, inhomogeneous density distributions in nanopores, volume partitioning in nanopores and connected macropores/natural fractures to study the complex multi-phase transitions of multi-component fluids in multi-scale volumes. We found that vapor-like and liquid-like phases can coexist in nanopores when pressure is between the bubble and dew point pressures of nanoconfined fluids, both of which are much lower than those of the originally injected hydrocarbon mixtures. As the volume ratio of bulk at the initial condition to pores decreases, both bubble and dew points in nanopores increase and the pore two-phase region expands. Within the pore two-phase region, both C_1 and C_3 are released from the nanopores to the bulk as pressure declines. Meanwhile, both liquid and vapor phases become denser as pressure drops. Only further decreasing pressure below the dew point of confined fluids, C_3 in nanopore can be recovered. Throughout the process, the bulk phase composition varies, which is in line with the field observation. Collectively, this work captures the coupled complexity of multi-component and multi-phase fluids in multiscale geometries that is inherent to shale reservoirs and provides a theoretical foundation for reservoir simulation, which is significant for accurate prediction of well productivity and ultimate oil recovery in shale reservoirs.

In **Chapter 4**, engineering density functional theory (DFT) is used to study phase behaviors of hydrocarbon mixtures in multi-scale nanoporous media with PSD effect during constant composition expansion (CCE) and constant volume depletion (CVD) processes. We found that under PSD effect, due to the chemical equilibrium between various nanopores and connected bulk

as well as competitive adsorption in nanopores, the interplay between nanopores and bulk region influences phase behaviors and properties of fluids in the multi-scale system. Phase transitions first occur in the bulk region, then the larger pores followed by the smaller pores. The bulk bubble point pressure increases as the volume ratio of the smaller pores in the system increases, while the bulk dew point decreases. When fluids in one specific pore begin to vaporize, in other pores, the heavier component would be adsorbed, while the lighter component would be released, which suppresses the phase transitions in the smaller pores because of the heavier component accumulation. The higher volume ratio of the smaller pores suppresses the heavier component production when pressure is below the bulk dew point.

In **Chapter 5**, we use engineering density functional theory (DFT) which can explicitly consider the inhomogeneous density distributions and fluid-surface interactions under nanoconfinement to compare with the EOS based models on hydrocarbon mixture phase behaviors in the canonical ensemble. We found that compared to the engineering DFT, due to the negligence of surface adsorption, EOS-based models drastically underestimate the molar densities of nanoconfined C_1-C_3 mixtures in the entire phase diagram. In 5-nm carbon slit pores, the underestimations in dewpoint density and bubble point density can be up to 90% and 50%, respectively. The critical temperature is overestimated for around 3% while the critical density is underestimated up to ~60%. Within the two-phase region, the EOS-based models significantly underestimate both the molar density and heavier component composition of vapor phase (up to ~80% and ~60%, respectively, in 5-nm carbon slit pores). This work underscores that adsorption layer caused by fluid-surface interaction plays a significant role on nanoconfined fluids phase behaviors in canonical ensemble. Adding adsorption layer effect in EOS-based modeling is imperative for vapor phase properties and critical density calculation in the canonical ensemble.

In **Chapter 6**, we use molecular dynamics (MD) simulations to investigate oil (represented by n-octane) displacement by water through 2-nm kerogen (represented by Type II-C kerogen) pore throat. We find that although the Type II-C kerogen is generally oil-wet, water has an excellent displacement efficiency without oil film on the substrate thanks to the hydrogen bonding formed between water and heteroatoms (such as O, N, and S) on kerogen surface. Unlike previous studies, the capillary pressure from the widely used Young-Laplace equation shows a good agreement with the breakthrough pressure obtained from MD simulations for the ~2 nm kerogen pore throat. Our work indicates that explicitly considering intermolecular interactions as well as atomistic and molecular level characteristics is imperative to study two-phase displacement process through ultra-narrow pore throats.

7.2 Suggested Future Works

7.2.1 Hydrocarbon phase behaviors

Based on our works, the surface adsorption, volume partition, as well as heterogeneous pore size distribution, can play important roles in the phase behaviors of hydrocarbon mixtures in shale reservoirs. While EOS-based models have been combined into reservoir simulators, updating EOS-based models by implementing surface adsorption, volume partition as well as heterogeneous pore size distribution effects are of significant meaning and could be the potential directions for future works.

7.2.2 water-driven flow

For two-phase displacement process, we used a relatively-smooth kerogen substrate with a simple slit geometry for a relatively fair comparison against the prediction from the Y-L equation. However, pore throats have varying degrees of surface roughness and pore tortuosity in actual kerogen matrices. Second, kerogen matrices consisting of its macromolecules have a varying

degree of flexibility which can deform under different pressure strains, its effect on the oil-water two-phase displacement is not fully taken into account in our work. Furthermore, we used octane to stand for oil phase and pure water as water phase. However, shale/tight oil is a hydrocarbon mixture containing polar components while the underground water (either injected or connate) contains a large number of salt ions (so-called brine). As a result, studying the effect of surface roughness, pore tortuosity, kerogen flexibility, polar component and salinity on the breakthrough procedure could be the potential future works.

Appendix A

A1 Engineering Density Functional Theory

At equilibrium, chemical potentials μ_i of component i in the nanopore and bulk region are the same. The equilibrium properties in the nanopore can be obtained by the minimization of grand potential functional $\Omega\left[\{\rho_i(\mathbf{r})\}\right]$, which is the functional of density distributions $\{\rho_i(\mathbf{r})\}$ and Helmholtz free energy functional $F\left[\{\rho_i(\mathbf{r})\}\right]$[158],

$$\Omega\left[\{\rho_i(\mathbf{r})\}\right] = F\left[\{\rho_i(\mathbf{r})\}\right] + \sum_i \int \rho_i(\mathbf{r})\left[\Psi_i(\mathbf{r}) - \mu_i\right] d\mathbf{r}, \tag{A-1}$$

where $d\mathbf{r}$ is differential volume, and $\rho_i(\mathbf{r})$ is the density distribution of component i at position $\mathbf{r}$; $\Psi_i(\mathbf{r})$ is the external potential of the component i at position $\mathbf{r}$. μ_i is chemical potential of component i in pore which is equal to that in bulk obtained from the PR-EOS.

At equilibrium, the grand potential functional is minimum,

$$\frac{\delta\Omega\left[\{\rho_i(\mathbf{r})\}\right]}{\delta\rho_i(\mathbf{r})} = 0. \tag{A-2}$$

In **Eq.(A-2)**, the symbol δ represents the functional derivative.

The Helmholtz free energy $F\left[\{\rho_i(\mathbf{r})\}\right]$ is composed by ideal-gas term $F^{id}\left[\{\rho_i(\mathbf{r})\}\right]$ without intermolecular interactions and excess term $F^{ex}\left[\{\rho_i(\mathbf{r})\}\right]$ accounting for the intermolecular interactions,

$$F\left[\{\rho_i(\mathbf{r})\}\right] = F^{id}\left[\{\rho_i(\mathbf{r})\}\right] + F^{ex}\left[\{\rho_i(\mathbf{r})\}\right]. \tag{A-3}$$

The ideal-gas term is known as,

$$\beta F^{id}\left[\{\rho_i(\mathbf{r})\}\right] = \sum_i \int d\mathbf{r}\rho_i(\mathbf{r})\left[\ln\rho_i(\mathbf{r}) - 1\right], \tag{A-4}$$

where $\beta = 1/(k_B T)$; k_B and T represent Boltzmann constant and the absolute temperature, respectively.

Accurate representation of the excess Helmholtz free energy $F^{ex}\left[\{\rho_i(\mathbf{r})\}\right]$ is key to the DFT calculations. As in previous works [5, 56], The excess term $F^{ex}\left[\{\rho_i(\mathbf{r})\}\right]$ is given as,

$$F_{ph}^{ex}\left[\{\rho_i(\mathbf{r})\}\right] = \int d\mathbf{r}\phi_{ph}\left[\rho_i(\mathbf{r})\right], \tag{A-5}$$

where $\phi_{ph}\left[\rho_i(\mathbf{r})\right]$ is the reduced excess Helmholtz energy density functional. $\phi_{ph}\left[\rho_i(\mathbf{r})\right]$ could be subdivided into two parts: the first part is the extended PR-EOS with weighted density approximation (WDA) to account for inhomogeneous conditions [153]. The second part is using quadratic density expansion (QDE) to supplement the long-range interactions [154, 236].

In our engineering DFT, we ignore molecules structures so that they could be considered as spherical particles to adopt the WDA method. We use $n_{0i}(\mathbf{r})$ and $n_{3i}(\mathbf{r})$ functions from Rosenfeld's fundamental measure theory [153] to mathematically represent the "geometrical properties" of molecules and account interactions in inhomogeneous conditions,

$$n_{0i}(\mathbf{r}) = \frac{1}{\pi\sigma_i^2}\int d\mathbf{r}'\rho_i(\mathbf{r}')\delta\left(\frac{\sigma_i}{2} - |\mathbf{r}-\mathbf{r}'|\right),$$

$$n_{3i}(\mathbf{r}) = \int d\mathbf{r}'\rho_k(\mathbf{r}')\theta\left(\frac{\sigma_i}{2} - |\mathbf{r}-\mathbf{r}'|\right), \tag{A-6}$$

where $\delta(\mathbf{r})$ is the Dirac delta function and $\theta(\mathbf{r})$ is the Heaviside step function. σ_i is the "effective diameter" of component i. As a result, the reduced excess Helmholtz $\phi_{ph}\left[\{\rho_i(\mathbf{r})\}\right]$ extended by WDA is,

$$\phi_{ph}\left[\left\{\rho_i(\mathbf{r})\right\}\right]=\phi_{ph}\left[\left\{n_{\alpha i}(\mathbf{r})\right\}\right]$$
$$=-n_0\ln\left(1-4n_3\right)-\frac{\sum_{j,k}n_{0j}n_{0k}a_{jk}}{8\sqrt{2}n_3k_BT}\ln\left[\frac{1+4\left(1+\sqrt{2}\right)n_3}{1+4\left(1-\sqrt{2}\right)n_3}\right], \tag{A-7}$$

where $n_0=\sum_i n_{0i}$, $n_3=\sum_i n_{3i}$; $a_{jk}=\sqrt{a_ja_k}\left(1-k_{jk}\right)$ and a_i represents energy parameter of component i; k_{jk} is the binary interaction coefficient (BIC) between components j and k.

WDA could be used to describe the short-range characteristic of repulsions and partially represent long-range intermolecular attractions. To fully include the effect of long-range attractions, the second part of the reduced excess Helmholtz is supplemented by the QDE potential expansion [154, 236].

$$\beta F_{pe}^{ex}=-\frac{1}{4}\sum_{i,j}\iint d\mathbf{r}d\mathbf{r}'\beta u_{ij}^{pe}\left(\left|\mathbf{r}-\mathbf{r}'\right|\right)\left[\rho_i(\mathbf{r})-\rho_i(\mathbf{r}')\right]\times\left[\rho_j(\mathbf{r})-\rho_j(\mathbf{r}')\right], \tag{A-8}$$

where the pair potential $u_{ij}^{pe}(r)$ is modeled by the attraction part of Lennard-Jones potential,

$$u_{ij}^{pe}(r)=\begin{cases}0, & r<\sigma_{ij}\\ -\varepsilon_{ij}^{pe}\left(\dfrac{\sigma_{ij}}{r}\right)^6, & r\geq\sigma_{ij}\end{cases}, \tag{A-9}$$

where ε_{ij}^{pe} and σ_{ij} are the potential expansion parameter and cross molecular diameter between components i and j . In this work, we use the simple combing rules to calculate ε_{ij}^{pe} and σ_{ij}, i.e. $\varepsilon_{ij}^{pe}=\sqrt{\varepsilon_i^{pe}\varepsilon_j^{pe}}$, $\sigma_{ij}=\left(\sigma_i+\sigma_j\right)/2$.

With an appropriate expression for excess Helmholtz free energy functional $F^{ex}\left[\left\{\rho_i(\mathbf{r})\right\}\right]$, the minimization of grand potential functional yields the Euler-Lagrange equation [56],

$$\rho_i(\mathbf{r})=\exp\left[\beta\mu_i-\beta\varphi_i(\mathbf{r})-\delta\beta F^{ex}\left[\left\{\rho_i(\mathbf{r})\right\}\right]/\delta\rho_i(\mathbf{r})\right], \tag{A-10}$$

where $\beta = 1/(k_B T)$, k_B is the Boltzmann constant and T is the absolute temperature. $\rho_i(\mathbf{r})$ is solved by the Picard iteration method [237].

Accurate representation of the excess Helmholtz free energy $F^{ex}\left[\{\rho_i(\mathbf{r})\}\right]$ is key to the DFT calculations. As in previous works [5, 56], $F^{ex}\left[\{\rho_i(\mathbf{r})\}\right]$ are subdivided into two parts: the first part is to extend the PR-EOS to inhomogeneous conditions by using the weighted density approximation (WDA) [153]; the second part is to use the quadratic density expansion (QDE) to account for the long-range intermolecular attractions [154, 236]. More details about $F^{ex}\left[\{\rho_i(\mathbf{r})\}\right]$ can be referred to the work by Li and Firoozabadi [156].

As in the PR-EOS [238], we use the volume translation to correct the equilibrium density distribution obtained from Eq.(A-10). The PR-EOS parameters are given in **Table A-1**. The binary interaction coefficient between C_1 and C_3 is fixed as 0.006, which is obtained by fitting with experimental data [48].

In a carbon-slit pore, density distributions only vary in the z direction perpendicular to the solid surfaces, i.e., $\rho_i(\mathbf{r}) = \rho_i(z)$. The fluid-surface interaction φ_{wi} is given by the 10-4-3 Steele potentials [58],

$$\varphi_{wi}(z) = 2\pi\rho_w\varepsilon_{wi}\sigma_{wi}^2\Delta\left[\frac{2}{5}\left(\frac{\sigma_{wi}}{z}\right)^{10} - \left(\frac{\sigma_{wi}}{z}\right)^4 - \frac{\sigma_{wi}^4}{3\Delta(0.61\Delta + z)^3}\right], \tag{A-11}$$

where $\varepsilon_{wi} = \sqrt{\varepsilon_w\varepsilon_i}$, $\sigma_{wi} = \frac{1}{2}(\sigma_w + \sigma_i)$, $\sigma_w = 0.34$ nm, $\rho_w = 114$ nm^{-3}, $\varepsilon_w / k_B = 28$ K, and $\Delta = 0.335$ nm, respectively. Similar to our previous works [58, 239], for C_1, we use one CH_4-wall interaction, while for C_3, we use the sum of two CH_3-wall and one CH_2-wall interactions. We use

the modified Buckingham exponential-6 intermolecular potential to describe the energy and size parameters of methyl group (-CH_3), methylene group (-CH_2-), and CH_4. This force field combined with united atom model has shown an excellent agreement with experimental data on interfacial tensions of various hydrocarbons [240] and GCMC simulations on the phase behavior of nanoconfined hydrocarbons [5, 58]. The parameters σ_i and ε_i are 0.3679 nm and 129.63 K, respectively, for -CH_3 group, 0.4 nm and 73.5 K, respectively, for -CH_2- group, and 0.373 nm and 160.3 K, respectively, for CH_4. The external potential Ψ_i in a slit pore is given as

$$\Psi_i(z) = \varphi_{wi}(z) + \varphi_{wi}(W - z). \tag{A-12}$$

The average density of component i in nanopores $\rho_{i,p}$ is given as,

$$\rho_{i,p} = \frac{\int_0^W \rho_i(z)\,dz}{W_{eff}}, \tag{A-13}$$

where $W_{eff} = W - \sigma_w$.

Table A1. Critical temperature T_c , critical pressure P_c, acentric factor ω, molar weight M_w, volume shift parameter *VSP*, and attraction energy parameter ε_g in the QDE [156].

Component	T_c (K)	P_c (bar)	ω	M_w (g/mol)	*VSP*	ε_g / k_B (K)
C_1	190.56	45.99	0.011	16.04	-0.154	1178
C_3	369.83	42.48	0.153	44.1	-0.08501	1866

Figure A1. $P-T$ diagram of bulk C_1-C_3 mixtures of $y_{C_1,b} / y_{C_3,b} = 0.2/0.8$ from the PR-EOS and the bulk pressure path in our IBV calculation.

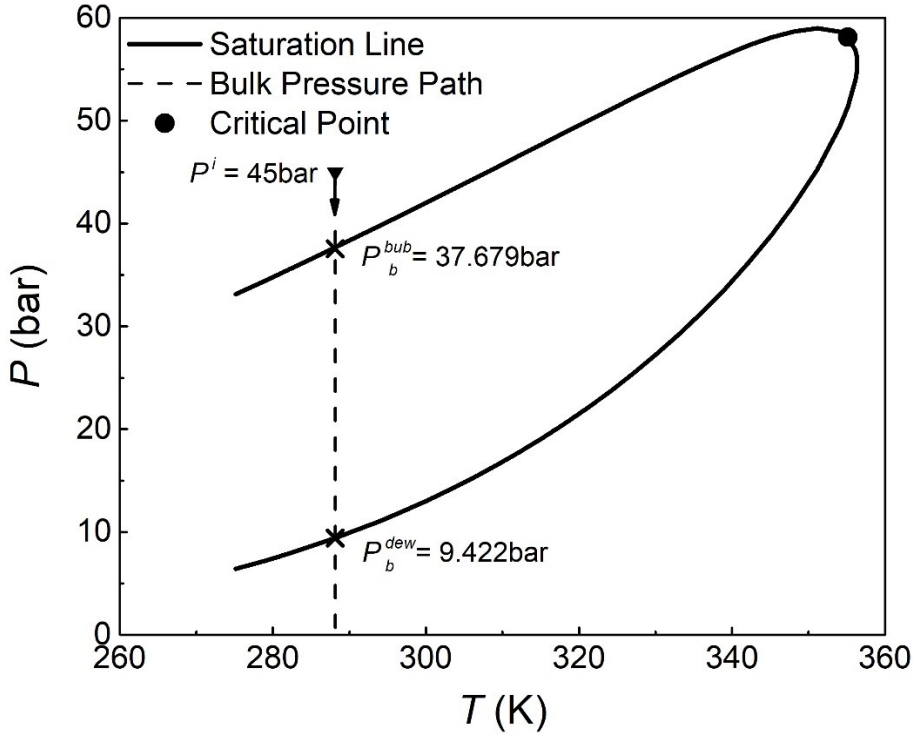

Figure A2. (a) GP from pressure increasing/decreasing branches in nanopores of $W = 5$ nm at 288.15K. (b) For clarity, we depict the GP up to P_b^{dew} .

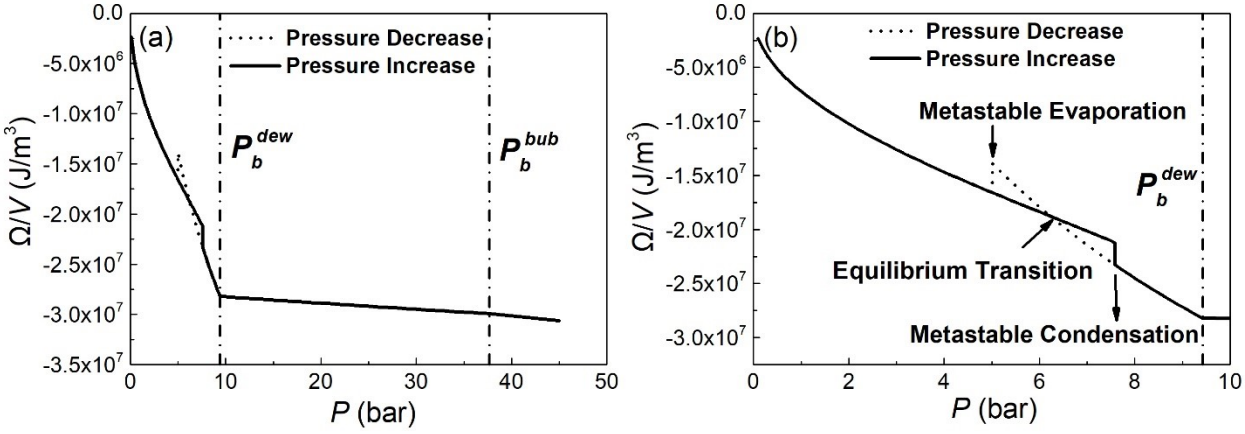

Figure A3. The pressure-composition diagram of C_1-C_3 mixtures from the PR-EOS at $T = 288.15$ K. For clarity, we also present the range of trial $x_{C_3,b}$ calculations at (a) $P^i = 45$ bar; (b) $P < P^i$ bar.

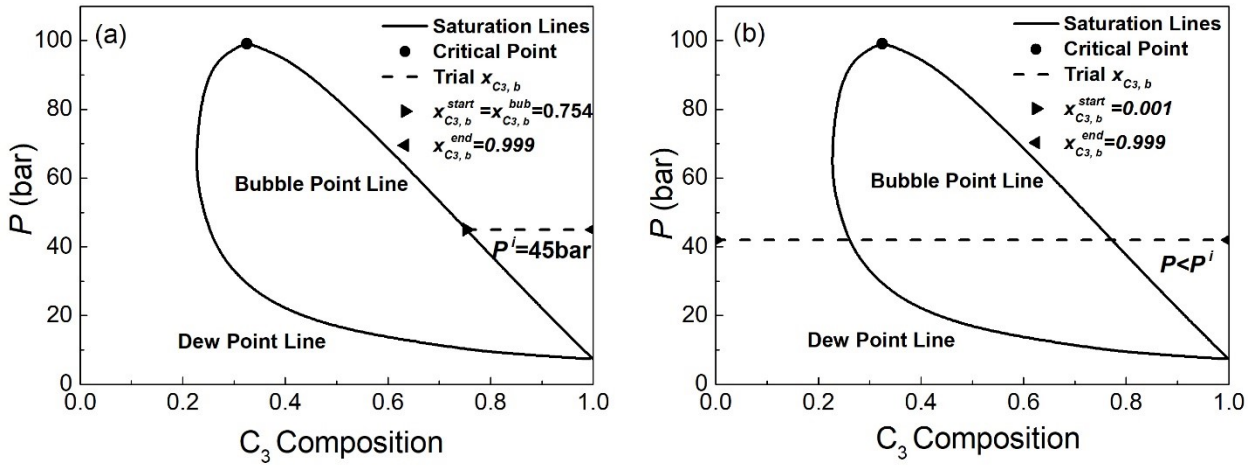

Figure A4. The $V_b - x_{C_3,b}$ plots for hysteresis parts from C_1 and C_3 branches at (a) $P = 42$ bar; (b) $P = 38.249$ bar; (c) $P = 25$ bar; (d) $P = 9.677$ bar at $T = 288.15$ K for $V_b^i / V_p = 10$ and $W = 5$ nm. The solid and dotted lines represent $x_{C_3,b}$ increasing and decreasing processes, respectively; the red and blue lines depict C_1 and C_3 branches, respectively.

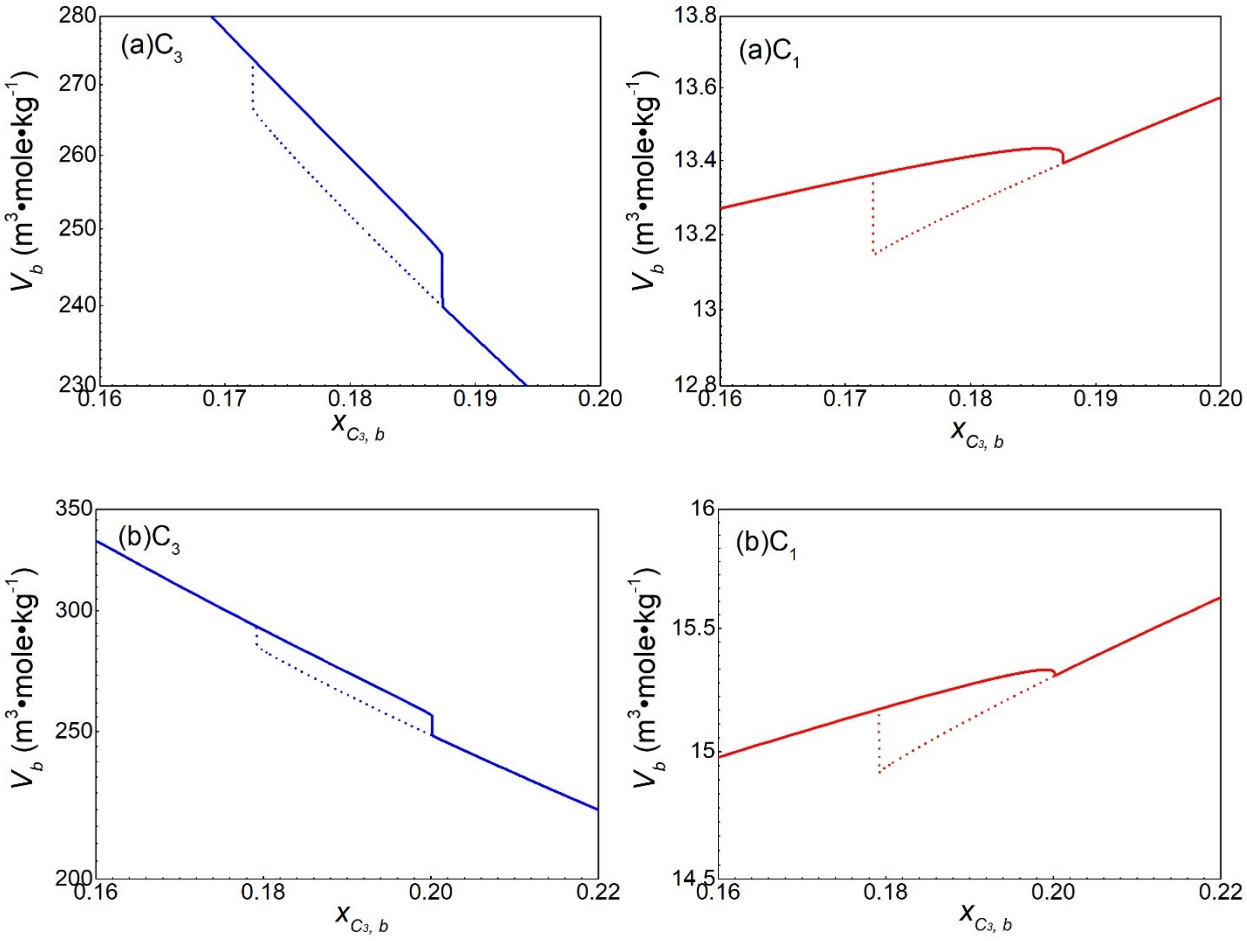

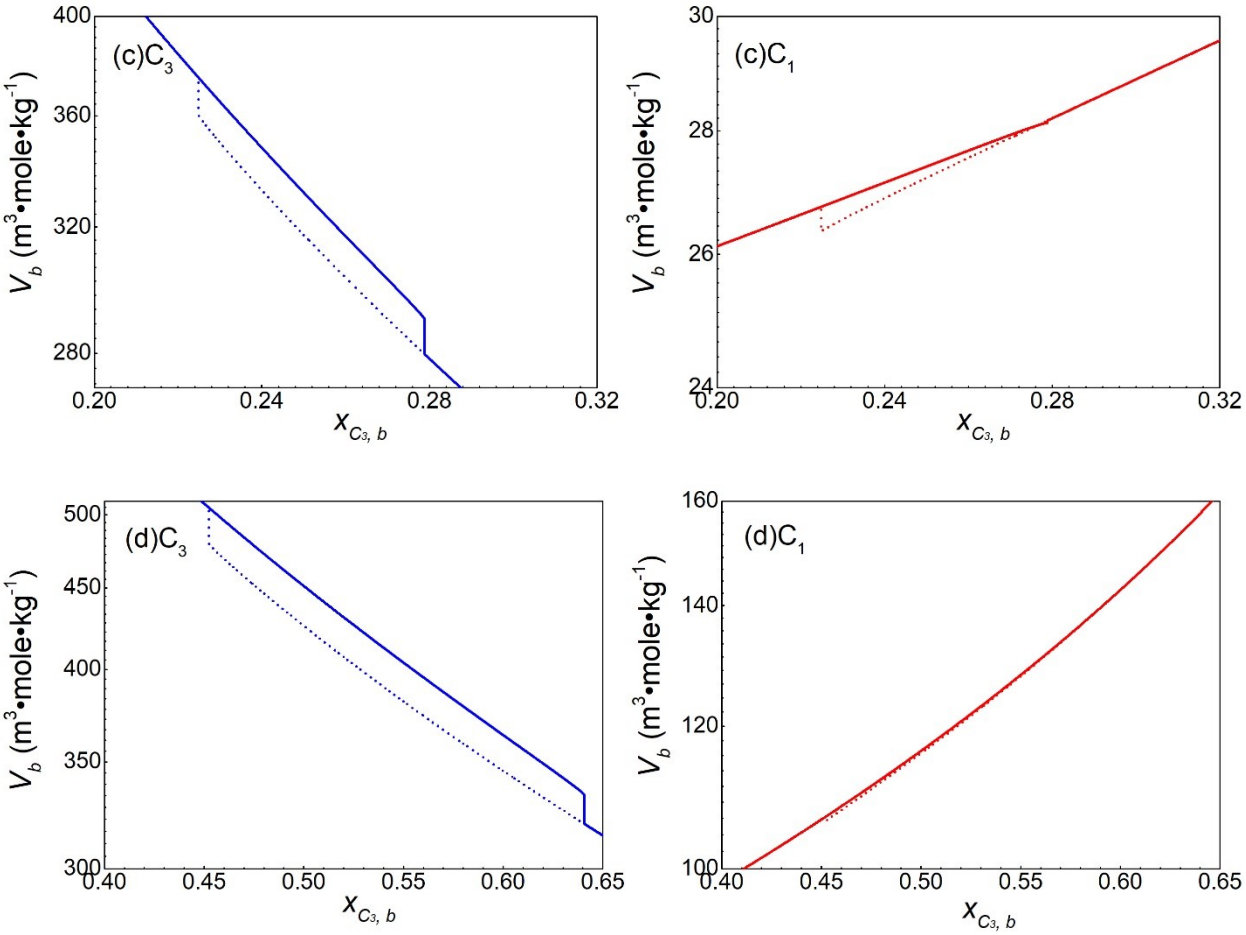
(c)C3
(c)C1
(d)C3
(d)C1
Vb (m3•mole•kg-1)
xC3, b

Figure A5. The instantaneous $P-T$ diagrams of the equilibrium C_1-C_3 mixtures in the bulk region at various pressures and $T = 288.15$ K for $V_b^i / V_p = 10$ and $W = 5$ nm. The symbols depict the corresponding pressures and lines represent the saturation lines at given pressures.

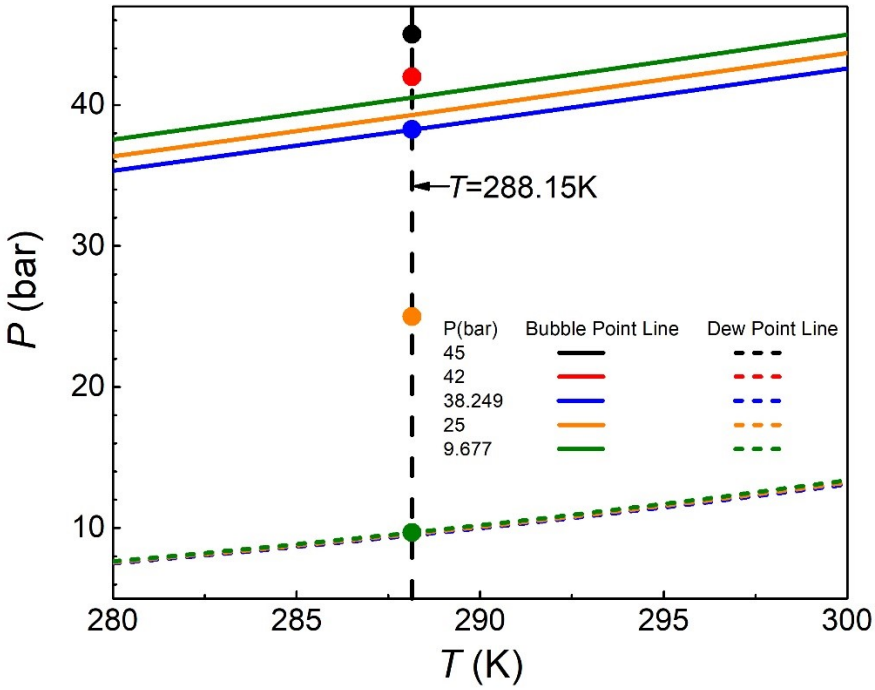

Appendix B

B1: Calculation Details

For $V_b - X_{C_3,b}$ plots shown in **Figs. 3.4** and **3.5**, for given P and T, trial C_3 composition in the bulk region $x_{C_3,b}$ can be divided into three different regions corresponding to liquid phase region, vapor-liquid coexist region, vapor phase region for the bulk hydrocarbon mixtures. Since the hysteresis region can only happen within the bulk vapor phase region as illustrated in our previous work [8], for trial C_3 composition in the bulk region $x_{C_3,b}$ which corresponds to the liquid phase region and vapor-liquid coexist region of bulk fluids, the average densities of component i in bulk, $\rho_{i,b}$ and nanopores, $\rho_{i,p}$ are obtained from the PR-EOS and DFT, respectively. Note that in the vapor-liquid coexistence region of the bulk fluids, we use the liquid phase chemical potentials from the PR-EOS to calculate fluid properties in nanopore. $\rho_{i,b}$ in this region stand for the average density of component i in bulk and are given as

$$\rho_{i,b} = \rho_{i,b(L)}\left(\frac{1}{1+V_{b(V)}/V_{b(L)}}\right) + \rho_{i,b(V)}\left(\frac{V_{b(V)}/V_{b(L)}}{1+V_{b(V)}/V_{b(L)}}\right), \quad i = C_1, C_3 , \tag{B-1}$$

$V_{b(V)}/V_{b(L)}$ can be obtained from PR-EOS.

For $x_{C_3,b}$ corresponding to the vapor phase region of bulk fluids, we use the GP minimum branch to represent the hydrocarbon mixture behavior within the hysteresis zone as illustrated in part **a)** of **Methods** section. Same as the liquid phase and vapor-liquid coexistence region of bulk fluids, the average densities of component i in bulk, $\rho_{i,b}$ and nanopores, $\rho_{i,p}$ along the GP minimum branch are obtained from the PR-EOS and DFT, respectively.

By varying $x_{C_3,b}$, we could form the $V_b - x_{C_3,b}$ plots as shown in **Figs. 3-4** and **3-5** by using

$$V_b = \left(N_i - \rho_{i,p} V_p \right) / \rho_{i,b}, \quad i = C_1, C_3 \,. \tag{B-2}$$

The intersections between two $V_b - x_{C_3,b}$ curves from C_1 and C_3 stand for the equilibrium $\{y_{i,b}\}$ as the dotted lines shown in **Figs. 3-4** and **3-5**.

Appendix C

C1. The Modified Buckingham Exponential-6 Intermolecular Potential

Similar to our previous works [12, 13], for C_1, we use one CH_4-wall interaction, while for C_3, we use the sum of two CH_3-wall and one CH_2-wall interactions. We use the modified Buckingham exponential-6 intermolecular potential to describe the energy and size parameters of methyl group (-CH_3), methylene group (-CH_2-), and CH_4. This force field combined with united atom model has shown an excellent agreement with experimental data on interfacial tensions of various hydrocarbons [14] and GCMC simulations on the phase behavior of nanoconfined hydrocarbons [8, 13]. The parameters σ_i and ε_i are shown in **Table C1**.

Table C1. The energy and size parameters of methyl group (-CH_3), methylene group (-CH_2-), and CH_4 in the modified Buckingham exponential-6 intermolecular potential.

Parameters	σ_i (nm)	ε_i (K)
-CH_3	0.3679	129.63
-CH_2-	0.4	73.5
CH_4	0.373	160.3

Figure C1. The material balance calculation procedure for CCE process.

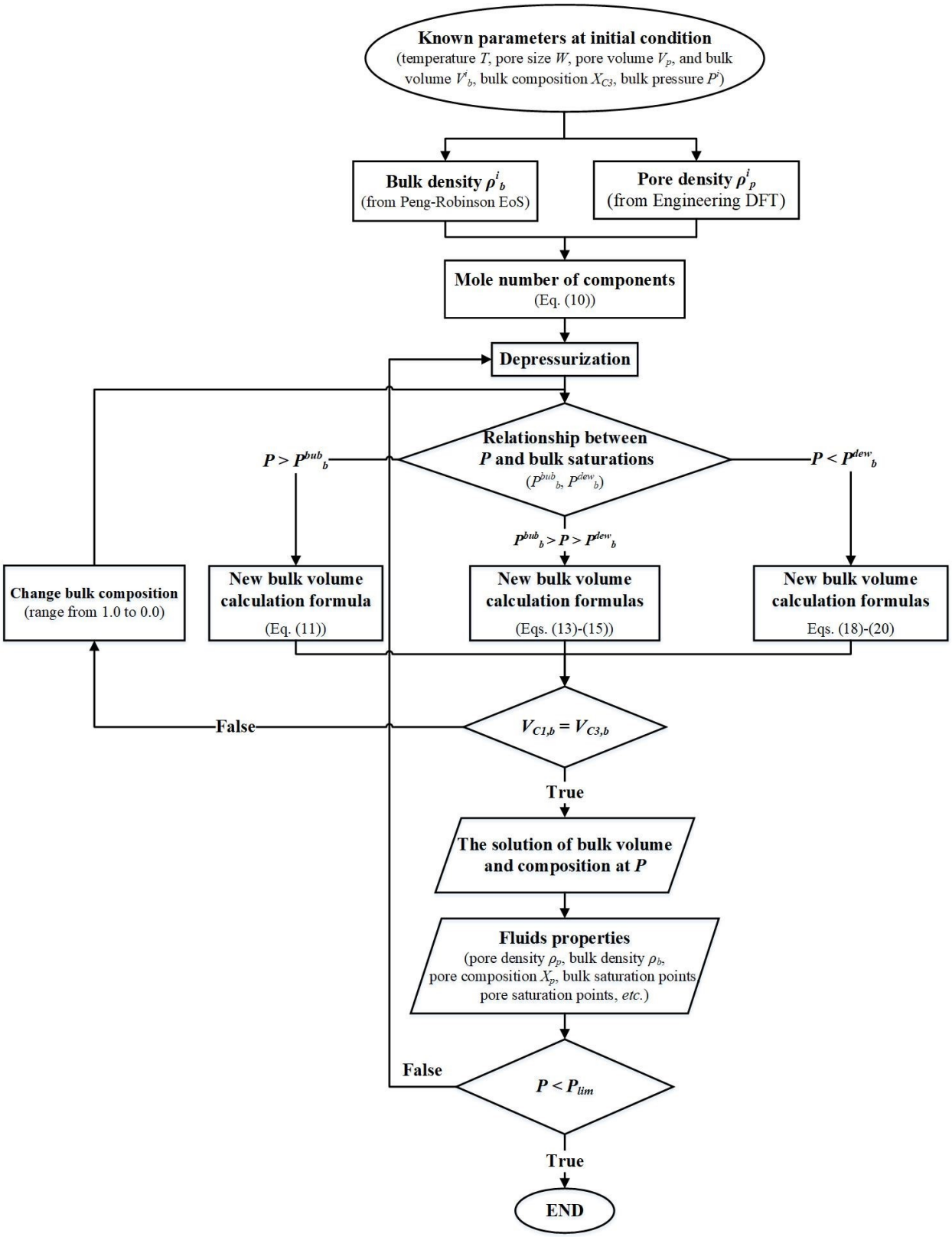

Figure C2. The material balance calculation procedure for CVD process.

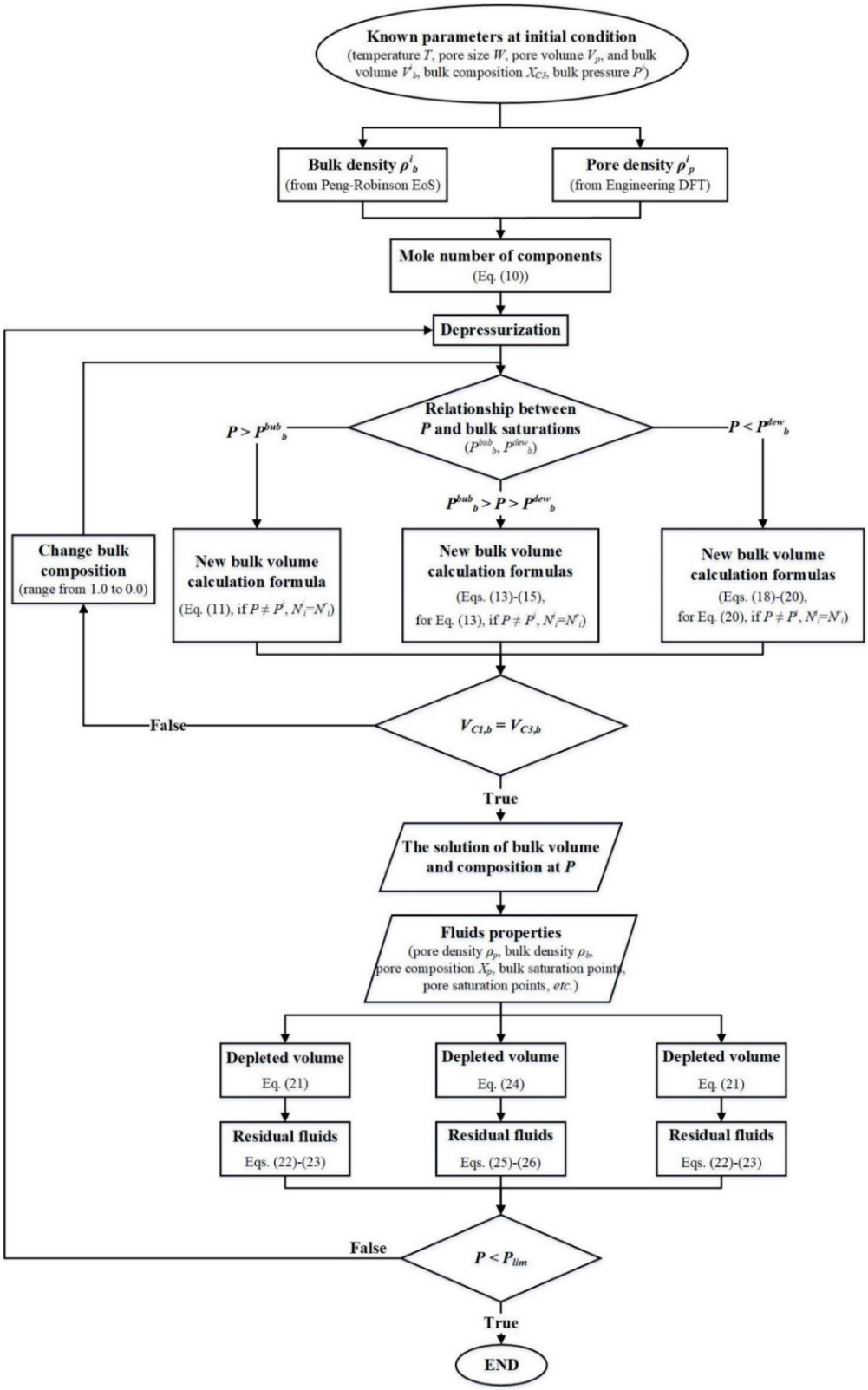

Figure C3. $V_b - X_{C_3,b}$ plots from C_1 (red lines) and C_3 (blue lines) for $V_{5\text{nm}} : V_{10\text{nm}} : V_b^i = 0.5 : 0.5 : 1$ when $P \geq P_b^{dew}$ during the CCE process at 288.15 K. (a) $P > P_b^{bub}$ ($P = 44$ bar); (b) $P = P_b^{bub}$ ($P_b^{bub} = 37.731$ bar); (c) $P_b^{bub} > P > P_b^{dew}$ ($P = 20$ bar); (d) $P = P_b^{dew}$ ($P_b^{dew} = 11.723$ bar).

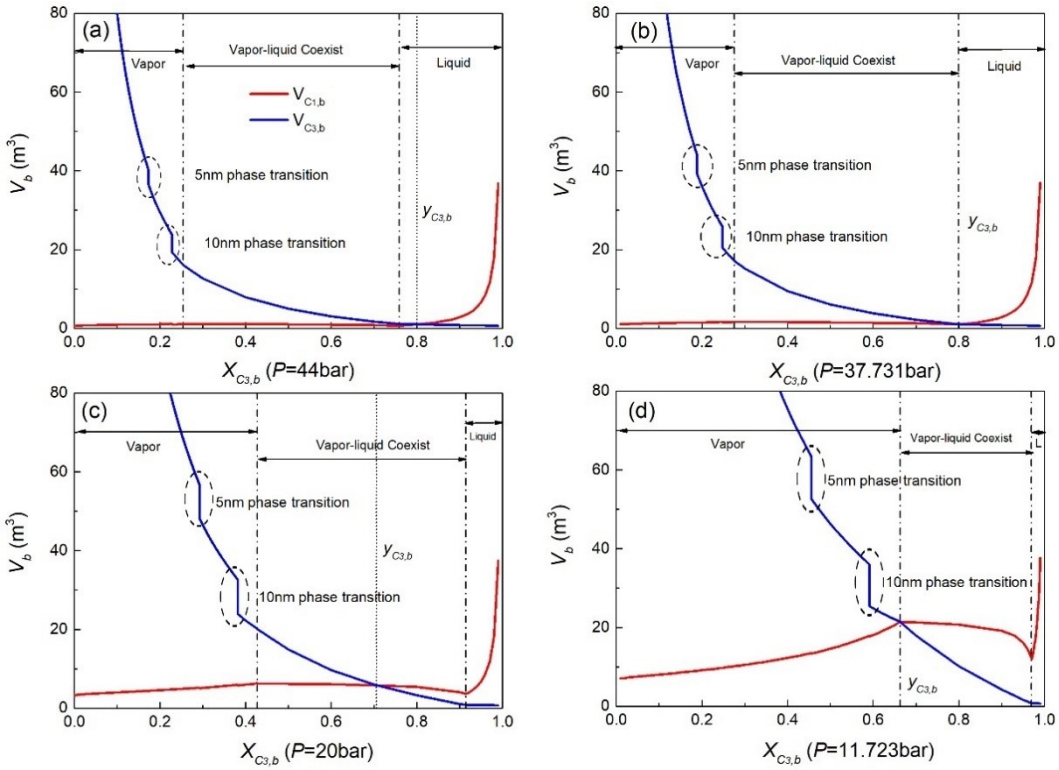

Figure C4. $V_b - X_{C_3,b}$ plots from C_1 (red lines) and C_3 (blue lines) for $V_{5\text{nm}} : V_{10\text{nm}} : V_b^i = 0.5 : 0.5 : 1$ when $P < P_b^{dew}$ during the CCE process at 288.15 K. (a) $P_b^{dew} > P > P_{10\text{nm}}^{bub}$ ($P = 11$ bar); (b) $P = P_{10\text{nm}}^{bub}$ ($P_b^{bub} = 10.2$ bar); (c) $P_{10\text{nm}}^{bub} > P > P_{10\text{nm}}^{dew}$ ($P = 10$ bar); (d) $P = P_{10\text{nm}}^{dew}$ ($P_{10\text{nm}}^{dew} = 9.13$ bar); (e) $P_{10\text{nm}}^{dew} > P > P_{5\text{nm}}^{bub}$ ($P = 8.5$ bar); (f) $P = P_{5\text{nm}}^{bub}$ ($P_{5\text{nm}}^{bub} = 6.7$ bar); (c) $P_{5\text{nm}}^{bub} > P > P_{5\text{nm}}^{dew}$ ($P = 6.5$ bar); (d) $P = P_{5\text{nm}}^{dew}$ ($P_{5\text{nm}}^{dew} = 6.39$ bar).

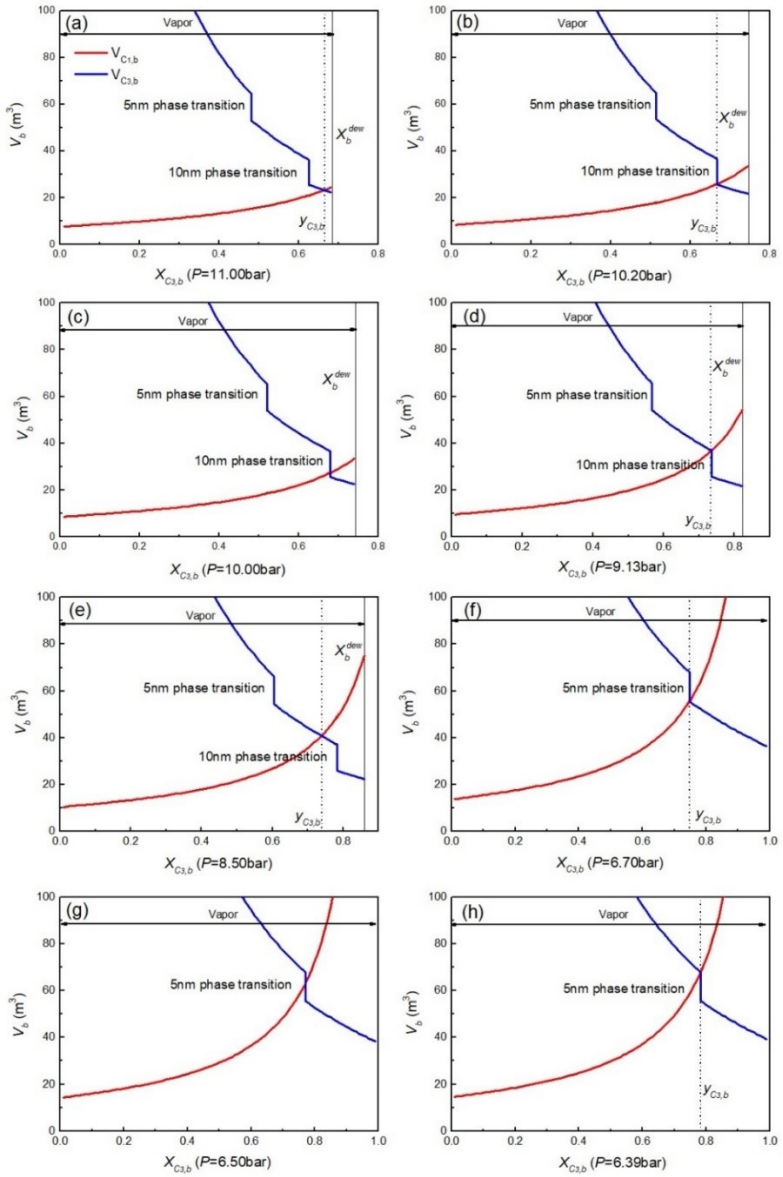

Figure C5. Ratio of molar percentage of C_1 in bulk to that in total system for Case A, B, and C during the CCE process. The open circles represent P_b^{bub}, the solid circles represent P_b^{dew}, the open squares represent $P_{10\text{nm}}^{bub}$, the solid squares represent $P_{10\text{nm}}^{dew}$, the open triangles represent $P_{5\text{nm}}^{bub}$, and the solid triangles represent $P_{5\text{nm}}^{dew}$.

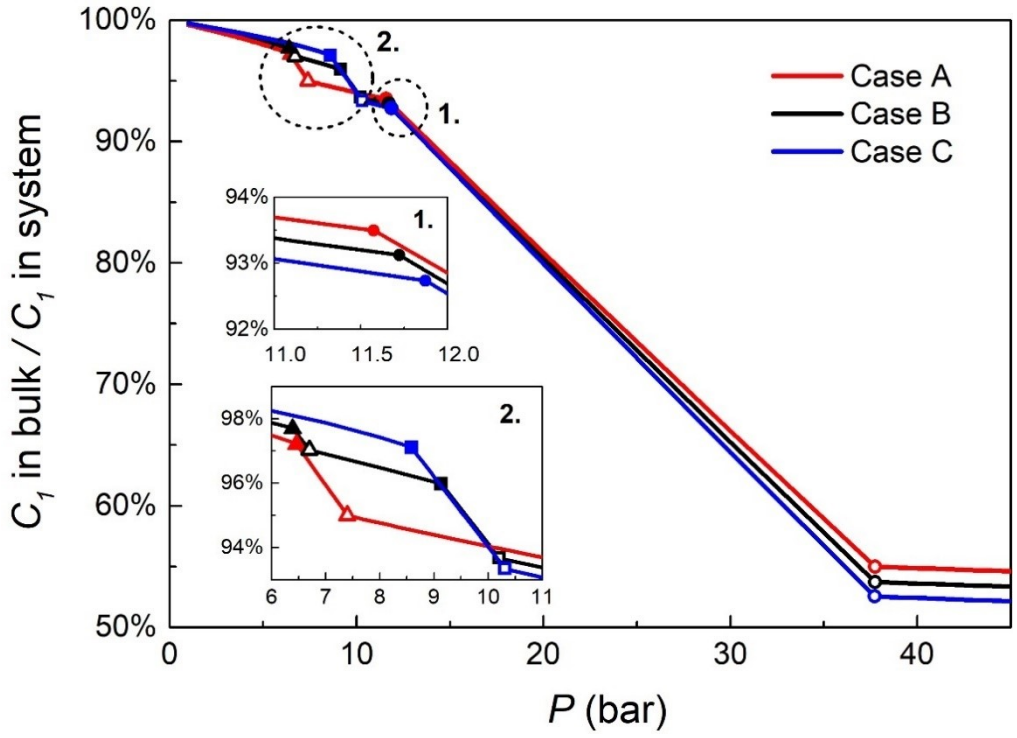

Appendix D

Figure D1. Pressure-C_3 bulk composition ($P - y_{C_3,b}$) and pressure-C_3 pore composition ($P - x_{C_3,p}$) for C_1-C_3 mixtures at 288.15 K in bulk and 5-nm pores. The blue dashed line is the equilibrium C_3 composition in nanopore $x_{C_3,p}^{eq}$ while the dashed black line is the equilibrium C_3 composition in bulk $y_{C_3,b}^{eq}$. The gray-, blue-, yellow- and pink regions corresponding to supercritical-, single liquid phase-, two-phases and single vapor phase regions of nanoconfined C_1-C_3 mixtures which satisfy $x_{C_1,p}^{eq} : x_{C_3,p}^{eq} = 0.2 : 0.8$.

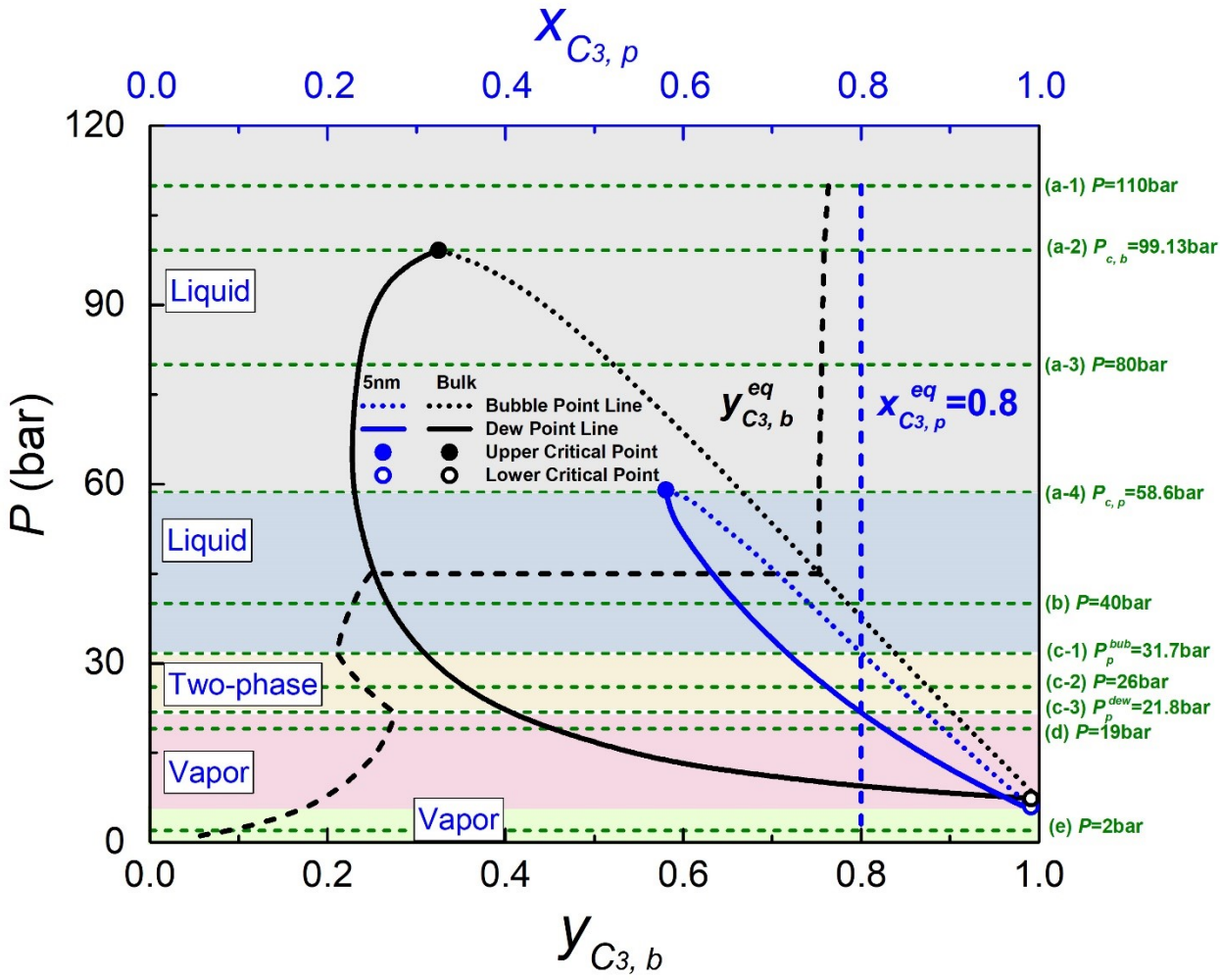

Figure D2. C_3 pore density-C_3 bulk composition ($\rho_{C_3,p} - y_{C_3,b}$) plots for C_1-C_3 mixtures at 288.15K at different P in POBR highlighted in Figure S1. (a-1) $P > P_{c,b}^{upper}$ ($P = 110$ K); (a-2) $P = P_{c,b}^{upper}$ ($P = 99.13$ K); (a-3) $P_{c,b}^{upper} > P > P_{c,p}^{upper}$ ($P = 80$ K); (a-4) $P = P_{c,p}^{upper}$ ($P = 58.6$ K); (b) $P_{c,p}^{upper} > P > P_p^{bub}$ ($P = 40$ K); (c-1) $P = P_p^{bub}$ ($P = 31.7$ K); (c-2) $P_p^{bub} > P > P_p^{dew}$ ($P = 26$ K); (c-3) $P = P_p^{dew}$ ($P = 21.8$ K); (d) $P_p^{dew} > P > P_{c,p}^{lower}$ ($P = 19$ K); (e) $P < P_{c,p}^{lower}$ ($P = 2$ K). The hollow black and solid black circles represent bulk bubble point and dew point C_3 compositions, y_b^{bub} and y_b^{dew} respectively. The hollow blue and solid blue circles represent bubble point and dew point C_3 densities in 5nm nanopore, $\rho_{C_3,p}^{bub}$ and $\rho_{C_3,p}^{dew}$, respectively. The blue dotted lines are reference lines for equilibrium C_3 density in pore $\rho_{C_3,p}^{eq}$ while the black dash-dotted lines represent equilibrium C_3 composition in bulk $y_{C_3,b}^{eq}$.

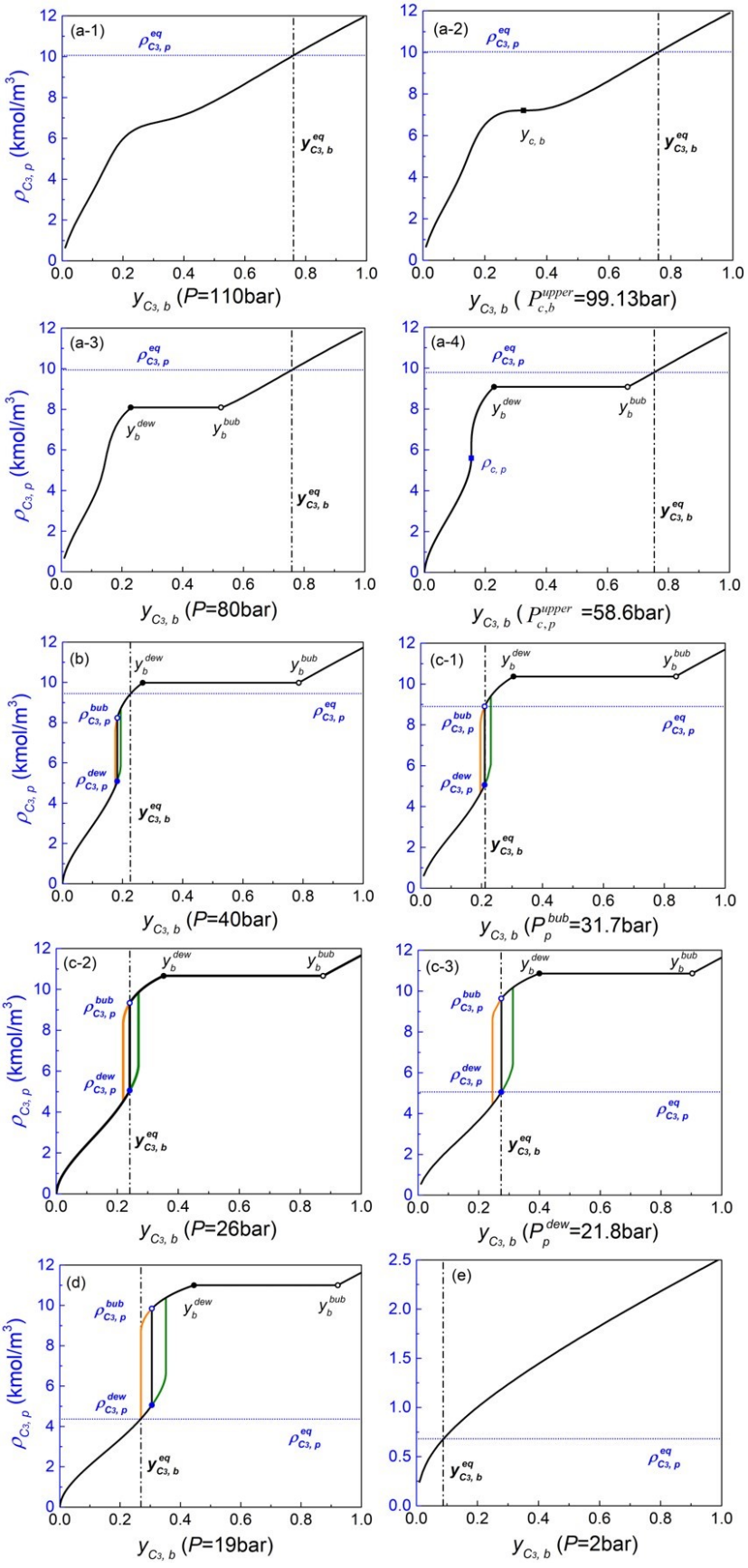
(a-1)
(a-2)
(a-3)
(a-4)
(b)
(c-1)
(c-2)
(c-3)
(d)
(e)
$\rho_{C3,p}$ (kmol/m^3)
$y_{C3,b}$ (P=110bar)
$y_{C3,b}$ ($P_{c,b}^{upper}$=99.13bar)
$y_{C3,b}$ (P=80bar)
$y_{C3,b}$ ($P_{c,p}^{upper}$ =58.6bar)
$y_{C3,b}$ (P=40bar)
$y_{C3,b}$ (P_p^{bub}=31.7bar)
$y_{C3,b}$ (P=26bar)
$y_{C3,b}$ (P_p^{dew}=21.8bar)
$y_{C3,b}$ (P=19bar)
$y_{C3,b}$ (P=2bar)

Figure D3. C_3 pore composition-C_3 bulk composition ($x_{C_3,p} - y_{C_3,b}$) plots for C_1-C_3 mixtures at 288.15K at different P in POBR highlighted in Figure S1. (a-1) $P > P_{c,b}^{upper}$ ($P = 110$ K); (a-2) $P = P_{c,b}^{upper}$ ($P = 99.13$ K); (a-3) $P_{c,b}^{upper} > P > P_{c,p}^{upper}$ ($P = 80$ K); (a-4) $P = P_{c,p}^{upper}$ ($P = 58.6$ K); (b) $P_{c,p}^{upper} > P > P_p^{bub}$ ($P = 40$ K); (c-1) $P = P_p^{bub}$ ($P = 31.7$ K); (c-2) $P_p^{bub} > P > P_p^{dew}$ ($P = 26$ K); (c-3) $P = P_p^{dew}$ ($P = 21.8$ K); (d) $P_p^{dew} > P > P_{c,p}^{lower}$ ($P = 19$ K); (e) $P < P_{c,p}^{lower}$ ($P = 2$ K). The hollow black and solid black circles represent bulk bubble point and dew point C_3 compositions, y_b^{bub} and y_b^{dew} respectively. The hollow blue and solid blue circles represent bubble point and dew point C_3 compositions in 5nm nanopore, x_p^{bub} and x_p^{dew}, respectively. The blue dotted lines are reference lines for equilibrium C_3 composition in pore $x_{C_3,p}^{eq}$ while the black dash-dotted lines represent equilibrium C_3 composition in bulk $y_{C_3,b}^{eq}$.

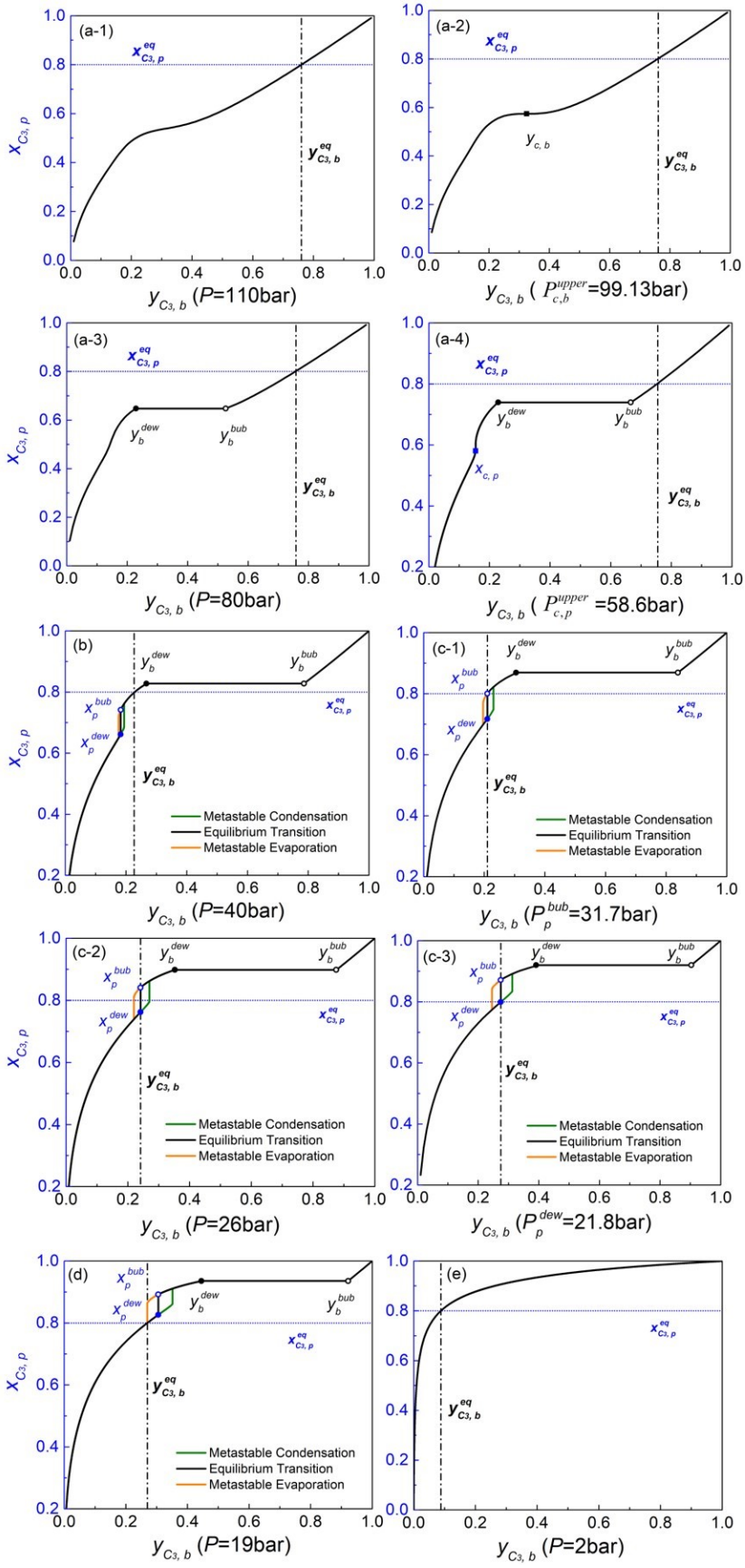
(a-1)
(a-2)
(a-3)
(a-4)
(b)
(c-1)
(c-2)
(c-3)
(d)
(e)
Metastable Condensation
Equilibrium Transition
Metastable Evaporation
$y_{C3,\,b}$ (P=110bar)
$y_{C3,\,b}$ ($P_{c,b}^{upper}$=99.13bar)
$y_{C3,\,b}$ (P=80bar)
$y_{C3,\,b}$ ($P_{c,p}^{upper}$ =58.6bar)
$y_{C3,\,b}$ (P=40bar)
$y_{C3,\,b}$ (P_p^{bub}=31.7bar)
$y_{C3,\,b}$ (P=26bar)
$y_{C3,\,b}$ (P_p^{dew}=21.8bar)
$y_{C3,\,b}$ (P=19bar)
$y_{C3,\,b}$ (P=2bar)

Appendix E

E1. Procedure of Constructing Kerogen Matrix

The process for constructing kerogen matrix is shown in **Figure E1**. First, as shown in **Figure E1 (a)**, 72 kerogen molecules are placed between two graphene sheets generated with a size of 22.10 nm × 5.10 nm in the *x*-*y* plane by VMD package. Only the repulsive interaction between graphene sheet and kerogen molecule is considered. Then, an annealing simulation with temperature linearly decreases from 900 K to 330 K is conducted for 2.5 ns, then another 1.5 ns of simulation at 330 K is conducted for the system to reach equilibrium. At the same time, an external acceleration of -0.9 nm/ps^2 in the *z*-direction (the negative sign represents the direction of acceleration is in the counter z-direction) on the upper graphene sheet atoms to compress the kerogen, the bottom graphene sheet is fixed in the original position. The system is periodic in three dimensions and the final configuration is shown in **Figure E1 (b)**. Next, replace the upper kerogen sheet by the same one as the lower graphene sheet and add two identical graphene sheets with a size of 5.11 × 3.91 nm^2 on the left ($x = 0$ nm) and right ($x = 22$ nm) side of the kerogen. The interaction between graphene carbon atoms is set as zero to avoid collapsing of the system. An external acceleration of -0.66 nm/ps^2 in the *x*-direction is exerted on the carbon atoms of the right graphene sheet while other three graphene sheets are always fixed. The annealing process is conducted by increasing the temperature gradually from 330 K to 1000 K for 1 ns, kept at 1000 K for 1 ns to fully relax the kerogen molecules, then quickly drops the temperature to 330 K in 50 ps. Finally, another 450 ps of simulation at 330 K is conducted for the system to reach equilibrium condition. Similar as previous step, the total system is periodic in three dimensions with fixed volume. The final configuration of this step is shown in **Figure E1 (c)**.

Figure E1 (a) Type II-C kerogen molecule ; (b) the final configuration after applying an external pressure along the *z*-direction; (c) The final configuration after applying an external pressure along the *x*-direction.

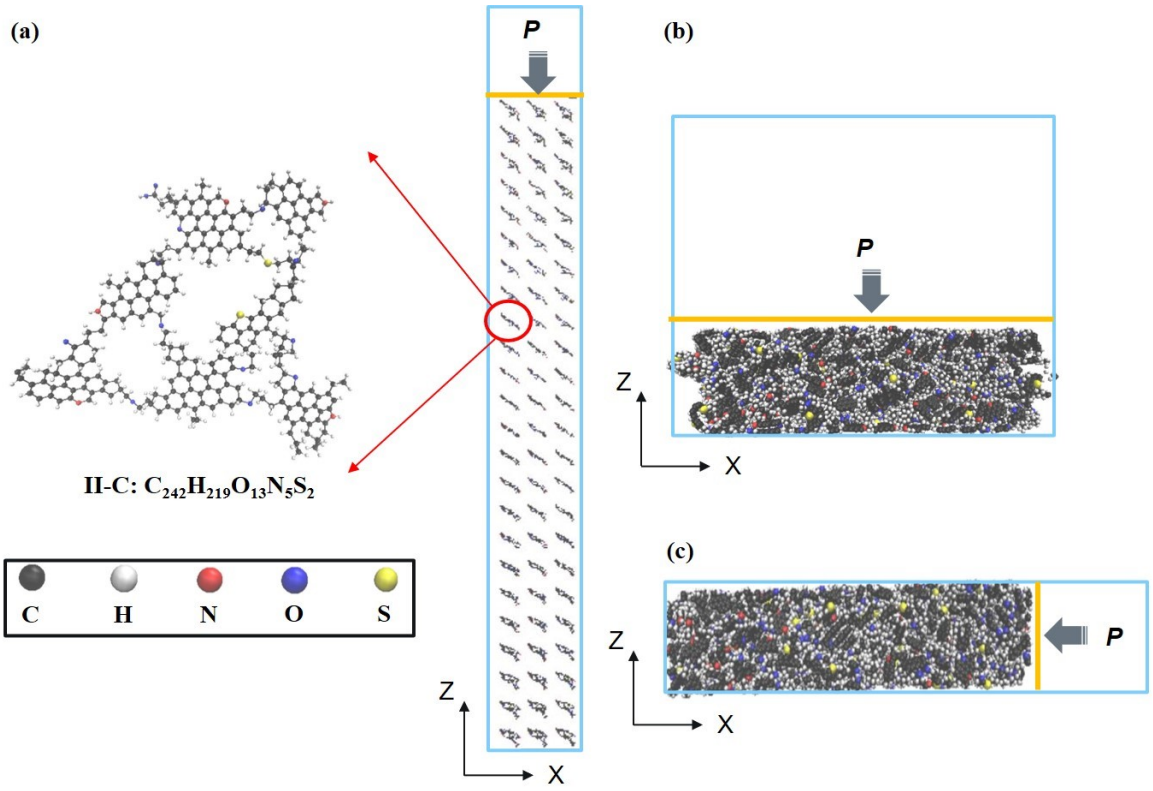

E2. Procedure of Constructing Kerogen Pore Throat

The final morphology of kerogen pore throats in the *x*-*z* plane is illustrated in **Figure E2 (a)**. The lengths of the bottom and upper kerogen matrices are 17.01 nm in the *x*-direction while the thicknesses of them are 3.91 nm in the *z*-direction. The upper kerogen matrix is obtained by rotating the lower one 180° along the *y*-direction and then shifting above for 5.91 nm. Surface A and B shown in **Figure E2 (a)** are the inner surfaces of kerogen pore throat, which essentially have the same surface morphology. The bottom kerogen matrix is used as the substrate in the nC_8-H_2O-kerogen contact angle calculation. The morphology of Surface B in the *x*-*y* plane is shown in **Figure E2 (b)**.

Figure E2 (a) Kerogen pore throat; (b) Morphology of Surface B in the *x*-*y* plane.

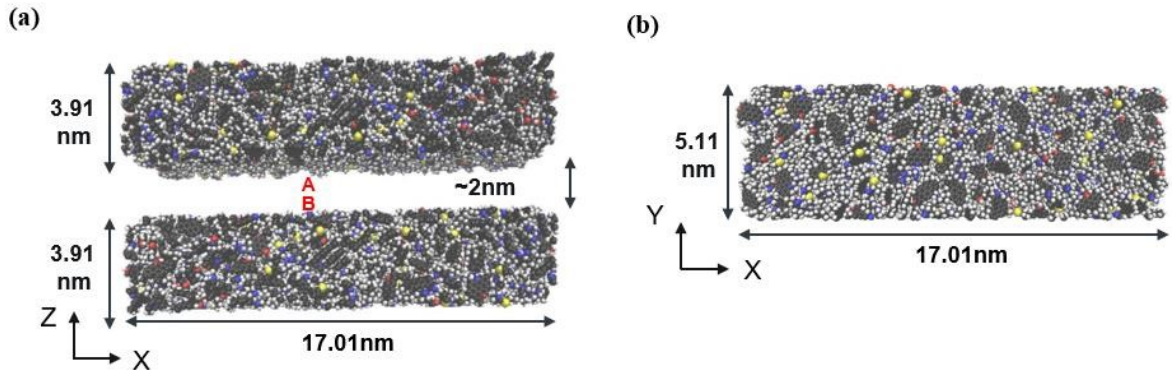

E3. Procedure of Contact Angle Calculation

Figure E3. Schematic representation of nC_8-H_2O-kerogen system for contact angle calculation. (a) Initial configuration (H_2O box length in the *x*- and *z*-direction equal to 5.5 nm). (b) Configurations of nC_8 and H_2O in bulk condition after equilibration at 330 K and 300 bar. (c) Combination of piston (hard graphene wall), kerogen substrate and H_2O droplet in nC_8. (d) The final configurations after a 50-ns MD simulation.

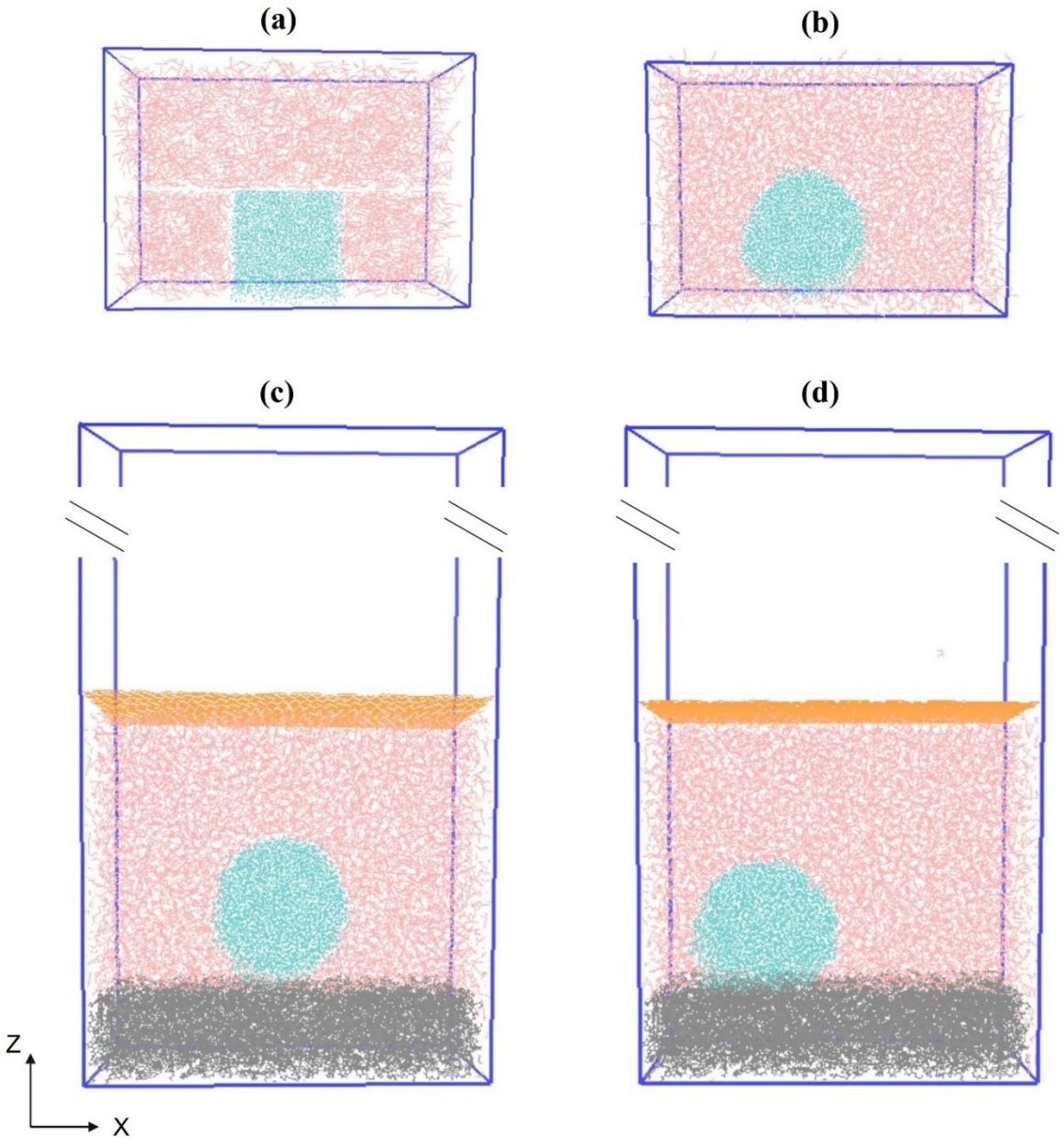

E4. Interfacial Tension Calculation System

Figure E4. Schematic representation of H_2O-nC_8 interfacial tension calculation system.

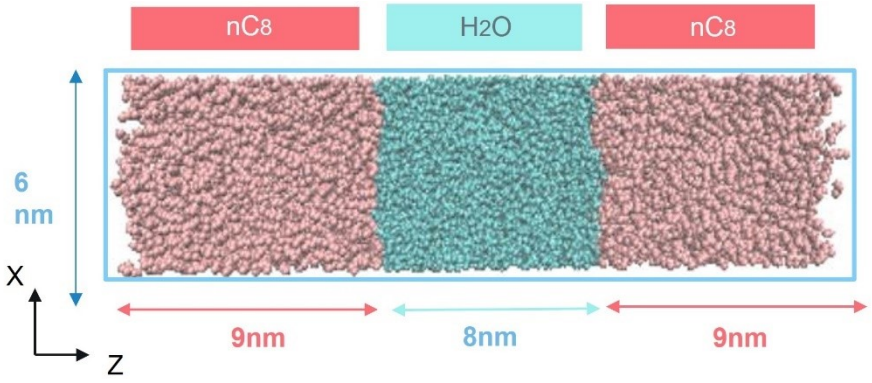

E5. Helium Adsorption System

Figure E5. Schematic representation of helium adsorption system.

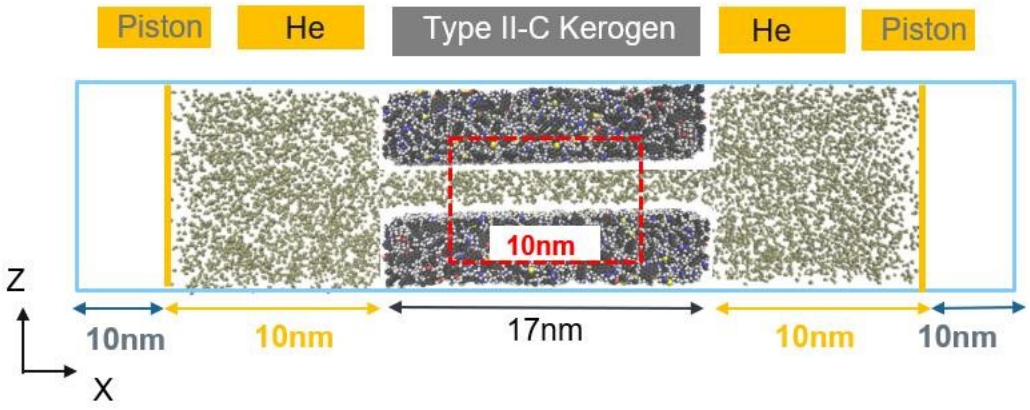

E6. System size test in terms of breakthrough pressure

In this part, to test system size effect on the breakthrough pressure, initially, the upstream reservoir contains both a water slab (20 nm thick in the x-direction) and an octane slab (10 nm thick in the x-direction) as shown in **Figure E4 (a)**, which are twice of the size compared with original water slab and octane slab in the displacement system as shown in **Figure 6-1 (a)**. The system temperature and reservoir pressure (P_d) conditions are kept same as the displacement system in **Figure 6-1 (a)**. By changing the upstream pressure (P_u) to exert different external pressures (pressure difference between P_u and P_d) on the large size of system, the breakthrough pressure P_B is in the range between 430 and 440 bar after 200 ns of MD simulation. Compared with the range between 420 and 430 bar in the original system, the system size effect is minor.

Figure E6. Testing for system size effect on breakthrough pressure (larger volume of fluids in system).

E7. Kerogen substrate size and surface morphology test for wettability

To test the generalization of the contact angle result, a different type II-C kerogen substrate is built. Compared with the original substrate used in wettability test as shown in **Figure E2 (b)**, the newly built kerogen substrate has a different geometrical size and surface morphology as shown in the **Figure E5 (a)** and **(b)**. The system setting for wettability test is shown in **Figure E5 (c)**. After the system reaches equilibrium, 10000 of snapshots are used to get the contact angle result. Based on result shown in **Figure E5 (d)**, the result is in line with that in original wettability system. Note that the different kerogen substrate is constructed by similar annealing process with similar surface roughness compared to the original substrate. As a result, the roughness effect is not truly considered in this test.

Figure E7. (a) The smaller kerogen substrate in the *x-z* plane. (b) The smaller kerogen substrate in the *x-y* plane. (c) System setting for wettability test with another kerogen substrate. (d) The dependence of θ on D with different kerogen substrates.

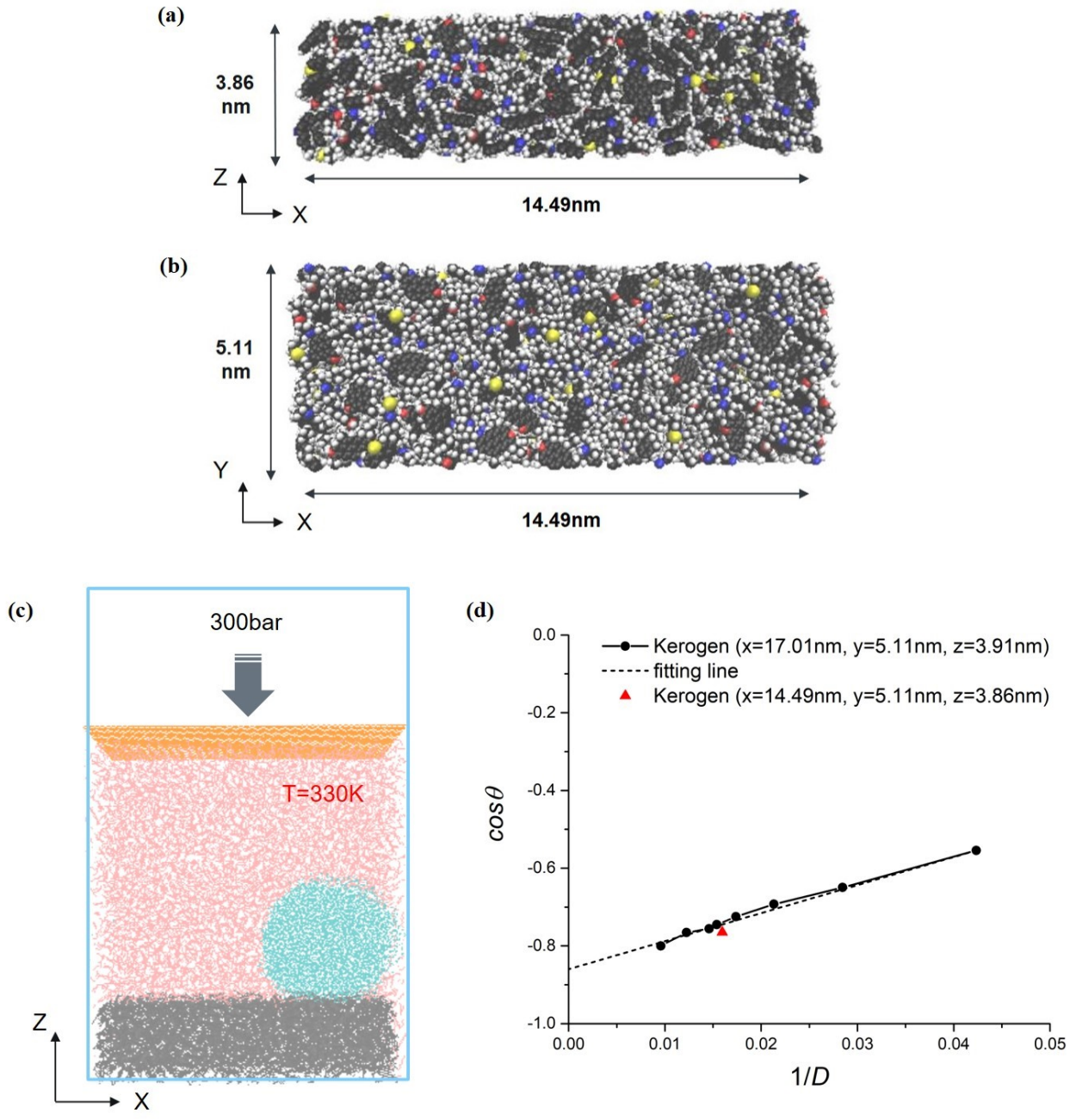

Table E1. Number of H_2O and nC_8 molecules in the oil-water two-phase displacement system

Upstream Reservoir		Kerogen Pore Throat	Downstream Reservoir
H_2O	nC_8	nC_8	nC_8
16720	926	643	926

Table E2. Number of H_2O and nC_8 molecules in the nC_8-H_2O -kerogen contact angle system

Case No.	*D* (nm)	H_2O	nC_8 (Left/ Right)	nC_8 (Above)
1	2.361	680	283	3208
2	3.513	1532	396	2887
3	4.688	2723	491	2566
4	5.752	4255	566	2245
5	6.492	5149	597	2085
6	6.852	6127	623	1925
7	8.163	8340	661	2245

Table E3. Original dimension of H_2O and nC_8 boxes in *x*- and *z*-directions in nC_8-H_2O-kerogen contact angle system

Case No.	H_2O		nC_8 (Left/ Right)		nC_8 (Above)	
	***x*-direction (nm)**	***z*-direction (nm)**	***x*-direction (nm)**	***z*-direction (nm)**	***x*-direction (nm)**	***z*-direction (nm)**
1	**2**	**2**	**7.5**	**2**	**17**	**10**
2	**3**	**3**	**7**	**3**	**17**	**9**
3	**4**	**4**	**6.5**	**4**	**17**	**8**
4	**5**	**5**	**6**	**5**	**17**	**7**
5	**5.5**	**5.5**	**5.75**	**5.5**	**17**	**6.5**
6	**6**	**6**	**5.5**	**6**	**17**	**6**
7	**7**	**7**	**5**	**7**	**17**	**7**

Table E4. Number of H_2O and nC_8 molecules in interfacial tension calculation

nC_8 Slab (Left)	H_2O Slab	nC_8 Slab (Right)
nC_8	H_2O	nC_8
1197	**9602**	**1197**

Table E5. Number of helium molecules in helium adsorption system

Left of the Kerogen Pore Throat	Kerogen Pore Throat	Right of the Kerogen Pore Throat
2926	914	2926

REFERENCE

1. EIA, U.S., *U.S. EIA's International Energy Outlook 2021.* 2021.
2. Thomas, M., et al., *Deliberating the perceived risks, benefits, and societal implications of shale gas and oil extraction by hydraulic fracturing in the US and UK.* Nature Energy, 2017. **2**(5): p. 17054.
3. Ross, D.J.K. and R. Marc Bustin, *The importance of shale composition and pore structure upon gas storage potential of shale gas reservoirs.* Marine and Petroleum Geology, 2009. **26**(6): p. 916-927.
4. Ma, Y., J.-H. Chen, and A. Jamili, *Adsorption and Capillary Condensation in Heterogeneous Nanoporous Shales*, in *SPE/AAPG/SEG Unconventional Resources Technology Conference*. 2016, Unconventional Resources Technology Conference: San Antonio, Texas, USA. p. 17.
5. Jin, Z. and A. Firoozabadi, *Thermodynamic modeling of phase behavior in shale media.* SPE Journal, 2016. **21**(01): p. 190-207.
6. Nguyen, N.T.B., et al., *Optimization of Hydraulic Fracturing Design with Future EOR Considerations in Shale Oil Reservoirs*, in *EUROPEC 2015*. 2015, Society of Petroleum Engineers: Madrid, Spain. p. 20.
7. Zhang, Y., et al., *The pore size distribution and its relationship with shale gas capacity in organic-rich mudstone of Wufeng-Longmaxi Formations, Sichuan Basin, China.* Journal of Natural Gas Geoscience, 2016. **1**(3): p. 213-220.
8. Zhao, Y., et al., *Bubble Point Pressures of Hydrocarbon Mixtures in Multiscale Volumes from Density Functional Theory.* Langmuir, 2018. **34**(46): p. 14058-14068.
9. Luo, S., J.L. Lutkenhaus, and H. Nasrabadi, *Use of differential scanning calorimetry to study phase behavior of hydrocarbon mixtures in nano-scale porous media.* Journal of Petroleum Science and Engineering, 2018. **163**: p. 731-738.
10. Pathak, M., H. Cho, and M. Deo, *Experimental and Molecular Modeling Study of Bubble Points of Hydrocarbon Mixtures in Nanoporous Media.* Energy & Fuels, 2017. **31**(4): p. 3427-3435.
11. Cho, H., M.H. Bartl, and M. Deo, *Bubble point measurements of hydrocarbon mixtures in mesoporous media.* Energy & Fuels, 2017. **31**(4): p. 3436-3444.
12. Zhong, J., et al., *Nanoscale Phase Measurement for the Shale Challenge: Multicomponent Fluids in Multiscale Volumes.* Langmuir, 2018. **34**(34): p. 9927-9935.
13. Alfi, M., H. Nasrabadi, and D. Banerjee, *Experimental investigation of confinement effect on phase behavior of hexane, heptane and octane using lab-on-a-chip technology.* Fluid Phase Equilibria, 2016. **423**: p. 25-33.
14. Zhong, J., et al., *Condensation in One-Dimensional Dead-End Nanochannels.* ACS Nano, 2017. **11**(1): p. 304-313.
15. Xie, Q., S. Xiao, and C. Duan, *Geometry-Dependent Drying in Dead-End Nanochannels.* Langmuir, 2017. **33**(34): p. 8395-8403.
16. Zuo, J.Y., et al., *Impact of Capillary Pressure and Nanopore Confinement on Phase Behaviors of Shale Gas and Oil.* Energy & Fuels, 2018. **32**(4): p. 4705-4714.
17. Nojabaei, B., R.T. Johns, and L. Chu, *Effect of Capillary Pressure on Phase Behavior in Tight Rocks and Shales.* SPE Reservoir Evaluation & Engineering, 2013. **16**(03): p. 281-289.

18. Teklu, T.W., et al., *Phase Behavior and Minimum Miscibility Pressure in Nanopores.* SPE Reservoir Evaluation & Engineering, 2014. **17**(03): p. 396-403.
19. Dong, X., et al., *Phase Equilibria of Confined Fluids in Nanopores of Tight and Shale Rocks Considering the Effect of Capillary Pressure and Adsorption Film.* Industrial & Engineering Chemistry Research, 2016. **55**(3): p. 798-811.
20. Tan, S.P., et al., *Critical Point of Fluid Confined in Nanopores: Experimental Detection and Measurement.* The Journal of Physical Chemistry C, 2019. **123**(15): p. 9824-9830.
21. Evans, R. and P. Tarazona, *Theory of Condensation in Narrow Capillaries.* Physical Review Letters, 1984. **52**(7): p. 557-560.
22. Bruno, E., U.M.B. Marconi, and R. Evans, *Phase transitions in a confined lattice gas: Prewetting and capillary condensation.* Physica A: Statistical Mechanics and its Applications, 1987. **141**(1): p. 187-210.
23. Morishige, K., et al., *Capillary Critical Point of Argon, Nitrogen, Oxygen, Ethylene, and Carbon Dioxide in MCM-41.* Langmuir, 1997. **13**(13): p. 3494-3498.
24. Zhao, Y. and Z. Jin, *Hydrocarbon-Phase Behaviors in Shale Nanopore/Fracture Model: Multiscale, Multicomponent, and Multiphase.* SPE Journal, 2019. **24**(6): p. 2524-2540.
25. Didar, B.R. and I.Y. Akkutlu, *Pore-size Dependence of Fluid Phase Behavior and Properties in Organic-Rich Shale Reservoirs*, in *SPE International Symposium on Oilfield Chemistry*. 2013, Society of Petroleum Engineers: The Woodlands, Texas, USA. p. 19.
26. Nojabaei, B., R.T. Johns, and L. Chu, *Effect of Capillary Pressure on Fluid Density and Phase Behavior in Tight Rocks and Shales.* SPE Reservoir Evaluation & Engineering, 2012. **16**(3): p. 281-289.
27. Fang, C., F. Zhang, and R. Qiao, *Invasion of gas into mica nanopores: a molecular dynamics study.* Journal of Physics: Condensed Matter, 2018. **30**(22): p. 224001.
28. Sokhan, V.P., D. Nicholson, and N. Quirke, *Fluid flow in nanopores: Accurate boundary conditions for carbon nanotubes.* The Journal of Chemical Physics, 2002. **117**(18): p. 8531-8539.
29. Zhan, S., et al., *Study of liquid-liquid two-phase flow in hydrophilic nanochannels by molecular simulations and theoretical modeling.* Chemical Engineering Journal, 2020. **395**: p. 125053.
30. Li, B., K. Bui, and I.Y. Akkutlu. *Capillary pressure in nanopores: Deviation from Young-Laplace equation*. in *SPE Europec featured at 79th EAGE Conference and Exhibition*. 2017. Society of Petroleum Engineers.
31. Wang, X., et al., *Insight into the pressure-induced displacement mechanism for selecting efficient nanofluids in various capillaries.* Environmental Science: Nano, 2020. **7**(9): p. 2785-2794.
32. Sheng, L., N. Hadi, and L.J. L., *Effect of confinement on the bubble points of hydrocarbons in nanoporous media.* AIChE Journal, 2016. **62**(5): p. 1772-1780.
33. Luo, S., J.L. Lutkenhaus, and H. Nasrabadi, *Confinement-Induced Supercriticality and Phase Equilibria of Hydrocarbons in Nanopores.* Langmuir, 2016. **32**(44): p. 11506-11513.
34. Jin, Z. and A. Firoozabadi, *Thermodynamic Modeling of Phase Behavior in Shale Media.* SPE Journal, 2016. **21**(01): p. 190 - 207.
35. Hughes, J.D., *A reality check on the shale revolution.* Nature, 2013. **494**.
36. Utpalendu, K. and P. Manika, *Specific surface area and pore-size distribution in clays and shales.* Geophysical Prospecting, 2013. **61**(2): p. 341-362.

37. Zargari, S., K.L. Canter, and M. Prasad, *Porosity evolution in oil-prone source rocks.* Fuel, 2015. **153**: p. 110-117.
38. Sigal, R.F., *Pore-Size Distributions for Organic-Shale-Reservoir Rocks From Nuclear-Magnetic-Resonance Spectra Combined With Adsorption Measurements.* SPE Journal, 2015. **20**(04): p. 824 - 830.
39. Liu, J., et al., *Adsorption and Phase Behavior of Pure/Mixed Alkanes in Nanoslit Graphite Pores: An iSAFT Application.* Langmuir, 2017. **33**(42): p. 11189-11202.
40. Nojabaei, B., R.T. Johns, and L. Chu, *Effect of Capillary Pressure on Fluid Density and Phase Behavior in Tight Rocks and Shales*, in *SPE Annual Technical Conference and Exhibition*. 2012, Society of Petroleum Engineers: San Antonio, Texas, USA. p. 281 - 289.
41. Fu, J., Y. Tian, and J. Wu, *Classical density functional theory for methane adsorption in metal-organic framework materials.* ALCHE journal, 2015. **61**(9): p. 3012-3021.
42. Davis, M.E., *Zeolite-based catalysts for chemicals synthesis.* Microporous and Mesoporous Materials, 1998. **21**(4-6): p. 173-182.
43. Debe, M.K., *Electrocatalyst approaches and challenges for automotive fuel cells.* Nature, 2012. **486**: p. 43.
44. Rodenas, T., et al., *Metal–organic framework nanosheets in polymer composite materials for gas separation.* Nature Materials, 2014. **14**: p. 48-55.
45. Cho, H., et al., *Measurements of hydrocarbon bubble points in synthesized mesoporous siliceous monoliths.* Chemical Engineering Science, 2018. **177**: p. 481-490.
46. Liu, Y., H.A. Li, and R. Okuno, *Phase behavior of N2/n-C4H10 in a partially confined space derived from shale sample.* Journal of Petroleum Science and Engineering, 2018. **160**: p. 442-451.
47. Wang, L., et al., *Experimental Study and Modeling of the Effect of Nanoconfinement on Hydrocarbon Phase Behavior in Unconventional Reservoirs*, in *SPE Western North American and Rocky Mountain Joint Meeting*. 2014, Society of Petroleum Engineers: Denver, Colorado.
48. Zhong, J., et al., *Nanoscale phase measurement for the shale challenge: multi-component fluids in multi-scale volumes.* Langmuir, 2018. **Accepted**.
49. Sandoval, D., et al., *Phase Envelope Calculations for Reservoir Fluids in the Presence of Capillary Pressure*, in *SPE Annual Technical Conference and Exhibition*. 2015, Society of Petroleum Engineers: Houston, Texas, USA.
50. Sandoval, D.R., et al., *The Phase Envelope of Multicomponent Mixtures in the Presence of a Capillary Pressure Difference.* Industrial & Engineering Chemistry Research, 2016. **55**(22): p. 6530-6538.
51. Sherafati, M. and K. Jessen, *Stability Analysis and Equilibrium Considerations in Tight Formations*, in *SPE Low Perm Symposium*. 2016, Society of Petroleum Engineers: Denver, Colorado, USA.
52. Shardt, N. and J.A.W. Elliott, *Isobaric Vapor–Liquid Phase Diagrams for Multicomponent Systems with Nanoscale Radii of Curvature.* The Journal of Physical Chemistry B, 2018. **122**(8): p. 2434-2447.
53. Yu, W. and K. Sepehrnoori, *Shale Gas and Tight Oil Reservoir Simulation*. 1st ed. 2019: Elsevier. 430.
54. Pitakbunkate, T., et al., *Effect of Confinement on Pressure/Volume/Temperature Properties of Hydrocarbons in Shale Reservoirs.* SPE Journal, 2016. **21**(02): p. 621 - 634.

55. Pitakbunkate, T., et al., *Phase Behavior of Methane–Ethane Mixtures in Nanopores.* Industrial & Engineering Chemistry Research, 2017. **56**(40): p. 11634-11643.
56. Li, Z., Z. Jin, and A. Firoozabadi, *Phase Behavior and Adsorption of Pure Substances and Mixtures and Characterization in Nanopore Structures by Density Functional Theory.* SPE Journal, 2014. **19**(06): p. 1,096 - 1,109.
57. Löhr, S.C., et al., *Is organic pore development in gas shales influenced by the primary porosity and structure of thermally immature organic matter?* Organic Geochemistry, 2015. **87**: p. 119-132.
58. Jin, Z., *Bubble/dew point and hysteresis of hydrocarbons in nanopores from molecular perspective.* Fluid Phase Equilibria, 2018. **458**: p. 177-185.
59. Ravikovitch, P.I., et al., *Capillary Hysteresis in Nanopores: Theoretical and Experimental Studies of Nitrogen Adsorption on MCM-41.* Langmuir, 1995. **11**(12): p. 4765-4772.
60. Zhong, J., et al., *Capillary Condensation in 8 nm Deep Channels.* The Journal of Physical Chemistry Letters, 2018. **9**(3): p. 497-503.
61. Alfarge, D., M. Wei, and B. Bai, *CO2-EOR mechanisms in huff-n-puff operations in shale oil reservoirs based on history matching results.* Fuel, 2018. **226**: p. 112-120.
62. Falk, K., et al., *Subcontinuum mass transport of condensed hydrocarbons in nanoporous media.* Nature Communications, 2015. **6**: p. 6949.
63. Lee, T., L. Bocquet, and B. Coasne, *Activated desorption at heterogeneous interfaces and long-time kinetics of hydrocarbon recovery from nanoporous media.* Nature Communications, 2016. **7**: p. 11890.
64. Wu, K., et al., *A model for multiple transport mechanisms through nanopores of shale gas reservoirs with real gas effect–adsorption-mechanic coupling.* International Journal of Heat and Mass Transfer, 2016. **93**: p. 408-426.
65. Donnelly, J., *Comments: The Implications of Shale.* Journal of Petroleum Technology, 2010. **62**(10): p. 18-18.
66. Bui, K. and I.Y. Akkutlu, *Hydrocarbons Recovery From Model-Kerogen Nanopores.* SPE Journal, 2017. **22**(03): p. 854-862.
67. Jatukaran, A., et al., *Natural gas vaporization in a nanoscale throat connected model of shale: multi-scale, multi-component and multi-phase.* Lab on a Chip, 2019. **19**(2): p. 272-280.
68. Barsotti, E., et al., *A review on capillary condensation in nanoporous media: Implications for hydrocarbon recovery from tight reservoirs.* Fuel, 2016. **184**: p. 344-361.
69. Li, H., et al., *Direct visualization of fluid dynamics in sub-10 nm nanochannels.* Nanoscale, 2017. **9**(27): p. 9556-9561.
70. Zhong, J., et al., *Nanomodel visualization of fluid injections in tight formations.* Nanoscale, 2018. **10**(46): p. 21994-22002.
71. Ko, L.T., et al., *Origin and characterization of Eagle Ford pore networks in the south Texas Upper Cretaceous shelf.* AAPG Bulletin, 2017. **101**(3): p. 387-418.
72. Luo, S., J.L. Lutkenhaus, and H. Nasrabadi, *Multiscale Fluid-Phase-Behavior Simulation in Shale Reservoirs Using a Pore-Size-Dependent Equation of State.* SPE Reservoir Evaluation & Engineering, 2018. **21**(04): p. 806-820.
73. Bi, R. and H. Nasrabadi, *Molecular simulation of the constant composition expansion experiment in shale multi-scale systems.* Fluid Phase Equilibria, 2019. **495**: p. 59-68.

74. Freeman, C., et al., *Measurement, Modeling, and Diagnostics of Flowing Gas Composition Changes in Shale Gas Wells*, in *SPE Latin America and Caribbean Petroleum Engineering Conference*. 2012, Society of Petroleum Engineers: Mexico City, Mexico. p. 25.
75. Jia, H. and J.J. Sheng, *Discussion of the feasibility of air injection for enhanced oil recovery in shale oil reservoirs.* Petroleum, 2017. **3**(2): p. 249-257.
76. McCain Jr, W.D., *Properties of petroleum fluids*. 2017: PennWell Corporation.
77. Li, Z., Z. Jin, and A. Firoozabadi, *Phase Behavior and Adsorption of Pure Substances and Mixtures and Characterization in Nanopore Structures by Density Functional Theory.* SPE Journal, 2014. **19**(06): p. 1096-1109.
78. Zou, C., *Chapter 1 - Introduction*, in *Unconventional Petroleum Geology (Second Edition)*, C. Zou, Editor. 2017, Elsevier. p. 3-48.
79. Patade, V.Y., et al., *Chapter 18 - Omics Approaches in Biofuel Technologies: Toward Cost Effective, Eco-Friendly, and Renewable Energy*, in *Omics Technologies and Bio-Engineering*, D. Barh and V. Azevedo, Editors. 2018, Academic Press. p. 337-351.
80. Qiu, X., et al., *Experimental Study on the Criticality of a Methane/Ethane Mixture Confined in Nanoporous Media.* Langmuir, 2019. **35**(36): p. 11635-11642.
81. Alfi, M., H. Nasrabadi, and D. Banerjee, *Effect of Confinement on Bubble Point Temperature Shift of Hydrocarbon Mixtures: Experimental Investigation Using Nanofluidic Devices*, in *SPE Annual Technical Conference and Exhibition*. 2017, Society of Petroleum Engineers: San Antonio, Texas, USA. p. 12.
82. Tripathy, A., V. Srinivasan, and T.N. Singh, *A Comparative Study on the Pore Size Distribution of Different Indian Shale Gas Reservoirs for Gas Production and Potential CO2 Sequestration.* Energy & Fuels, 2018. **32**(3): p. 3322-3334.
83. Clarkson, C.R., et al., *Characterization of tight gas reservoir pore structure using USANS/SANS and gas adsorption analysis.* Fuel, 2012. **95**: p. 371-385.
84. Clarkson, C.R., et al., *Pore structure characterization of North American shale gas reservoirs using USANS/SANS, gas adsorption, and mercury intrusion.* Fuel, 2013. **103**: p. 606-616.
85. Dong, T., et al., *The impact of composition on pore throat size and permeability in high maturity shales: Middle and Upper Devonian Horn River Group, northeastern British Columbia, Canada.* Marine and Petroleum Geology, 2017. **81**: p. 220-236.
86. Hu, Q., R.P. Ewing, and H.D. Rowe, *Low nanopore connectivity limits gas production in Barnett formation.* Journal of Geophysical Research: Solid Earth, 2015. **120**(12): p. 8073-8087.
87. Chen, G., et al., *Investigation of pore size effects on adsorption behavior of shale gas.* Marine and Petroleum Geology, 2019. **109**: p. 1-8.
88. Jin, L., Y. Ma, and A. Jamili, *Investigating The Effect of Pore Proximity on Phase Behavior And Fluid Properties in Shale Formations*, in *SPE Annual Technical Conference and Exhibition*. 2013, Society of Petroleum Engineers: New Orleans, Louisiana, USA. p. 16.
89. Jin, B., R. Bi, and H. Nasrabadi, *Molecular simulation of the pore size distribution effect on phase behavior of methane confined in nanopores.* Fluid Phase Equilibria, 2017. **452**: p. 94-102.
90. Liu, Y., et al., *Competitive adsorption behavior of hydrocarbon(s)/CO2 mixtures in a double-nanopore system using molecular simulations.* Fuel, 2019. **252**: p. 612-621.
91. Leu, L., et al., *Multiscale Description of Shale Pore Systems by Scanning SAXS and WAXS Microscopy.* Energy & Fuels, 2016. **30**(12): p. 10282-10297.

92. Boruah, A., et al., *Specific surface area and pore size distribution in gas shales of Raniganj Basin, India.* Journal of Petroleum Exploration and Production Technology, 2019. **9**(2): p. 1041-1050.
93. Wang, L., et al., *Experimental Study and Modeling of the Effect of Pore Size Distribution on Hydrocarbon Phase Behavior in Nanopores*, in *SPE Annual Technical Conference and Exhibition*. 2014, Society of Petroleum Engineers: Amsterdam, The Netherlands. p. 15.
94. Wang, L., et al., *Effect of Pore-Size Distribution on Phase Transition of Hydrocarbon Mixtures in Nanoporous Media.* SPE Journal, 2016. **21**(06): p. 1981-1995.
95. Luo, S., J.L. Lutkenhaus, and H. Nasrabadi, *Effect of Nano-Scale Pore Size Distribution on Fluid Phase Behavior of Gas IOR in Shale Reservoirs*, in *SPE Improved Oil Recovery Conference*. 2018, Society of Petroleum Engineers: Tulsa, Oklahoma, USA. p. 14.
96. Liu, J., et al., *Multicomponent Shale Oil Flow in Real Kerogen Structures via Molecular Dynamic Simulation.* Energies, 2020. **13**(15): p. 3815.
97. Wang, Y., et al., *Characteristics of the Nanoscale Pore Structure in Northwestern Hunan Shale Gas Reservoirs Using Field Emission Scanning Electron Microscopy, High-Pressure Mercury Intrusion, and Gas Adsorption.* Energy & Fuels, 2014. **28**(2): p. 945-955.
98. Liu, Q. and B. Xu, *Actuating Water Droplets on Graphene via Surface Wettability Gradients.* Langmuir, 2015. **31**(33): p. 9070-9075.
99. Jagadisan, A. and Z. Heidari, *Impacts of Geochemical Properties on Wettability of Kerogen and Organic-rich Mudrocks*, in *Unconventional Resources Technology Conference, Houston, Texas, 23-25 July 2018*. 2018, Society of Exploration Geophysicists, American Association of Petroleum Geologists, Society of Petroleum Engineers. p. 3149-3166.
100. Jagadisan, A. and Z. Heidari, *Experimental Quantification of Kerogen Wettability as a Function of Thermal Maturity*, in *SPWLA 59th Annual Logging Symposium*. 2018, Society of Petrophysicists and Well-Log Analysts: London, UK. p. 14.
101. Wang, S., et al., *Wettability and Surface Free Energy of Graphene Films.* Langmuir, 2009. **25**(18): p. 11078-11081.
102. Ho, T.A., et al., *Differential retention and release of CO2 and CH4 in kerogen nanopores: Implications for gas extraction and carbon sequestration.* Fuel, 2018. **220**: p. 1-7.
103. Wu, T., et al., *Absolute adsorption of light hydrocarbons and carbon dioxide in shale rock and isolated kerogen.* Fuel, 2019. **235**: p. 855-867.
104. Medeiros, F., et al., *Analysis of Production Data From Hydraulically Fractured Horizontal Wells in Shale Reservoirs.* SPE Reservoir Evaluation & Engineering, 2010. **13**(03): p. 559-568.
105. Fan, L., J.W. Thompson, and J.R. Robinson, *Understanding Gas Production Mechanism and Effectiveness of Well Stimulation in the Haynesville Shale Through Reservoir Simulation*, in *Canadian Unconventional Resources and International Petroleum Conference*. 2010, Society of Petroleum Engineers: Calgary, Alberta, Canada. p. 15.
106. Peng, D.-Y. and D.B. Robinson, *A New Two-Constant Equation of State.* Industrial & Engineering Chemistry Fundamentals, 1976. **15**(1): p. 59-64.
107. Firoozabadi, A., *Thermodynamics and Applications of Hydrocarbons Energy Production*. 2015: McGraw-Hill Education.
108. Whitson, C.H. and S.B. Torp, *Evaluating Constant-Volume Depletion Data.* Journal of Petroleum Technology, 1983. **35**(03): p. 610-620.
109. Behnous, D., N. Zeraibi, and D. Belgacem. *Study of Gas Condensate Reservoir Behaviour using PVT Experiment*. 2017.

110. Evans, R., U.M.B. Marconi, and P. Tarazona, *Fluids in narrow pores: Adsorption, capillary condensation, and critical points.* The Journal of Chemical Physics, 1986. **84**(4): p. 2376-2399.
111. Li, L., et al., *Experimental investigation of shale oil recovery from Qianjiang core samples by the CO2 huff-n-puff EOR method.* RSC Advances, 2019. **9**(49): p. 28857-28869.
112. Ma, Q., et al., *Experimental investigation on the influence factors and oil production distribution in different pore sizes during CO2 huff-n-puff in an ultra-high-pressure tight oil reservoir.* Journal of Petroleum Science and Engineering, 2019. **178**: p. 1155-1163.
113. Liu, B.-T., et al., *Extraordinary pseudocapacitive energy storage triggered by phase transformation in hierarchical vanadium oxides.* Nature Communications, 2018. **9**(1): p. 1375.
114. Cervilla, A., et al., *Intercalation of [MoVIO2(O2CC(S)Ph2)2]2- in a Zn(II)-Al(III) Layered Double Hydroxide Host: A Strategy for the Heterogeneous Catalysis of the Air Oxidation of Thiols.* Journal of the American Chemical Society, 1994. **116**(4): p. 1595-1596.
115. Kim, H., et al., *Water harvesting from air with metal-organic frameworks powered by natural sunlight.* Science, 2017. **356**(6336): p. 430.
116. Tröstl, J., et al., *The role of low-volatility organic compounds in initial particle growth in the atmosphere.* Nature, 2016. **533**(7604): p. 527-531.
117. Ehn, M., et al., *A large source of low-volatility secondary organic aerosol.* Nature, 2014. **506**(7489): p. 476-479.
118. Yuan, J., et al., *Superwetting nanowire membranes for selective absorption.* Nature Nanotechnology, 2008. **3**(6): p. 332-336.
119. Lee, M., et al., *Noncontact friction via capillary shear interaction at nanoscale.* Nature Communications, 2015. **6**(1): p. 7359.
120. Scherer, G.W., *Theory of Drying.* Journal of the American Ceramic Society, 1990. **73**(1): p. 3-14.
121. Vorhauer, N., et al., *Drying with Formation of Capillary Rings in a Model Porous Medium.* Transport in Porous Media, 2015. **110**(2): p. 197-223.
122. Nambo, A., et al., *Ultrafast Carbon Dioxide Sorption Kinetics Using Lithium Silicate Nanowires.* Nano Letters, 2017. **17**(6): p. 3327-3333.
123. Wang, J., et al., *Vapor-Condensation-Assisted Optical Microscopy for Ultralong Carbon Nanotubes and Other Nanostructures.* Nano Letters, 2014. **14**(6): p. 3527-3533.
124. Wu, Q., et al., *Development of a New Generation of Stable, Tunable, and Catalytically Active Nanoparticles Produced by the Helium Nanodroplet Deposition Method.* The Journal of Physical Chemistry Letters, 2016. **7**(15): p. 2910-2914.
125. Administration, U.E.I., *Annual Energy Outlook 2020.* 2020.
126. Jones, D.G. and H.M. Fretwell, *Condensation and Freezing of a Binary Gas Mixture Adsorbed in Mesoporous Vycor Glass.* Langmuir, 2003. **19**(21): p. 9018-9022.
127. Yun, J.-H., et al., *Adsorption of Methane, Ethane, and Their Binary Mixtures on MCM-41: Experimental Evaluation of Methods for the Prediction of Adsorption Equilibrium.* Langmuir, 2002. **18**(7): p. 2693-2701.
128. Qiao, S.Z., S.K. Bhatia, and D. Nicholson, *Study of Hexane Adsorption in Nanoporous MCM-41 Silica.* Langmuir, 2004. **20**(2): p. 389-395.
129. Yang, Q., et al., *Direct visualization and molecular simulation of dewpoint pressure of a confined fluid in sub-10 nm slit pores.* Fuel, 2019. **235**: p. 1216-1223.

130. Liu, X. and D. Zhang, *A review of phase behavior simulation of hydrocarbons in confined space: Implications for shale oil and shale gas.* Journal of Natural Gas Science and Engineering, 2019. **68**: p. 102901.
131. Jin, B. and H. Nasrabadi, *Phase Behavior in Shale Organic/Inorganic Nanopores From Molecular Simulation.* SPE Reservoir Evaluation & Engineering, 2018. **21**(03): p. 626-637.
132. Panagiotopoulos, A.Z., *Direct determination of phase coexistence properties of fluids by Monte Carlo simulation in a new ensemble.* Molecular Physics, 1987. **61**(4): p. 813-826.
133. Ritschel, T.K.S. and J.B. Jørgensen, *Dynamic optimization of thermodynamically rigorous models of multiphase flow in porous subsurface oil reservoirs.* Journal of Process Control, 2019. **78**: p. 45-56.
134. Lee, S.H., et al., *A conservative sequential fully implicit method for compositional reservoir simulation.* Journal of Computational Physics, 2021. **428**: p. 109961.
135. Polívka, O. and J. Mikyška, *Compositional modeling in porous media using constant volume flash and flux computation without the need for phase identification.* Journal of Computational Physics, 2014. **272**: p. 149-169.
136. Zidane, A. and A. Firoozabadi, *Fracture-cross-flow equilibrium in compositional two-phase reservoir simulation.* SPE Journal, 2017. **22**(03): p. 950-970.
137. Nichita, D.V., *New unconstrained minimization methods for robust flash calculations at temperature, volume and moles specifications.* Fluid Phase Equilibria, 2018. **466**: p. 31-47.
138. Jindrová, T. and J. Mikyška, *Fast and robust algorithm for calculation of two-phase equilibria at given volume, temperature, and moles.* Fluid Phase Equilibria, 2013. **353**: p. 101-114.
139. Mikyška, J. and A. Firoozabadi, *A new thermodynamic function for phase-splitting at constant temperature, moles, and volume.* AIChE Journal, 2011. **57**(7): p. 1897-1904.
140. Lu, C., Z. Jin, and H.A. Li, *A two-phase flash algorithm with the consideration of capillary pressure at specified mole numbers, volume and temperature.* Fluid Phase Equilibria, 2019. **485**: p. 67-82.
141. Kou, J. and S. Sun, *A stable algorithm for calculating phase equilibria with capillarity at specified moles, volume and temperature using a dynamic model.* Fluid Phase Equilibria, 2018. **456**: p. 7-24.
142. Rangarajan, B., C.T. Lira, and R. Subramanian, *Simplified local density model for adsorption over large pressure ranges.* AIChE Journal, 1995. **41**(4): p. 838-845.
143. Shapiro, A.A. and E.H. Stenby, *Potential Theory of Multicomponent Adsorption.* Journal of Colloid and Interface Science, 1998. **201**(2): p. 146-157.
144. Polanyi, M., *Über die Adsorption vom Standpunkt des dritten Wärmesatzes.* Verh. Dtsch. Phys. Ges, 1914. **16**: p. 1012-1016.
145. Polanyi, M., *Adsorption of gases (vapors) by a solid non-volatile adsorbent.* Verh. Dtsch. Phys. Ges, 1916. **18**: p. 55-80.
146. Travalloni, L., et al., *Thermodynamic modeling of confined fluids using an extension of the generalized van der Waals theory.* Chemical Engineering Science, 2010. **65**(10): p. 3088-3099.
147. Travalloni, L., et al., *Critical behavior of pure confined fluids from an extension of the van der Waals equation of state.* The Journal of Supercritical Fluids, 2010. **55**(2): p. 455-461.
148. Sandoval, D.R., et al., *Influence of Adsorption and Capillary Pressure on Phase Equilibria inside Shale Reservoirs.* Energy & Fuels, 2018. **32**(3): p. 2819-2833.

149. Wang, Y., et al., *Validity of the Kelvin equation and the equation-of-state-with-capillary-pressure model for the phase behavior of a pure component under nanoconfinement.* Chemical Engineering Science, 2020. **226**: p. 115839.
150. Liu, Y., Z. Jin, and H.A. Li, *Comparison of Peng-Robinson Equation of State With Capillary Pressure Model With Engineering Density-Functional Theory in Describing the Phase Behavior of Confined Hydrocarbons.* SPE Journal, 2018. **23**(05): p. 1784-1797.
151. Yu, W. and K. Sepehrnoori, *Shale Gas and Tight Oil Reservoir Simulation*. 2018: Elsevier Science.
152. Li, Z., Z. Jin, and A. Firoozabadi, *Phase Behavior and Adsorption of Pure Substances and Mixtures and Characterization in Nanopore Structures by Density Functional Theory.* SPE Journal, 2014. **19**(6): p. 1096-1109.
153. Rosenfeld, Y., *Free-energy model for the inhomogeneous hard-sphere fluid mixture and density-functional theory of freezing.* Physical Review Letters, 1989. **63**(9): p. 980-983.
154. Ebner, C. and W.F. Saam, *New Phase-Transition Phenomena in Thin Argon Films.* Physical Review Letters, 1977. **38**(25): p. 1486-1489.
155. Jin, Z., *Bubble/dew point and hysteresis of hydrocarbons in nanopores from molecular perspective.* Fluid Phase Equilibria, 2017. **458**.
156. Li, Z. and A. Firoozabadi, *Interfacial tension of nonassociating pure substances and binary mixtures by density functional theory combined with Peng–Robinson equation of state.* The Journal of Chemical Physics, 2009. **130**(15): p. 154108.
157. Demirel, Y., *Chapter 1 - Fundamentals of Equilibrium Thermodynamics*, in *Nonequilibrium Thermodynamics (Third Edition)*, Y. Demirel, Editor. 2014, Elsevier: Amsterdam. p. 1-74.
158. Evans, R., *The nature of the liquid-vapour interface and other topics in the statistical mechanics of non-uniform, classical fluids.* Advances in Physics, 1979. **28**(2): p. 143-200.
159. Weinaug, C.F. and D.L. Katz, *Surface Tensions of Methane-Propane Mixtures.* Industrial & Engineering Chemistry, 1943. **35**(2): p. 239-246.
160. Li, Y., J. Kou, and S. Sun, *Thermodynamically Stable Two-Phase Equilibrium Calculation of Hydrocarbon Mixtures with Capillary Pressure.* Industrial & Engineering Chemistry Research, 2018. **57**(50): p. 17276-17288.
161. Mi, J., et al., *Prediction of phase behavior of nanoconfined Lennard-Jones fluids with density functional theory based on the first-order mean spherical approximation.* The Journal of Chemical Physics, 2006. **124**(14): p. 144709.
162. Vishnyakov, A., et al., *Critical Properties of Lennard-Jones Fluids in Narrow Slit-Shaped Pores.* Langmuir, 2001. **17**(14): p. 4451-4458.
163. Jiang, J. and S.I. Sandler, *Adsorption and phase transitions on nanoporous carbonaceous materials: insights from molecular simulations.* Fluid Phase Equilibria, 2005. **228-229**: p. 189-195.
164. Rahmani Didar, B. and I.Y. Akkutlu, *Confinement Effects on Hydrocarbon Mixture Phase Behavior in Organic Nanopore*, in *Unconventional Resources Technology Conference*. 2015, Unconventional Resources Technology Conference: San Antonio, Texas, USA. p. 11.
165. Singh, S.K., A.K. Saha, and J.K. Singh, *Molecular Simulation Study of Vapor−Liquid Critical Properties of a Simple Fluid in Attractive Slit Pores: Crossover from 3D to 2D.* The Journal of Physical Chemistry B, 2010. **114**(12): p. 4283-4292.

166. Boersma, T. and C. Johnson, *The Shale Gas Revolution: U.S. and EU Policy and Research Agendas.* Review of Policy Research, 2012. **29**(4): p. 570-576.
167. Euzen, T., *Shale Gas—an Overview*, in *Technique Report*. 2011, IFP Technologies (Canada) Inc.
168. Chalmers, G., R. Bustin, and I. Power, *Characterization of gas shale pore systems by porosimetry, pycnometry, surface area, and field emission scanning electron microscopy/transmission electron microscopy image analyses: Examples from the Barnett, Woodford, Haynesville, Marcellus, and Doig units.* AAPG Bulletin, 2012. **96**: p. 1099-1119.
169. Kondash, A.J., N.E. Lauer, and A. Vengosh, *The intensification of the water footprint of hydraulic fracturing.* Science Advances, 2018. **4**(8): p. eaar5982.
170. Chen, C., et al., *A Many-Body Dissipative Particle Dynamics Study of Forced Water–Oil Displacement in Capillary.* Langmuir, 2012. **28**(2): p. 1330-1336.
171. Zou, C., et al., *Do Shale Pore Throats Have a Threshold Diameter for Oil Storage?* Scientific Reports, 2015. **5**(1): p. 13619.
172. Sedghi, M., M. Piri, and L. Goual, *Atomistic Molecular Dynamics Simulations of Crude Oil/Brine Displacement in Calcite Mesopores.* Langmuir, 2016. **32**(14): p. 3375-3384.
173. Zhang, Y., et al., *Molecular insight into the oil charging mechanism in tight reservoirs.* Chemical Engineering Science, 2020. **211**: p. 115297.
174. Coskun, S.B. and N.C. Wardlaw, *Influences of pore geometry, porosity and permeability on initial water saturation — An empirical method for estimating initial water saturation by image analysis.* Journal of Petroleum Science and Engineering, 1995. **12**(4): p. 295-308.
175. Taktak, F., et al., *Modelling approaches for the estimation of irreducible water saturation and heterogeneities of the commercial Ashtart reservoir from the Gulf of Gabès, Tunisia.* Journal of Petroleum Science and Engineering, 2011. **78**(2): p. 376-383.
176. Brown, H.W., *Capillary pressure investigations.* Journal of Petroleum Technology, 1951. **3**(03): p. 67-74.
177. Amirpour, M., et al., *Experimental investigation of wettability alteration on residual oil saturation using nonionic surfactants: Capillary pressure measurement.* Petroleum, 2015. **1**(4): p. 289-299.
178. Bear, J., B. Rubinstein, and L. Fel, *Capillary Pressure Curve for Liquid Menisci in a Cubic Assembly of Spherical Particles Below Irreducible Saturation.* Transport in Porous Media, 2011. **89**(1): p. 63-73.
179. Sigal, R.F., *Mercury capillary pressure measurements on Barnett core.* SPE Reservoir Evaluation & Engineering, 2013. **16**(04): p. 432-442.
180. Tian, S., et al., *Dynamic effect of capillary pressure in low permeability reservoirs.* Petroleum Exploration and Development, 2012. **39**(3): p. 405-411.
181. Eijkel, J., *Liquid slip in micro- and nanofluidics: recent research and its possible implications.* Lab on a chip, 2007. **7**(3): p. 299-301.
182. Sbragaglia, M., et al., *Surface roughness-hydrophobicity coupling in microchannel and nanochannel flows.* Physical review letters, 2006. **97**(20): p. 204503.
183. Cottin-Bizonne, C., et al., *Dynamics of simple liquids at heterogeneous surfaces: Molecular-dynamics simulations and hydrodynamic description.* The European Physical Journal E, 2004. **15**(4): p. 427-438.

184. Zhang, H., et al., *A theoretical discussion and case study on the oil-charging throat threshold for tight reservoirs.* Petroleum Exploration and Development, 2014. **41**(3): p. 408-416.
185. Hou, D., J. Yu, and P. Wang, *Molecular dynamics modeling of the structure, dynamics, energetics and mechanical properties of cement-polymer nanocomposite.* Composites Part B: Engineering, 2019. **162**: p. 433-444.
186. Sedghi, M., M. Piri, and L. Goual, *Molecular dynamics of wetting layer formation and forced water invasion in angular nanopores with mixed wettability.* The Journal of Chemical Physics, 2014. **141**(19): p. 194703.
187. Zhang, Y. and W. Guo, *Molecular insight into the tight oil movability in nano-pore throat systems.* Fuel, 2021. **293**: p. 120428.
188. Lu, Y., et al., *Wetting Behavior of Shale Rocks and Its Relationship to Oil Composition.* Energy & Fuels, 2019. **33**(12): p. 12270-12277.
189. Yu, H., et al., *Roughness Factor-Dependent Transport Characteristic of Shale Gas through Amorphous Kerogen Nanopores.* The Journal of Physical Chemistry C, 2020. **124**(23): p. 12752-12765.
190. Breger, I.A. and A. Brown, *Kerogen in the Chattanooga Shale: Study of its origin and composition suggests why these shales are not source beds for petroleum.* Science, 1962. **137**(3525): p. 221-4.
191. Ungerer, P., J. Collell, and M. Yiannourakou, *Molecular modeling of the volumetric and thermodynamic properties of kerogen: Influence of organic type and maturity.* Energy & Fuels, 2015. **29**(1): p. 91-105.
192. Tian, Y., C. Yan, and Z. Jin, *Characterization of Methane Excess and Absolute Adsorption in Various Clay Nanopores from Molecular Simulation.* Scientific Reports, 2017. **7**(1): p. 12040.
193. Gelb, L.D. and K. Gubbins, *Pore size distributions in porous glasses: a computer simulation study.* Langmuir, 1999. **15**(2): p. 305-308.
194. Young, T., *III. An essay on the cohesion of fluids.* Philosophical Transactions of the Royal Society of London, 1805. **95**: p. 65-87.
195. Laplace, P., *Mécanique celeste 10.* Supplement to the tenth edition, 1806.
196. Parrinello, M. and A. Rahman, *Polymorphic transitions in single crystals: A new molecular dynamics method.* Journal of Applied Physics, 1981. **52**(12): p. 7182-7190.
197. Talu, O. and A.L. Myers, *Reference potentials for adsorption of helium, argon, methane, and krypton in high-silica zeolites.* Colloids and Surfaces A: Physicochemical and Engineering Aspects, 2001. **187**: p. 83-93.
198. Gelb, L.D. and K. Gubbins, *Characterization of porous glasses: Simulation models, adsorption isotherms, and the Brunauer− Emmett− Teller analysis method.* Langmuir, 1998. **14**(8): p. 2097-2111.
199. Martínez, L., et al., *PACKMOL: a package for building initial configurations for molecular dynamics simulations.* Journal of computational chemistry, 2009. **30**(13): p. 2157-2164.
200. Berendsen, H.J., D. van der Spoel, and R. van Drunen, *GROMACS: a message-passing parallel molecular dynamics implementation.* Computer physics communications, 1995. **91**(1-3): p. 43-56.
201. Van Der Spoel, D., et al., *GROMACS: fast, flexible, and free.* Journal of computational chemistry, 2005. **26**(16): p. 1701-1718.

202. Ho, T.A., et al., *Supercritical CO2-induced atomistic lubrication for water flow in a rough hydrophilic nanochannel.* Nanoscale, 2018. **10**(42): p. 19957-19963.
203. Chong, L., et al., *Molecular characterization of carbon dioxide, methane, and water adsorption in micropore space of kerogen matrix.* Fuel, 2021. **283**: p. 119254.
204. Michalec, L. and M. Lísal, *Molecular simulation of shale gas adsorption onto overmature type II model kerogen with control microporosity.* Molecular Physics, 2017. **115**(9-12): p. 1086-1103.
205. Berendsen, H.J.C., J.R. Grigera, and T.P. Straatsma, *The missing term in effective pair potentials.* The Journal of Physical Chemistry, 1987. **91**(24): p. 6269-6271.
206. Martin, M.G. and J.I. Siepmann, *Transferable Potentials for Phase Equilibria. 1. United-Atom Description of n-Alkanes.* The Journal of Physical Chemistry B, 1998. **102**(14): p. 2569-2577.
207. Miyamoto, S. and P.A. Kollman, *Settle: An analytical version of the SHAKE and RATTLE algorithm for rigid water models.* Journal of computational chemistry, 1992. **13**(8): p. 952-962.
208. Hess, B., et al., *LINCS: A linear constraint solver for molecular simulations.* Journal of Computational Chemistry, 1997. **18**(12): p. 1463-1472.
209. Bussi, G., D. Donadio, and M. Parrinello, *Canonical sampling through velocity rescaling.* The Journal of Chemical Physics, 2007. **126**(1): p. 014101.
210. Allen, M. and D. Tildesley, *Computer Simulation of Liquids (Clarendon Press, Oxford, 1987).*
211. Sun, Z., et al., *Molecular dynamics of methane flow behavior through realistic organic nanopores under geologic shale condition: Pore size and kerogen types.* Chemical Engineering Journal, 2020. **398**: p. 124341.
212. York, D.M., T.A. Darden, and L.G. Pedersen, *The effect of long-range electrostatic interactions in simulations of macromolecular crystals: A comparison of the Ewald and truncated list methods.* The Journal of chemical physics, 1993. **99**(10): p. 8345-8348.
213. Jiménez-Ángeles, F. and A. Firoozabadi, *Contact Angle, Liquid Film, and Liquid–Liquid and Liquid–Solid Interfaces in Model Oil–Brine–Substrate Systems.* The Journal of Physical Chemistry C, 2016. **120**(22): p. 11910-11917.
214. Padró, J., L. Saiz, and E. Guardia, *Hydrogen bonding in liquid alcohols: a computer simulation study.* Journal of Molecular Structure, 1997. **416**(1-3): p. 243-248.
215. Smith, W.O. and M.D. Crane, *THE JAMIN EFFECT IN CYLINDRICAL TUBES.* Journal of the American Chemical Society, 1930. **52**(4): p. 1345-1349.
216. Liang, M., et al., *Minimum applied pressure for a drop through an abruptly constricted capillary.* Microfluidics and Nanofluidics, 2015. **19**(1): p. 1-8.
217. Jagadisan, A. and Z. Heidari, *Impact of Geochemical Properties on Wettability of Kerogen and Organic-Rich Mudrocks.* SPE Reservoir Evaluation & Engineering, 2020. **23**(02): p. 758-771.
218. Tesson, S. and A. Firoozabadi, *Methane Adsorption and Self-Diffusion in Shale Kerogen and Slit Nanopores by Molecular Simulations.* The Journal of Physical Chemistry C, 2018. **122**(41): p. 23528-23542.
219. Hansen, G., A.A. Hamouda, and R. Denoyel, *The effect of pressure on contact angles and wettability in the mica/water/n-decane system and the calcite+stearic acid/water/n-decane system.* Colloids and Surfaces A: Physicochemical and Engineering Aspects, 2000. **172**(1): p. 7-16.

220. López-Cuevas, J., et al., *A Practical Procedure for Measuring Contact Angles in Wettability Studies by the Sessile Drop Method.* MRS Advances, 2019. **4**(57): p. 3143-3152.
221. Kwok, D.Y., et al., *Contact Angle Measurements and Contact Angle Interpretation. 1. Contact Angle Measurements by Axisymmetric Drop Shape Analysis and a Goniometer Sessile Drop Technique.* Langmuir, 1997. **13**(10): p. 2880-2894.
222. McCaffery, F.G. and N. Mungan, *Contact Angle And Interfacial Tension Studies of Some Hydrocarbon-Water-Solid Systems.* Journal of Canadian Petroleum Technology, 1970. **9**(03).
223. Jiang, H. and A.J. Patel, *Recent advances in estimating contact angles using molecular simulations and enhanced sampling methods.* Current Opinion in Chemical Engineering, 2019. **23**: p. 130-137.
224. Scocchi, G., et al., *Wetting and contact-line effects for spherical and cylindrical droplets on graphene layers: A comparative molecular-dynamics investigation.* Physical review. E, Statistical, nonlinear, and soft matter physics, 2011. **84**: p. 061602.
225. Weijs, J.H., et al., *Origin of line tension for a Lennard-Jones nanodroplet.* Physics of Fluids, 2011. **23**(2): p. 022001.
226. Wang, S., F. Javadpour, and Q. Feng, *Confinement correction to mercury intrusion capillary pressure of shale nanopores.* Scientific reports, 2016. **6**(1): p. 1-12.
227. Kirkwood, J.G. and F.P. Buff, *The statistical mechanical theory of surface tension.* The Journal of Chemical Physics, 1949. **17**(3): p. 338-343.
228. McCaffery, F.G., *Measurement of interfacial tensions and contact angles at high temperature and pressure.* Journal of Canadian Petroleum Technology, 1972. **11**(03).
229. Pang, W. and Z. Jin, *Revisiting methane absolute adsorption in organic nanopores from molecular simulation and Ono-Kondo lattice model.* Fuel, 2019. **235**: p. 339-349.
230. Gelb, L.D. and K.E. Gubbins, *Characterization of Porous Glasses: Simulation Models, Adsorption Isotherms, and the Brunauer−Emmett−Teller Analysis Method.* Langmuir, 1998. **14**(8): p. 2097-2111.
231. Gelb, L.D. and K.E. Gubbins, *Pore Size Distributions in Porous Glasses: A Computer Simulation Study.* Langmuir, 1999. **15**(2): p. 305-308.
232. Ho, T.A., et al., *Interfacial water on crystalline silica: a comparative molecular dynamics simulation study.* Molecular Simulation, 2011. **37**(3): p. 172-195.
233. Li, Z., J. Yao, and A. Firoozabadi, *Kerogen Swelling in Light Hydrocarbon Gases and Liquids and Validity of Schroeder's Paradox.* The Journal of Physical Chemistry C, 2021. **125**(15): p. 8137-8147.
234. Tesson, S. and A. Firoozabadi, *Deformation and Swelling of Kerogen Matrix in Light Hydrocarbons and Carbon Dioxide.* The Journal of Physical Chemistry C, 2019. **123**(48): p. 29173-29183.
235. Bett, G., et al., *Determination of polar compounds in Rundle shale oil.* Fuel, 1983. **62**(12): p. 1445-1454.
236. Ebner, C., W.F. Saam, and D. Stroud, *Density-functional theory of simple classical fluids. I. Surfaces.* Physical Review A, 1976. **14**(6): p. 2264-2273.
237. Yu, Y.-X. and J. Wu, *Density functional theory for inhomogeneous mixtures of polymeric fluids.* The Journal of Chemical Physics, 2002. **117**(5): p. 2368-2376.

238. Jhaveri, B.S. and G.K. Youngren, *Three-Parameter Modification of the Peng-Robinson Equation of State To Improve Volumetric Predictions.* SPE Reservoir Engineering, 1988. **3**(03): p. 1033-1040.
239. Liu, Y., Z. Jin, and H.A. Li, *Comparison of PR-EOS with Capillary Pressure Model with Engineering Density Functional Theory on Describing the Phase Behavior of Confined Hydrocarbons.* SPE Journal, 2018. **In Press**.
240. Singh, S.K., et al., *Vapor−Liquid Phase Coexistence, Critical Properties, and Surface Tension of Confined Alkanes.* The Journal of Physical Chemistry C, 2009. **113**(17): p. 7170-7180.